

ADVANCED TECHNIQUES FOR FUTURE
GENERATION GRAVITATIONAL WAVE
DETECTORS

TENG ZHANG

BSc

SUBMITTED IN FULFILMENT OF THE REQUIREMENTS FOR THE DEGREE OF

Doctor of Philosophy

SCHOOL OF PHYSICS AND ASTRONOMY
COLLEGE OF SCIENCE AND ENGINEERING
UNIVERSITY OF GLASGOW

JULY 2019

Abstract

After the first direct detection of gravitational waves (GW) from a system of two colliding black holes, we have stepped into the era of gravitational-wave astronomy. In order to observe the broader and deeper universe, increase the detection rate for various sources and do better source parameter extraction, it is essential to further enhance the sensitivity of gravitational wave detectors. The design sensitivities of the current detectors are limited by quantum noise nearly over the whole detection band.

Various *quantum non-demolition* technologies have been proposed to suppress the quantum noise, one of which is called speed meter. Speed meter aims to improve the detector sensitivity at low frequencies. Not only it can beat the standard quantum limit but also gives lots of astrophysics prospects. For example, it gives longer warning time before the merge stage of binaries and it significantly improves the detection rate of massive binary black holes (so far we have not observe any systems with component masses prior to merger greater than 50 solar masses) allowing to uncover the potential existence of black hole population in this range.

One speed meter experiment, Sagnac speed meter (SSM) proof of concept experiment is currently carried out in Glasgow. This experiment aims to prove the superiority of speed meters in terms of quantum radiation pressure noise in the low frequency compared with an equivalent Michelson. One property of the Sagnac interferometer is that the light fields returning from the arms in two directions share the same path and always interfere destructively at the signal port. This property is unsuitable for conventional DC readout and pushes the utilisation of balanced homodyne readout. Balanced homodyne readout is also planned to be implemented in advanced LIGO upgrade, A+. This thesis introduces several research topics around speed meters and balanced homodyne readout.

One problem of implementing balanced homodyne readout is the optical loss because of the misalignment and mismatch between the separate local oscillator and signal beam in balanced homodyne readout. A theoretical framework is built for analysing the static and dynamic optical higher order modes effects. The results are applied to the Glasgow proof of concept experiment. Misalignment is not only a problem in the balanced homodyne readout, but also in the Sagnac interferometer itself. The effect of misalignment inside the Sagnac interferometer on the quantum noise limited sensitivity is calculated with the example of the Glasgow SSM experiment. Strategies for the implementation of an auto-alignment scheme in SSM experiment are investigated.

I also investigate several aspects of considerations on implementing balanced homodyne readout in A+, including local oscillator stability requirement, output mode cleaner arrangement, local oscillator backscattering effects and sensing and control for different degrees of freedom in the balanced homodyne readout.

For Sagnac speed meter with Fabry-Pérot resonators in the arms, it was shown theoretically that an asymmetry of the main beamsplitter can lead to a reduction of the quantum limited sensitivity at low frequencies. We propose an approach to solve this problem by utilising balanced homodyne readout and choosing a proper local oscillator delivery port.

In Sagnac speed meter interferometer, ring cavities are required. Different from linear cavities, the circulating beam in the ring cavities and the normal of the input mirror are not on the same line. The backscattering inside the ring cavity due to mirrors micro-roughness can induce coupling between the two counter-propagating modes. I analyse the effect of backscattering on quantum noise of a ring cavity when conducting measurement at one output port. Starting from previous work in [1], I develop here a more in depth analysis of the backscattering mechanism and present the results distinguished into three characteristic levels of backscattering amplitude. Again this is carried out using the Glasgow SSM experiment as an example.

In addition to Sagnac interferometer, other more advanced types of speed meter have been proposed by the community, including one based on the principle of Einstein Podolsky Rosen entanglement. I analyse the effect of several imperfections on quantum noise and the potential sensitivity improvement by injecting frequency dependent squeezing.

Another new speed meter configuration is based on a standard Michelson interferometer featuring additional polarisation optics in the output port, named as polarisation circulation speed meter. I propose an acceleration meter configuration based on the combination of the Sagnac speed meter and the polarisation circulation speed meter.

With no doubt that the loss-less variational readout scheme is better than speed meter, however, it is more susceptible to optical loss compared with speed meter in real environment. Here I develop a comparison between speed meters and position meters with lossy variational readout.

Revision history

Version	Date	Description
1.0.0	2019-07-02	Submitted for examination
1.1.0	2019-10-12	Corrected version sent to senate

Content from this work may be used under the terms of the Creative Commons *Attribution-NonCommercial-ShareAlike 4.0 International* licence.

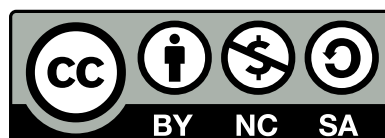


Table of contents

Abstract	iii
Revision history	v
Licence	vi
Table of contents	vii
List of figures	xi
Acknowledgements	xv
Preface	xvii
1 Introduction	1
1.1 Gravitational waves	1
1.2 Noise sources of the ground based interferometer	3
1.2.1 Seismic noise	4
1.2.2 Laser noise	4
1.2.3 Thermal noise	6
1.2.4 Quantum noise	7
1.3 Fundamental features of gravitational wave detector	9
1.3.1 Fabry-Perot cavity	9
1.3.2 Power recycling cavity	12
1.3.3 Signal recycling cavity	13
1.3.4 Homodyne readout	13
1.4 Overcoming standard quantum limit	14
1.4.1 Standard quantum limit	14
1.4.2 Squeezed vacuum injection	16
1.4.3 Variational readout	16
1.4.4 Speed meter	17

2	Sagnac Speed meter proof of concept experiment and laser stabilisation	21
2.1	Conceptual design and sensitivity	21
2.2	Optical layout	22
2.3	Suspensions	23
2.4	Vacuum system	24
2.5	Linear cavity and frequency stabilisation	24
2.5.1	Alignment and mode matching of linear cavity	24
2.5.2	Linear cavity locking	27
2.5.3	Frequency Stabilisation	28
2.5.4	Amplitude Stabilisation	29
2.6	Summary	30
3	Balanced-homodyne readout with higher optical modes	31
4	Balanced-homodyne readout for aLIGO+	45
4.1	Requirement for local oscillator path stability	46
4.1.1	Output mode cleaner (OMC) stability	48
4.2	Local oscillator delivery options	53
4.3	Sensing and control	54
4.3.1	Degrees of freedom	54
4.3.2	BHD readout angle control	55
4.3.3	Length of each of the two OMCs	57
4.3.4	Alignment between LO and signal beam	58
4.3.5	Input alignment of the combined LO and signal beams to OMCs . .	60
4.3.6	Summary	62
5	Quantum noise cancellation in asymmetric speed meters with balanced homodyne readout	63

6	On the misalignment and alignment of Sagnac speed meter interferometer	75
6.1	Sagnac interferometer in plane wave mode profile	76
6.2	I/O relations for misaligned optics	78
6.3	Static misalignments in Sagnac Interferometer and quantum noise	81
6.4	Autoalignment strategies for dynamic misalignment	84
6.5	Summary	90
7	Backscattering effects on quantum noise of ring cavities	93
7.1	Optical I/O relations of a beamsplitter	94
7.2	Opto-mechanical I/O relations of a ring cavity	95
7.3	Amplitude quantum noise spectral density in displacement	99
7.3.1	Strain sensitivity calibration	102
7.3.2	Quantum constraints of 2×4 pole system	104
7.3.3	Summary	107
8	Analysis of imperfections of EPR type speed meters and squeezing	109
8.1	EPR speed meter conception	109
8.2	Impacts of imperfections	110
8.3	Squeezing enhancement	115
8.4	Summary	118
9	An acceleration meter	121
9.1	Acceleration measurement	122
9.2	Quantum noise	123
9.3	Summary	127
10	Conclusions	129
A	Comparison of lossy variational readout versus speed meter	133
B	Finesse input file of A+ for balanced homodyne readout	137
C	Finesse input file of Glasgow SSM experiment	149
	Bibliography	161

List of figures

1.1	Effects of gravitational waves on a ring of free test masses on the plane orthogonal to its propagation. The distance between two test mass get squeezed or stretched by δL following the rule of Eq. 1.2.	3
1.2	The schematic of a simple Michelson interferometer. BS represents the beamsplitter. The two ports are labeled as symmetric port (laser port) and asymmetric port (signal port), respectively.	4
1.3	Measured horizontal and vertical ground motion in the lab of University of Glasgow [7]	5
1.4	Schematic of a Fabry-Perot cavity. The input field ' a ' at the can be misaligned respected to the dashed line reference, the reflection field are represented by ' b ', the transmission field is represented by ' t ', ' t' ' is the input from the end test mass port.	9
1.5	The schematic of a continuous linear measurement system.	15
1.6	Conceptual scheme of speed measurement. The laser photons consecutively hit on the front surface and rear surface with a time delay. The laser phase is modulated by the test mass motion and measured by a phase meter.	17
1.7	Schematic of Sagnac speed meter.	18
1.8	Schematic of polarisation circulation speed meter.	19
2.1	Design sensitivity of the Glasgow SSM experiment and equivalent Michelson.	22
2.2	Optical layout of Glasgow SSM experiment. For a detailed description please refer to the main text. [7]	23
2.3	Optical layout of the linear cavity.	24
2.4	The layout of the linear cavity experiment.	25
2.5	The snapshot of the design of mode matching.	26
2.6	The optical mode pictures while scanning the whole free spectral range. .	27

2.7	The displacement noise spectral density of the linear cavity in vacuum.	28
2.8	The amplitude spectral density of laser intensity noise.	29
4.1	Schematic of simple balanced homodyne readout layout. ‘IFO’ represents the main interferometer, ‘Sig’ represents the signal beam, ‘LO’ represents the local oscillator beam, P_1 and P_2 are two fields after the BHD beamsplitter, I_1 and I_2 are the photocurrents of two photodiodes.	46
4.2	Stability requirement of the LO phase for aLIGO and A+ employing BHD.	49
4.3	Level of OMC induced phase noise fluctuations which would cause a noise contribution similar to the design sensitivity of Advanced LIGO and A+.	50
4.4	Options of output mode cleaners arrangement to eliminate the mode cleaners phase noise coupling.	51
4.5	Simplified aLIGO optical layout. This plot is taken from [65] and is modified to indicate two local oscillator pick off port options, <i>i.e.</i> POP port and BSAR port.	52
4.6	The ratio of the scattering transfer functions in POP option over BSAR option.	53
4.7	The schematic of the optical layout design of A+ BHD and sensing schemes.	55
4.8	The error signal of the homodyne angle.	56
4.9	The error signal of OMCA length variation.	58
4.10	Simulated errors signal for alignment between signal beam reflection and local oscillation beam transmission of BHD beamsplitter in pitch and yaw degrees of freedom.	59
4.11	The error signal for input alignment of the combined beam from BHD beam splitter to OMCA in pitch and yaw degrees of freedom.	61
6.1	Simplified diagram of optical layout of the Glasgow Sagnac speed meter proof of concept experiment.	79
6.2	Simplified flow chart of the I/O relation of the interferometer according to Fig. 6.1.	80
6.3	The quantum noise limited sensitivity of Glasgow speed meter experiment in cases of different misalignment conditions.	82
6.4	Diagram of showing the locations of differential wave front sensing schemes.	84
6.5	Results of the computation of quality parameter of \mathbb{O}_A in pitch indicating the relation of two sets of mirrors: (1) M5, M7, M4, M11; (1) M5, M7, M4, M6 and four signals of QPDa and QPDb.	85

6.6	Results of the computation of quality parameter of \mathbb{O}_D in pitch indicating the relation of mirrors: M8, M10 and two signals of QPDc.	86
6.7	Results of the computation of quality parameter of $\mathbb{O}_{\text{con}}^{ab}$ in pitch indicating the control relation of the four signals of QPDa and QPDb and two sets of mirrors: (1) M5, M7, M4, M11; (1) M5, M7, M4, M6.	87
6.8	Results of the computation of quality parameter of $\mathbb{O}_{\text{con}}^c$ in pitch indicating the control relation of two signals of QPDc and mirrors, M8, M10.	88
6.9	Results of the computation of quality parameter of \mathbb{O}_A in pitch for mirrors: M1a, M2a, M1b, M2b.	88
7.1	Left: The diagram that shows the input beam, transmission scattering beam (blue) and reflection back scattering beam (red) around a beamsplitter; Right: the diagram showing the relations among input fields, output fields and intra cavity fields in a ring cavity.	94
7.2	The quantum noise limited sensitivity (QNLS), quantum noise (QN) and response of a single ring cavity which is pump by two identical beams. The backscattering magnitudes are weak backscattering.	101
7.3	The QNLS, QN and response of a single ring cavity which is pumped by two identical beams. The backscattering strength is critical backscattering.	101
7.4	The QNLS, QN and response of a single ring cavity which is pumped by two identical beam in the case of strong backscattering.	103
7.5	The QNLS in strain, QN and strain response of a single ring cavity which is pumped by two identical beams for weak backscattering.	104
7.6	The determinate of spectral density \mathbb{S} in terms of different values of backscattering coefficients.	106
8.1	Conceptual demonstration of the EPR speed meter.	112
8.2	Quantum noise limited sensitivity of Michelson position meter, Sagnac speed meter and EPR speed meters which also include various types of imperfections.	115
8.3	Quantum noise limited sensitivity in strain of Michelson position meter, Sagnac speed meter and EPR speed meters with optimised different levels of squeezing injection from '+' and '-' port.	118
9.1	Schematic of Sagnac based circulation polarisation acceleration meter. The measurement process is described in the main text.	123

9.2	Quantum noise limited sensitivity of three different types of interferometer: polarisation circulation acceleration meter, Sagnac speed meter and Michelson position meter.	125
9.3	Quantum noise limited sensitivity of three different types of interferometer: polarisation circulation acceleration meter, Sagnac speed meter and Michelson position meter.	127
A.1	Quantum noise limited strain sensitivities of a Michelson, Michelson with ideal variational readout, Michelson with lossy variational readout and a speed meter.	134
A.2	The relation of frequency and loss factor at the crossing point of the sensitivity between lossy variational readout position meter and the sensitivity of the speed meter.	136
A.3	The relation of frequency and loss factor at the crossing point of the sensitivity between lossy variational readout position meter and the sensitivity of low frequency optimised speed meter.	136

Acknowledgements

I need to thank all the people around me who provided both technical and emotional support to this thesis and my Phd life and made my life in Glasgow enjoyable.

I would very thank my first supervisor Stefan Hild. From the starting of my Phd to the end, he taught me the scientific way to conduct research and knowledges, helped me to grasp international exchange opportunities and provides advice on the personal career arrangement. He always opens a broader horizon in my research. He is so kind and enthusiasm on students. On my life, I thank him for the occasional whisky time in his office usually after a whole day lab work, I appreciate my first experience of hiking on Scotland Munro. He is the most important people who makes me determinate in the past four years. This thesis will not be here without his all round comments.

I would very thank my second supervisor Ken Strain. He is so experienced and intelligent in my research field. His personal charisma inspires me a lot. He can always concentrate on crucial point and give concrete advice in my research.

I would very thank to Stefan Danilishin and Sebastian Steinlechner. They give me the most detailed advices on my research. Stefan Danilishin is an theorist, he taught me the methods on treating theoretical problems, especially on quantum noise and optomechanics. I very appreciate his patience. His elegant way of conducting theory research impress and inspired me. I thank to Stefan Danilishin for his invitation of visiting AEI. Sebastian Steinlechner is an experimentalist, under the guidance of whom I spent significant time in the lab. His flexible working style and exploring spirit impressed me. He can always rise up key questions in my research and came up ideas of solving problems. Without them, most of the chapters in this thesis are not possible.

I would very thank to Bryan Barr, Borja Sorazu Lucio and Angus Bell. Bryan Barr shared his experimental experience when I got stuck in the lab. Borja Sorazu Lucio helped me on programming and advanced computer operation. Angus Bell was my officemate and shared his knowledge generously every time I asked him questions.

I very thank to my working colleagues, Sean Leavey, Jan Simon Henning, Daniela Pascucci and Peter Dupej. I learned knowledges and skills from my colleagues in the cooperations with them projects. They are all generous and great guys. The working circumstances made my research enjoyable. Thanks to Sean Leavey for providing his thesis template.

I also thank to the group IT staff, Jamie Scott, the group secretary, Jenny Anderson and Karen Hegyi. Jamie Scott helped a lot on my computer software and hardware issues. Jenny Anderson and Karen Hegyi were kind on helping me arrange my travel every time.

My research are supported by the Science and Engineering College scholarship. My visit to Caltech was supported by Lord Kelvin travel funding, my visit to the University of Tokyo

was supported by mobility funding. My visit to AEI was supported IP@Leibniz scholarship. Finally, I am indebted my parents and my family for your love.

Preface

Credits specific to the chapters are listed below.

Chapter 1 presents an introduction on gravitational waves, several noise sources of the gravitational wave detector, some fundamental instruments of the gravitational wave detector and techniques for overcoming the standard quantum limit.

Chapter 2 presents the design of Sagnac speed meter experiment conducting in Glasgow and laser stabilisation schemes. The conceptual design of the Sagnac speed meter experiment was developed by Stefan Hild, Christian Gräf, Sebastian Steinlechner and Ken Strain. Jan Simon Hennig and Roland Schilling developed the optical layout. The linear cavity experiment was mentored by Sebastian Steinlechner. The linear cavity optical layout is drawn by Sebastian Steinlechner. Yutaro Enomoto and Koji Nagano contributed to the development of locking the strategy of locking the linear cavity in laser frequency stabilisation performance test. Ewan Houston built up the foundation of initial amplitude stabilisation scheme.

Chapter 3 discusses the effects of misalignment and mismatch between the separate local oscillator and signal beam in balanced homodyne readout. The idea of this work is from Stefan Hild. The theoretical calculation was carried out by me in collaboration with Stefan Danilishin. Fig. 2 and Fig. 3 are drawn by Stefan Danilishin. Fig. 1 is drawn by Sebastian Steinlechner. The writing was in cooperation with Stefan Danilishin and Sebastian Steinlechner. Bryan W. Barr, Angus S. Bell, Peter Dupej, Christian Gräf, Jan-Simon Hennig, E. Alasdair Houston, Sabina H. Huttner, Sean S. Leavey, Daniela Pascucci, Borja Sorazu, Andrew Spencer, Jennifer Wright contributed to various fruitful discussions relevant to this article.

Chapter 4 discusses several practical issues in terms of implementing balanced homodyne readout in A+. The motivations for this work were from Peter Fritschel and Stefan Hild. The first consideration of local oscillator mode cleaner length stability originated from Hang Yu. The initial sensing strategies of the different degrees of freedom in balanced homodyne readout were developed by Hang Yu. The simulation is based on the Finesse file with contributions from Charlotte Bond, Paul Fulda, Daniel Brown, Antonio Perreca, Andreas Freise.

Chapter 5 presents the way of quantum noise cancellation in asymmetric Sagnac speed meter interferometer. The idea of this work was from Stefan Hild. The theoretical analysis was carried out in collaboration with Eugene Knyazev and Stefan Danilishin. The writing was in cooperation with Stefan Danilishin. Sebastian Steinlechner noticed the effect of Sagnac speed meter main beam splitter imbalanced on quantum noise. Farid Ya Khalili, Bryan W Barr, Angus Bell, Peter Dupej, Christian Gräf, Jack Callaghan, Jan-Simon Hennig,

Ewan A Houston, Sabina H Huttner, Sean S Leavey, Daniela Pascucci, Borja Sorazu, Andrew Spencer, Jennifer Wright, Kenneth A Strain contributed to various fruitful discussions relevant to this article.

Chapter 6 discusses the misalignments and their impacts on quantum in the Sagnac interferometer. Strategies for the implementation of an auto-alignment scheme in the Glasgow Sagnac speed meter experiment are discussed. The simulation is based on the Finesse file with contributions from Christian Graef, Andreas Freise, Stefan Danilishin, Sebastian Steinlechner and myself.

Chapter 7 presents the effect of backscattering on quantum noise of a ring cavity. The idea of this work is from Stefan Hild. The theoretical work was carried out in collaboration with Daniela Pascucci, Miroslav Tugolukov, Stefan Danilishin, Sergey Petrovich Vyatchanin.

Chapter 8 presents the effect of several imperfections on quantum noise in the EPR speed meter and calculates the performance of injecting squeezing. The idea of this work is from Stefan Danilishin. The theoretical work was carried in collaboration with Eugene Knyazev and Stefan Danilishin.

Chapter 9 presents an acceleration meter configuration. The work is carried out by myself.

Appendix A develops a comparison between speed meters and position meters with lossy variational readout. The motivation of this work was from Stefan Hild.

Appendix B shows the Finesse input file of A+ for balanced homodyne readout. The file is for the simulation done in Chapter 4. It was written by Daniel Brown with contributions from the Balanced Homodyne Detection for A+ workshop. I was one of the participants of the workshop and contributed the design of arrangements of OMCs in the file.

Appendix C shows the Finesse input file of Glasgow Sagnac speed meter experiment. The file is for the simulations done in Chapter 6. It was written by Christian Gräf with contributions from Andreas Freise, Stefan Danilishin, Sebastian Steinlechner and myself.

Chapter 1

Introduction

This chapter provides the fundamental information related to the work presented in the rest of this thesis. Sec. 1.1 starts with the basic concepts of gravitational waves. Sec. 1.2 describes several sources of disturbances in ground based gravitational wave detectors; Sec. 1.3 provides the overview of fundamental concepts of current gravitational wave detectors which are directly related to the enhancement of the signal to noise ratio of detectors; Sec. 1.4 focuses on the quantum noise limited sensitivity of gravitational wave detectors and illustrates several techniques for overcoming the so called standard quantum limit which is a result of Heisenberg's uncertainty principle.

1.1 Gravitational waves

On 14th September 2015, humanity made its first gravitational wave detection from binary black holes merging [2]. The event GW150914 marked the beginning of a new era, gravitational wave astronomy. In this section, I briefly introduce the basic concepts related to gravitational waves. The gravitational waves are generated if there is non-zero value of the second time derivative of the quadrupole moment of an isolated system's stress-energy tensor, for example, from a spinning non-axisymmetric object or binary objects coalescing with elliptical orbits [3]. In general relativity, space-time curvature is associated with the stress-energy tensor of matter fields, described by the *Einstein Equation*. In the Einstein field equations, matter tells space-time how to curve, but the curved space-time also tells matter how to move [4]. Considering the weak gravitational field limit, when the observer is far away from the source, the Einstein equation can be linearized and analytically solved. The general solution can be represented as a travelling plane wave with an amplitude tensor, which can be reduced to two physical degrees of freedom by adopting a gauge called

Tensor Traceless (TT) as

$$h_{\mu\nu} = \begin{bmatrix} 0 & 0 & 0 & 0 \\ 0 & h_+ & h_\times & 0 \\ 0 & h_\times & -h_+ & 0 \\ 0 & 0 & 0 & 0 \end{bmatrix}. \quad (1.1)$$

Here h_+ and h_\times represent the two polarisations of the gravitational wave. The effects of a passing gravitational wave can be described as tidal force effects on the orthogonal plane of its propagation. In terms of two free masses with distance L on the plane, the passing gravitational wave introduces a distance variation δL which follows

$$\delta L = \frac{h_{+,\times}}{2} L, \quad (1.2)$$

The influences of gravitational waves on a ring of free falling test masses that is perpendicular to the gravitational wave traveling direction are shown in Fig. 1.1. As we can see, gravitational waves always squeeze and stretch the distance between two test masses. When the distance of two test masses gets squeezed, the distance of two test masses in the orthogonal direction gets stretched. The laser interferometer gravitational wave detector is actually to sense the differential phase variances of two interfered beams which are modulated differentially by the motions of test masses. A simple Michelson scheme that describes how the gravitational wave signals can be measured is shown in Fig. 1.2. In a simple Michelson, a coherent laser source incidents on the central beamsplitter and is divided into two beams. Each beam accumulates the phase change during traveling in the arm and the phase shift modulated by the motion of the test mass. The two beams reflected back recombine on the beamsplitter and interfere with each other. Usually, the asymmetric port is tuned nearly dark to measure the differential phase term between two recombined beams which can be caused by gravitational waves.

The gravitational wave detector measures such strain signals with the corresponding response to both polarisations,

$$h = F^+(t)h_+ + F^\times h_\times, \quad (1.3)$$

where $F^{+/\times}$ are so-called antenna patterns which depend on the interferometer opening angle, sources sky location and signal polarisation angle. The sources that can be detected by ground-based gravitational wave detector are mainly in the frequency range between 10 to 10^4 Hz. By the end of the second observation run, ten events of coalescence of binary black holes and one event of coalescence of binary neutron stars have been detected.

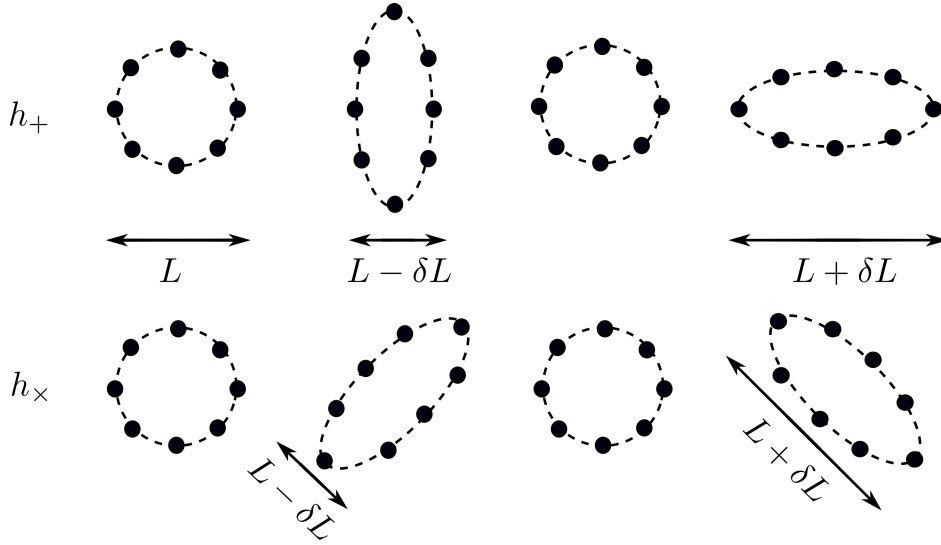


Figure 1.1: Effects of gravitational waves on a ring of free test masses on the plane orthogonal to its propagation. The distance between two test masses get squeezed or stretched by δL following the rule of Eq. 1.2.

1.2 Noise sources of the ground based interferometer

A thorough understanding of the noise characteristics is a both, basic and crucial step to build gravitational wave detectors and achieve the expected sensitivity in each frequency band for corresponding types of astrophysics sources. In this section, I introduce several noise sources including laser noise, seismic noise, thermal noise and quantum noise. Seismic noise highly depends on local geographical situation, so it is usually concerned at the primary stage of building a gravitational wave detector. Laser noise is a technical noise that originates from the detector probe itself. Decreasing laser noise is usually a common topic for precision measurement research utilising a laser. Especially, in the audio band, the frequency band of interest for gravitational wave detection, the laser noise coupling is significant. Besides this section, in Chapter. 2, two essential laser stabilisation techniques will be introduced in more detail. Thermal noises, mainly including coating thermal noise and suspension thermal noise, cause test masses displacements directly. We have almost isolated the system from the classical world, the fundamental worries will be quantum noise, which consists of quantum shot noise and quantum radiation pressure noise, is the focus of the majority of the chapters in this thesis. Note that the quantum shot noise is a sensing noise, however, quantum radiation pressure noise is a displacement noise. There are proposed configurations allowing displacement noise-free measurement based on the understanding that gravitational waves and test mass displacement disturbances act differently on light propagation and also allowing laser noise insusceptible measurement [5, 6].

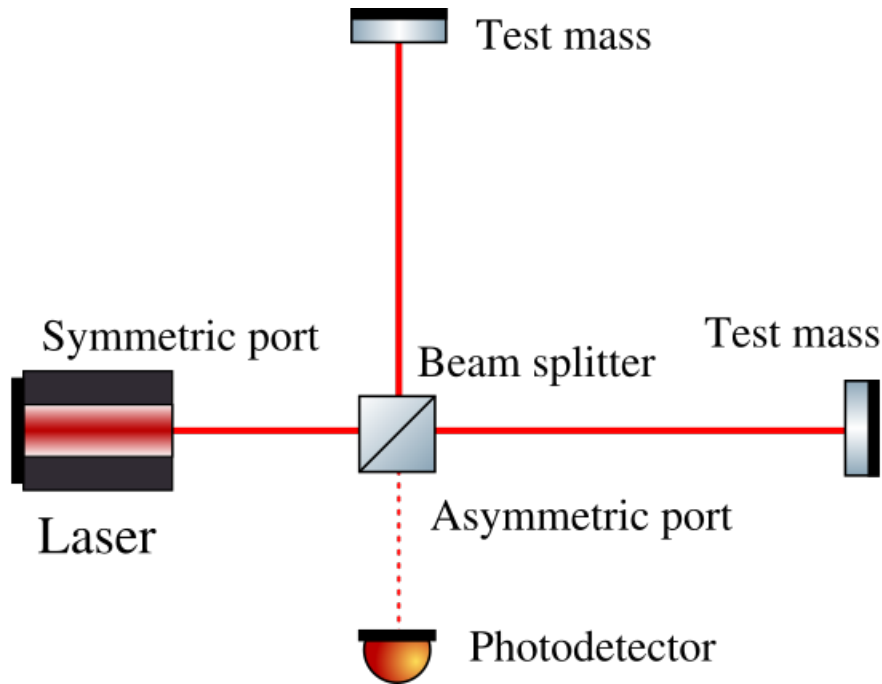


Figure 1.2: The schematic of a simple Michelson interferometer. BS represents the beamsplitter. The two ports are labeled as symmetric port (laser port) and asymmetric port (signal port), respectively.

1.2.1 Seismic noise

Seismic noise comes from the ground motion of the earth. Reducing the seismic noise is a key task for ground-based gravitational wave detector. The suspension systems based on pendulum mechanism which have several isolation stages are developed as the seismic noise passive suppression platforms. For a multistage isolation system, each stage attenuates the fluctuating the fluctuations above the resonance frequencies following frequency dependence of $\frac{1}{f^2}$.

Seismic noise presents in both horizontal and vertical directions. Fig. 1.3 shows the measured seismic motion of the floor in the Glasgow interferometry lab. The horizontal mode does couple into the gravitational wave channel. The vertical mode contamination to the gravitational wave channel is tiny. It can be caused by the manufacturing imperfections of the suspensions itself. In large scale gravitational wave detector cavity, input test mass (ITM) and end test mass (ETM) have unparallel locally defined vertical directions because of the curvature of the earth surface. The local vertical displacement of one end mirror can thus couple to the longitudinal gravitational wave channel.

1.2.2 Laser noise

Intensity noise

There are two ways that the laser intensity noise could show up as detection noise, which

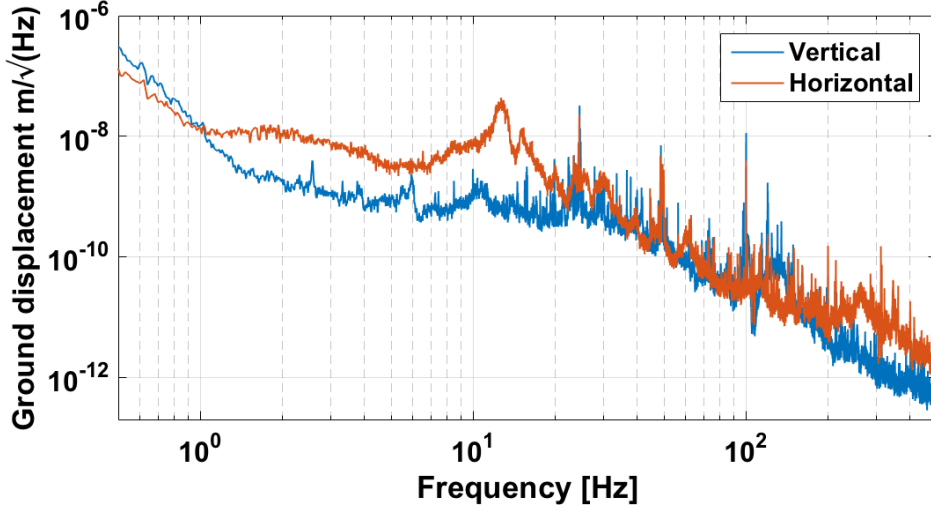


Figure 1.3: Measured horizontal and vertical ground motion in the lab of University of Glasgow [7]

will be discussed below. In a resonate cavity, the test mass displacements sensed by photodiode are obtained as intensity variations, thus the laser intensity fluctuation can mimic the test mass displacement. This measurement noise can be written as [8, 9]

$$\begin{aligned} x_{in} &= \text{RIN} \cdot x_{\text{RMS}} [\text{m}/\sqrt{\text{Hz}}], \\ \text{RIN} &= \frac{\Delta P}{P} [1/\sqrt{\text{Hz}}], \end{aligned} \quad (1.4)$$

where RIN is short for the relative intensity noise, x_{RMS} is the RMS value of the residual displacement of the cavity test mass. Another effect comes from the classical radiation pressure noise. The relationship between classical radiation pressure noise and quantum radiation pressure noise can be represented by

$$\frac{x_{rp}^{qu}}{\sqrt{\frac{\hbar\omega}{2}}} = \frac{x_{rp}^{cla}}{\text{RIN}\sqrt{P}}, \quad (1.5)$$

where x_{rp}^{qu} and x_{rp}^{cla} are the amplitude spectral density in displacement of quantum and classical radiation pressure noise, respectively. We notice that, if the RIN level is constant, the classical radiation pressure noise amplitude spectral density is proportional to P , which is different from the case of quantum radiation pressure noise which is proportional to \sqrt{P} . The difference is because the radiation pressure force for both cases are proportional to \sqrt{P} , however, the amplitude of vacuum fluctuation is constant but the laser field amplitude fluctuation is proportional to \sqrt{P} .

In the tuned Fabry-Perot Michelson interferometer operated near to dark, since the two beams from the two arms interference destructively, the laser intensity noise and classical

radiation pressure noise should be cancelled mostly as common mode information. However, there will still be finite noise coupling depending on the strength of common mode rejection. Even starting from very stable laser sources, we find that for gravitational wave detectors we usually have to employ additional intensity stabilisation schemes for achieving the RIN requirements.

Frequency noise

Practically, the laser frequency cannot be treated as constant. The fluctuations can for instance originate from either the variance of laser linewidth or the variance of linewidth central frequency [10]. Thus for one laser beam with a travel distance L , the frequency instability will introduce additional dephasing as $\frac{2\pi L}{c}\delta f$ with the frequency variations δf in Hz. The laser frequency noise effect is equal to a length variation with the relation

$$\frac{\delta f}{f} = \frac{\delta L}{L}, \quad (1.6)$$

where f the laser frequency and δL is displacement noise. L is defined as the beam travelling distance or the cavity length of a Fabry-Perot cavity. The typical frequency noise of a free running laser used in gravitational wave detectors is recognised as [11]

$$\delta f = 100\left(\frac{100\text{Hz}}{f}\right) [\text{Hz}/\sqrt{\text{Hz}}]. \quad (1.7)$$

Like the laser intensity noise, the laser frequency noise is also a common noise. Even though, in order to acquire the lock of the arm cavities, it is helpful to develop a pre-laser frequency stabilisation scheme [12]. The frequency stabilisation was typically realised by locking the laser frequency on a reference cavity by Pound-Drever-Hall technique [13, 14].

1.2.3 Thermal noise

According to the fluctuation-dissipation theorem [15–17], the energy dissipation in a system causes thermal fluctuation. The thermal noises in gravitational wave detectors mainly come from the suspension and the test mass, so-called suspension thermal noise and mirror thermal noises. Their amplitudes are proportional to mechanical loss and temperature.

Coating Brownian thermal noise

There are various types of thermal noises associated with the mirrors, *e.g.* Brownian noise, thermoelastic noise and thermorefractive noise which arise from both coatings and substrate. As it turns out, in the frequency band of interest of ground-based gravitational wave detector, the coating Brownian noise is the dominating thermal noise associated with the mirror. It results from the mechanical loss in the numerous layers of high and low index

materials coatings. Its power spectral density can then be estimated as [18]

$$S_{Brownian} = \frac{4k_B T (1 + \delta_s)(1 - 2\delta_s) d}{\pi^2 f E_s w} \phi_C, \quad (1.8)$$

where k_B is Boltzmann constant, T is the temperature, δ_s is Poisson ratio, E_s is Young's modulus of the substrate, d is the coating thickness, w is the beam diameter on the mirror and ϕ_C is the mechanical loss of coating.

Suspension thermal noise

Suspension thermal noise originates from the fibres and their connections to the test mass. Above the fundamental pendulum frequency, the longitudinal thermal motion decreases with increasing frequency f , following $\sqrt{\frac{1}{f^5}}$ [9][19]. In high frequency, the violin modes manifest the fibre oscillations excited by the thermal force [20]. Increasing the stress of the fibre pushes the reduction of the bounce mode frequency and the raise of the first violin mode frequencies. Increasing the stress of the fibre could be achieved by reducing fibre diameters [21].

1.2.4 Quantum noise

Quantum noise originates from the quantum nature of laser light and is induced via the measurement process measurement. In a gravitational wave detector, it manifests itself in two ways, *Shot noise* (sensing noise), which dominates in high frequency band, and *radiation pressure noise* (back-action noise), which dominates in low frequency band.

Shot noise

Shot noise is a kind of sensing noise. A photo diode counts photons and converts the optical information into electronic information. In this process, due to the non-uniform distribution, *i.e.*, a Poissonian distribution, of the photons of a laser beam in space, the shot noise limits the accuracy of probing the correct information. The shot noise is directly proportional to the square root of incident power on the photo diode, however, the signal information is proportional to the incident power. Thus the shot noise limited sensitivity of the detector can be improved by increasing the laser power.

For a broadband photo counting device with a unit quantum efficiency, the shot noise current can be written as [9]

$$i_{sn} = \sqrt{2ei_{DC}} [A/\sqrt{\text{Hz}}], \quad (1.9)$$

where e is an electron charge, i_{DC} is the photocurrent of a photodiode.

The relative intensity of shot noise can be written as

$$\text{RIN}_{sn} = \sqrt{2e/(R \cdot P)} [1/\sqrt{\text{Hz}}], \quad (1.10)$$

where R is the photocurrent response to a certain power P of a photodiode device.

To detect gravitational waves using a simple Michelson interferometer, the shot noise amplitude spectral density in displacement can be represented by

$$x_{sn} = \sqrt{\frac{\hbar c \lambda}{2\pi P}} \text{ [m}/\sqrt{\text{Hz}}], \quad (1.11)$$

where \hbar is the reduced Planck's constant, λ is the laser wavelength and P is the optical power circulating in the interferometer arms.

For a Fabry-Perot cavity, the shot noise amplitude spectral density can be approximated to [9, 22]

$$x_{sn} \approx \frac{1}{4F} \sqrt{\frac{\pi \hbar \lambda c}{P_{in}} (1 + (\Omega \tau_{sto})^2)} \text{ [m}/\sqrt{\text{Hz}}], \quad (1.12)$$

$$\tau_{sto} = \frac{2LF}{c\pi} \text{ [s]}$$

Here F is the finesse of the cavity, L is the cavity length, and τ_{sto} is the storage time of the cavity, P_{in} is the input power to the cavity. $\frac{1}{2\pi\tau_{sto}}$ is the corner frequency of the cavity. We notice that the shot noise is inverse proportional to the cavity finesse. So Fabry-Perot cavities play an essential role in improving the shot noise limited sensitivity in current generation gravitational wave detectors.

Radiation pressure noise

Radiation pressure noise is also referred to back action noise, because it is induced by the back action of the probe itself onto the test mass. Since the light field is quantized, then the non-uniform distributed photons will also provide fluctuating radiation pressure over time, which will cause position variations of the test mass. The amplitude spectral density of the quantum radiation pressure noise in a simple Michelson is given by

$$x_{rp} = \frac{1}{m\Omega^2} \sqrt{\frac{2\pi\hbar P}{c\lambda}} \text{ [m}/\sqrt{\text{Hz}}], \quad (1.13)$$

where m is the mirror mass. For a Fabry-Perot cavity, the radiation pressure noise can be expressed as [9]:

$$x_{rp} = \frac{4F}{\pi m\Omega^2} \sqrt{\frac{4\pi\hbar P}{\lambda c [1 + (\Omega\tau_{sto})^2]}} \text{ [m}/\sqrt{\text{Hz}}]. \quad (1.14)$$

According to Eq. 1.12, 1.14, when $\Omega\tau_{sto}$ is much smaller than 1, we can see that the shot noise can still be treated as white noise approximately but the radiation pressure noise amplitude spectral density arises towards low frequency following $1/\Omega^2$, which results from the test mass' mechanical susceptibility.

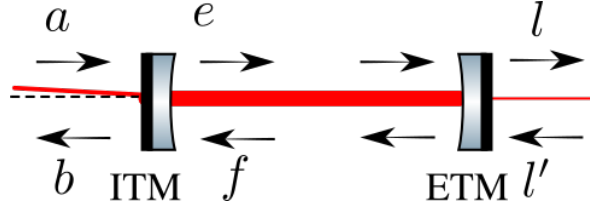


Figure 1.4: Schematic of a Fabry-Perot cavity. The input field 'a' at the can be misaligned respected to the dashed line reference, the reflection field are represented by 'b', the transmission field is represented by 'l', 'l'' is the input from the end test mass port.

1.3 Fundamental features of gravitational wave detector

In this section, I introduce several fundamental concepts relevant for the understanding of the second generation gravitational wave detectors.

1.3.1 Fabry-Perot cavity

Fabry-Perot cavities [23] play essential roles in gravitational wave detectors. As I showed in the Sec. 1.2.4, by implementing Fabry-Perot cavity, the shot noise limited sensitivity can be significantly increased due to the amplified output response to the mirror motion which is characterised by cavity Finesse. As a laser beam resonator, a Fabry-Perot cavity also defines its eigen spatial mode. So it can be used as a mode cleaner by designing its geometric construction. Detuned Fabry-Perot cavities are essential elements in some techniques for beating standard quantum limit, for example, frequency dependent squeezing and variational readout. In this section, I introduce both the optical input-output (I/O) relation of the Fabry-Perot cavity and its optomechanical I/O relation in *two-photon formalism*.

Optical input-output relation

Like shown in Fig.1.4, a represents the input field, b is the output field, e and f are the inner fields, l is the transmission field and ' l' ' is the input from the end test mass port. By solving a set of equations in which each equation demonstrates the relation between two fields right next to each other, I can write down

$$l = \eta a \frac{-t_{\text{ITM}} t_{\text{ETM}} e^{-ikL}}{1 - r_{\text{ITM}} r_{\text{ETM}} e^{-2ikL}}, \quad (1.15)$$

$$b = a \left(\sqrt{1 - \eta^2} + \eta \frac{r_{\text{ITM}} - r_{\text{ETM}} e^{-2ikL}}{1 - r_{\text{ITM}} r_{\text{ETM}} e^{-2ikL}} \right), \quad (1.16)$$

$$e = \eta a \frac{it_{\text{ITM}}}{1 - r_{\text{ITM}}r_{\text{ETM}}e^{-2ikL}}, \quad (1.17)$$

where η represents the mode overlap factor of the input beam to the cavity, r_{ITM} and r_{ETM} are the reflectivity of input test mass (ITM) and end test mass (ETM), respectively. k is the wave number of the laser beam and L is the length of the cavity. The free spectral range of one cavity is defined as

$$\text{FSR} = \frac{c}{2L}, \quad (1.18)$$

which is the interval frequency range between two resonance frequencies of the cavity. And the cavity half bandwidth is given as the half width at half-maximal circulating power, which can be written in angular frequency as

$$\gamma = 2\arcsin\left(\frac{1 - r_{\text{ITM}}r_{\text{ETM}}}{2\sqrt{r_{\text{ITM}}r_{\text{ETM}}}}\right) \text{FSR}. \quad (1.19)$$

In the gravitational wave detector, the cavities can be treated as a single-mode lumped resonator [27]. Using the single-mode approximation, there is

$$\gamma = \frac{cT_{\text{ITM}}}{4L} + \frac{cT_{\text{ETM}}}{4L}, \quad (1.20)$$

where T_{ITM} and T_{ETM} are the power transmissivity of the cavity input mirror and end mirror, respectively. The Finesse of the cavity can be written as the ratio of the cavity free spectral range and the cavity full linewidth

$$F = \frac{\text{FSR}}{\gamma} \pi. \quad (1.21)$$

Based on above equations, the loss terms of the cavity can be estimated by monitoring the reflection power [28],

$$P_R = |a|^2 \left(1 - 4\eta^2 \frac{T_{\text{ETM}} + |l|^2}{T_{\text{ITM}}}\right), \quad (1.22)$$

Here I consider the overall loss as the transmission of cavity l . And

$$l = \sqrt{l_{\text{ITM}}^2 + l_{\text{ETM}}^2}. \quad (1.23)$$

The loss of ITM can be identified by misaligning or removing the ETM, thus

$$P_R = |a|^2(1 - T_{\text{ITM}} - |l_{\text{ITM}}|^2). \quad (1.24)$$

Two-photon formalism

The so-called *two-photon formalism* [29, 30] describes, locally, an arbitrary quasi-monochromatic modulated electromagnetic wave with strain $E(t) = \mathcal{E}_0 [(A_c + a_c(t)) \cos \omega_p t + (A_s + a_s(t)) \sin \omega_p t]$ in terms of 2-dimensional vectors of quadrature amplitudes $\mathbf{A} + \mathbf{a}$, where $\mathbf{A} = \{A_c, A_s\}^T$ stands for DC mean amplitudes vector and $\mathbf{a} = \{a_c, a_s\}^T$ stands for zero-mean non-stationary variations and fluctuations of light. $\mathcal{E}_0 = \sqrt{\frac{4\pi\hbar\omega_p}{\mathcal{A}c}}$ is the normalisation constant, c is the speed of light, and ω_p is the carrier light angular frequency. It is usually more convenient to work in the frequency domain:

$$a_{c,s}(t) = \int_{-\infty}^{\infty} \frac{d\Omega}{2\pi} a_{c,s}(\Omega) e^{-i\Omega t}, \quad (1.25)$$

where we define quadratures spectra at the modulation sidebands off-set frequency $\Omega = \omega - \omega_p$.

Opto mechanical input-output relation

In general, the input-output relation can be written in the form of [27]

$$\mathbf{b} = \eta(\mathbb{R}\mathbf{a} + \mathbf{R}x) + \sqrt{1 - \eta^2}\mathbf{a} + \mathbb{T}\hat{\mathbf{I}}, \quad (1.26)$$

where η is the alignment coefficients of the input beam to the cavity,

$$\mathbf{R} = 2\omega_0 \sqrt{\frac{\gamma_1}{cL}} \mathbb{L} \begin{bmatrix} -E_s \\ E_c \end{bmatrix}, \quad (1.27)$$

and

$$\begin{bmatrix} E_s \\ E_c \end{bmatrix} = \sqrt{\frac{2I}{\hbar\omega_0}} \begin{bmatrix} \sin \zeta \\ \cos \zeta \end{bmatrix}, \quad (1.28)$$

with ζ defining the phase of a complex amplitude. Then

$$\mathbb{L} = \frac{1}{(\gamma - i\Omega)^2 - \delta^2} \begin{bmatrix} \gamma - i\Omega & -\delta \\ \delta & \gamma - i\Omega \end{bmatrix}, \quad (1.29)$$

with δ is the detuning from pump frequency. And

$$\begin{aligned} \mathbb{R} &= 2\gamma_1 \mathbb{L} - \mathbb{I}, \\ \mathbb{T} &= 2\sqrt{\gamma_1\gamma_2} \mathbb{L}. \end{aligned} \quad (1.30)$$

The intra cavity mode can be written as

$$e = \sqrt{\frac{c}{L}} \mathbb{L} \left(\sqrt{\gamma_1} \hat{a} + \sqrt{\gamma_2} \hat{l} + \omega_0 \sqrt{\frac{1}{cL}} \begin{bmatrix} -E_s \\ E_c \end{bmatrix} \right) \quad (1.31)$$

Furthermore, concerning the mirror dynamics, the equation of motion can be written as

$$(\mathcal{X} + K)x = F_{b,a}^0 + F_{GW}. \quad (1.32)$$

$\mathcal{X} = -\frac{1}{\mu\Omega^2}$ is the effective mechanical susceptibility, $\mu = (\frac{1}{m_1} + \frac{1}{m_2})^{-1}$ is the effective mass of the longitudinal mechanical mode. K is the ponderomotive rigidity,

$$K = \frac{\mu J \delta}{(\gamma - i\Omega)^2 - \delta^2}, \quad (1.33)$$

with

$$J = \frac{4\omega_0 I}{\mu c L}, \quad (1.34)$$

the normalised circulating power. And the random back action force can be represented by

$$F_{b,a}^0 = 2\hbar k E^T e. \quad (1.35)$$

In the special case of a single, optical detuning-less and lossless Fabry-Pérot cavity, the I-O relation can be derived as,

$$\mathbf{b} = \underbrace{e^{2i\beta(\Omega)} \begin{bmatrix} 1 & 0 \\ -\mathcal{K} & 1 \end{bmatrix}}_{\mathbb{T}^{\text{arm}}} \hat{\mathbf{a}} + \underbrace{e^{i\beta(\Omega)} \begin{bmatrix} 0 \\ \sqrt{2\mathcal{K}} \end{bmatrix}}_{\mathbf{R}} \frac{x}{x_{\text{SQL}}}, \quad (1.36)$$

with \mathcal{K} is the Kimble optomechanical coupling factor [25],

$$\mathcal{K} = \frac{2\Theta\gamma}{\Omega^2(\gamma^2 + \Omega^2)}, \quad (1.37)$$

where $\gamma = \gamma_1$ is the half bandwidth of the cavities. $\beta = \arctan(\frac{\Omega}{\gamma})$ is the phase shift that the light sidebands at frequency Ω acquire when propagating through and reflecting off the cavity. And

$$x_{\text{SQL}} = \sqrt{\frac{2\hbar}{\mu\Omega^2}}, \quad (1.38)$$

is the free mass amplitude spectral density of the standard quantum limit in displacement.

1.3.2 Power recycling cavity

The interferometer shot noise limited sensitivity can be further enhanced by implementing an additional mirror at the symmetric port forming a so-called power recycling cavity with two arm cavities input test masses. As we know, the symmetric port is the bright port and common motion port. The sidebands which contain differential gravitational wave

signal will only couple into the asymmetric port, *i.e.* the dark port. So the power recycling cavity only enhances the circulating power in arm cavities rather affects signal beam. The choice of the reflectivity of the power recycling mirror should satisfy a wider bandwidth of the power recycling cavity compared with the arm cavity. The appearance of the power recycling cavity also utilises the power reflected from arm cavities and enhances the laser light utilisation efficiency.

1.3.3 Signal recycling cavity

In contrast to the power recycling cavity, by adding a mirror at the asymmetric port, the corresponding signal recycling cavity has no effect on carrier field that comes from the symmetric port. However, at the asymmetric port, the differential GW signal sidebands will be partially reflected back to the main interferometer and go out again. The signal recycled Fabry-Perot cavity thus results in a modified decay rate and resonate frequency of the interferometer, which is determined by the signal recycling mirror reflectivity and detuning. Hence it allows to gain the flexibility of shaping the interferometer response. In two special cases, 0 or $\frac{\pi}{2}$ phase detuning (signal-recycling (SR) and resonant-sideband-extraction (RSE) [31, 32]), can be used to realise an increased response function in a narrow band a broadened bandwidth of the responseor. However, due to the bandwidth and peak sensitivity product limit, also named Mizuno limit [33], the interferometer sacrifices the peak sensitivity in RSE mode. Even though, the RSE mode is the default mode utilised in current gravitation wave detector. In the detuned case, the signal recycling cavity can generate equivalent optical spring effect, thus allows the detector sensitivity overcome the standard quantum limit (SQL) in a narrow band around the frequency of *optical resonance* and *mechanical resonance* [32, 34].

1.3.4 Homodyne readout

That one can extract the gravitational wave signal passing through the interferometer from the probe laser relies on the readout scheme. One popular and currently in use technology is homodyne readout. Due to interference of the two laser beams returning from the arms and the particular operating point of the interferometer, at the dark fringe, the gravitational wave effects on laser parameters are maximised in principle. However, there are two tasks that need to be solved in reality. First of all, considering that the gravitational waves only provide very weak modulations on laser phase, if the photodiode is operating at the dark fringe, the signal photocurrent would be of second order of smallness. Secondly, to keep the interferometer on its operating point, a bipolar error signal is required for control purposes. These two issues can be solved by introducing a reference laser, *i.e.* the local oscillator. One

way to create the presence of a local oscillator local oscillator is to slightly offset the interferometer operating point at the readout port from dark fringe by introducing an arms length difference, so-called DC readout [35, 36]. An advantage of this scheme is that the local oscillator is automatically phase locked with the signal sidebands. Another way is to introduce a split local oscillator which still originates from the interferometer pump. The split local oscillator is mixed with the dark port sidebands on a beam splitter. Two photodiodes are placed behind the two output ports of the beam splitter, respectively. Finally, we read out the subtraction of the photocurrents of two photodiodes. This technology is named as balanced homodyne readout [37]. The advantages of this scheme are that it allows to arbitrarily choose the readout quadrature and that the noises in the local oscillator itself can be subtracted. In Chapter. 3,4,5, greater details on the realistic implementation of balanced homodyne readout will be introduced.

1.4 Overcoming standard quantum limit

In Sec. 1.2.4, the quantum noise was introduced as a fundamental noise source for gravitational wave detection. In the second generation gravitational wave detectors, quantum noise limits the detector sensitivity over a broad frequency band. In this section, I present the basics of standard quantum limit (SQL) and introduce several *quantum non-demolition techniques* for beating SQL [24–26].

1.4.1 Standard quantum limit

Conventionally, the quantum noise consists of the low frequency back action noise (radiation pressure noise) and high frequency sensing noise (shot noise). The minimal sum of the two types of noises builds a sensitivity bound, standard quantum limit. It was noted as a consequence of Heisenberg uncertainty principle in continuous linear measurements by Braginsky [38]. Considering that the test masses' mechanical eigenfrequencies are usually much smaller than the gravitational wave signal frequency concerned by the ground based gravitational wave detectors, I treat the test masses as free masses. As a result, the power spectral density of free mass the standard quantum limit for a displacement measurement can be written as [27]

$$S_{SQL} = 2\hbar|\chi|, \quad (1.39)$$

where \hbar is the Planck constant, and χ is the free mass mechanical susceptibility. As shown in Fig. 1.5, in a linear continuous measurement system, the displacement measurement can

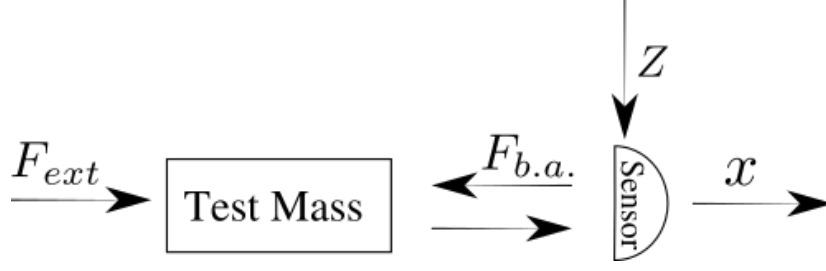


Figure 1.5: The schematic of a continuous linear measurement system. F_{ext} is the external force applied onto the test mass, $F_{b.a.}$ represents the back action force, z is the sensing noise, x is the measurement output in displacement.

be represented mathematically by a linear equation as

$$x(\Omega) = \chi(\Omega)[F_{b.a.}(\Omega) + F_{ext}(\Omega)] + Z(\Omega), \quad (1.40)$$

where $Z(\Omega)$ is the measurement noise of the meter and $F_{b.a.}$ is the back action force induced by the probe laser and F_{ext} is the excitation force, which can be the gravitational wave tidal force. Considering a conventional interferometer with resonant arm cavities, there will not be correlations between shot noise and radiation pressure noise, the quantum noise spectral density normalised to displacement ($\chi(\Omega)F_{ext}(\Omega)$) can be written as

$$S = S_Z + |\chi(\Omega)|^2 S_F, \quad (1.41)$$

with S_Z and S_F quantifying the spectral densities of sensing noise and back action noise. There is Heisenberg-like Uncertainty relation that constrain the relation between S_Z and S_F as [39]

$$S_F S_Z \geq \hbar. \quad (1.42)$$

So that one can get the minimal noise spectral density, S_{SQL} , as shown in Eq. 1.39. The normalised S_Z refers to shot noise which is white noise in terms of position measurement in low frequency, and $|\chi(\Omega)|^2 S_F$ refers to back action noise. Since

$$\chi(\Omega) = -\frac{1}{\mu\Omega^2}, \quad (1.43)$$

where μ is the effective mass of corresponding mechanical displacement mode, we can read that the back action power noise spectral density arises in low frequency following $1/\Omega^4$ and is inversely proportional to the square of the mirror mass.

It is also straightforward to derive the SQL in terms of other normalisations. The power spectral density of SQL in force can be written as

$$S_{SQL}^F = \frac{2\hbar}{\chi}. \quad (1.44)$$

And for advanced LIGO type Michelson interferometer, the power spectral density of SQL in strain can be derived as

$$S_{SQL}^h = \frac{4S_{SQL}^F}{\mu^2 L^2 \Omega^2}, \quad (1.45)$$

since

$$F(t) = \frac{\mu L}{2} \ddot{h}(t). \quad (1.46)$$

1.4.2 Squeezed vacuum injection

Squeezed vacuum injection is one of the most mature technologies for suppressing the quantum noise. It has been demonstrated in larger scale gravitational wave detector GEO600 [40–42] and later on LIGO [43]. Eq. 1.4.1 shows the result of Heisenberg uncertainty principle when there is no correlation between input state phase quadrature and amplitude quadrature, *i.e.* for a vacuum state or a coherent state. However, there are ways of building the correlation between two quadratures of the input field by means of non-linear optical effects. Thus the squeezed state field can be prepared. Technically, by manipulating the input quantum state in our favour, *i.e.* suppressing both S_z and S_F in their corresponding dominating frequencies, an overall improvement of quantum noise limited sensitivity can be achieved. This technique is named as frequency dependent squeezing [25].

The picture can be understood as following. In one case, *e.g.* phase quadrature squeezing, the uncertainty on phase quadrature is suppressed in company with the sacrifice of the measurement accuracy on the amplitude quadrature. This kind of squeezing can already provide a high frequency sensitivity improvement. However, in low frequency, the detector itself applies strong ponderomotive squeezing to the input field, *i.e.* the amplitude quadrature fluctuations couple to phase quadrature in a frequency dependent way. Thus, to evade the contamination of the amplified noise by antisqueezing, a frequency dependent rotation is required for the input state. The rotation process can be realised by a detuned filter cavity. Utilising frequency dependent squeezing is currently planned for future upgrade of current gravitational wave detectors and future generation gravitational wave detectors. The mathematical description of realising ideal frequency dependent squeezing can be found in [27, 44].

1.4.3 Variational readout

Another way to suppress the quantum noise is to modify the output pass [25]. Since the detector itself generates the correlation between phase and amplitude quadrature in the so-called ponderomotive squeezing process, one can measure a certain combination of the two quadratures realising an evasion of the contribution from the amplitude quadrature of the

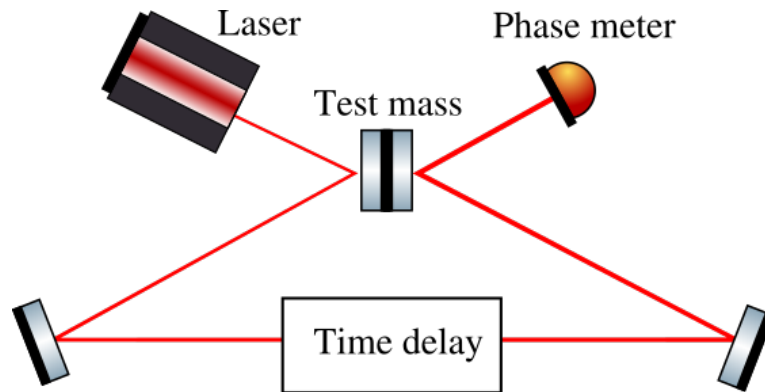


Figure 1.6: Conceptual scheme of speed measurement. The laser photons consecutively hit on the front surface and rear surface with a time delay. The laser phase is modulated by the test mass motion and measured by a phase meter.

input field, which raises the radiation pressure noise. This certain combination of quadratures measurement can be achieved by utilising balanced homodyne readout and choosing a proper homodyne angle. Again, the homodyne angle needs to be frequency dependent, which can be realised by filtering the low frequency sidebands by a detuned cavity. The obstruction to implement variational readout in the future is mainly from optical loss. A more detailed analysis relating to lossy variational readout can be found in Appendix. A.

1.4.4 Speed meter

Another approach of quantum non-demolition measurement can be conducted by choosing commuting observables. In 1990, Braginsky came up with the speed meter concept [45] since momentum is recognised as conserved observable. At that time, the idea was still formulated in the context of application to resonant bar detectors. The first speed meter configuration based on laser interferometer is called sloshing cavity speed meter. It is based on a Michelson interferometer and a so-called sloshing cavity is added at the output port of the interferometer [46].

How the speed measurement can help improving the strain sensitivity of gravitational wave detectors can be understood by the following picture. Utilising the concept of laser interferometry, one is always observing the differential phase of two interfered beams. In terms of speed measurement of the test masses, smaller phase variances of the laser beam are recognised towards lower frequency. In other words, the signal response decreases linearly towards low frequency. Meanwhile, the radiation pressure force on the test mass is also cancelled partially and decrease linearly towards low frequency. A conceptual scheme of speed measurement is shown in Fig. 1.6. Similar to Eq. 1.40, the speed measurement at low

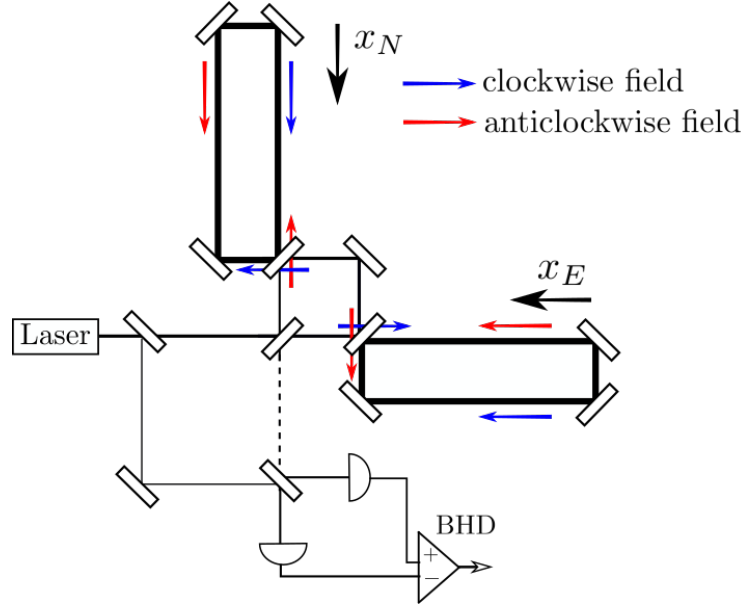


Figure 1.7: Schematic of Sagnac speed meter. The blue arrows indicate the clockwise propagation direction of the laser beam; The red arrows indicate the anticlockwise propagation direction of the laser beam. The signal beam is represented by the dash line and sensed with a balanced homodyne detector (BHD). The measurement process is described in the main text.

frequencies can be represented approximately by

$$\dot{x}(\Omega) = \Omega \cdot \chi(\Omega)[\Omega \cdot F_{BA}(\Omega) + F_{ext}(\Omega)] + Z(\Omega) \quad (1.47)$$

One can write down the noise spectral density normalised to signal force induced displacement, *i.e.*, $\chi(\Omega)F_{ext}(\Omega)$,

$$S = \frac{S_Z}{\Omega^2} + \Omega^2 |\chi(\Omega)|^2 S_F \quad (1.48)$$

Obviously, according to Eq. 1.42, we can notice the speed meter noise spectral density will still be limited by SQL. However, the back action term $\Omega^2 |\chi(\Omega)|^2 S_F$ at low frequencies is relaxed with Ω^2 and follows the SQL trend. This provides evidence of the priority of the speed meter scheme on quantum noise limited sensitivity in low frequency. In the following I introduce two realisations of the speed meter.

Sagnac speed meter scheme

The differential speed measurement of the arm cavities length variations can be achieved by two consecutive measurements. In 2003, Chen pointed that the Sagnac interferometer is automatically a speed meter interferometer [47]. Like shown in Fig. 1.7, for Sagnac interferometer, the differential speed measurement of the two arm cavities length variations is realised by two counter propagating beams sensing the test masses position in two cavities with a time delay respectively and interfering destructively at the dark port. The mirror

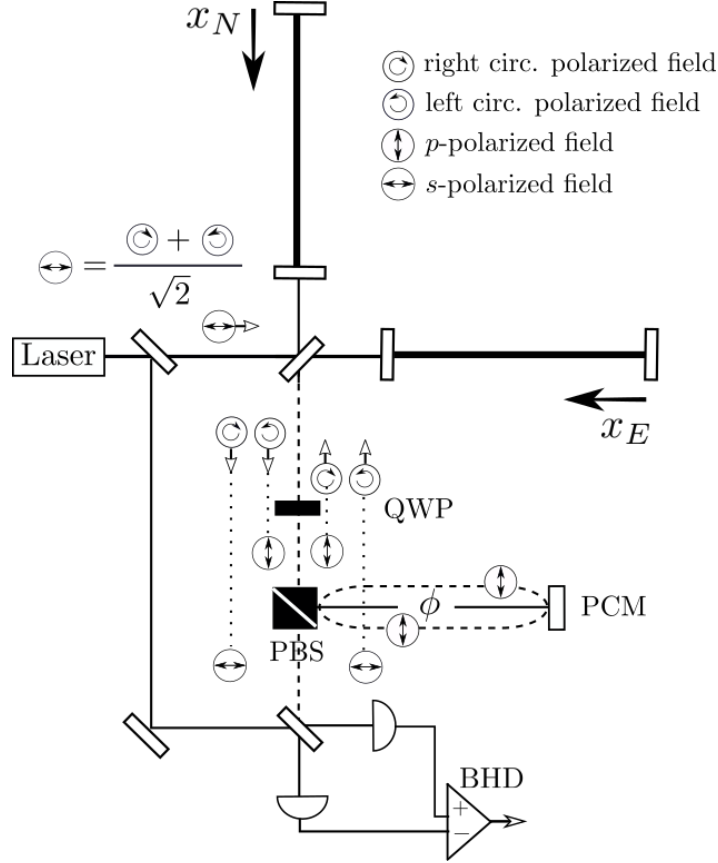


Figure 1.8: Schematic of polarisation circulation speed meter. The different polarisation laser field are indicated on the top right corner of the figure. PBS represents a polarisation beam splitter, QWP represents a quarter wave plate, PCM is the polarisation circulating mirror and BHD is the balanced homodyne detector. The measurement process is described in the main text.

displacement information carried by the two traveling beams can be presented as

$$\begin{aligned}\delta\phi_{CW} &\propto \sqrt{R}[x_N(t_1) + x_E(t_2)], \\ \delta\phi_{CCW} &\propto \sqrt{T}[x_E(t_1) + x_N(t_2)].\end{aligned}\quad (1.49)$$

After the destructive interference at the main beam splitter, the differential speed information can be expressed as

$$\dot{x}_{\text{darm}}(t_1) \propto -\sqrt{R}\phi_{CW} + \sqrt{T}\phi_{CCW} = \dot{x}_N(t_1) - \dot{x}_E(t_1), \quad (1.50)$$

when $T = R = \frac{1}{2}$.

Polarisation circulation speed meter scheme

Another Sagnac type of speed meter can be realised by utilising polarised light like shown in Fig. 1.8 [48]. The main interferometer is pumped by p-polarised laser field that can be represented by a linear combination of two circulation polarisation fields. The vacuum that enters from dark port will be set to the left circulation polarisation mode after transmitting

through the polarisation beamsplitter (PBS) and a quarter wave plate (QWP). Then the vacuum field will couple with the left circulation component in the laser field and convey the differential mode displacement at time t_1 , $x_{darm}(t_1) = x_N(t_1) - x_E(t_1)$ which includes the differential displacement driven by the laser radiation pressure. These sidebands will go through QWP and be converted to s-polarisation. The sidebands reflected from the so-called polarisation circulation mirror (PCM) will go back to the interferometer again after gaining a phase shift ϕ . They will be in right circulation polarisation after travelling through the QWP. The right polarisation field will sense the differential displacement of two arm cavities at time t_2 . Finally, the field read out from dark port will be on p-polarisation again. When $\phi = \pi$, the speed measurement is acquired as

$$\dot{x}_{darm}(t_1) = x_{darm}(t_2) - x_{darm}(t_1). \quad (1.51)$$

Chapter 2

Sagnac Speed meter proof of concept experiment and laser stabilisation

In this chapter, I introduce several design aspects of the Sagnac speed meter (SSM) proof of concept experiment in Glasgow, which will also serve as a specific example for demonstrating several investigations later on Chapter. 3, 5, 6, 7 in this thesis. One aspect of special relevance for later chapters are the amplitude and frequency stabilisation of the laser and hence they will be discussed in a bit more detail.

2.1 Conceptual design and sensitivity

The SSM proof of concept experiment aims to prove the superiority of speed meters in terms of quantum radiation pressure noise compared with an equivalent Michelson interferometer and to pave the way of the application of speed meters in future generation detectors. The equivalent Michelson owes the identical shot noise limited sensitivity to that of Sagnac in high frequency range. This equivalence comparison can be realised by designing the Michelson interferometer with same arm cavity round trip length, same effective mass of cavity mirrors, doubled input laser power and choosing the readout quadrature of Sagnac speed meter on 45 degree. Any arbitrary readout quadratures can be chosen by implementing the balanced homodyne readout.

The target band of this experiment is between 100 Hz and 1 kHz. The interferometer will be pumped by a laser with 1.7 W power and 1064 nm wavelength at the main beam splitter. The transmission of the ITM is chosen around 700 ppm. About 4.8 kW circulating power should build up inside the arm cavities which are of 2.8 m round trip length. It provides significant radiation pressure forces on the mirrors. The two arm cavities are in triangular shape consisting of one 1 g ITM and two 100 g ETMs, so the effective mass of each cavity

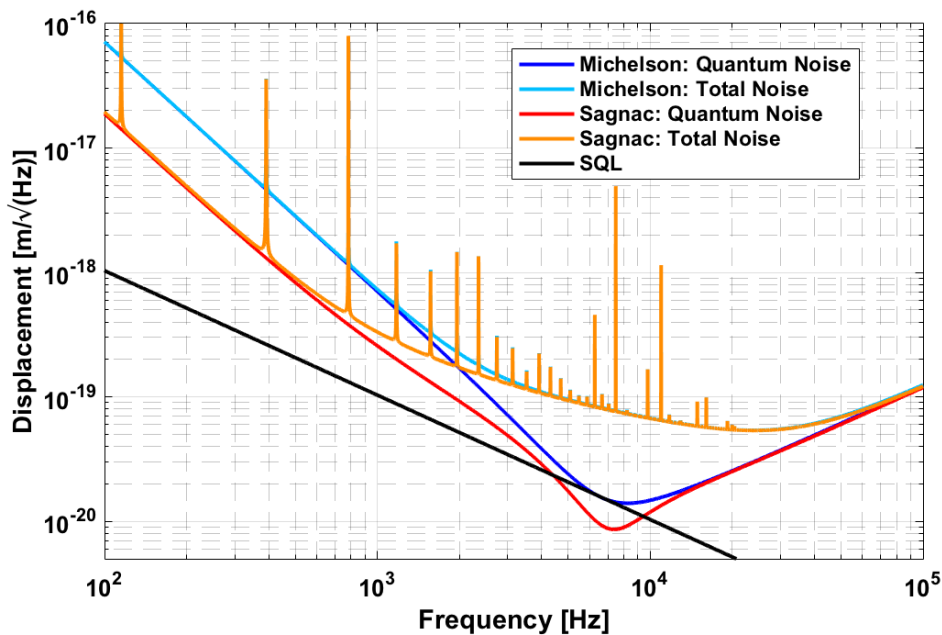


Figure 2.1: Design sensitivity of the Glasgow SSM experiment and equivalent Michelson. The red trace is the quantum noise limited sensitivity of the Sagnac speed meter, the orange trace is the total noise budget. Compared with the Michelson quantum noise and total noise budget, which are coloured in blue and light blue, there is a factor of 3-5 superiority of the SSM quantum noise and total noise between 100 Hz and 1 kHz. The black curve is the free mass stand quantum limited in displacement with the effective mechanical displacement mode mass.

mode is 0.995 g. Great care was taken in the design of the experiment to ensure that all classical noises are kept below the quantum noise and hence quantum radiation pressure noise can dominate the total noise budget in the frequency range from 100 Hz to 1 kHz. The quantum noise and total noise budget is shown in Fig. 2.1.

2.2 Optical layout

The layout of the in-vacuum part of this experiment is shown in Fig. 2.2. There are nine auxiliary suspensions in total. Suspensions with M4, M5, M7, M11 are for the alignment of the input beam and serve as a passive seismic isolation system on the input pass. M8, M10 are for the alignment between two cavities. M9 is a curved mirror, which is used for the mode matching between the two arm cavities. The suspensions with M12, M13 are on the local oscillator path and suspensions with M14 and M15 are on the signal path in the balanced homodyne readout. They play the role of seismic isolation on the output pass. M1a, M1b are two 1g ITMs with a radius of curvature of 7.9 m, which helps prevent the higher order optical modes resonance in the cavities [1]. M2a, M3a, M2b, M3b are four 100g ETMs of the two triangular cavities. M6 is a thick 50:50 beamsplitter. It can help to eliminate the multiple interferences inside the substrate benefiting of the thickness.

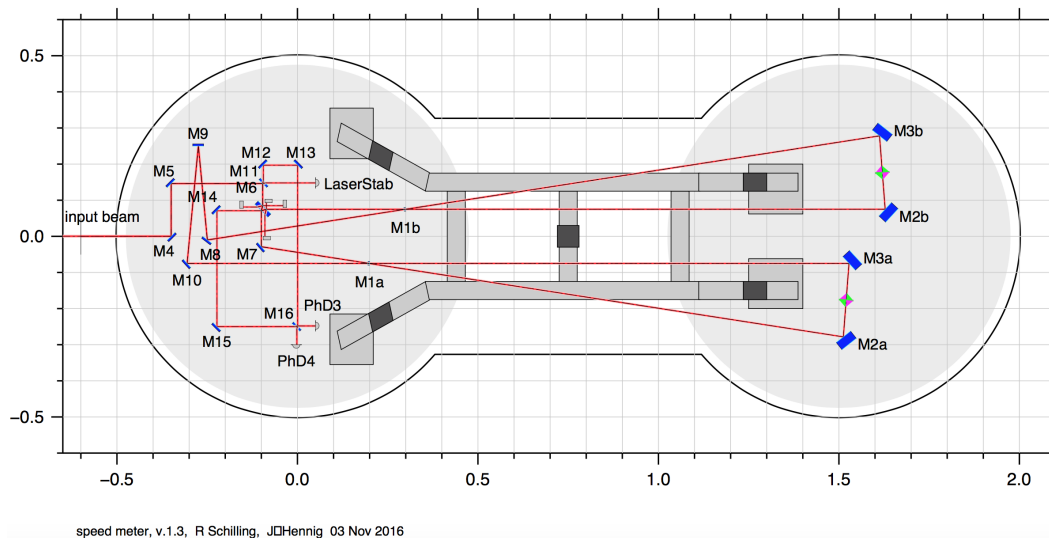


Figure 2.2: Optical layout of Glasgow SSM experiment. For a detailed description please refer to the main text. [7]

The local oscillator is derived from the interferometer bright port and transmits through M11. This choice enables wave front matching with the signal beam, assuming the relative length of the LO path and the signal path is set correctly, [7] and can also help to subtract the common motion noise in the signal beam due to the imbalance of main beamsplitter [49]. PhD3 and PhD4 are the two photodiodes in the balanced homodyne readout. After subtraction of the two photocurrents, the resulting data stream contains the differential speed information of the two arm cavities.

2.3 Suspensions

The auxiliary suspensions are two stage pendulums with coil drivers on the first stage which provides alignment control for both pitch and yaw degrees of freedom and eddy current damping. The cavity ETM suspensions (100g suspensions) are triple stage suspensions. Coil magnet actuators are available on both top mass and penultimate mass. The last stage test mass is suspended by four $20\ \mu\text{m}$ fused silica fibres from the penultimate mass. The fibres are welded directly on the ears of mass, so they compose a monolithic system. This design can significantly reduce the suspension thermal noise. In order to gain the controls of longitudinal motion of test mass in the high frequency range, electrostatic drive actuators [50, 51] are implemented on the last stage. It also has the advantage of evading the Barkhausen noise [52]. The cavity ITM suspensions (1g suspension) are four stages pendulum systems. The penultimate stage provides both actuation and switchable passive eddy-current damping of test mass motion [53]. The last two stages are also monolithic. Each fused silica fibre for the monolithic assembly is of $10\ \mu\text{m}$ diameter in the thin part and

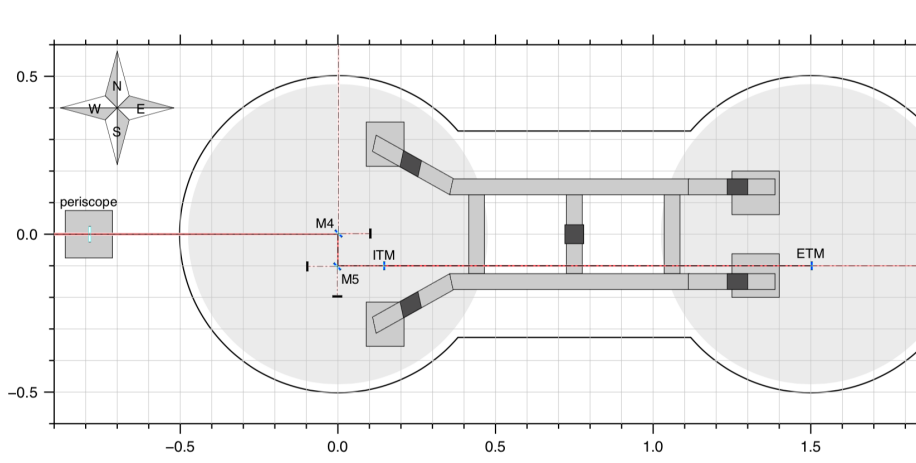


Figure 2.3: Optical layout of the linear cavity.

of 96 mm pulled length. More details can be found in [7].

2.4 Vacuum system

All the optics and suspensions are hosted in two connected vacuum chambers and located on two breadboards with 90 cm diameter of each. In order to suppress the differential motion of cavity ITM and ETMs which locate in the front and rear tank, respectively. The two breadboards are connected by a rigid bridge structure. Under the two breadboards, there are three layers of stacks and springs, which serve as a pre-isolation scheme. The whole system will be operated at pressures below 10^{-6} mbar.

2.5 Linear cavity and frequency stabilisation

As a pretest for the SSM experiment, we set up a linear cavity with two auxiliary suspensions located on the two breadboard to measure the differential residual motion induced by the environment. The linear cavity is designed to have a length of 1.35 m. The radius of curvature of the ITM is 3 m, while the ETM is a flat mirror. There are two input alignment mirrors M4 and M5 in front of the cavity. The optical layout is shown in Fig. 2.3.

2.5.1 Alignment and mode matching of linear cavity

In this section, I describe the alignment and mode matching work for the linear cavity.

Alignment

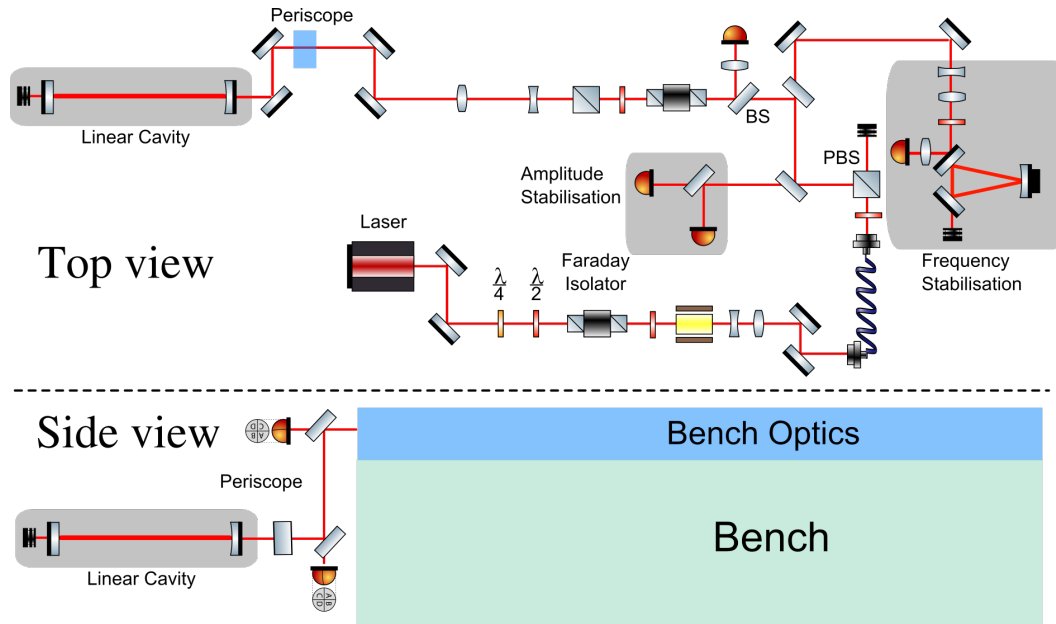


Figure 2.4: The layout of the linear cavity experiment. Both frequency and amplitude fluctuations are sensed in their corresponding stabilisation paths and corrected by feedback directly to the laser. The top part is an aerial view and the bottom part is a side view. Because the linear cavity is set in the vacuum tank which has a lower vertical height compared to the bench, a periscope is required to lead the input laser to the tank.

Firstly, we got an input beam with desired power. The schematic of optics on bench is shown in Fig. 2.4. We set the desired laser power by adjusting the relative polarisation angle of the two half wave plate (HWP)s. The second step was to align the pitch of the input beam on the bench in air. We adjusted the beam axis to be parallel to the surface of the bench top and to centre all laser beams on all of the optical elements.

In order to guide the beam on the bench to the vacuum tank, a periscope is set between as show in Fig. 2.4. At the transmission ports of the top and bottom mirror of the periscope, two spot position sensors are placed for recording the absolute beam spot position. Between the periscope mirrors and the spot position sensors, there are reflective mirrors which allow adjust the relative orientation of the reflective beams and spot position sensors. They are not draw in Fig. 2.4. We adjusted the reflective mirror at the transmission port of the periscope top mirror to keep the beam spot at the centre of spot position sensor as a reference. It helps to identify the beam alignment on the bench. The third step was to align the beam in the vacuum tank. We adjusted the beam axis to be parallel to the surface of the in-vacuum bread boards by adjusting the angle of the two mirrors on the bench which provide adjustable degrees of freedom for both beam tilt and shift in pitch and yaw direction. The laser beam is 10 cm above the breadboard. In this process, we moved away the two suspensions with mirror M4 and M5 for seeing the beam spot in a relative long distance for a better alignment. Then we re-adjusted the reflective mirrors behind the top and bottom periscope mirrors to centring the beam spots at the spot position sensors as a reference.

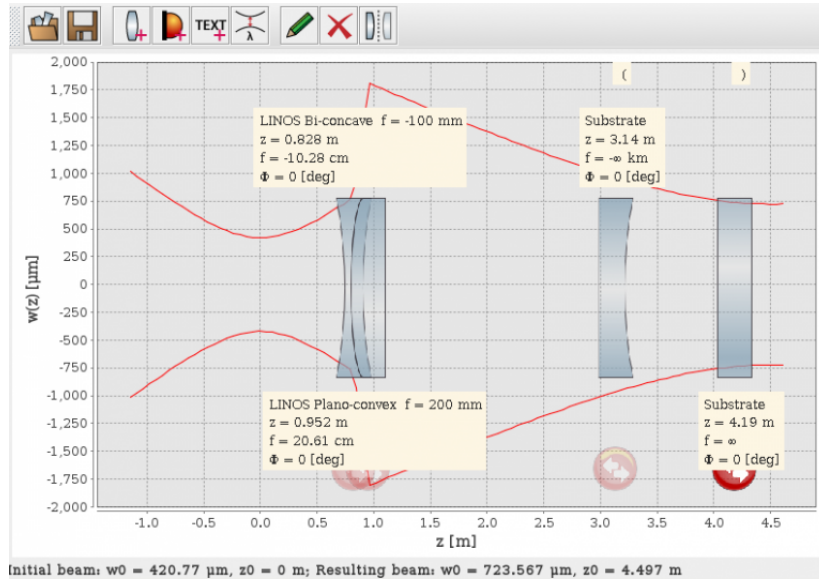


Figure 2.5: The snapshot of the design of mode matching.

The fourth step was to do pitch alignment for individual auxiliary suspensions using the aligned incoming beam. The fifth step was to align the linear cavity with the input beam. We started this by just installing the ETM and then aligned it so that the reflected beam overlaps the incoming beam. Only then we installed the ITM. The ITM was then aligned again to overlap the reflected beam with the incoming beam. At the transmission port of ETM, we put a camera outside the vacuum tank for observing the mode shape of the transmission beam of the cavity. Having completed this pre-alignment, the final alignment was done by actuating the mirror via the coil magnet actuators via Control and Data System (CDS) [3], thus observing flash of TEM₀₀ mode shape through the camera.

Mode matching

In order for maximum coupling of the input beam into the linear cavity, we need to establish good overlap of the transversal mode of the input beam and the cavity eigen mode. This is usually achieved by a set of lenses on the laser input path. I calculated the required lenses parameters with the software, JamMt. In this experiment, the initial waist position is defined at 0 m. The distance measured from initial waist to ITM is 3.14 m. The resulting beam waist position should be on ETM after mode matching since the ETM is a plane mirror while the ITM has a radius of curvature of 3 m. The cavity length is 1.35 m. With these settings, a lens with focus length -100 mm was chosen to be placed 0.83m away from the waist position and another lens with focus length 200 mm as chosen to be placed at 0.95 m from the waist position. Fig. 2.5 is the snapshot of the design of mode matching.

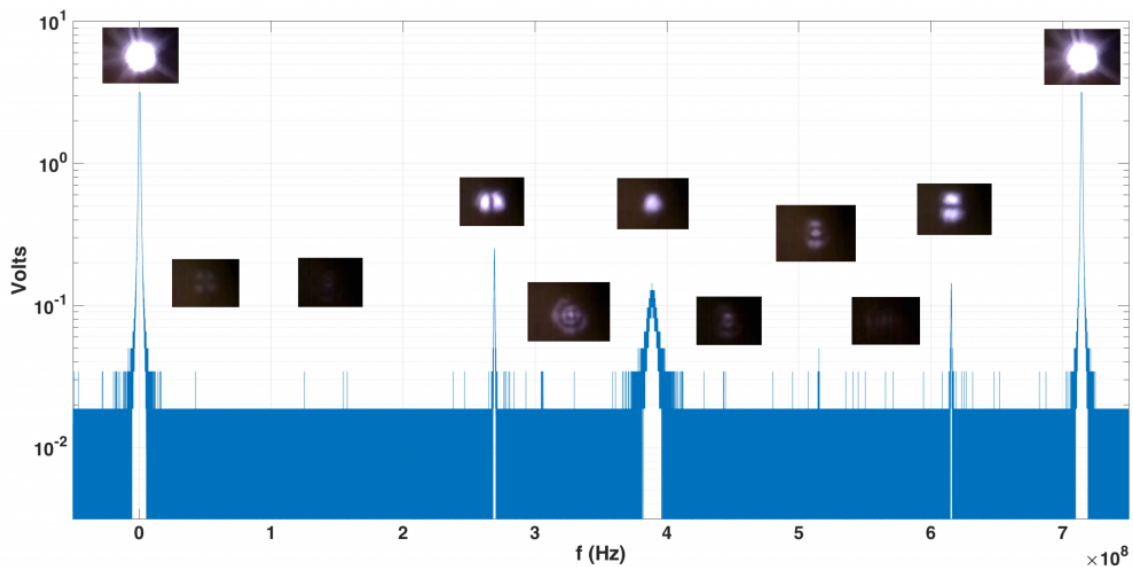


Figure 2.6: The optical mode pictures while scanning the whole free spectral range.

2.5.2 Linear cavity locking

The cavity was locked by utilising the Pound-Drever-Hall technique (PDH) [13]. The photodiode used to generate the PDH error signal was placed at the reflection of the linear cavity. A series of small steps and experimental tricks are useful to optimally set up the PDH scheme: 1) One needs to block extra beams reflected by other optical components in order to make sure the photodiode signal is dominated entirely by light reflected back from the cavity; 2) the reflected beam power needs to be attenuated for acquiring suitable laser power shining onto photodiode. 3) Often it is useful to place a positive lens before the photodiode to get a smaller beam size. The photodiode can then be placed close to the resulting beam waist, so that the beam is not clipped on the photodiode. Between 2) and 3), a reference needs to be set to keep the laser beam aligned. By slightly adjusting the height and angle of photodiode, the maximal output as judged by the DC photo current can be obtained. The error signal is measured from the demodulation of the photodiode output. The radio frequency (RF) modulation and demodulation scheme makes use of an RF oscillator which is used on one hand for creating the RF sidebands on the input light, but also on the other hand for demodulating the detected photo current. By scanning the length of the cavity, we obtain the error signals of the carrier light and two sidebands for the cavity length variation. The demodulated error signal is sent to CDS where we implemented a digital controller. The output of the filter bank in CDS is then sent to a high voltage amplifier driving the laser PZT adjusting the laser frequency. During later experiments we extended the servo to feature split feedback, *i.e.* high frequency feedback to the laser PZT and low frequency feedback to laser crystal temperature in order to increase the actuator range of this servo. By monitoring the feedback signal applied to the laser PZT

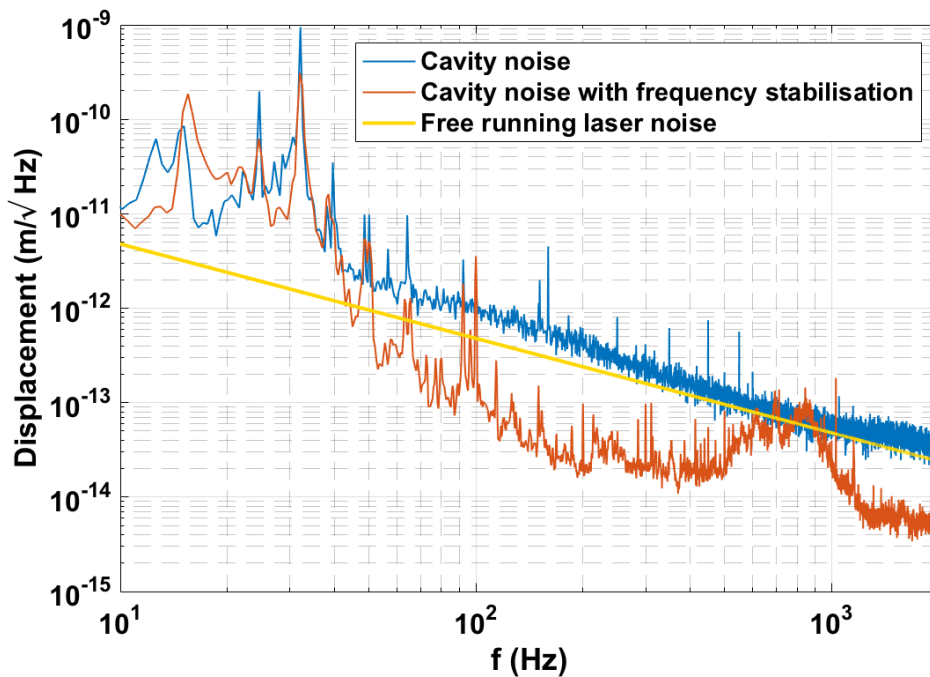


Figure 2.7: The displacement noise spectral density of the linear cavity in vacuum. The blue trace represents the total noise when the frequency stabilisation scheme is switch off, the yellow trace is the theoretical free running laser frequency noise and the red trace is the cavity total noise with frequency stabilisation active.

and using the calibration of the PZT provide by the laser manufacturer, it is possible, taking into account the servo loop gain, to derive a spectral density of the equivalent displacement noise of the cavity. This is shown as the blue trace in Fig. 2.7. Above 100 Hz, the free running laser frequency noise dominates the total noise. This motivates the work of frequency stabilisation.

2.5.3 Frequency Stabilisation

Like shown in Fig. 2.4, the laser frequency is stabilised by a rigid reference cavity whose round trip length is 40 cm. Also for the reference cavity proper alignment and mode matching must be ensured. With that accomplished I observed the transversal modes resonating the cavity by driving the mode cleaner piezo actuator over full free spectral range. As shown in Fig. 2.6, there are two strongest peaks which are the fundamental mode components. For triangular cavities where the lights do not incident along the normal of the mirrors, there is a π phase shift difference introduced by the mirrors reflection in a round trip between P-polarisation and S-polarisation lights [54]. The broad band peak around the middle is proved to be the fundamental mode in orthogonal polarisation. The slight offset to the middle could come from the nonlinearity during the scanning of the cavity length. The reference cavity is locked by both laser temperature control and laser crystal

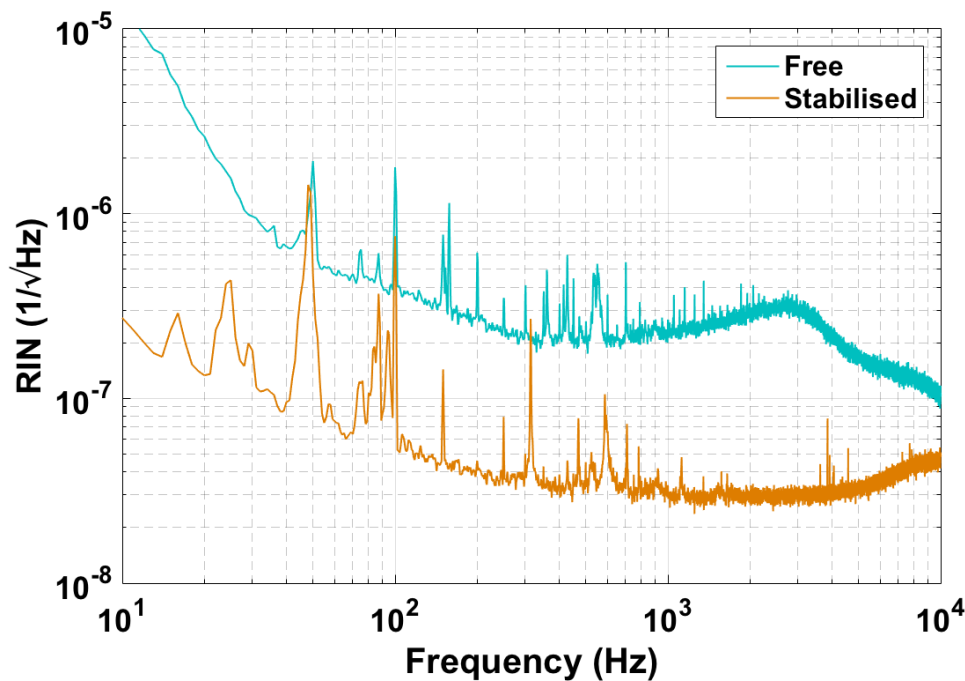


Figure 2.8: The amplitude spectral density of laser intensity noise. The cyan trace is the measured free laser intensity noise, the orange trace is the laser intensity noise with the stabilisation active.

piezo control. The linear cavity is locked by feeding its error signal to the reference cavity piezo actuator for evaluating the frequency stabilisation performance. The linear cavity total noise with the frequency stabilisation loop being active is shown as the red trace in Fig. 2.7. The reasons of the wide hill around 800 Hz was not further investigated.

What is the frequency noise stability requirement in the SSM experiment? Actually, the laser frequency noise does not couple to the dark signal port in the ideal case unless there is a main beamsplitter imbalance. This originates from the fact that any common motion will not couple to the dark part because of the character of the Sagnac interferometer typology (two beams share the same path). The laser frequency noise is also a common motion noise. In Chapter. 5, I will show that the common mode noise coupling can be canceled by choosing a proper local oscillator port in the balanced homodyne readout.

2.5.4 Amplitude Stabilisation

As shown in Fig. 2.4, another branch of the beam is used for the amplitude stabilisation. The amplitude stabilisation scheme consists two photodiodes. One is called in-loop photodiode, which is for measuring the laser power fluctuations. The in-loop photodiode DC output signal is sent to a servo box. In the servo box, it is subtracted from the reference voltage to obtain a bi-directional error signal. The subtracted signal is amplified by a variable gain and passes through filters and then is sent back to the laser diode current modulation.

The other photodiode is called out-loop photodiode, which is for monitoring the stabilisation performance. In the out-of-loop measurement the shot noise level is enhanced by a factor $\sqrt{2}$, since both photodiode's, in-loop and out-of-loop, shot noise contribute. In a single cavity, the laser intensity noise will be amplified due to opto-mechanical effect and couples to other quadratures. In the Glasgow SMM experiment, laser intensity noise is again a common mode noise similar to laser frequency noise. The strength the intensity noise coupling onto detection port due to main beam splitter imbalance can be strongly suppressed by adopting a special choice of local oscillator in balanced homodyne readout, which is the content of [49]. The relative intensity noise after stabilisation which is shown in Fig.2.8 shows the obtained intensity noise stabilisation performance which fulfils the relevant requirements for the SSM experiment.

2.6 Summary

In this chapter, I introduced the design features of the Glasgow Sagnac speed meter proof of concept experiment, including its conceptual design, optical layout and suspensions. I introduced the preliminary experiments carried out using a suspended linear cavity, based on which I tested the laser frequency stabilisation scheme. I also showed the performance of the laser amplitude stabilisation. Both of these two laser noises fulfil the design requirements of the SSM experiment. These work pave the way of building the complete prototype at the laser input end. With the current stabilised laser, we can start to construct the vacuum optics gradually, modelling the length and angular control schemes [55] and construct the balanced homodyne detector at the signal output end. In Chapter. 3, I will describe the investigations on realistic implementation of balanced homodyne readout in the SSM experiment considering beam misalignment and jittering. In Chapter, 6, I will describe the potential angular control schemes for the SSM experiment.

Chapter 3

Balanced-homodyne readout with higher optical modes

Balanced homodyne detection (BHD) helps to eliminate the dark fringe offset in advanced LIGO type gravitational wave detectors and allows arbitrary quadratures readout of light field compared with DC readout [56], thus has been suggested as a block for the advanced LIGO upgrade and third-generation observatories (More details can be found in Chapter. 4). The Sagnac speed meter interferometer is even incompatible to DC readout [57], and therefore pushes the implementation of BHD. So investigations on realistic implementation of BHD are important.

In this chapter, the work is about the implementation of BHD considering the local oscillator (LO) beam or signal beam misalignment and mismatch. I investigate how the high order modes (HOMs) in either LO and signal beam due to mismatch and misalignment effect the output of the BHD. I develop a full framework for analyzing the static optical HOMs occurring in the BHD paths related to the misalignment or mode matching at the input and output ports of the laser interferometer. I also calculate the LO beam jitter noise coupling into the output of BHD. The analyses can be applied to general types of interferometers with BHD. As it turns out, the beam misalignment at output port only degrades the shot noise limited sensitivity at high frequencies similar to the effect of imperfect quantum efficiency of the photodetector. The beam misalignment at input port not only degrades the shot noise limited sensitivity but also effects the sensitivity at low frequencies because of the decrease of circulating power in the interferometer arm cavities. Further more, taking the Glasgow speed meter proof of concept experiment as an example, we find that the beam jitter noise introduced by seismic motion is well below the quantum noise level in the frequency range of 10 Hz to 1000 Hz.

This work, which I lead has been published as a journal article. It is reproduced in the following.

Effects of static and dynamic higher-order optical modes in balanced homodyne readout for future gravitational waves detectors

Teng Zhang,¹ Stefan L. Danilishin,¹ Sebastian Steinlechner,^{1,2} Bryan W. Barr,¹ Angus S. Bell,¹ Peter Dupej,¹ Christian Gräf,¹ Jan-Simon Hennig,¹ E. Alasdair Houston,¹ Sabina H. Huttner,¹ Sean S. Leavey,¹ Daniela Pascucci,¹ Borja Sorazu,¹ Andrew Spencer,¹ Jennifer Wright,¹ Kenneth A. Strain,¹ and Stefan Hild¹

¹*SUPA, School of Physics and Astronomy, The University of Glasgow,
Glasgow G128QQ, United Kingdom*

²*Institut für Laserphysik und Zentrum für Optische Quantentechnologien der Universität Hamburg,
Luruper Chaussee 149, 22761 Hamburg, Germany*

(Received 7 December 2016; published 6 March 2017)

With the recent detection of gravitational waves (GWs), marking the start of the new field of GW astronomy, the push for building more sensitive laser-interferometric gravitational wave detectors (GWDs) has never been stronger. Balanced homodyne detection (BHD) allows for a quantum-noise (QN) limited readout of arbitrary light field quadratures, and has therefore been suggested as a vital building block for upgrades to Advanced LIGO and third-generation observatories. In terms of the practical implementation of BHD, we develop a full framework for analyzing the static optical high-order modes (HOMs) occurring in the BHD paths related to the misalignment or mode matching at the input and output ports of the laser interferometer. We find the effects of HOMs on the quantum-noise limited sensitivity is independent of the actual interferometer configuration; e.g. Michelson and Sagnac interferometers are affected in the same way. We show that misalignment of the output ports of the interferometer (output misalignment) only affects the high-frequency part of the quantum-noise limited sensitivity (detection noise). However, at low frequencies, HOMs reduce the interferometer response and the radiation pressure noise (back-action noise) by the same amount and hence the quantum-noise limited sensitivity is not negatively affected in that frequency range. We show that the misalignment of the laser into the interferometer (input misalignment) produces the same effect as output misalignment and additionally decreases the power inside the interferometer. We also analyze dynamic HOM effects, such as beam jitter created by the suspended mirrors of the BHD. Our analyses can be directly applied to any BHD implementation in a future GWD. Moreover, we apply our analytical techniques to the example of the speed meter proof-of-concept experiment under construction in Glasgow. We find that for our experimental parameters, the performance of our seismic isolation system in the BHD paths is compatible with the design sensitivity of the experiment.

DOI: [10.1103/PhysRevD.95.062001](https://doi.org/10.1103/PhysRevD.95.062001)

I. INTRODUCTION

After a half-century search, the first detection of gravitational waves in 2015 [1] further inspired the worldwide effort to increase the sensitivity of laser-interferometric gravitational wave detectors (GWDs). As the design sensitivity of the second-generation detectors is limited by quantum noise over most of the detection frequency band, the development and implementation of novel techniques which reduce or even circumvent quantum noise is a major task within the detector collaborations [2].

Quantum noise originates from the quantum nature of laser light and manifests itself in two ways. Shot noise, or

sensing noise, dominates at high frequencies, while radiation pressure noise, or back-action noise, dominates at low frequency. At each frequency there is an optimal laser power which balances the two noise sources, giving rise to the so-called “standard quantum limit” (SQL). Using quantum nondemolition (QND) techniques [3], it is in principle possible to achieve sensitivities beyond the SQL [4,5]. These techniques often require the readout of a specific quadrature of the interferometer output light field, e.g. in the variational readout scheme [4]. Balanced homodyne detection (BHD) allows for arbitrary readout quadratures and therefore naturally offers itself for this task. Another approach to surpass the SQL is the speed meter topology [6], in which the speed of a test mass is detected instead of its position. In 2003, Chen [7] pointed out that the Sagnac interferometer topology behaves as a speed meter, and a proof-of-principle experiment is currently being set up in Glasgow [8]. As it turns out, there is no suitable carrier field available in the output port of Sagnac

Published by the American Physical Society under the terms of the Creative Commons Attribution 4.0 International license. Further distribution of this work must maintain attribution to the author(s) and the published article's title, journal citation, and DOI.

interferometers and so an external local oscillator (LO) is required, which is provided by BHD.

Current GWDs employ a dc readout [9] (sometimes also referred to as a “homodyne readout”), in which a small differential arm-length offset is introduced that leads to some carrier light in the signal port and which serves as the LO for detection with a single photodetector. The local oscillator power needs to be chosen such that the photon shot noise is well above the electronic noise of the detector. Now that quantum-noise reduction using squeezed light has become a key ingredient of current detectors [10,11], the requirements for the local oscillator power and the resulting voltages in the photodetector electronics are close to reaching technical limitations as the squeezing strength further improves [12]. Here, the current-subtracting design of BHD helps to bring the requirements down again to manageable levels [13].

Thus, there is significant interest in applying BHD in GWDs as an enabling technology for further improvements in the quantum-noise limited sensitivity. So far there is surprisingly little experience with BHD in gravitational wave detectors [13,14], especially with regards to the requirements and difficulties that come with suspended optics, long baselines and highest sensitivities in the few hundred hertz regime. Here we develop a framework to investigate and define those effects. In Sec. II, we introduce a general calculation in a BHD readout involving the higher-order mode components; in Sec. III, we consider how HOMs enter the quantum noise picture that describes interferometers such as GWDs; in Sec. IV, we then illustrate how HOMs come about from misalignment and mismatch in BHD; in Sec. V, we derive how static misalignment or mismatch affect the quantum-noise limited sensitivity of a Michelson interferometer; in Sec. VI, we look at the example of the Glasgow SSM experiment to verify the effects on such a QND techniques candidate configuration; in Sec. VII, we calculate the dynamic beam jitter noise coupling in a BHD readout.

II. FUNDAMENTALS OF BALANCED HOMODYNE DETECTION WITH HIGHER-ORDER MODES

Let us start by establishing the fundamental equations which describe BHD readout with HOMs. We define the time-varying electrical fields of the signal and LO beams as $s(r, t)$ and $l(r, t)$, respectively, where we collected the transverse spatial coordinates in r . For both fields, we separate the dc components S_{mn}, L_{mn} from the fluctuations s_{mn} and l_{mn} , where $m, n \geq 0$ are the indices of the Hermite-Gaussian mode expansions, TEM _{mn} . A natural reference for the mode expansion is the fundamental mode of the optical instrument, e.g. the fundamental mode defined by the arm cavities in a GWD. The two optical fields can then be written as

$$s(r, t) \propto \sum_{m,n \geq 0} u_{mn}(r, z)[S_{mn} + s_{mn}]e^{-i\omega t} + \text{H.c.} \quad (1)$$

$$l(r, t) \propto \sum_{m,n \geq 0} u_{mn}(r, z)[L_{mn} + l_{mn}]e^{-i\omega t} + \text{H.c.} \quad (2)$$

where $u_{mn}(r, z)$ is the spatial distribution of the electric field of Hermite-Gaussian modes of orders m, n in the plane transverse of the direction of propagation z ; ω is the carrier frequency; and H.c. denotes the Hermitian conjugate.

Afterwards, the signal and LO beams are overlapped on the BHD beam splitter with a relative phase ϕ_h that defines the homodyne angle, i.e. the detected light field quadrature. The fields in the two beam splitter outputs are given by

$$P_1 = \frac{le^{i\phi_h} + s}{\sqrt{2}}, \quad P_2 = \frac{-le^{i\phi_h} + s}{\sqrt{2}}. \quad (3)$$

These fields are detected by two photodiodes, and the resulting photocurrents are subtracted from each other, resulting in the output photocurrent

$$I_{\text{BHD}} \propto P_1 P_1^\dagger - P_2 P_2^\dagger = \sum_{m,n \geq 0} (L_{mn} + l_{mn})(S_{mn} + s_{mn})^\dagger e^{i\phi_h} + \text{H.c.} \quad (4)$$

To simplify the notation, in the following we use a single index j to enumerate the mode indices mn , i.e. for $j = 0$, $\{mn\} = \{00\}$; for $j = 1$, $\{mn\} = \{01\}$; for $j = 2$, $\{mn\} = \{02\}$, etc.

For future purposes, we separate the BHD photocurrent into the classical dc and the fluctuation parts using so-called “two-photon formalism” [15,16] which is used to describe the fields using a two-dimensional vector of two orthogonal quadrature amplitudes. Then the dc components and fluctuations in signal beam and LO beam are defined as S, s, L, l , in which e.g. $s = (s_c, s_s)^\text{T}$, where the superscript T stands for transpose. The additional homodyne angle ϕ_h is used to single out the particular readout quadrature. Mathematically, it means that the LO field needs to be multiplied by a rotation matrix of the following form:

$$\mathbb{H}_{\phi_h} = \begin{bmatrix} \cos(\phi_h) & -\sin(\phi_h) \\ \sin(\phi_h) & \cos(\phi_h) \end{bmatrix}. \quad (5)$$

Then the classical dc part reads

$$I_{\text{BHD}}^{\text{dc}} \propto \sum_{j \geq 0} S_j^\dagger \mathbb{H}_{\phi_h} L_j + \text{H.c.}, \quad (6)$$

while the fluctuating part, containing classical and quantum noise as well as modulation sidebands, is given by

$$I_{\text{BHD}}^{\text{fl}} \propto \sum_{j \geq 0} s_j^\dagger \mathbb{H}_{\phi_h} L_j + \sum_{j \geq 0} S_j^\dagger \mathbb{H}_{\phi_h} l_j + \sum_{j \geq 0} s_j^\dagger \mathbb{H}_{\phi_h} l_j + \text{H.c.} \quad (7)$$

III. QUANTUM-NOISE CHARACTER IN BALANCED HOMODYNE READOUT

In this section, we focus on the effect the HOMs have on the quantum noise of an interferometer with BHD readout. We denote the input light fields at the dark port (DP) and

bright port (BP) of the interferometer i and p , respectively. Then o and q stand for the respective output fields. Those will contribute to the signal and LO light fields. Then we can introduce the I/O relations by defining the interferometer transfer matrix (TM):

$$\underbrace{\begin{pmatrix} o_0 \\ o_1 \\ \vdots \end{pmatrix}}_{\vec{O}} = \underbrace{\begin{pmatrix} A_{00} & A_{01} & \cdots \\ A_{10} & A_{11} & \cdots \\ \vdots & \vdots & \ddots \end{pmatrix}}_{\text{A: DP} \rightarrow \text{DPTM}} \underbrace{\begin{pmatrix} i_0 \\ i_1 \\ \vdots \end{pmatrix}}_{\vec{I}} + \underbrace{\begin{pmatrix} B_{00} & B_{01} & \cdots \\ B_{10} & B_{11} & \cdots \\ \vdots & \vdots & \ddots \end{pmatrix}}_{\text{B: BP} \rightarrow \text{DPTM}} \underbrace{\begin{pmatrix} p_0 \\ p_1 \\ \vdots \end{pmatrix}}_{\vec{P}} + \underbrace{\begin{pmatrix} E_{01} & E_{02} & \cdots & E_{0N} \\ E_{11} & E_{12} & \cdots & E_{1N} \\ \vdots & \vdots & & \vdots \end{pmatrix}}_{\mathbb{R}_o} \underbrace{\begin{pmatrix} x_1 \\ x_2 \\ \vdots \\ x_N \end{pmatrix}}_{\vec{X}} \quad (8)$$

$$\underbrace{\begin{pmatrix} q_0 \\ q_1 \\ \vdots \end{pmatrix}}_{\vec{Q}} = \underbrace{\begin{pmatrix} C_{00} & C_{01} & \cdots \\ C_{10} & C_{11} & \cdots \\ \vdots & \vdots & \ddots \end{pmatrix}}_{\text{C: DP} \rightarrow \text{BPTM}} \underbrace{\begin{pmatrix} i_0 \\ i_1 \\ \vdots \end{pmatrix}}_{\vec{I}} + \underbrace{\begin{pmatrix} D_{00} & D_{01} & \cdots \\ D_{10} & D_{11} & \cdots \\ \vdots & \vdots & \ddots \end{pmatrix}}_{\text{D: BP} \rightarrow \text{BPTM}} \underbrace{\begin{pmatrix} p_0 \\ p_1 \\ \vdots \end{pmatrix}}_{\vec{P}} + \underbrace{\begin{pmatrix} F_{01} & F_{02} & \cdots & F_{0N} \\ F_{10} & F_{11} & \cdots & F_{1N} \\ \vdots & \vdots & & \vdots \end{pmatrix}}_{\mathbb{R}_q} \underbrace{\begin{pmatrix} x_0 \\ x_1 \\ \vdots \\ x_N \end{pmatrix}}_{\vec{X}}. \quad (9)$$

Any single transfer matrix, e.g. A_{kj} , is a 2×2 matrix that stands for the transformation from the TEM_j input field to the TEM_k output field. E_{kj} is a two-dimensional vector of the optomechanical response functions of the k th output mode at the DP to the displacement, $x_j(\Omega)$, of the j th mechanical degree of freedom of the interferometer, with N being the total number of mechanical degrees of freedom. The BP response function F_{kj} is defined in the same way. We use notations \mathbb{R}_o and \mathbb{R}_q for the whole response matrices for DP and BP, respectively.

Since gravitational waves couple to the differential degree of freedom of the arm cavities, it is sufficient for us to consider only the longitudinal motion of the two end test masses, i.e. x_+ and x_- , defining their common mode x_+ and differential mode x_- via

$$x_1 = \frac{x_+ + x_-}{2}, \quad x_2 = \frac{x_+ - x_-}{2}. \quad (10)$$

Then the response functions E_{01} and E_{02} for the fundamental light mode we measure can be written in terms of the latter ones, \mathbf{R}_+ and \mathbf{R}_- , as

$$\mathbf{E}_{01} = \mathbf{R}_+ + \mathbf{R}_-, \quad \mathbf{E}_{02} = \mathbf{R}_+ - \mathbf{R}_-. \quad (11)$$

The output fields o and q are sent towards the BHD through a train of steering optics. The LO beam can be derived from various sources. For example, in the particular case of the Glasgow SSM (that will be discussed in detail later in this article), the reflection from the interferometer is used to provide the LO for the BHD, i.e. the BP as shown in Figs. 1 and 2. Note that this scenario is more general than

the simpler case of getting the LO beam by picking off some light from the pumping laser directly (by turning the beam splitter after the laser by 90 degrees in Fig. 1), for mathematically this amounts to setting to zero all C_{ij} and F_{ij} in Eq. (9), and also setting $D_{ij} = \mathbb{1}_2 \delta_{ij}$ with $\mathbb{1}_2$ being a 2×2 identity matrix and δ_{ij} the Kronecker delta.

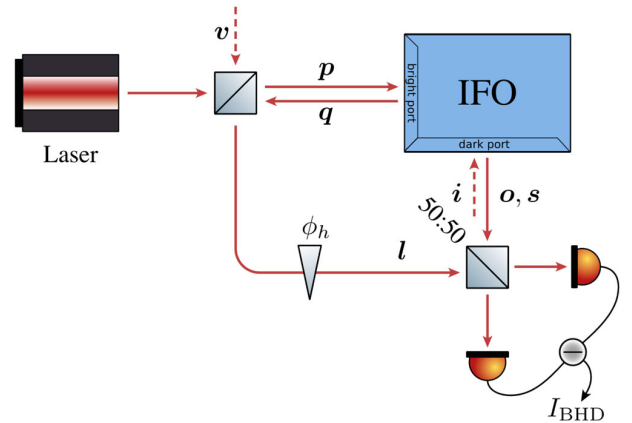


FIG. 1. Schematic of a balanced homodyne readout setup of a generic interferometer. The input and output fields at the bright port of the interferometer are denoted as p and q , respectively, while the corresponding fields at the dark port of the interferometer are denoted as i and o , respectively. Then the o field and q field enter into the BHD path as signal beam s and LO beam l . There is also a vacuum field v that couples into the l field due to the LO pickoff mirror. l and s are overlapped with each other at the balanced homodyne beam splitter. The output photo current I_{BHD} is a subtraction of the output of two photodiodes. The homodyne angle ϕ_h is the relative phase of the two beams entering the BHD.

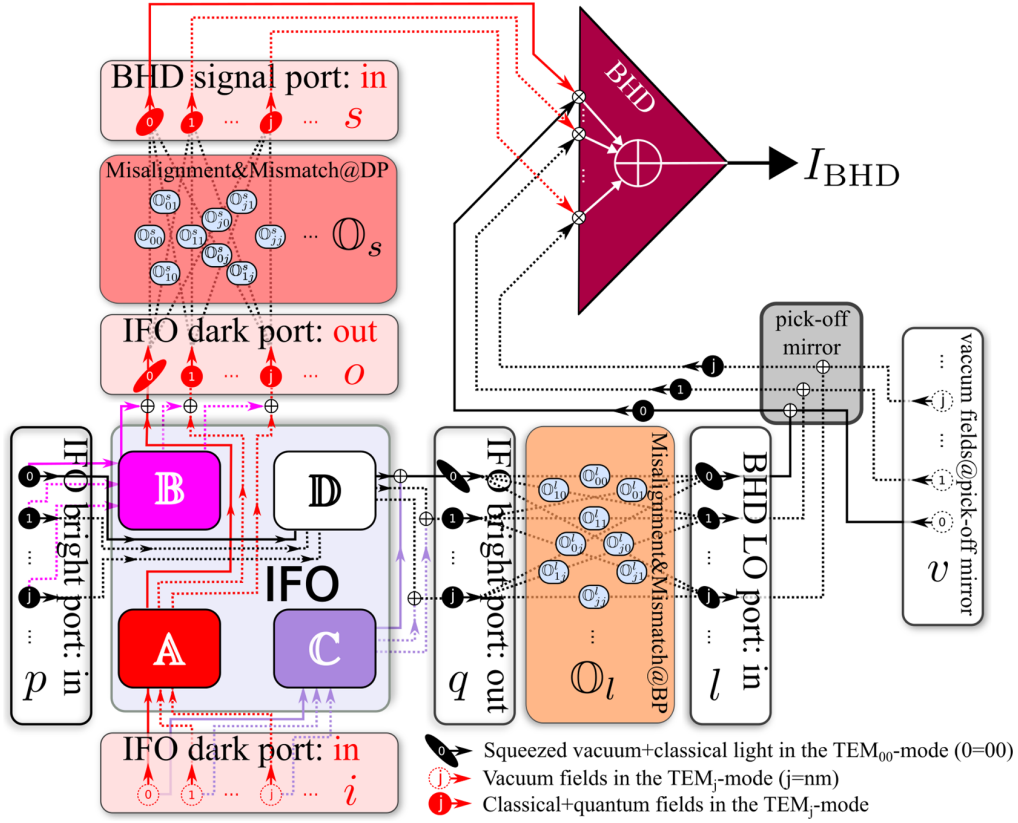


FIG. 2. Schematic of the HOM fields transformation in the interferometer with BHD readout. Multiple modes field p and i can enter into the interferometer from BP and DP, and only the interferometer mode field will suffer the ponderomotive squeezing effect, which can be explained by the four transfer matrices A, B, C, D. The output fields from BP and DP are q and o . We represent the misalignment and mismatch in both paths, signal and LO, by a separate block, i.e. \mathbb{O}_s and \mathbb{O}_l . The necessity for a pickoff mirror in order to create the LO beam causes additional vacuum noise v to couple into the BHD readout.

Due to imperfect optics, and alignment fluctuations originating from residual pendulum motion, o and q will suffer from misalignment and mismatch with respect to the interferometer modes. A redistribution of different modes will ensue and the new modes of the LO, l , and signal beam, s , will be a mixture of the original modes o and q . Mismatch and misalignment can be described by scattering matrices \mathbb{O}_l and \mathbb{O}_s for the LO beam and signal beam, respectively, defined as

$$\begin{pmatrix} s_0 \\ s_1 \\ \vdots \end{pmatrix} = \underbrace{\begin{pmatrix} \mathbb{O}_{00}^s & \mathbb{O}_{01}^s & \cdots \\ \mathbb{O}_{10}^s & \mathbb{O}_{11}^s & \cdots \\ \vdots & \vdots & \ddots \end{pmatrix}}_{\mathbb{O}_s} \begin{pmatrix} o_0 \\ o_1 \\ \vdots \end{pmatrix},$$

$$\begin{pmatrix} l_0 \\ l_1 \\ \vdots \end{pmatrix} = \underbrace{\begin{pmatrix} H_{\phi_h} \mathbb{O}_{00}^l & H_{\phi_h} \mathbb{O}_{01}^l & \cdots \\ H_{\phi_h} \mathbb{O}_{10}^l & H_{\phi_h} \mathbb{O}_{11}^l & \cdots \\ \vdots & \vdots & \ddots \end{pmatrix}}_{\mathbb{O}_l} \begin{pmatrix} q_0 \\ q_1 \\ \vdots \end{pmatrix}, \quad (12)$$

where (as shown in Fig. 2) the matrix component \mathbb{O}_{kj}^s (\mathbb{O}_{kj}^l) describes how the j th mode of the o field (q field) contributes to the k th mode of the s field (l field). Each \mathbb{O}_{kj}^s (\mathbb{O}_{kj}^l) is a 2×2 matrix. \mathbb{O}^s (\mathbb{O}^l) are not arbitrary; rather they need to satisfy the unitarity relation $\mathbb{O}_s^\dagger \mathbb{O}_s = \mathbb{O}_l^\dagger \mathbb{O}_l = \mathbb{I}$, where \mathbb{I} is the identity matrix, as a consequence of the law of energy conservation.

As the LO field mixes in a vacuum field v coming from the open port of the pickoff mirror (see Fig. 2), the actual LO field at the BHD reads

$$l' = \sqrt{R_p} l + \sqrt{T_p} v, \quad (13)$$

where R_p and T_p are the power reflectivity and transmissivity of the pickoff mirror, respectively. Then according to Eq. (7), we can write out the BHD readout photocurrent in terms of quantum noise and differential mode motion as

$$I_{\text{BHD}} \propto \sqrt{R_p} \mathbf{L}^\dagger [\mathbb{O}_s(\mathbf{A}\mathbf{i} + \mathbf{B}\mathbf{p})] + \mathbf{S}^\dagger [\sqrt{R_p} \mathbb{O}_l(\mathbf{C}\mathbf{i} + \mathbf{D}\mathbf{p}) + \sqrt{T_p} \mathbf{v}] + \sqrt{R_p} \mathbf{L}^\dagger \begin{pmatrix} \mathbb{O}_{00}^s \\ \mathbb{O}_{10}^s \\ \vdots \end{pmatrix} \mathbf{R}_{-x_-} + \text{H.c.}, \quad (14)$$

in which we neglect the term $\propto \mathbf{I}^\dagger \mathbf{s}$, the second-order term in the noise fluctuations. Finally, using the formalism of Eq. (12) in [17], one can write down the quantum-noise power spectral density as

$$\begin{aligned} S \propto & \left[\mathbf{L}^\dagger \mathbb{O}_s (\mathbf{A} \mathbb{S}_i \mathbf{A}^\dagger + \mathbf{B} \mathbb{S}_p \mathbf{B}^\dagger) \mathbb{O}_s^\dagger \mathbf{L} \right. \\ & + \mathbf{S}^\dagger \mathbb{O}_l (\mathbf{C} \mathbb{S}_i \mathbf{C}^\dagger + \mathbf{D} \mathbb{S}_p \mathbf{D}^\dagger) \mathbb{O}_l^\dagger \mathbf{S} \\ & + \mathbf{L}^\dagger \mathbb{O}_s (\mathbf{A} \mathbb{S}_i \mathbf{C}^\dagger + \mathbf{B} \mathbb{S}_p \mathbf{D}^\dagger) \mathbb{O}_l^\dagger \mathbf{S} \\ & + \mathbf{S}^\dagger \mathbb{O}_l (\mathbf{C} \mathbb{S}_i \mathbf{A}^\dagger + \mathbf{D} \mathbb{S}_p \mathbf{B}^\dagger) \mathbb{O}_s^\dagger \mathbf{L} \\ & \left. + \frac{T_p}{R_p} \mathbf{S}^\dagger \mathbf{S} \right] \left/ \left| \mathbf{L}^\dagger \begin{pmatrix} \mathbb{O}_{00}^s \\ \mathbb{O}_{10}^s \\ \vdots \end{pmatrix} \mathbf{R}_- \right|^2 \right., \quad (15) \end{aligned}$$

where \mathbb{S}_i and \mathbb{S}_p are the power spectral density matrices of \mathbf{i} and \mathbf{p} input fields [18]. For each optical mode, the components of \mathbb{S}_i and \mathbb{S}_p are defined as

$$\begin{aligned} \pi \mathbb{S}_{ij}^i \delta_{jj} \delta(\Omega - \Omega') &\equiv \langle \hat{i}_j(\Omega) \hat{i}_j^\dagger(\Omega') + \hat{i}_j^*(\Omega') \hat{i}_j^\dagger(\Omega) \rangle \\ \pi \mathbb{S}_{ij}^p \delta_{jj} \delta(\Omega - \Omega') &\equiv \langle \hat{p}_j(\Omega) \hat{p}_j^\dagger(\Omega') + \hat{p}_j^*(\Omega') \hat{p}_j^\dagger(\Omega) \rangle, \quad (16) \end{aligned}$$

where we define the Hermitian conjugate of the two-dimensional vector of light quadratures of the j th mode as $\mathbf{i}_j^\dagger = (\hat{i}_{c,j}, \hat{i}_{s,j})$ and the complex conjugate of the same vector as $\mathbf{i}_j^* = (\hat{i}_{c,j}^\dagger, \hat{i}_{s,j}^\dagger)^T$. $\mathbb{S}_{ij}^{i,p}$ are 2×2 matrices of power spectral densities of input fields in the j th mode when $j = j'$ and cross spectral densities between the j th and j' th modes of the corresponding input fields, if there are any.

IV. MATHEMATICAL TREATMENT OF MISMATCH AND MISALIGNMENT OF MULTIMODE HERMITE-GAUSSIAN BEAMS IN A LINEAR OPTICAL SETUP

In this section, following the formalism of [19,20], we calculate scattering matrices that describe transformation of the multimode Gaussian beam as it undergoes misalignment in the imperfect optical steering train from an input or output port of the interferometer to the corresponding input port of the balanced homodyne detector.

Firstly, we define the Cartesian coordinate system (x, y, z) for the mode at the output port of the interferometer. We assume the beam propagates along the z -axis with z_0 being the position of the beam waist and $z = 0$ is the location of the observation plane. x, y are the transverse spatial coordinates. Then, the spatial profile of the Hermite-Gaussian beam is given by

$$u_{mn}(x, y, z) = (1 + \zeta^2)^{\frac{1}{2}} N_{mn} H_m \left[\left(\frac{2}{1 + \zeta^2} \right)^{\frac{1}{2}} \frac{x}{w_0} \right] H_n \left[\left(\frac{2}{1 + \zeta^2} \right)^{\frac{1}{2}} \frac{y}{w_0} \right] e^{-ikz + i(m+n+1) \arctan(\zeta) - \frac{x^2 + y^2}{w_0^2(1 + \zeta^2)}}, \quad (17)$$

where $\zeta = \frac{z - z_0}{z_R}$ is a normalized z -coordinate and z_R is the Rayleigh range of the beam. We define the angular aperture of the beam as $\gamma = w_0/z_R$. The normalization factor N_{mn} is given by $N_{mn} = \pi w_0^2 2^{m+n-1} m! n!$. The individual modes satisfy the orthogonality condition

$$\iint_{-\infty}^{+\infty} dr u_{mn}(x, y, z) u_{kl}^*(x, y, z) = \delta_{mk} \delta_{nl}. \quad (18)$$

We then introduce a misalignment of the beam by an angle θ around the $-y$ -axis at the beam waist location, followed by transverse displacements Δx and Δy . These transformations yield the new misaligned beam coordinate system (x', y', z') (see Fig. 3). In addition, we allow for a

mismatch of the beam parameters, which can be described by the two coefficients

$$\begin{aligned} K_0 &= \frac{z_0 - z'_0}{z_R}, \\ K_R &= \frac{z'_R - z_R}{z_R} = \frac{w_0'^2 - w_0^2}{w_0^2}. \quad (19) \end{aligned}$$

Therefore, misalignment of the two beams is parametrized by $\Delta x, \Delta y$ and θ , while the mismatch in beam size and wavefront curvature is parametrized by K_0 and K_R . The transformation between (x, y, z) and (x', y', z') can then be written as

$$\begin{aligned}
\frac{x'}{w'_0} &= \frac{x + \Delta x + z \sin(\theta)}{(1 + K_R)^{\frac{1}{2}} w_0}, \\
\frac{y'}{w'_0} &= \frac{y + \Delta y}{(1 + K_R)^{\frac{1}{2}} w_0}, \\
\zeta' &= \frac{\zeta + K_0}{1 + K_R}.
\end{aligned} \quad (20)$$

As the spatial modes of the initial beam, $u_{mn}(x, y, z)$, comprise a full orthonormal set, any mode $u_{m'n'}$ of the misaligned beam can be expressed in terms of the former,

$$u_{m'n'}(x', y', z') = \sum_{m=0}^{\infty} \sum_{n=0}^{\infty} c_{mn}^{m'n'} u_{mn}(x, y, z). \quad (21)$$

The coupling coefficients $c_{mn}^{m'n'}$ are obtained from Eqs. (18) and (20), resulting in

$$c_{mn}^{m'n'} = e^{-ik(z'_0 - z_0)} e^{i2kz \sin^2(\frac{\theta}{2})} \iint_{-\infty}^{+\infty} dr u_{m'n'}^* u_{mn} e^{ikx \sin(\theta)}. \quad (22)$$

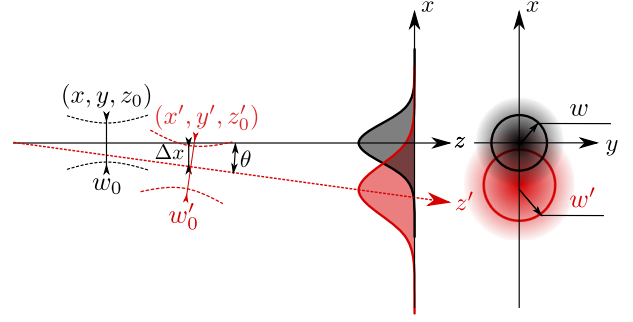


FIG. 3. Schematic of the general mismatch and misalignment transformation of the Gaussian beam. The waist sizes of the initial beam and the transformed beam are given by w_0 , w'_0 , respectively. z_0 and z'_0 stand for the coordinates of the waist position of the two beams in the corresponding coordinate systems. The observation plane is located at $z = 0$ and $z' = 0$. The misalignment can be described by the angular misalignment θ , as well as by the displacements Δx and Δy .

Since Hermite-Gaussian modes are factorizable in x and y , the same applies to the coupling coefficients, i.e. $c_{mn}^{m'n'} = c_m^{m'} c_n^{n'}$. According to [19], the factorized coupling coefficient reads

$$c_m^{m'} = (-1)^m E^{(x)} (m'! m! (1 + K_R)^{m' + \frac{1}{2}} (1 + K^*)^{-(m+m'+1)})^{\frac{1}{2}} [S_g - S_u] e^{-\frac{ik(z'_0 - z_0)}{2}}, \quad (23a)$$

$$S_g = \sum_{\mu=0}^{[m'/2]} \sum_{\mu=0}^{[m/2]} \frac{(-1)^{\mu'} X^{m'-2\mu'} X'^{m-2\mu}}{(m' - 2\mu')!(m - 2\mu)!} \sum_{\sigma=0}^{\min(\mu, \mu')} \frac{(-1)^{\sigma} F^{\mu'-\sigma} F'^{\mu-\sigma}}{(2\sigma)!(\mu' - \sigma)!(\mu - \sigma)!}, \quad (23b)$$

$$S_u = \sum_{\mu=0}^{[(m-1)/2]} \sum_{\mu=0}^{[(m'-1)/2]} \frac{(-1)^{\mu'} X^{m'-2\mu'-1} X'^{m-2\mu-1}}{(m' - 2\mu' - 1)!(m - 2\mu - 1)!} \sum_{\sigma=0}^{\min(\mu', \mu)} \frac{(-1)^{\sigma} F^{\mu'-\sigma} F'^{\mu-\sigma}}{(2\sigma + 1)!(\mu' - \sigma)!(\mu - \sigma)!}. \quad (23c)$$

The symbol $[m/2]$ stands for the integer part of $\frac{m}{2}$. $S_u = 0$ for $m = 0$ or $m' = 0$. The notations in Eqs. (23) are given in Table I. For the y -axis, m , m' have to be replaced by n , n' and X , X' by Y .

As misalignment angles and shifts are usually small compared to the wave front curvature scale, hereafter we neglect the effect of wave front tilting.

The above calculated coefficients can be translated into the components of the scattering matrices $\mathbb{O}_{jj'}^s$ and $\mathbb{O}_{jj'}^l$, which describe the misalignment effects in the signal and LO path, in two-photon formalism, for the individual optical modes at the corresponding input ports of the BHD:

$$\mathbb{O}_{kj}^s = |c_j^k| \mathbb{H} \phi_{kj}, \quad \mathbb{O}_{kj}^l = |d_j^k| \mathbb{H} \psi_{kj} \quad (24)$$

where $c_j^k \rightarrow c_{mn}^{m'n'} = c_m^{m'} c_n^{n'}$ and $\phi_{kj} \equiv \arg(c_j^k)$, and similarly for d_j^k and ψ_{kj} .

The many elements in the optical paths that connect the output ports of the interferometer to the corresponding input port of the BHD each apply their own misalignment and mismatch transformations. Here we reduce this

TABLE I. Notations used in Eqs. (23).

K	$\frac{K_R + iK_0}{2}$
X	$(1 + K^*)^{-\frac{1}{2}} \left(\frac{\Delta x}{w_0} - \left(\frac{-z_0}{z_R} - i \right) \frac{\theta}{\gamma} \right)$
X'	$(1 + K^*)^{-\frac{1}{2}} \left(\frac{\Delta x}{w_0} - \left(\frac{-z'_0}{z_R} + i(1 + 2K^*) \right) \frac{\theta}{\gamma} \right)$
Y	$(1 + K^*)^{-\frac{1}{2}} \frac{\Delta y}{w_0}$
F	$\frac{K}{2(1 + K_R)}$
F'	$\frac{K^*}{2}$
$E^{(x)}$	$e^{-\frac{X^2 X'}{2} - i \frac{\Delta x \theta}{w_0 \gamma}}$
$E^{(y)}$	$e^{-\frac{Y^2}{2}}$

complexity to a single effective beam rotation (θ), and lateral (Δx and Δy) shifts of the beam and modified beam parameters (z'_0, z'_R) as they are measured at the detection point, i.e. at the input of the BHD. It can be easily shown that this does not undermine the generality of our treatment, and the transform that any linear optical system does to the HG optical beam can be represented in that way [19,21].

V. INFLUENCE OF HIGHER-ORDER MODES ON THE QUANTUM NOISE IN A MICHELSON INTERFEROMETER WITH BALANCED HOMODYNE DETECTION

In this section, we provide the application of the above framework on the conventional Fabry-Pérot-Michelson interferometer. The interferometer transfer matrices, \mathbb{A} , \mathbb{B} , \mathbb{C} , \mathbb{D} , defined in Eqs. (8), can be written for our particular case as [4]

$$\mathbb{A}_{00} = e^{2i\beta_{\text{arm}}} \begin{bmatrix} 1 & 0 \\ -\mathcal{K}_{\text{MI}} & 1 \end{bmatrix}, \quad \mathbb{B}_{00} = \begin{bmatrix} 0 & 0 \\ 0 & 0 \end{bmatrix}, \quad (25a)$$

$$\mathbb{C}_{00} = \begin{bmatrix} 0 & 0 \\ 0 & 0 \end{bmatrix}, \quad \mathbb{D}_{00} = e^{-2i\beta_{\text{arm}}} \begin{bmatrix} 1 & 0 \\ -\mathcal{K}_{\text{MI}} & 1 \end{bmatrix} \quad (25b)$$

for the fundamental mode of the interferometer. \mathcal{K}_{MI} is the optomechanical coupling factor of a Fabry-Pérot-Michelson interferometer defined as

$$\mathcal{K}_{\text{MI}} = \frac{2\Theta\gamma_{\text{arm}}}{\Omega^2(\gamma_{\text{arm}}^2 + \Omega^2)}, \quad (26)$$

where $\gamma_{\text{arm}} = \frac{cT_{\text{ITM}}}{4L}$ is the half-bandwidth of the arm cavities of length L and with input mirror power transmittance T_{ITM} , and $\Theta = \frac{4\omega P_{\text{arm}}}{McL}$ is the normalized circulating power in both arms.

For the HOMs, i.e. for $j, k > 0$, we assume the high-finesse arm-cavity interferometer to be a highly selective mode filter that does not let HOMs in, rather reflecting them off without any dispersion (frequency dependent phase shift). Therefore the corresponding transfer matrices take a particularly simple form:

$$\mathbb{A}_{kj} = \mathbb{D}_{kj} = \delta_{kj} \begin{bmatrix} 1 & 0 \\ 0 & 1 \end{bmatrix}, \quad \mathbb{B}_{kj} = \mathbb{C}_{kj} = \begin{bmatrix} 0 & 0 \\ 0 & 0 \end{bmatrix}, \quad (27)$$

indicating that the vacuum noise in HOMs is reflected to the output port right away, without any additional phase shift. However, the fundamental mode light interacts with the interferometer and thereby it gets ponderomotively squeezed by the optomechanical interaction with the mechanical degrees of freedom of the interferometer.

This fact is reflected in Fig. 3 by the squeezed error ellipse of the TEM_{00} mode at both IFO output ports, \mathbf{o} and \mathbf{q} .

The response of the interferometer to the differential mechanical modes of the arm mirrors, that are of particular interest in the context of gravitational wave detectors, can be written as

$$\mathbf{R}_- = e^{i\beta_{\text{arm}}} \frac{\sqrt{2\mathcal{K}_{\text{MI}}}}{x_{\text{SQL}}} \begin{bmatrix} 0 \\ 1 \end{bmatrix}, \quad (28)$$

where x_{SQL} stands for the single-sided spectral density of the standard quantum limit in terms of displacement, and $\beta_{\text{arm}} = \arctan(\frac{\Omega}{\gamma_{\text{arm}}})$ is the phase shift that the light sidebands with frequency Ω acquire when propagating through and reflecting off the arm cavity [22].

We can distinguish three different cases of how misalignments can couple into the BHD readout:

- (1) Output misalignment occurring in one or both of the BHD paths, which refers to (a) in Fig. 4.
- (2) Input misalignment in the interferometer, which will cause multiple mode fields to be injected into the interferometer as shown in Fig. 2 and is referred to as (b) in Fig. 4.
- (3) Combination of the input and output misalignment, which refers to (c) in Fig. 4.

We note that the pickoff mirror is set to pick up the reflection beam of the interferometer as the LO beam. As the specific design for implementing the BHD readout in a full large scale GW detector, i.e. Advanced LIGO, is still under discussion, in the following we use similar instrument parameters as for the Fabry-Pérot-Michelson interferometer considered in [8]. The input power is 3.4 W, the

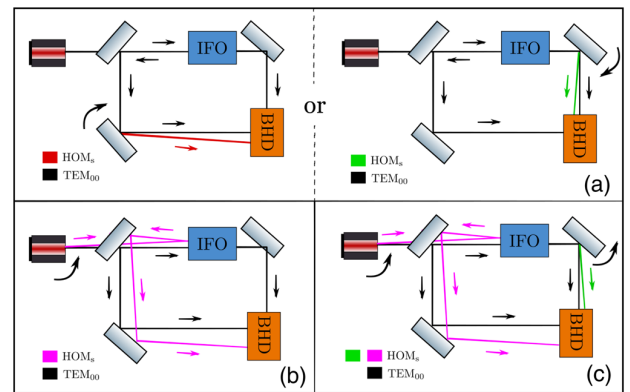


FIG. 4. Schematic of the output ports and input ports misalignment. The black line indicates the fundamental mode defined by the arm cavities of the interferometer. The colored lines show the HOM components caused by different misalignment conditions. (a) Output misalignment, i.e. misaligned LO path, or misaligned signal path, respectively. (b) Input misalignment, i.e. misaligned input laser beam, which will contribute HOMs to the LO beam and reduce power inside the main interferometer. (c) Combination of input port misalignment and output signal port misalignment.

power transmissivity of the cavity input test mass is 700 ppm, the effective cavity mass is around 1g, and the arm cavity length is around 1.4 m.

A. Output misalignment

The left-hand plot of Fig. 5 shows the effect of output misalignment onto the quantum-noise limited displacement sensitivity of our example Fabry-Pérot-Michelson interferometer with BHD using a phase quadrature readout. The differently colored traces indicate different magnitudes of misalignments. The right-hand top plot shows the amplitude spectral density (ASD) of the quantum noise, while the lower plot on the right-hand side shows the response of the differential arm length degree of the interferometer.

For output misalignment we obtain that at the frequencies below 5 kHz, where radiation pressure noise dominates in the interferometer, there is no visible influence on the quantum-noise limited sensitivity due to HOMs in the BHD paths. The most pronounced effect can be seen in the shot-noise dominated frequency band, i.e. above 5 kHz. This can be understood by the following chain of arguments. The ponderomotive squeezing, which is described by \mathcal{K}_{MI} , is responsible for the radiation pressure noise at low frequencies and affects only the TEM_{00} mode. The effect of misalignment on this mode can be described by a simple multiplication by the factors $|d_0^0| < 1$ and $|c_0^0| < 1$ of the fundamental mode contributions to the LO and the signal beams, including the arm mirrors' displacement signal. While the contribution of the HOMs can have in general a complicated structure at the level of field operators, the fact that all fluctuating parts of the HOM fields are in the vacuum state, which is invariant to phase shifts, the resulting additional noise in the BHD photocurrent can be described by the noise operators, \mathbf{n}^{HOM} , that absorb all the HOM vacuum fields and enter the readout signal with effective coefficients $\sqrt{1 - |d_0^0|^2}$ and $\sqrt{1 - |c_0^0|^2}$, correspondingly. Assuming that there is no significant classical field leaving the Michelson interferometer at the dark port, one can safely neglect the noise contribution of the cross term between the classical component in the signal beam and quantum noise in the LO beam. Then we write out the BHD photocurrent in the phase quadrature for the case of a misaligned LO beam as

$$I_{\text{BHD}} \propto |\mathbf{L}| \left(|c_0^0| \left[e^{2i\beta_{\text{arm}}} (-\mathcal{K}_{\text{MI}} \hat{l}_c^0 + \hat{l}_s^0) + e^{i\beta_{\text{arm}}} \frac{\sqrt{2\mathcal{K}_{\text{MI}}}}{x_{\text{SQL}}} x_- \right] + \sqrt{1 - |c_0^0|^2} \Delta \mathbf{n}_s^{\text{HOM}} \right) + \text{H.c.} \quad (29)$$

where $|\mathbf{L}|$ represents the magnitudes of the LO dc components. Analogously we can describe the case of a misaligned signal beam by replacing c_0^0 with d_0^0 .

Therefore, the effect of misalignment and HOM contamination of the readout signal is mathematically equivalent to the effect of loss at the readout photodetectors, with the misalignment coefficient $|c_0^0|^2$ serving as an effective quantum efficiency of the readout. Indeed, radiation pressure noise creates the real displacement of the mirrors of the interferometer indistinguishable from the signal displacement. Therefore, apparently the signal-to-noise ratio (SNR) for back-action noise is not influenced by the output beam's misalignment, hence the back-action dominated part of QNLS. Shot noise, on the contrary, remains the same regardless of the level of output loss while the signal magnitude decreases proportionally. Thus SNR for shot noise goes down, worsening the QNLS, as can be seen in Fig. 5 and in the following two formulas for QN and QNLS, respectively:

$$S^{\text{QN}} \approx |c_0^0|^2 (S_{s,\text{SN}}^0(f) + S_{s,\text{BA}}^0(f)) + (1 - |c_0^0|^2), \quad (30)$$

where $S_{s,\text{SN}}^0(f) = 1$ and $S_{s,\text{BA}}^0(f)$ are the shot-noise and back-action components of the power spectral density (PSD) of the quantum noise on phase quadrature at the dark port in the TEM_{00} mode, respectively, and for QNLS,

$$S_x^{\text{QN}} \approx \frac{|c_0^0|^2 (1 + S_{s,\text{BA}}^0(f)) + (1 - |c_0^0|^2)}{|c_0^0|^2 |\mathbf{R}_{-s}|^2} = \frac{S_{s,\text{BA}}^0(f)}{|\mathbf{R}_{-s}|^2} + \frac{1}{|c_0^0|^2 |\mathbf{R}_{-s}|^2}, \quad (31)$$

where $|c_0^0|^2 |\mathbf{R}_{-s}|^2$ stands for the optomechanical response function, emphasizing the signal contents reduced by $|c_0^0|^2$.

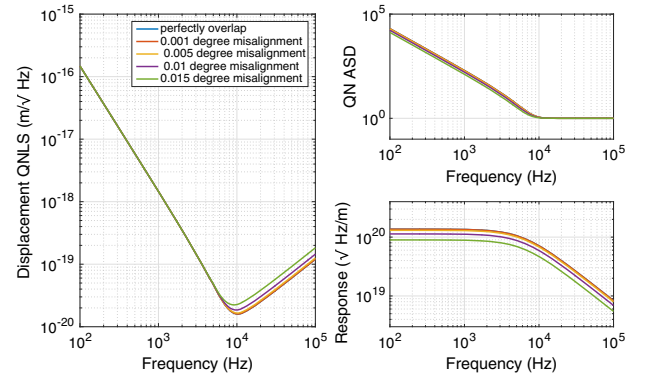


FIG. 5. Left panel: Displacement quantum-noise limited sensitivity (QNLS). Upper right panel: Quantum-noise (QN) amplitude spectral density. Lower right panel: Response function of the interferometer for different values of the misalignment angle between the LO beam and the signal one at the BHD. It refers to part (a) in Fig. 4. This gives the following values of equivalent relative lateral displacement of the two beams normalized by the beam radius on the photodiode: 0.05, 0.25, 0.5, 0.7.

B. Input misalignment

Figure 6 shows the effect of input misalignment, which refers to part (b) in Fig. 4. We find that in the low-frequency range the sensitivity suffers more than in the case of output misalignment, while the low-frequency sensitivity benefits instead.

The effect of input misalignment is twofold: on the one hand, HOMs contaminate the local oscillator beam and lead to the decrease of the LO fundamental mode amplitude by a factor of $|e_0^0| < 1$, which amounts to the same effect as described above for output misalignment. On the other hand, this also reduces the amount of classical light circulating in the fundamental mode of the interferometer by $|e_0^0|^2$, thereby reducing the back-action noise, represented by the optomechanical coupling factor \mathcal{K}_{MI} in the I/O relations [23].

Thus the BHD photocurrent can be approximately expressed as

$$I_{\text{BHD}} \propto |L| \left(|e_0^0| \left[e^{2i\beta_{\text{arm}}} (-|e_0^0|^2 \mathcal{K}_{\text{MI}} \hat{i}_c + \hat{i}_s) + e^{i\beta_{\text{arm}}} \frac{|e_0^0| \sqrt{2\mathcal{K}_{\text{MI}}}}{x_{\text{SQL}}} x_- \right] + \sqrt{1 - |e_0^0|^2} \Delta \mathbf{n}_s^{\text{HOM}} \right) + \text{H.c.}, \quad (32)$$

so that the quantum-noise power spectral density is given by

$$S^{\text{QN}} \simeq |e_0^0|^6 S_{s,BA}^0(f) + 1, \quad (33)$$

and for the PSD of the QNLS, the above PSD is divided by the modulus squared of the optomechanical response function that is proportional to $|e_0^0|^4 |\mathbf{R}_{-s}|^2$:

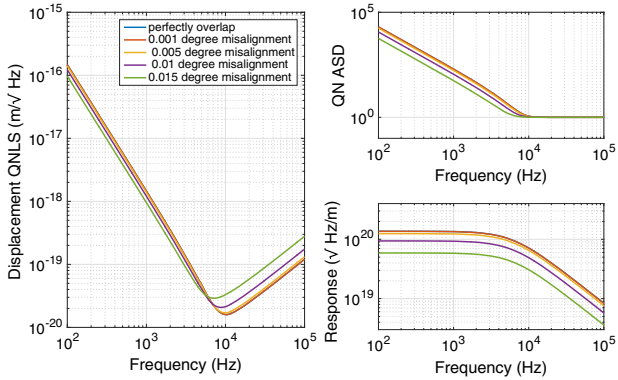


FIG. 6. Left panel: Displacement QNLS. Upper right panel: QN amplitude spectral density. Lower right panel: Response function of the interferometer for different values of the misalignment angle between the input laser beam and the interferometer. It refers to part (b) in Fig. 4.

$$S_x^{\text{QN}} \simeq \frac{|e_0^0|^2 S_{s,BA}^0(f)}{|\mathbf{R}_{-s}|^2} + \frac{1}{|e_0^0|^4 |\mathbf{R}_{-s}|^2}. \quad (34)$$

So in the back-action dominated frequency band the SNR is improved by $1/|e_0^0|^2$ due to lower power, circulating in the interferometer. While at the shot-noise dominated band the SNR is decreased to a much stronger degree, i.e. $|e_0^0|^4$, since the signal is reduced both due to the misalignment of the LO beam and due to the reduced response of the lower-power interferometer to the mirror displacement.

C. Combined output and input misalignment

In Fig. 7, we show a special case when input and output misalignment compensate each other so as to produce a perfect overlap of the LO and the signal beam at the BHD photodiodes. This somewhat artificial situation demonstrates the fact that the effects of input and output misalignment can partially compensate each other. Here the reduction of SNR is caused solely by the effect of the decrease of power circulating in the interferometer.

Hence, the QN PSD can be written as

$$S^{\text{QN}} \simeq |e_0^0|^4 S_{s,BA}^0(f) + 1, \quad (35)$$

and the response of the interferometer is reduced by the factor $|e_0^0|$. Combining these two effects in the QNLS PSD, one obtains

$$S_x^{\text{QN}} \simeq \frac{|e_0^0|^2 S_{s,BA}^0(f)}{|\mathbf{R}_{-s}|^2} + \frac{1}{|e_0^0|^2 |\mathbf{R}_{-s}|^2}. \quad (36)$$

For arbitrary misalignment combinations, it is necessary to specify the exact field distribution among different modes.

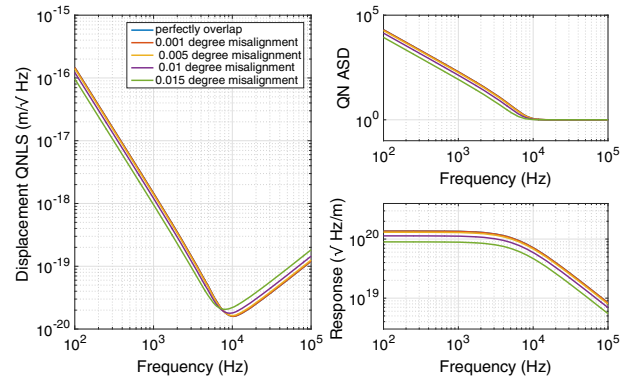


FIG. 7. Left panel: Displacement QNLS. Upper right panel: QN amplitude spectral density. Lower right panel: Response function of the interferometer for different values of the misalignment angle between the input laser beam and the interferometer, and at the same time the same amount and same direction of misalignment for the signal beam is set to recover perfect overlap between the signal field and LO field. It refers to part (c) of Fig. 4.

In that case the general framework provided in Sec. III can be used.

VI. EXAMPLE OF THE SAGNAC SPEED METER INTERFEROMETER

In this section, we give another illustrating example of the influence of HOMs on the quantum noise, i.e. the particular configuration of the zero-area Sagnac speed meter interferometer [24,25] which is proposed as a candidate for suppressing the SQL. To be specific, we use the parameters for the ERC-funded proof-of-principle prototype Sagnac speed meter (SSM) interferometer being constructed at the University of Glasgow [8,17], featuring equivalent parameters as the Michelson configuration in the previous section.

We introduce a general Sagnac interferometer with R_{BS} and T_{BS} representing the main BS power reflectivity and transmissivity. The interferometer transfer matrices, \mathbb{A} , \mathbb{B} , \mathbb{C} , \mathbb{D} , defined in Eqs. (8), can be written for our particular case as [17]

$$\mathbb{A}_{00} = 2\sqrt{R_{BS}T_{BS}}e^{2i\beta_{\text{sag}}}\begin{bmatrix} 1 & 0 \\ -\mathcal{K}_{\text{sym}} & 1 \end{bmatrix}, \quad (37a)$$

$$\mathbb{B}_{00} = (R_{BS} - T_{BS})e^{2i\beta_{\text{sag}}}\begin{bmatrix} 1 & 0 \\ -4\mathcal{K}_{\text{MI}} & 1 \end{bmatrix}, \quad (37b)$$

$$\mathbb{C}_{00} = (R_{BS} - T_{BS})e^{2i\beta_{\text{sag}}}\begin{bmatrix} 1 & 0 \\ 0 & 1 \end{bmatrix}, \quad (37c)$$

$$\mathbb{D}_{00} = -2\sqrt{R_{BS}T_{BS}}e^{2i\beta_{\text{sag}}}\begin{bmatrix} 1 & 0 \\ -\mathcal{K}_{\text{asym}} & 1 \end{bmatrix}, \quad (37d)$$

where $\beta_{\text{sag}} = 2\beta_{\text{arm}} + \frac{\pi}{2}$ is the corresponding phase shift for the full Sagnac interferometer. The symmetric and asymmetric Sagnac interferometer optomechanical coupling factors are defined as

$$\mathcal{K}_{\text{sym}} = 2\mathcal{K}_{\text{MI}}\sin^2\beta_{\text{arm}} \simeq \frac{8\Theta\gamma_{\text{arm}}}{(\Omega^2 + \gamma_{\text{arm}}^2)^2},$$

$$\mathcal{K}_{\text{asym}} = 2\mathcal{K}_{\text{MI}}\cos^2\beta_{\text{arm}} \simeq \frac{8\Theta\gamma_{\text{arm}}^3}{\Omega^2(\Omega^2 + \gamma_{\text{arm}}^2)^2}. \quad (38)$$

The response of the interferometer to the common (cARM) and differential (dARM) mechanical modes of the arm mirrors, that are of particular interest in the context of gravitational wave detectors, can be written as

$$\mathbf{R}_- = -ie^{2i\beta_{\text{arm}}}\frac{\sqrt{2\mathcal{K}_{\text{sym}}}}{x_{\text{SQL}}}\begin{bmatrix} 0 \\ 1 \end{bmatrix}, \quad (39)$$

$$\mathbf{R}_+ = -e^{2i\beta_{\text{arm}}}\frac{(R_{BS} - T_{BS})\sqrt{2\mathcal{K}_{\text{asym}}}}{x_{\text{SQL}}}\begin{bmatrix} 0 \\ 1 \end{bmatrix}. \quad (40)$$

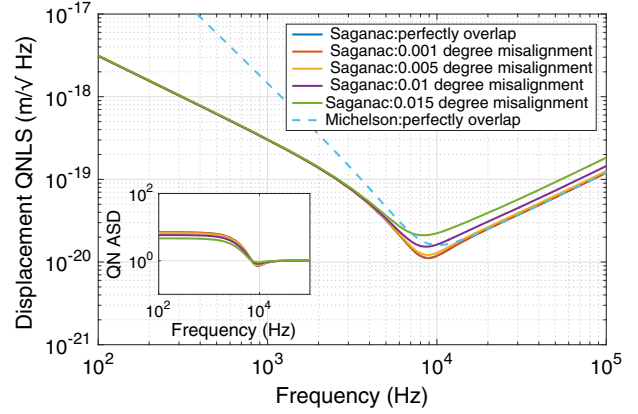


FIG. 8. Displacement QNLS of the Glasgow Sagnac interferometer for different values of the misalignment angle between the LO beam and the signal one at the BHD. (The blue dashed curve indicates the QNLS of a perfectly aligned Michelson interferometer with equivalent parameters as the speed meter.) The inset shows the amplitude spectral density of the QN only for the respective case. This gives the following values of equivalent lateral displacement of the two beams normalized by the beam radius on the photodiode: 0.05, 0.25, 0.5, 0.7.

Figures 8 and 9 show the effect of output and input misalignment of the Sagnac speed meter with BHD readout, using similar levels of misalignment as were presented earlier for the example of the Fabry-Pérot-Michelson interferometer. As expected, the observed effects from misalignment are the same for the Sagnac speed meter and the Michelson interferometer.

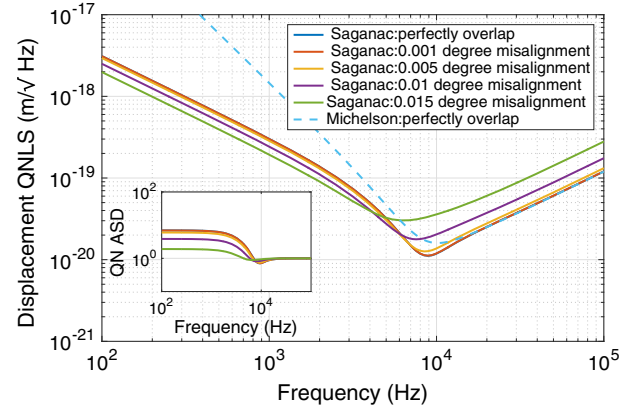


FIG. 9. Displacement QNLS of the Glasgow Sagnac interferometer for different values of the misalignment angle between the input laser and the interferometer. (The blue dashed curve indicates the QNLS of a perfectly aligned Michelson interferometer with equivalent parameters as the speed meter.) The inset shows the amplitude spectral density of the QN only for the respective case. These are the same beam parameters and misalignment conditions as in Fig. 8.

VII. NONSTATIONARY MISALIGNMENT EFFECTS IN THE BALANCED HOMODYNE DETECTOR

All the beams' misalignment and mismatch effects considered thus far were assumed stationary. However, in the real interferometer with suspended optics the optical paths of the LO and the signal beams are disturbed in a nonstationary way as a result of seismic motion of the ground. Therefore, the initially static parameters describing the misalignment of the Gaussian beams given in Sec. IV now have to be considered as random functions of time defined by the local seismic noise of the lab. It is the subject of this section to estimate the additional noise in the BHD readout incurring from the random seismically driven movements of the suspended optical components, such as steering mirrors. Specifically, we look at the influence of tilt (pitch) motion, which has a much stronger coupling from the longitudinal ground motion than the rotation direction, which is a consequence of the suspension design.

For simplicity, we assume the two input beams of the BHD, the LO and the signal beams, are Gaussian with nonzero dc components only in the fundamental TEM₀₀ mode, which can be justified by the use of output mode cleaners for these two beams [13]. We also assume ac parts, encompassing quantum and classical fluctuations, to be much smaller in magnitude than the dc components.

The signal beam is the interferometer DP \mathbf{o} , while the LO is taken from the reflected light \mathbf{q} . As in Eq. (12), we can thus write

$$\mathbf{L}_0 = \mathbf{Q}_0, \quad S_0 = \mathbb{H}_{\phi_h} \mathbb{O}_{00}^{s-l}(t) \mathbf{O}_0, \quad (41)$$

where \mathbf{Q}_0 and \mathbf{O}_0 are TEM₀₀ mode dc parts in \mathbf{q} and \mathbf{o} , respectively. We choose the coordinate system of the LO beam as a reference, and the relative misalignment of the signal beam is represented by \mathbb{O}_{00}^{s-l} , defined in terms of coupling coefficients c_0^0 as in Eq. (24). According to Eq. (5), the main dynamic photocurrents can be written as

$$I_{\text{BHD}}^{\text{dy}} \propto \mathbf{Q}_0^\dagger \mathbb{H}_{\phi_h} \mathbb{O}_{00}^{s-l}(t) \mathbf{O}_0 + \text{H.c.} \quad (42)$$

We further assume that the two beams are perfectly matched in the static case; i.e. they have the same waist size w_0 and Rayleigh range z_R and thus the same spot size on the photodetectors. According to Eq. (23), in misalignment condition, $c_0^0(t)$ in terms of the small jitter angle θ or equivalent beam shift Δr and beam size $w(z)$ on the photodetectors is given by

$$\begin{aligned} c_0^0(t) &= \exp\left(-\frac{k^2 w^2(z) \Delta r^2(t)}{8(z^2 + z_R^2)}\right) \\ &= \exp\left(-\frac{k^2 w^2(z) \theta^2(t)}{8}\right), \end{aligned} \quad (43)$$

where $w(z) = w_0 \sqrt{1 + (z/z_R)^2}$. In general, $\theta(t)$ contains a dc part and the fluctuation part, which means $\theta(t) = \theta_{\text{DC}} + \theta_{\text{n}}(t)$.

In order to calculate the jitter noise spectral density, we need an additional step to calculate the spectral density of the quadratic random process $\theta^2(t)$, after which it is straightforward to write the spectral density of the jitter noise as

$$S_{\text{jitter}} = |\mathbf{Q}_0^\dagger \mathbb{H}_{\phi_h} \mathbf{O}_0|^2 \frac{k^4 w^4(z)}{64} (4\theta_{\text{dc}}^2 S_{\theta_{\text{n}}} + S_{\theta_{\text{n}}^2}). \quad (44)$$

According to Eqs. (2)–(44) in [26], $S_{\theta_{\text{n}}^2}$ turns out to be the convolution of the spectral density of $S_{\theta_{\text{n}}}(\Omega)$, which reads

$$S_{\theta_{\text{n}}^2}(\Omega) = \int_{-\infty}^{\infty} S_{\theta_{\text{n}}}(\Omega') S_{\theta_{\text{n}}}(\Omega - \Omega') d\Omega'. \quad (45)$$

In the Sagnac interferometer, the fundamental mode amplitude \mathbf{O}_0 mainly comes from the imbalance of the main beam splitter, $\eta_{BS} = R_{BS} - 0.5$, and then $\mathbf{O}_0 = 2\eta_{BS} \mathbf{P}_0$.

Taking again the Glasgow SSM as an example, we calculated the expected additional nonstationary beam jitter noise due to seismic motion coupling into the LO and signal path. While the double-pendulum suspensions of these mirrors [8] strongly suppress seismic noise at frequencies in our experiment band, there is still significant motion of the mirrors at the pendulum eigenfrequencies. Starting from a measured displacement noise spectral density, we apply our simulated suspension transfer function for longitudinal motion to pitch motion coupling. This result in the pitch noise spectral density is shown in the inset in Fig. 10. From this, and using Eqs. (44) and (45), we

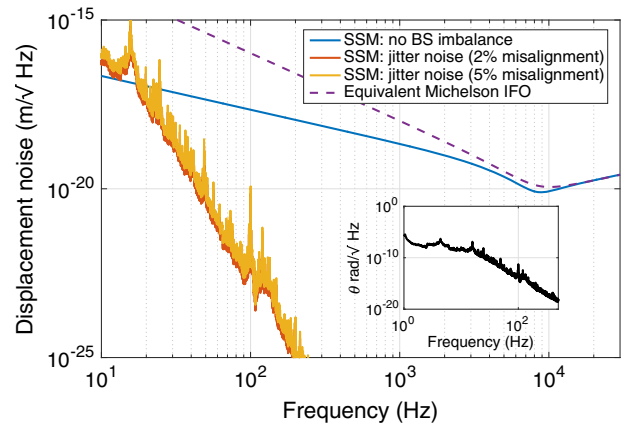


FIG. 10. Additional nonstationary beam jitter noise driven by seismic motion in the lab plotted against the QNLS curves of the equivalent Michelson interferometer and of the Sagnac speed meter interferometer with no imbalance in the beam-splitting ratio and with 0.1% BS imbalance. The beam waist size is 0.925 mm, with beam travel distance 2.038 m. The inset is the spectral density of jitter angle θ .

arrive at the total noise contribution due to seismically driven beam jitter noise in the Glasgow SSM experiment as shown by the orange curve in Fig. 10. This traditional noise is far below the quantum-noise limited sensitivity in our measurement band between 100 and 1000 Hz.

VIII. SUMMARY

In this article, we investigated the performance of a balanced homodyne readout in practical applications including degradation effects from optical higher-order Hermite Gaussian modes. We provided a general solution for considering the effect of HOMs which are related to the input and output ports' misalignment on the quantum-noise limited sensitivity. The solution provides a framework for solving arbitrary conditions of input and output port misalignments or mismatch. This framework can be applied to any interferometer; i.e. it is independent of the actual interferometer configuration. We found that output port misalignments only degrade the amplitude spectral density of the shot-noise limited part of the quantum-noise sensitivity by a factor of c_0^0 or d_0^0 , while the sensitivity in the back-action noise limited range will not degrade. In the case of input misalignment, i.e. the laser beam being misaligned with respect to the eigenmode of the interferometer, firstly the laser amplitude inside the interferometer will be reduced by a factor e_0^0 , thus changing the quantum-noise limited sensitivity, and secondly it will also contribute to the LO beam misalignment and worsen the amplitude spectral density of the quantum-noise limited

sensitivity on high frequencies by a factor of e_0^{02} in total. In addition, we investigated the noise coupling mechanisms from beam jitter, i.e. time varying HOM contributions. Using the case of the speed meter proof-of-concept experiment under construction in Glasgow as an illustrating example, we found that the seismically introduced beam jitter noise is well below the quantum-noise level in our sensitive frequency range 10–1000 Hz. We note that though our framework supports the injection of squeezed light states, for clarity we have refrained from a detailed discussion of squeezing light injection in this article.

In conclusion, we have developed and applied a general framework for investigating realistic applications of balanced homodyne detection in suspended interferometers with realistic (i.e. imperfect) optics, thus paving the way for technical design studies of future upgrades to gravitational wave detectors featuring balanced homodyne readout.

ACKNOWLEDGMENTS

The authors would like to thank colleagues from the LIGO Scientific Collaboration, especially Keita Kawabe for fruitful discussion. The work described in this article is funded by the European Research Council (ERC-2012-StG: 307245). We are grateful for support from the Science and Technology Facilities Council (Grant No. ST/L000946/1). S. S. was supported by the European Commission H2020-MSCA-IF2014 actions, Grant No. 658366.

-
- [1] B. Abbott, R. Abbott, T. Abbott, M. Abernathy, F. Acernese, K. Ackley, C. Adams, T. Adams, P. Addesso, R. Adhikari *et al.* (LIGO Scientific Collaboration and Virgo Collaboration), *Phys. Rev. Lett.* **116**, 061102 (2016).
- [2] Y. Chen, S. L. Danilishin, F. Y. Khalili, and H. Müller-Ebhardt, *Gen. Relativ. Gravit.* **43**, 671 (2011).
- [3] V. B. Braginsky, Y. I. Vorontsov, and K. S. Thorne, *Science* **209**, 547 (1980).
- [4] H. J. Kimble, Y. Levin, A. B. Matsko, K. S. Thorne, and S. P. Vyatchanin, *Phys. Rev. D* **65**, 022002 (2001).
- [5] T. Corbitt and N. Mavalvala, *J. Opt. B* **6**, S675 (2004).
- [6] V. Braginsky and F. Khalili, *Phys. Lett. A* **147**, 251 (1990).
- [7] Y. Chen, *Phys. Rev. D* **67**, 122004 (2003).
- [8] C. Gräf *et al.*, *Classical Quantum Gravity* **31**, 215009 (2014).
- [9] S. Hild, H. Grote, J. Degallaix, S. Chelkowski, K. Danzmann, A. Freise, M. Hewitson, J. Hough, H. Lück, M. Prijatelj, K. A. Strain, J. R. Smith, and B. Willke, *Classical Quantum Gravity* **26**, 055012 (2009).
- [10] J. Aasi *et al.*, *Nat. Photonics* **7**, 613 (2013).
- [11] H. Grote, K. Danzmann, K. L. Dooley, R. Schnabel, J. Slutsky, and H. Vahlbruch, *Phys. Rev. Lett.* **110**, 181101 (2013).
- [12] H. Grote, M. Weinert, R. X. Adhikari, C. Affeldt, V. Kringel, J. Leong, J. Lough, H. Lück, E. Schreiber, K. A. Strain, H. Vahlbruch, and H. Wittel, *Opt. Express* **24**, 20107 (2016).
- [13] P. Fritschel, M. Evans, and V. Frolov, *Opt. Express* **22**, 4224 (2014).
- [14] S. Steinlechner, B. W. Barr, A. S. Bell, S. L. Danilishin, A. Gläfke, C. Gräf, J.-S. Hennig, E. A. Houston, S. H. Huttner, S. S. Leavey, D. Pascucci, B. Sorazu, A. Spencer, K. A. Strain, J. Wright, and S. Hild, *Phys. Rev. D* **92**, 072009 (2015).
- [15] C. M. Caves and B. L. Schumaker, *Phys. Rev. A* **31**, 3068 (1985).
- [16] B. L. Schumaker and C. M. Caves, *Phys. Rev. A* **31**, 3093 (1985).
- [17] S. L. Danilishin, C. Gräf, S. S. Leavey, J. Hennig, E. A. Houston, D. Pascucci, S. Steinlechner, J. Wright, and S. Hild, *New J. Phys.* **17**, 043031 (2015).
- [18] Note that the dimensions of \mathbb{S}_i and \mathbb{S}_p correspond to the number of optical modes taken into consideration. In general, they have the same dimensions as TMs.

- [19] F. Bayer-Helms, *Appl. Opt.* **23**, 1369 (1984).
- [20] A. Freise and K. A. Strain, *Living Rev. Relativ.* **13**, 70 (2010).
- [21] H. Kogelnik, *Appl. Opt.* **4**, 1562 (1965).
- [22] S. L. Danilishin and F. Y. Khalili, *Living Rev. Relativ.* **15** (2012).
- [23] Depending on the cause of input misalignment, e.g. a limited gain in the autoalignment system or an unwanted offset in the autoalignment system, it could be detuned by monitoring optical power inside the main interferometer and compensated for by increasing the input laser power.
- [24] P. T. Beyersdorf, M. M. Fejer, and R. L. Byer, *Opt. Lett.* **24**, 1112 (1999).
- [25] Y. Chen, *Phys. Rev. D* **67**, 122004 (2003).
- [26] L. J. Ippolito, NASA Technical Reports Server (NTRS) 19660021045.

Chapter 4

Balanced-homodyne readout for aLIGO+

Different from DC readout, balanced homodyne detection (BHD) uses a spatially separated local oscillator (LO). Thus, the signal port can be tuned to be nearly dark with only leaving the signal sidebands and tiny DC beam due to optics imperfection, *e.g.* differential arm cavity input test mass loss factor. There are several advantages as motivations to implement BHD in gravitational wave detectors. Firstly, the signal recycling cavity length noise coupling which is proportional to the arm detuning in DC readout can be essentially eliminated [58, 59]. Secondly, the backscattering of bright light into the asymmetric port can be reduced. (Although due to the new output mode cleaners position design which will be discussed below, the backscattering from mode cleaners to asymmetric port do not benefit.) Thirdly, the radio frequency sidebands offset in the asymmetric port can be eliminated [36, 60]. Fourthly, The balanced homodyne readout also has the advantages of tunability of the homodyne angle and subtracting local oscillator and single beam self noises [61]. Hence, the balanced homodyne readout will be an essential element of advanced LIGO (aLIGO) upgrade, *i.e.* aLIGO+ (A+).

In this chapter, I describe several aspects of considerations on implementing balanced homodyne readout in advanced LIGO, including the LO instability, output mode cleaner phase noise coupling, LO backscattering noise, balanced homodyne readout sensing and control. The research of local oscillator instability pushes the consideration of using three stages suspensions for relay optics on the LO path in A+; To eliminate the output mode cleaners phase noise coupling, I prove the scheme of dual mode cleaners at each output port of BHD beamsplitter can work for A+; The research of LO backscattering noise gives one motivation of taking LO from the power recycling cavity pick-off port (POP) in A+. These results were presented in the BHD working group for A+.

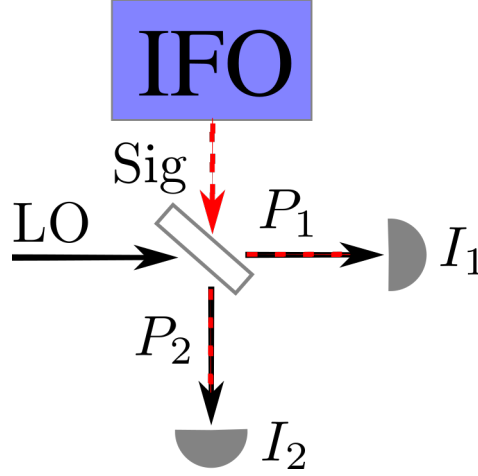


Figure 4.1: Schematic of simple balanced homodyne readout layout. ‘IFO’ represents the main interferometer, ‘Sig’ represents the signal beam, ‘LO’ represents the local oscillator beam, P_1 and P_2 are two fields after the BHD beamsplitter, I_1 and I_2 are the photocurrents of two photodiodes.

4.1 Requirement for local oscillator path stability

I start here by writing down the general calculation of balanced homodyne readout in the two-photo formalism. I define the LO field and signal field before the balanced homodyne beamsplitter by \mathbf{L} and \mathbf{S} , in which $\mathbf{L} = (L + l_c, l_s)^T$ and $\mathbf{S} = (S + s_c, s_s)^T$ in *two photo formalism*. L, S represent the classical amplitude and l, s represent the fluctuations. The gravitational wave signals are part of s_s . The two fields in balanced homodyne beamsplitter outputs with BHD angle on LO field can be written as

$$\begin{aligned} \mathbf{P}_1 &= \sqrt{T}\mathbb{H}(\phi)\mathbf{L} + \sqrt{R}\mathbf{S}, \\ \mathbf{P}_2 &= -\sqrt{R}\mathbb{H}(\phi)\mathbf{L} + \sqrt{T}\mathbf{S}. \end{aligned} \quad (4.1)$$

The homodyne angle is defined by one rotation matrix

$$\mathbb{H}(\phi) = \begin{bmatrix} \cos \phi & -\sin \phi \\ \sin \phi & \cos \phi \end{bmatrix}. \quad (4.2)$$

Thus the photocurrents of two photodiodes can be written as

$$I_1 = \mathbf{P}_1^\dagger \mathbf{P}_1, \quad I_2 = \mathbf{P}_2^\dagger \mathbf{P}_2. \quad (4.3)$$

And the balanced homodyne readout photocurrent can be written as

$$I_{BHD} \propto I_1 - I_2. \quad (4.4)$$

The term related to fluctuations read,

$$I_{BHD}^{fl} \propto s^\dagger \mathbb{H}L + S^\dagger \mathbb{H}l + s^\dagger \mathbb{H}l + h.c.. \quad (4.5)$$

When $R = T = \frac{1}{2}$ and $\phi = \frac{\pi}{2}$, I obtain

$$I_{BHD}^{fl} \propto 2(Ls_s - Sl_s). \quad (4.6)$$

We see that if there is non-zero laser power at the asymmetric port, then phase noise in the LO path will couple into the output signal. The phase noise from the displacement, δx , of reflective optics in the local oscillator can be written as

$$N = \frac{2\omega\sqrt{I_{sig}}}{c}\delta x, \quad (4.7)$$

where ω is the laser angular frequency, $I_{sig} = S^2$ is the normalised bright light power in signal port,

$$I_{sig} = \frac{2P_{sig}}{\hbar\omega}. \quad (4.8)$$

And P_{sig} is the power in unit of Watts. This local oscillator phase noise should not be larger than the product of the total noise budget of detector or the quantum noise for a quantum noise limited detector and the detector response. In other words, the second term in Eq. 4.6 should not be larger than the first term. This means

$$\frac{N}{|\begin{bmatrix} 0 & 1 \end{bmatrix} \mathbb{H}(\phi)\mathbf{R}_x|} < \sqrt{S_x}, \quad (4.9)$$

where $\sqrt{S_x}$ is the amplitude spectral density of the detector noise in displacement and \mathbf{R}_x is the detector response to the arm cavities differential motion. The relation between an reflective optics displacement, δx , and the phase variations, δ , caused by that is

$$\delta\phi = \frac{4\pi}{\lambda}\delta x. \quad (4.10)$$

Thus, in order to calibrate to spectral density in phase, a factor of $\frac{4\pi}{\lambda}$ should be applied to the displacement stability requirement. Assuming the signal port DC power is 1 mW, Fig. 4.2 shows additional phase noises caused by local oscillator phase fluctuations which indicates the equivalence to the design sensitivities of aLIGO and A+. In the high frequency, shot noise limited region (above 100 Hz), the phase fluctuations should be smaller than 4×10^{-9} rads/ $\sqrt{\text{Hz}}$ or 4×10^{-16} m/ $\sqrt{\text{Hz}}$. However, when we consider the additional noise contribution to the design noise budget, we expect the additional noise contribution

is less than 1% in power spectral density. Since nearly all the noise source incarnations are not correlated with each other, including this local oscillator instability noise, a factor of 10 safety margin in the local oscillator phase noise requirement in amplitude ensures the compatible to within 1% with the design sensitivity. The phase noise in local oscillator can originate from different sources, *e.g.* mirrors thermal fluctuations and seismic noise, in which the seismic coupling via the suspensions and their resonance dominates. For a single optics, considering the number of the reflective optics on LO path, *i.e.*, in current layout design, the requirement should be further divided by $\sqrt{5}$. We assume conservatively to obtain this requirement via a pure passive isolation system. Thus, considering the typical ground motion,

$$x_{ground} \approx 10^{-10} \left(\frac{10 \text{ Hz}}{f} \right) \text{ m}/\sqrt{\text{Hz}}, \quad (4.11)$$

A triple stage suspension design is required to achieve the single reflective optics phase noise requirement. One could be thinking about the use of a feedback scheme in combination with two stage suspensions. This would require a high gain loop and broad control bandwidth. However, the loop sensing noise is even larger than the LO phase noise. By taking the choice of a triple stage passive isolation scheme, a low bandwidth loop can be applied to keep the homodyne angle locked. Low bandwidth then allows to roll off any sensor noise so that no significant control noise will be introduced in the detection band.

4.1.1 Output mode cleaner (OMC) stability

Since the second term in Eq. 4.6 refers to the relative phase stability of the LO beam in respect to the signal beam, our phase noise requirement derived in the previous section also applies to the signal path. The current DC readout configuration features an OMC at the asymmetric port for getting rid of optical higher order modes (HOMs) and radio frequency (RF) sidebands and hence we have to analyse whether the OMC provides low enough noise to be compatible with the LO phase noise stability requirement.

In DC readout, the LO and signal beam are overlapped on the same path and the same quadrature, *i.e.* phase quadrature, because both the LO in DC readout and signal beam are generated from the length difference of two arms with the only difference, one (LO) is constant, the other (signal) is dynamic. The homodyne angle can only be changed due to the differential losses in the arms. arms optical loss. [27, 62]. Thus, any sidebands modulated by the mode cleaner mirror displacement on the bright beam should just couple onto the orthogonal quadrature, amplitude quadrature. So there is no contamination to the signal.

However, the situation is in the balanced homodyne readout if two mode cleaners are applied on the LO and signal path, respectively, and the interference between the two beams happens after two mode cleaners. The LO beam in balanced homodyne readout does not

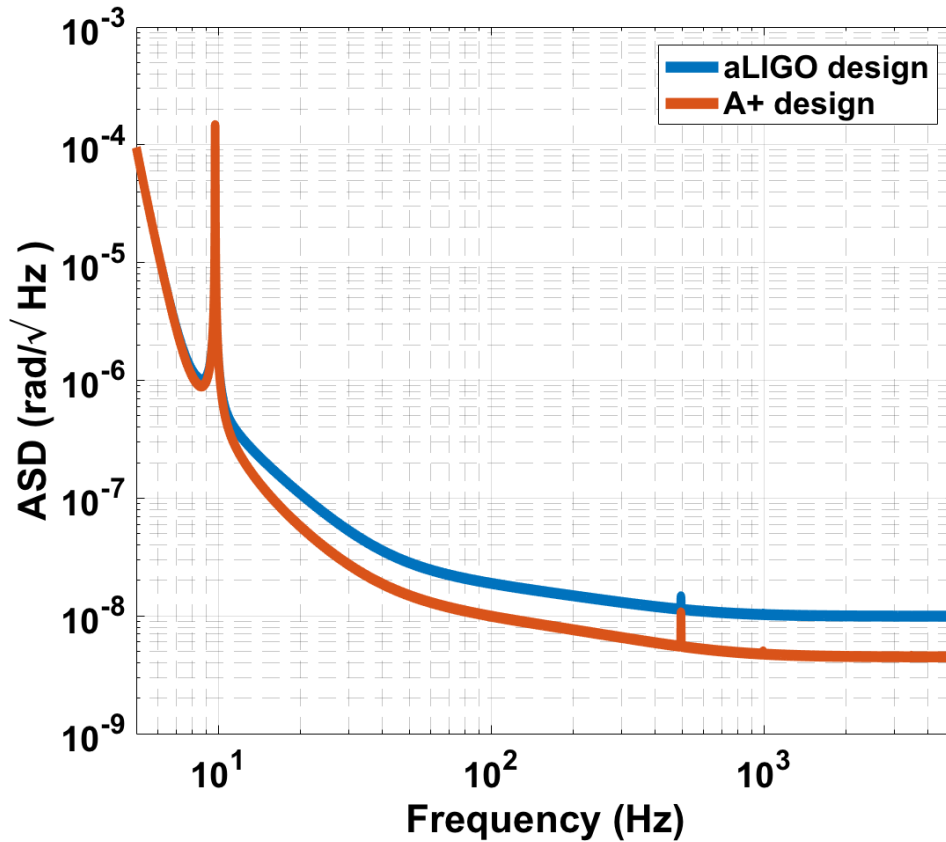


Figure 4.2: Stability requirement of the LO phase for aLIGO and A+ employing BHD. Phase fluctuations indicated by the different traces would cause an additional noise contribution equal to the design noise level of these instruments.

originate from the dark port, but instead a pick off beam from the bright port is used. So its amplitude locates on the amplitude quadrature. Thus the LO mode cleaner mirror displacements create sidebands on phase quadrature and contaminates the signal as phase noise. Even in case there is only one OMC on the signal path, the OMC mirror displacements also create phase noise. Because the DC components in the signal beam which arises due to the arms optical loss difference also locate on amplitude quadrature.

Similar to the reflective optics stability requirement for the LO path, we can define stability requirement δx_{MC} for the relative length of the two output mode cleaners. The relation is

$$\frac{\delta x}{\delta x_{MC}} = \frac{F_{MC}}{\pi}, \quad (4.12)$$

where F_{MC} is the finesse of the mode cleaner, which are assumed to have identical designs. The aLIGO output mode cleaner has a finesse around 400. Fig 4.3 shows the phase noise fluctuation requirement of the OMCs in case of balanced homodyne required to reach the aLIGO and A+ sensitivities. Unfortunately, after taking into account a factor of 10 as safety margin, even the mode clean thermal noise cannot fulfil the requirement. So, we had to

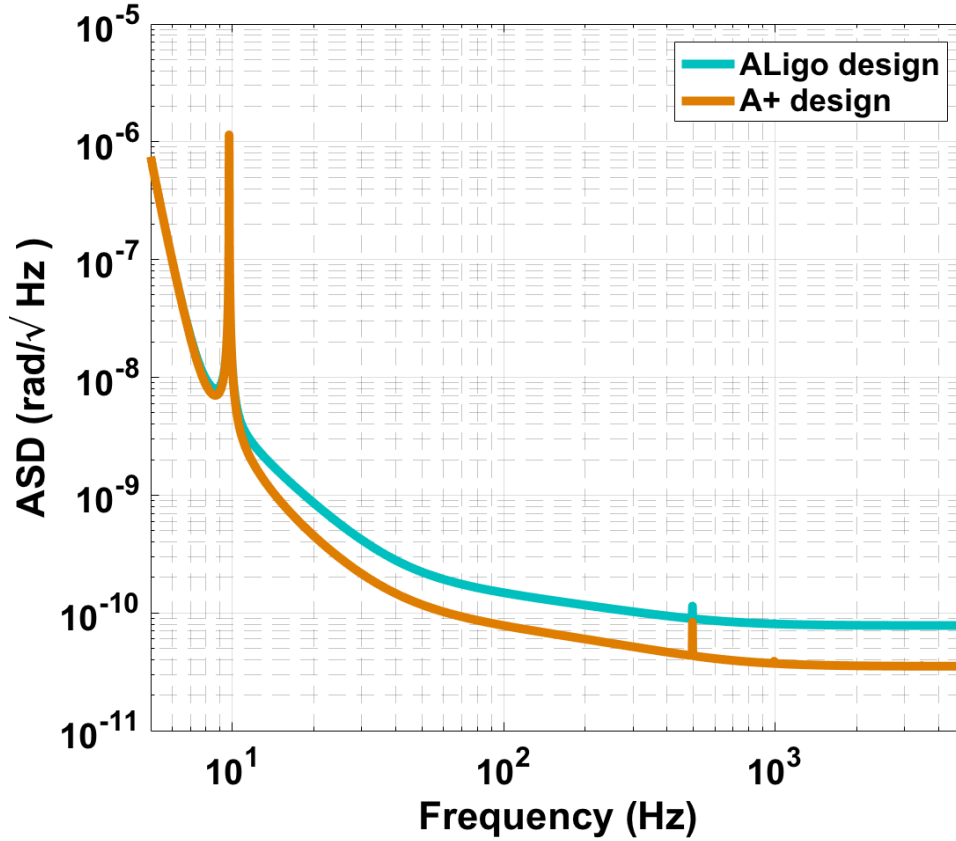


Figure 4.3: Level of OMC induced phase noise fluctuations which would cause a noise contribution similar to the design sensitivity of Advanced LIGO and A+.

find an alternative design. Fig. 4.4 sketches out several options for realising the evasion of mode cleaners noise contamination.

- A. One mode cleaner for both signal and LO beam: Two beams travel in the same direction, however, inject from different couplers. The mode cleaner mirrors motions modulate the two beams simultaneously and in the same way. Thus this phase noise becomes common noise for two beams and will be subtracted out according to Eq. 4.8. However, the signal beam and LO beam will exchange their HOMs and RF components, since the transmitted beams will be overlapped with the reflected components of the beam which comes from the other input coupler. So two beams after OMC still contain the same amount of HOMs and RF sidebands in total as before. These light fields will contribute additional shot noise and reduce the overall sensitivity [63].
- B. Two beams travelling in the opposite direction but injected from the same coupler. In this case, the local oscillator HOMs and RF components will be reflected to the interferometer from the asymmetric port. In the ideal case, the interferometer itself can reject these high order optical mode light fields. However, due to imperfect optics in the interferometer HOMs are created and can leak into the asymmetric port. Thus

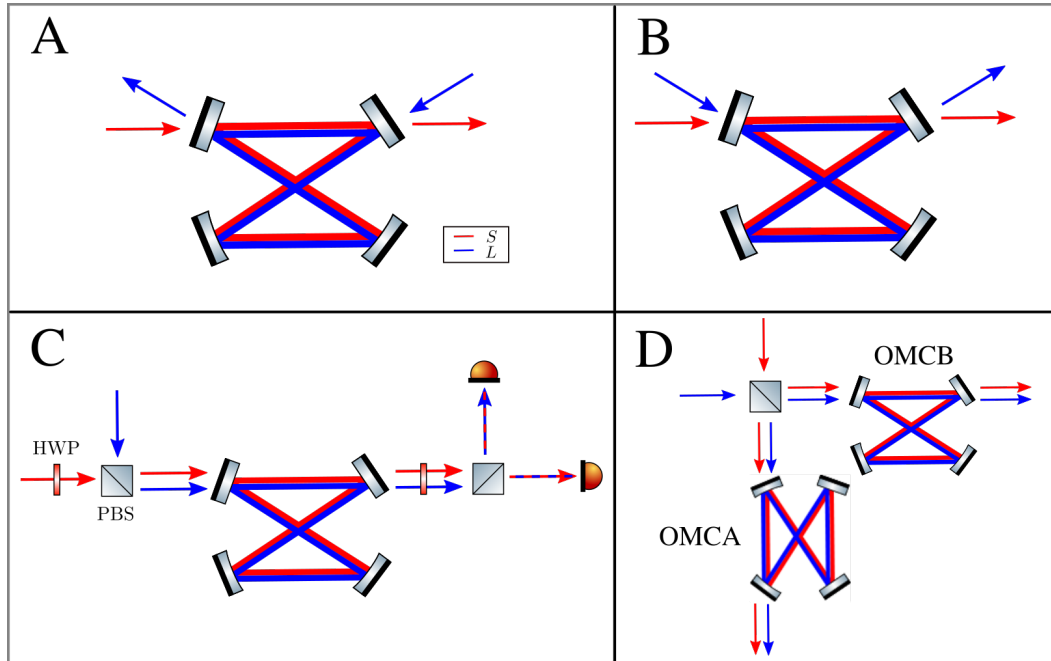


Figure 4.4: Options of output mode cleaners arrangement to eliminate the mode cleaners phase noise coupling. The red trace represents the signal beam; the blue trace represents the local oscillator beam.

these light fields which re-enter the interferometer from the asymmetric port will cause interactions with the interferometer that are not easy to predict. And even the fundamental mode components in LO will be reflected into the asymmetric port as long as there is mismatch between the transmission of input coupler and output coupler. This effect is equivalent to the effect of backscattering. There is no doubt that it will lead damages to the detector sensitivity.

- C. Two different polarisations are designed for local oscillator and signal beam in one mode cleaner. The signal beam can be transferred to p-polarisation and enters into the mode cleaner together with s-polarised LO beam. As long as the two beams co-resonate in the OMC, the same principle as options A and B, the OMC noise can be subtracted as common motion noise in the final photodiode current. To realise a balanced homodyne detection, we can add another half-wave plate at the transmission port of OMC and rotate the two beams polarisation angles by 45 degrees, respectively. Thus by utilising a polarisation beam splitter (PBS) as the BHD beamsplitter, the LO and signal beams can interference destructively or constructively at the transmission port or the reflection port of this PBS, depending on the rotation direction of the former mention 45 degrees polarisation angle.

However, the OMC finesse for p-polarisation beam needs to be identical to the s-polarisation beam. This requires the same phase relation and reflectivity of coatings for the two non-normal incidence beams in two polarisations. Thus it feels too risky

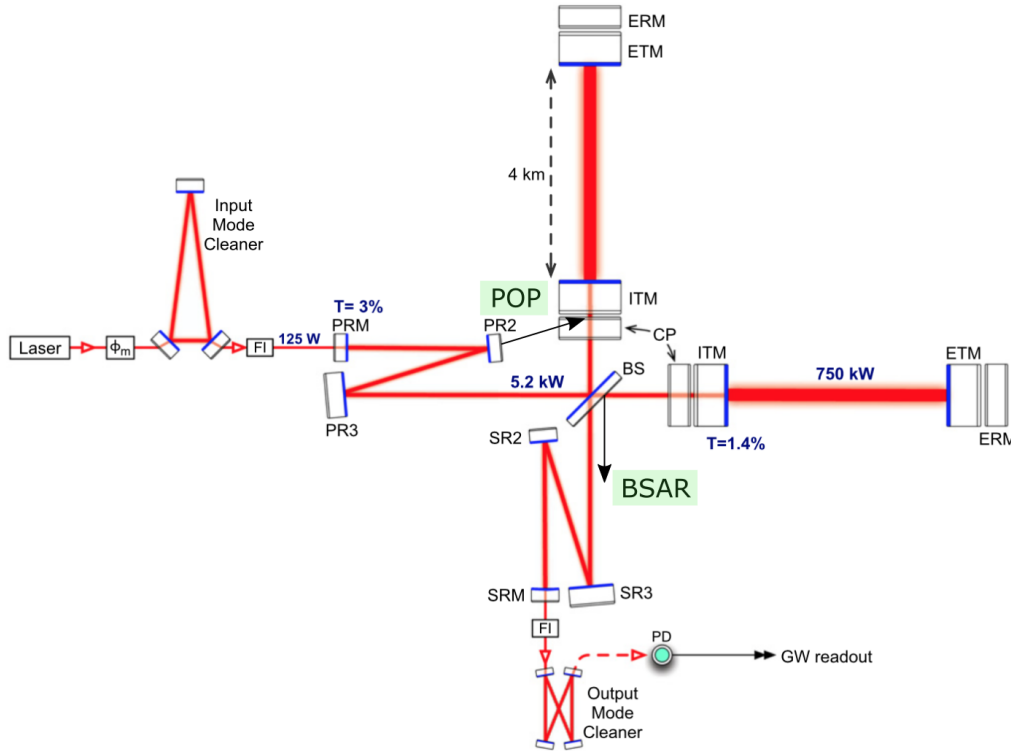


Figure 4.5: Simplified aLIGO optical layout. This plot is taken from [65] and is modified to indicate two local oscillator pick off port options, *i.e.* POP port and BSAR port. POP refers to the power recycling cavity pick off, BSAR refers to the anti-reflective coating surface of the main beamsplitter.

to rely on coatings providing good performance as the base-line plan for A+. However, in order to keep the door open for future options (beyond A+), the Caltech team will continue to investigate detailed aspects of this option [64].

- D. Two mode cleaners are placed behind the balanced homodyne beam splitter. In terms of displacement noises created by each OMC, this scheme is equivalent to the DC-readout. Since the local oscillator and signal beam interference before the mode cleaners, where the homodyne angle is defined, the mode cleaners motion will only couple to the orthogonal quadrature.

In the end, the D) option was chosen as the most practical way forward for the balanced homodyne detection for A+. Since the mode cleaners have very broad bandwidth, any asymmetries of two mode cleaners should be equivalent to two photodiodes imbalance. The drawback is that the LO field circulating in the OMCs could couple back into the interferometer asymmetric port due to the backscattering. However, the total backscattering will not be worse than in DC readout. At least, in this option, the backscattering field from the signal path before balanced homodyne readout beamsplitter is significantly reduced due to the significantly reduced DC power in that part of the path, compared to the case of DC readout.

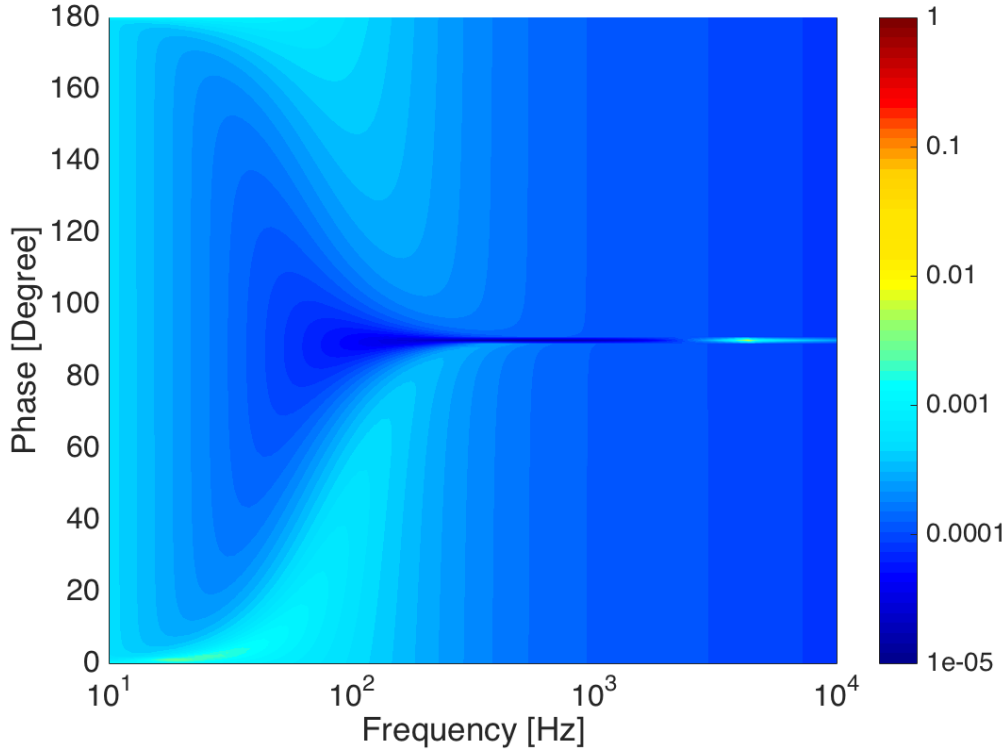


Figure 4.6: The ratio of the scattering transfer functions in POP option over BSAR option. The colour bar indicates the factor by how much less sensitive the POP option is in terms of backscattering within the LO path compared to the BSAR option. The y-axis indicates the quadrature in which the scattering source will couple. Note that most scattering sources will not have a fixed phase relation, but instead effectively scatter with an arbitrarily varying phase.

4.2 Local oscillator delivery options

Several options are currently discussed for deriving a local oscillator beam and guiding it to the vacuum chamber hosting the BHD. One interesting aspect of the local oscillator choice is the effect of backscattering from any components inside local oscillator path back into the main interferometer. The schematic of two local oscillator delivery options are shown in Fig. 4.5. Both options access a well filtered and stabilised laser beam from within the main interferometer. Intuitively one would assume that any backscattering from the BSAR local oscillator is much more harmful as it only enters one arm, i.e. it is intrinsically scattering into the differential mode, while backscattering from the POP local oscillator re-enters the interferometer via the power recycling cavity and is therefore in the common mode, which couples much less to the GW channel. The aim of this section is to investigate the magnitude of relative coupling of scattered light from the two local oscillator options.

For obvious reasons, it is very hard if not even impossible at the current stage to make any good predictions about the actual scattering sources, their scattering amplitudes and relative motions, that will be present in advanced A+ BHD. So, to gain insight into the

scattering susceptibility of the two different options we simulate a single scattering source of identical properties in both LO paths and look at the relative strength of the coupling transfer function from the backscattering field fluctuations to the detector's output (rather than any absolute values). I added one additional mirror with 100 ppm reflectivity in the local oscillator path. A signal is applied to this mirror (note this signal is much smaller than the laser wavelength). Note that depending on the microscopic position of the scatterer and its motion, the scattering will either be in the phase quadrature, the amplitude quadrature or anywhere in between. I account for this by simulating the scattering transfer function for different phases of the scattering mirror. As mentioned above, the key to look at here is the difference between the two transfer functions instead of their absolute values (which would change depending on the backscattering amplitude). Fig. 4.6 shows the ratio of the two scattering transfer functions. We find that, as expected from intuition, the POP option is in all cases less susceptible to scattering compared to the BSAR option.

4.3 Sensing and control

In this section, I simulate the error signals that can be used for controlling the different degrees of freedom in balanced homodyne readout for A+. I will start by introducing several degrees of freedom that require to be controlled. In a second step, I will detail potential locking strategies currently under consideration. The strategies mainly rely on the outcome of MIT BHD workshop [66].

4.3.1 Degrees of freedom

The following degrees of freedom are required to be controlled in the balanced homodyne readout:

- Balanced homodyne readout angle
- Length of each of the two OMCs
- Alignment between LO and signal beam (pitch/yaw)
- Input alignment of the combined LO and signal beams to OMCA/OMCB (pitch/yaw)

The possible locking strategies for these degrees of freedom will be discussed in the following.

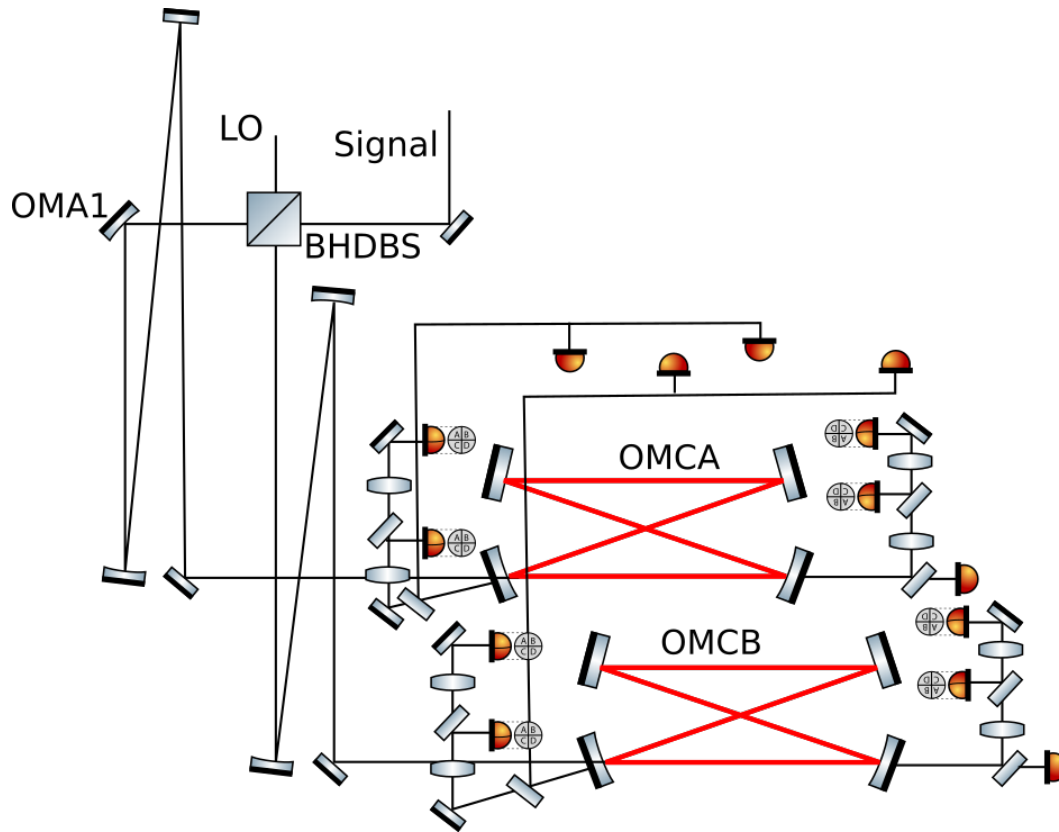


Figure 4.7: The schematic of the optical layout design of A+ BHD and sensing schemes.

4.3.2 BHD readout angle control

There are various strategies that can be utilised for locking the homodyne angle. One scheme is referred to as the **36 MHz scheme**. In advanced LIGO, 9 MHz and 45 MHz RF modulation sidebands are applied onto the input light. Both of them are resonant in the power-recycling cavity, but not in the arm cavities. A relatively small Schnupp asymmetry (8 cm) was chosen in order to couple the majority of the 45 MHz sideband power into the signal recycling cavity and suppresses the 9 MHz power in the signal recycling cavity, leading to a better separation of the error signals for the two recycling cavities. In the advanced LIGO case with a signal recycling mirror transmission of 35%, nearly all of the 45 MHz sidebands are transmitted to the AS output, while only about 0.3% of the 9 MHz sidebands leak to asymmetric port. We want to utilise the two sets of RF sidebands present in the LO and the signal beam to lock the homodyne angle. The two RF sidebands along with LO and signal beam carriers will interfere when the LO and signal beams overlap on the balanced homodyne readout beamsplitter. By demodulating the photodiode signals in the reflection of the two OMCs at the beat frequency of the two sets of RF sidebands, i.e. 36 MHz and subtracting the resulting signals derived from the two OMCs, we can get the error signal for the homodyne angle, which is shown in Fig. 4.8. This result is simulated by using Finesse (frequency domain interferometer simulation) software [67]. The corre-

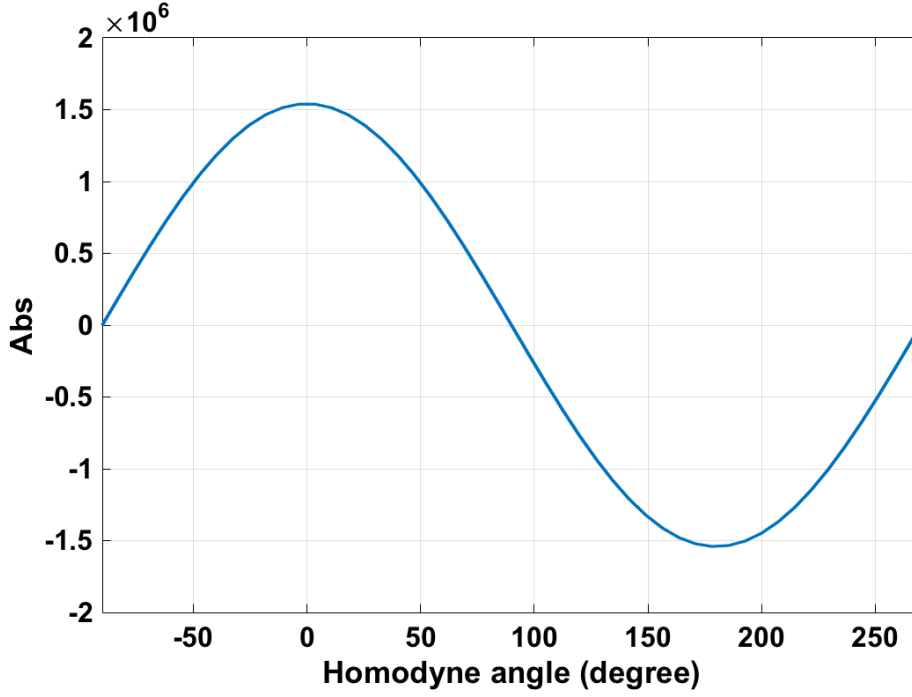


Figure 4.8: The error signal of the homodyne angle. It is the subtraction of demodulation signals of two photodiodes which are placed at the reflection of two OMCs. The operating point is at homodyne angle of 90 degree.

sponding commands are as following

```
pd1 err_A $fM nOMCA_ICb
pd1 err_B $fM nOMCB_ICb
```

More detailed analytical calculation to demonstrate the principle can be derived as follows. The signal and LO fields with the main RF sidebands can be expressed as

$$\begin{aligned} E_s &= |S|e^{i(\omega+\alpha \sin \Omega_1 t)}, \\ E_l &= |L|e^{i(\omega+\beta \sin \Omega_2 t)}. \end{aligned} \quad (4.13)$$

$|S|$ and $|L|$ are absolute amplitude of signal beam and LO beam, ω is the laser beam angular frequency, α and β are the RF modulation indices of the two beams, and Ω_1 and Ω_2 are the RF modulation frequencies of the two beams. With small modulation index, they can be expanded by Bessel functions up to the first order as

$$\begin{aligned} E_s &= |S|[J_0(\alpha)e^{i\omega t} + J_1(\alpha)e^{i(\omega+\Omega_1)t} - J_1(\alpha)]e^{i(\omega-\Omega_1)t}, \\ E_l &= |L|[J_0(\beta)e^{i\omega t} + J_1(\beta)e^{i(\omega+\Omega_2)t} - J_1(\beta)]e^{i(\omega-\Omega_2)t}. \end{aligned} \quad (4.14)$$

After the two beams are combined on the BHD beamsplitter, the two fields can be written as

$$P_1 = \frac{E_l + E_s}{\sqrt{2}}, P_2 = \frac{E_l - E_s}{\sqrt{2}}. \quad (4.15)$$

If no OMCs exist, the photocurrents of each photodiode can be written as

$$\begin{aligned} I_1 &= \frac{|E_s|^2 + |E_l|^2 + E_s E_l^* + E_l E_s^*}{2}, \\ I_2 &= \frac{|E_s|^2 + |E_l|^2 - E_s E_l^* - E_l E_s^*}{2}. \end{aligned} \quad (4.16)$$

Since there are two OMCs behind the BHD beamsplitter and we use the reflection of the OMCs for locking purpose, the carrier components transmit through the OMCs and hence at the photodiodes only the RF components remain. The subtraction of the photocurrents in reflection of the two OMCs are derived:

$$\begin{aligned} I_d &= J_1(\alpha)J_1(\beta)|S||L|\{e^{i[(\Omega_1 - \Omega_2)t - \phi]} - e^{i[(\Omega_1 + \Omega_2)t - \phi]} - e^{i[-(\Omega_1 + \Omega_2)t - \phi]} + e^{i[(\Omega_2 - \Omega_1)t - \phi]}\} + h.c. \\ &= 4J_1(\alpha)J_1(\beta)|S||L|[\cos(\Omega_1 - \Omega_2)t - \cos(\Omega_1 + \Omega_2)t] \cos \phi, \end{aligned} \quad (4.17)$$

where $h.c.$ denotes the hermitian conjugate. Then we mix the residual components with a demodulation signal $\cos(\Omega_1 - \Omega_2)t + \theta$, where θ is the demodulation phase. We filter out the any oscillation terms created in the demodulation process by sending the demodulated signal to a low pass filter and obtain

$$err \propto J_1(\alpha)J_1(\beta)|S||L|[\cos(\phi + \theta) + \cos(\phi - \theta)] = J_1(\alpha)J_1(\beta)|S||L| \cos \phi \cos \theta. \quad (4.18)$$

We can notice when the demodulation phase is 0 and homodyne angle is $\frac{\pi}{2}$, we get the zero crossing with maximum slope.

4.3.3 Length of each of the two OMCs

For locking the output mode cleaners longitudinal degree of freedom, we can use a dither scheme, *i.e.* dither the local oscillator in length and demodulate at the transmission of output mode cleaners. The Finesse commands are as following

```
fsig dither BHDANG phase 107 0 100
pd1 PD_MCA 107 90 nBHD1
pd1 PD_MCB 107 90 nBHD2
```

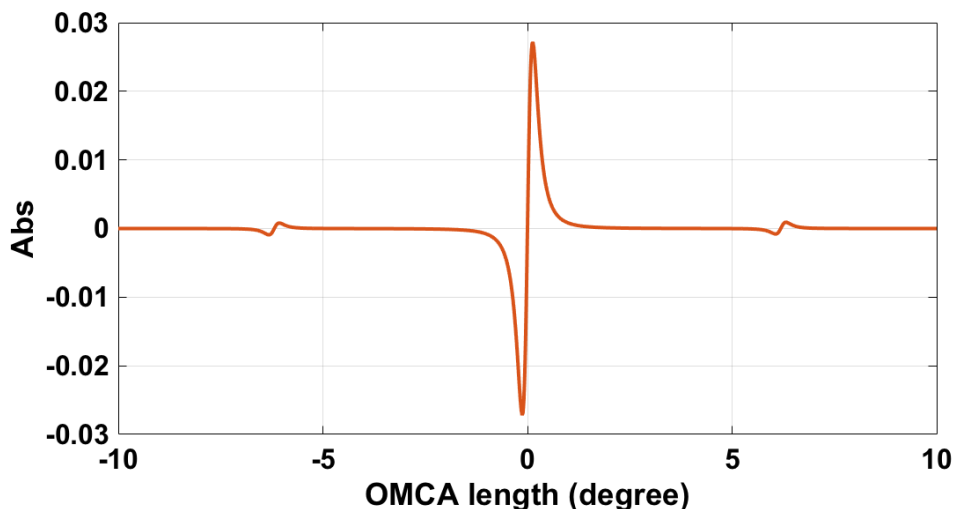


Figure 4.9: The error signal of OMCA length variation. The sensing photodiode is placed at the transmission of the OMCA. The error signal is measured by demodulating the current of the photodiode in quadrature at the dithering frequency.

I chose a dither frequency of 107 Hz and amplitude 100 in Finesse. There is good error signal in the case of in quadrature demodulation. The error signal of the OMCA longitudinal motion is shown in Fig. 4.9. The case is symmetric for OMCB.

4.3.4 Alignment between LO and signal beam

The alignment between the local oscillator and signal beam degrees of freedom can be covered by the beamsplitter, *i.e.*, we can always find a beamsplitter position to keep the transmission of the local oscillator and signal beam symmetric. Thus they are also overlapped with the reflected beams. Similar to the control of the BHD angle we can use the 36 MHz scheme as described above to generate error signals for the alignment between LO and signal beam. The misalignment between LO and signal beam could be caused by balanced homodyne beamsplitter angular rotation. Assuming the LO and signal beam are overlapped on beam splitter, the alignment between the local oscillator and signal beam degrees of freedom can be covered by the beamsplitter actually, *i.e.*, we can always find a right beamsplitter angle to keep the transmission beams of the LO and signal beam symmetric, so they are also overlapped with the reflected beams. In this section, I demonstrate the alignment sensing between LO and signal beam with the example of one of the possible misalignments caused by the beamsplitter tilting. Since the LO and signal beam waists are not on the beamsplitter, any jitter of the BHD beamsplitter alignment will induce both beam shift and tilt in both, pitch and yaw degrees of freedom. To find the correct gouy phase telescope at the reflection of the OMCs to decouple the shift and tilt, I find both the signal and local oscillator beams waist are 0.2 m away from the BHD beamsplitter in the

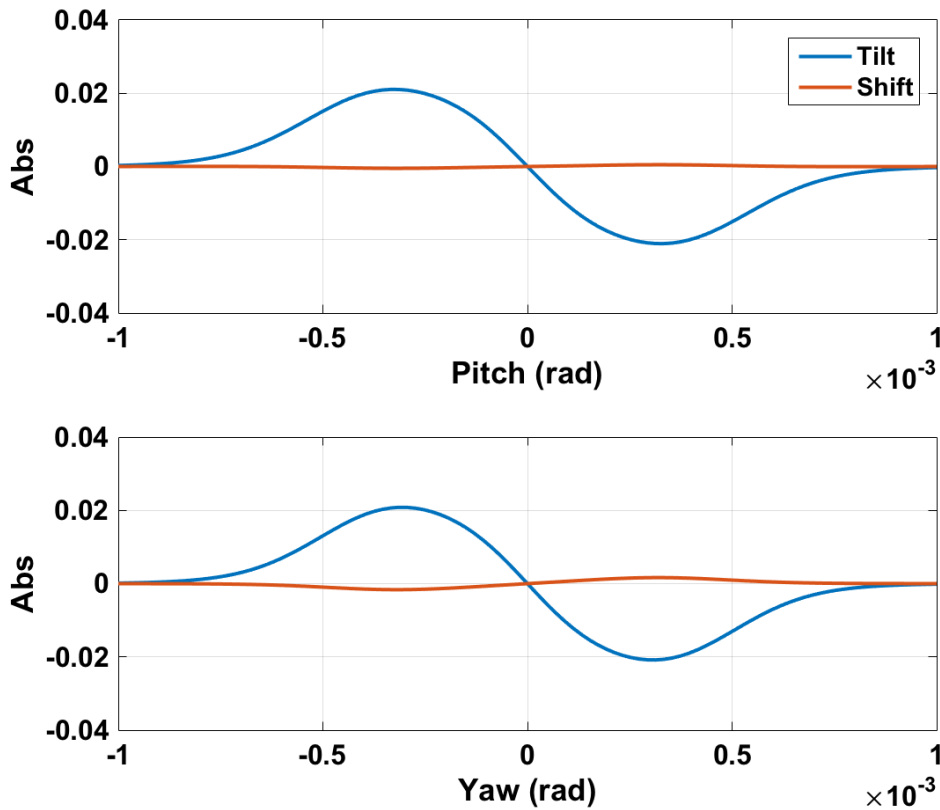


Figure 4.10: Simulated errors signal for alignment between signal beam reflection and local oscillation beam transmission of BHD beamsplitter in pitch and yaw degrees of freedom. The misalignment is created by tilting the BHD beamsplitter. The sensing QPDs are placed in the reflection of OMCA. The error signals are derived from the QPD photo current after demodulation at 36 MHz.

Finesse file which reflects our current thinking and planning on what the beam layout will look like. By adding a perfectly reflective mirror at the waist position in the LO path in the Finesse code and titling it, I can find the correct gouy phase for sensing pure shift if there is no response on the quadrant photodiode (QPD). So two QPDs are placed at OMCA reflection port and two QPDs are placed at the OMCA reflection port. The responses of the QPDs at the OMCA reflection port for balanced homodyne beamsplitter rotation are shown in Fig. 4.10.

The Finesse commands for sensing pitch degrees of freedom are

```
maxtem 3
s sMCABS 0.001 nOMCA_ICb nQPDABSA
bs1 QPDABS 0.5 0 0 0 nQPDABSA nQPDABSB nQPDABSC nQPDABSD
s sQPD_A_1 0.001 nQPDABSB nQPD_A_1
s sQPD_A_2 0.001 nQPDABSC nQPD_A_2

s sQPD_A_2 0.001 nQPDABSC nQPD_A_2
```

```
bs1 QPDBBS 0.5 0 0 0 nQPDBBSa nQPDBBSb nQPDBBSc nQPDBBSd
s sQPD_B_1 0.001 nQPDBBSb nQPD_B_1
s sQPD_B_2 0.001 nQPDBBSc nQPD_B_2
```

```
pd1 QPD_A_1 $fM 0 nQPD_A_1
pd1 QPD_A_2 $fM 0 nQPD_A_2
pd1 QPD_B_1 $fM 0 nQPD_B_1
pd1 QPD_B_2 $fM 0 nQPD_B_2
```

```
pdtype QPD_A_1 y-split
pdtype QPD_A_2 y-split
pdtype QPD_B_1 y-split
pdtype QPD_B_2 y-split
```

```
attr sQPD_A_1 g 25
attr sQPD_A_2 g 115
attr sQPD_B_1 g 25
attr sQPD_B_2 g 115
```

```
xaxis BHDBS ybeta lin -1m 1m 99
yaxis re:im
```

4.3.5 Input alignment of the combined LO and signal beams to OMCs

Another degree of freedom is the input alignment of the beam from BHD beamsplitter to the OMCs. Since we already established control of the overlap of the LO and signal beam the overlap of LO and signal beam (see Sec. 4.3.4 above), it should be equivalent to derive the alignment signals of the OMCs either from the dithering the LO beam or the signal beam so that we dither the local oscillator in length and demodulate at the transmission of output mode cleaners. The proper gouy phase telescope is derived following the same procedure as described in Sec. 4.3.4. In Fig. 4.11, I give an example of a mode cleaner input alignment error signal for the rotation of one of the reflective optics, OMA1, between BHD beamsplitter and OMCA. The Finesse commands for sensing pitch degrees of freedom are

```
maxtem 3
fsig dither BHDANG phase 107 0 100

s SOMCAWFS 0.001 nBHD1 nOMCAWFSa
```

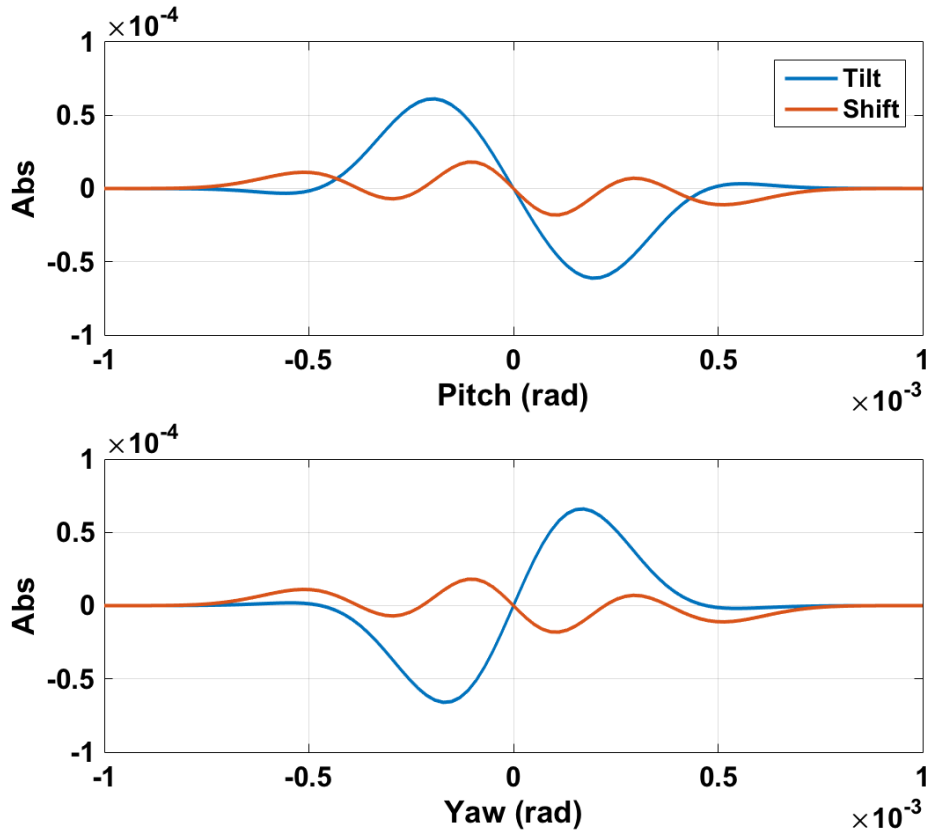


Figure 4.11: The error signal for input alignment of the combined beam from BHD beam splitter to OMCA in pitch and yaw degrees of freedom. The jittering signal is created by shaking one reflective mirror, OMA1 (see Fig. 4.7), between BHD beamsplitter and OMCA. The sensing QPDs are placed at the transmission of the OMCA. The error signals are measured by demodulating the current of the QPDs in phase at dithering frequency.

```

bs1 OMCAWFS 0.5 0 0 0 nOMCAWFSa nOMCAWFSb nOMCAWFSc nOMCAWFSd
s SOMCAQPD_1 0.001 nOMCAWFSb nQPDA_1
s SOMCAQPD_2 0.001 nOMCAWFSc nQPDA_2

s SOMCBWFS 0.001 nBHD2 nOMCBWFSa
bs1 OMCBWFS 0.5 0 0 0 nOMCBWFSa nOMCBWFSb nOMCBWFSc nOMCBWFSd
s SOMCBQPD_1 0.001 nOMCBWFSb nQPDB_1
s SOMCBQPD_2 0.001 nOMCBWFSc nQPDB_2

attr SOMCAQPD_1 g 15
attr SOMCAQPD_2 g 105
attr SOMCBQPD_1 g 15
attr SOMCBQPD_2 g 105

```

```
pd1 PD_MCA_1 107 0 nQPDA_1
pd1 PD_MCA_2 107 0 nQPDA_2
pd1 PD_MCB_1 107 0 nQPDB_1
pd1 PD_MCB_2 107 0 nQPDB_2
```

```
pdtype PD_MCA_1 y-split
pdtype PD_MCA_2 y-split
pdtype PD_MCB_1 y-split
pdtype PD_MCB_2 y-split
```

```
xaxis BHDBS ybeta lin -1m 1m 99
yaxis re:im
```

4.3.6 Summary

In this chapter, I introduced and discussed several design aspects relevant for the balanced homodyne readout implementation in A+. We found triple stage suspensions are required for the relay optics in the local oscillator path, guaranteeing the required local oscillator stability. I presented various options for the optical design considering noise requirements imposed by the OMC thermal noise and then discussed the advantages and disadvantages of the different options. In the end, the option of placing two OMCs after the BHD beam-splitter was chosen the most practical way forward for the balanced homodyne detection for A+. We found that the delivery of the local oscillator from the POP port is a better choice compared with the BSAR port in terms of the local oscillator backscattering noise. Moreover, I presented strategies for controlling the various degrees of freedom involved in the BHD system.

Chapter 5

Quantum noise cancellation in asymmetric speed meters with balanced homodyne readout

The design sensitivity of current generation and proposed future generation gravitational wave detectors is limited by quantum noise over nearly the whole frequency band, in which the radiation pressure noise dominates at low frequencies. The improvement of detector sensitivity at low frequencies not only can improve the SNR for various sources of gravitational waves but also can give longer warning time for electromagnetic (EM) counterparts of gravitational wave event. Moreover, it could significantly improve the detection rate of massive binary black holes. So far there are no observations of any systems with component masses prior to merger greater than 50 solar masses [68].

The speed meters have been identified to be a promising technique to reduce quantum radiation pressure noise in future generation gravitational-wave detectors, in which Sagnac interferometer can be served as a speed meter. In a Sagnac speed meter, the main beam splitter imbalance is recognised as one of the most significant challenges which limits the detector's sensitivity. In this chapter, one solution by implementing BHD readout and proper choice of the pick off port of the local oscillator (LO) is analysed. As it turns out, by taking the LO from the reflected light at the pumping port of the interferometer or the direct reflection off the main beam splitter's anti-reflective coating, the quantum noise contamination from the laser pumping port can be almost compensated. Taking the example of Glasgow Sagnac speed meter experiment, it is proved that with the proper choice of LO pick off port, at frequency of 100 Hz, the requirement of relative intensity noise of the pumping laser decreases by 3 orders of magnitude.

This work, which I lead has been published as a journal article. It is reproduced on the following pages.



PAPER

Quantum noise cancellation in asymmetric speed metres with balanced homodyne readout

OPEN ACCESS

RECEIVED
6 July 2018REVISED
27 September 2018ACCEPTED FOR PUBLICATION
15 October 2018PUBLISHED
29 October 2018

Original content from this work may be used under the terms of the [Creative Commons Attribution 3.0 licence](#).

Any further distribution of this work must maintain attribution to the author(s) and the title of the work, journal citation and DOI.

T Zhang¹, E Knyazev² , S Steinlechner^{1,3}, F Ya Khalili^{4,5}, B W Barr¹, A S Bell¹ , P Dupej¹, J Briggs¹, C Gräf¹, J Callaghan¹, J S Hennig¹, E A Houston¹, S H Huttner¹, S S Leavey¹, D Pascucci¹, B Sorazu¹, A Spencer¹, J Wright¹, K A Strain¹, S Hild¹ and S L Danilishin^{1,6} 

¹ School of Physics and Astronomy, The University of Glasgow, Glasgow, G12 8QQ, United Kingdom² LIGO, Massachusetts Institute of Technology, Cambridge, MA 02139, United States of America³ Institut für Laserphysik und Zentrum für Optische Quantentechnologien der Universität Hamburg, Luruper Chaussee 149, D-22761 Hamburg, Germany⁴ Faculty of Physics, M.V. Lomonosov Moscow State University, 119991 Moscow, Russia⁵ Russian Quantum Center, 143025 Skolkovo, Russia⁶ Institut für Theoretische Physik/Institut für Gravitationsphysik (Albert-Einstein-Institut), Leibniz Universität Hannover, Callinstraße 38, D-30167 Hannover, GermanyE-mail: stefan.danilishin@ligo.org

Keywords: balanced homodyne detector, speed metre, quantum noise

Abstract

The Sagnac speed metre topology has been identified as a promising technique to reduce quantum back-action in gravitational-wave interferometers. However, imbalance of the main beamsplitter has been shown to increase the coupling of laser noise to the detection port, thus reducing the quantum noise superiority of the speed metre, compared to conventional approaches, in particular at low frequencies. In this paper, we show that by implementing a balanced homodyne readout scheme with a suitable choice of the point from which the local oscillator (LO) is derived, the excess laser noise contribution is partly compensated, and the resulting speed metre can be more sensitive than state-of-the-art position metres. This is achieved by picking-off the LO from either the reflection port of the interferometer or the anti-reflective coating surface of the main beamsplitter. We show that either approach relaxes the relative intensity noise (RIN) requirement of the input laser. For example, for a beam splitter imbalance of 0.1% in the Glasgow speed metre proof of concept experiment, the RIN requirement at frequency of 100 Hz decreases from $4 \times 10^{-10}/\sqrt{\text{Hz}}$ to $4 \times 10^{-7}/\sqrt{\text{Hz}}$, moving the RIN requirement from a value that is hard to achieve in practice, to one which is routinely obtained.

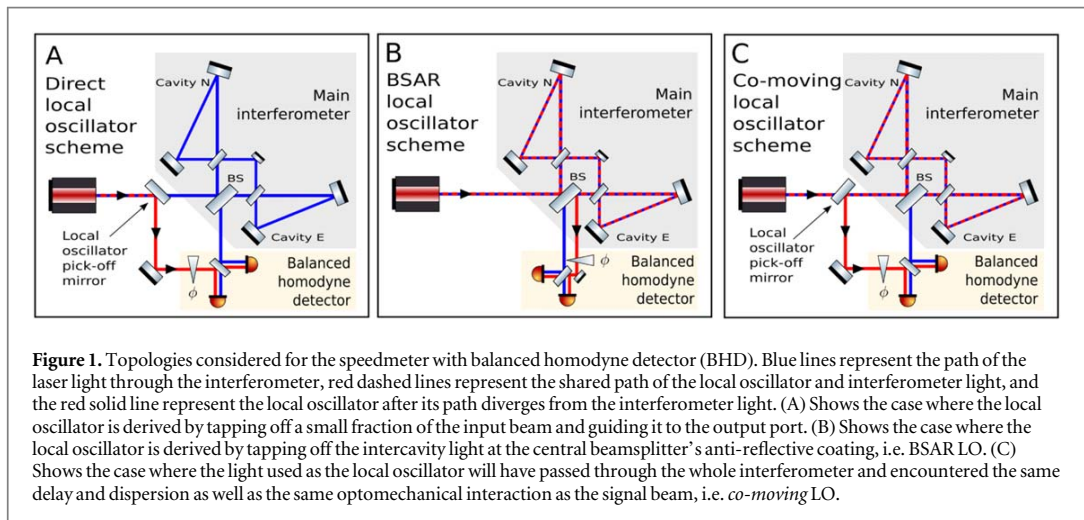
1. Introduction

In 2015, we stepped into the era of gravitational-wave astronomy with the first direct detection of gravitational waves (GW) from a colliding binary black hole (BBH) system by the two Advanced LIGO interferometers [1]. Two exciting years of discoveries have given us four more BBH merger events [2–5], and one collision of neutron stars [6], with the last system also being observed in the electromagnetic spectrum [7].

Those discoveries, apart from generating a great deal of fascinating new science hitherto unavailable to humanity, identified the need to improve the sensitivity of the existing detectors, particularly in the low frequency range (< 30 Hz) where the noise of the detector masks GW signals from massive black holes, i.e. with masses $> 30M_{\odot}$, where M_{\odot} is one solar mass. It also masks GWs from a stage in the evolution of binary neutron stars a few minutes before the end of the in-spiral, observation of which could allow an early warning to be issued to EM observers.

The design sensitivity of current and proposed laser interferometric gravitational-wave detectors is limited by quantum noise [8, 9] over much of their detection frequency band. This noise stems from fundamental quantum-mechanical fluctuations of the phase and amplitude of coherent laser light. In particular, amplitude fluctuations which produce a random back-action force on the test masses, will mimic the action of GWs when





the power in the arms reaches the design level of MW and could therefore have the largest potential impact at low frequencies where the noise amplitude rises as f^{-2} , in which f is the GW frequency.

Speed-metre interferometers were first proposed by Braginsky and Khalili [10] as a way to suppress quantum back-action noise in bar GW detectors. Later, this concept was generalised to laser GW interferometers [11]. Back-action noise reduction in speed metres stems from the quantum non-demolition (QND) nature of test mass' velocity [12] as a quantum observable, in contrast to the displacement measured by Michelson interferometers. This advantage of speed metre over position metres at low frequencies inspired the development of several different speed metre topologies [13–18].

One of these configurations, the zero-area Sagnac interferometer, was first identified as a QND speed-metre by Chen [14]. In a Sagnac interferometer, two counter-propagating light beams visit the arms sequentially in the opposite order and return to the main beam-splitter. In this process, each beam carries phase information resulting from mirror displacements in both arms but the light visits the two arms at times separated by the interval τ , equal to the arm cavity ring down time. The counter-propagating beams add at the beamsplitter and interfere destructively at the readout port of the interferometer. Detection of this light results in an output signal which carries phase information proportional to the mean relative velocity of the interferometer arm length changes. Hence the Sagnac interferometer performs a QND measurement of speed.

In the ideal case, a Sagnac interferometer is always operating at the dark fringe at DC. Only signal sidebands, with amplitude proportional to the relative differential velocity described above, propagate to the readout port. This robustness of Sagnac topology to optical path variations, compared to the usual Michelson interferometer, was deemed to be an advantage, warranting its application in GW detectors [19]. However, it was later recognised that any deviation of the main beamsplitter from the ideal 50:50 ratio would pose a limit to the sensitivity that could be achieved, due to coupling of laser-port fluctuations to the readout port [20, 21].

It has been shown that by adding appropriate readout methods to speedmeter interferometers, it is possible to reduce the coupling of laser noise fluctuations to the GW readout signal [20, 22, 23]. In this paper we take inspiration from that work, and analytically investigate the potential cancellation of quantum noise in asymmetric (i.e. non-ideal) Sagnac speedmeters that employ balanced homodyne detectors. By extending this analysis to the Glasgow Sagnac speed metre (SSM), we investigate potential additional cancellation of laser technical noise.

The Glasgow SSM employs balanced homodyne readout and we show three options for the arrangement of the required local oscillator (LO) in figure 1. We examine the quantum and classical noise reduction when using a balanced homodyne detector LO taken from the interferometer bright port (BP) versus the noisier option of using laser light which has not been through the interferometer. Given the partial cancellation of laser noise, we can allow for deviation from 50:50 ratio at the main beamsplitter and thus resolve the primary problem that has been identified with Sagnac interferometers.

In section 2, we conduct an analytical treatment of quantum noise of an asymmetric SSM interferometer, and show how balanced homodyne readout can help to suppress quantum noise, given the proper choice of the LO. In section 3 we show the analysis on the relaxed requirement of relative laser intensity noise base on simulation software FINESSE [24].

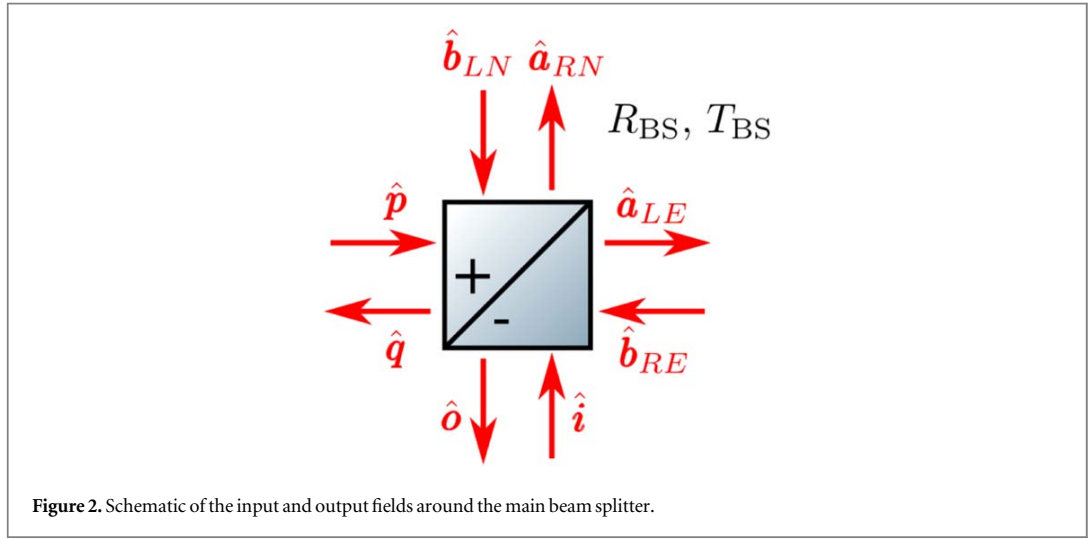


Figure 2. Schematic of the input and output fields around the main beam splitter.

2. Quantum noise of an imperfect speedmeter IFO

2.1. Two-photon formalism

In this section, we use the two-photon formalism of quantum optics [25, 26]. It describes, locally, an arbitrary quasi-monochromatic modulated electromagnetic wave with strain $\hat{E}(t) = \mathcal{E}_0[(A_c + \hat{a}_c(t))\cos\omega_p t + (A_s + \hat{a}_s(t))\sin\omega_p t]$ in terms of two-dimensional vectors of quadrature amplitudes $\mathbf{A} + \hat{\mathbf{a}}$, where $\mathbf{A} = \{A_c, A_s\}^T$ stands for DC mean amplitudes vector and $\hat{\mathbf{a}} = \{\hat{a}_c, \hat{a}_s\}^T$ stands for zero-mean non-stationary variations and fluctuations of light (superscript T denotes transpose of the matrix or vector). Here normalisation constant $\mathcal{E}_0 = \sqrt{\frac{4\pi\hbar\omega_p}{\mathcal{A}c}}$, \mathcal{A} is effective cross section of the beam, c the speed of light, and ω_p is the carrier light frequency. It is usually more convenient to work in the frequency domain:

$$\hat{a}_{c,s}(t) = \int_{-\infty}^{\infty} \frac{d\Omega}{2\pi} \hat{a}_{c,s}(\Omega) e^{-i\Omega t}, \quad (1)$$

where we define quadratures spectra at the modulation sidebands off-set frequency $\Omega = \omega - \omega_p$.

In order to understand how the fluctuations entering the pumping port of the interferometer influence all three variants, we need to analyse the input–output relations of the asymmetric interferometer with an emphasis on the transfer functions of the pump sideband fields to both, the readout port, and to the LO. Hereinafter we attain the result.

2.2. Input–output relations of the asymmetric Sagnac interferometer

We consider a Sagnac interferometer with main beam splitter non-unity ratio $R_{BS}/T_{BS} \neq 1$. The beam splitter is depicted in figure 2, with R_{BS} and T_{BS} representing the power reflectivity and transmissivity of the main beam splitter. The three LO choices that we investigate here require the knowledge of the following 3 output fields,

- (i) Readout port output field \hat{o} (for all three variants)
- (ii) Part \hat{b}^{RE} of the output field \hat{o} contributed by the clockwise propagating light beam that gives the LO field upon reflection off the main beam splitter anti-reflecting coating (variant figure 1(B))
- (iii) Return field \hat{q} at the pumping port (for the *co-moving* LO choice of figure 1(C))

Expressed in terms of the dark port (DP) input field, \hat{i} and BP input field \hat{p} and signal displacements. Following the [21], those can be written as:

$$\hat{o} = \mathbb{T}_i \hat{i} + \mathbb{T}_p \hat{p} + \mathbf{t}_d x_d + \mathbf{t}_c x_c, \quad (2)$$

$$\hat{q} = \mathbb{R}_i \hat{i} + \mathbb{R}_p \hat{p} + \mathbf{q}_d x_d + \mathbf{q}_c x_c, \quad (3)$$

$$\hat{b}^{RE} = \mathbb{T}_i^{RE} \hat{i} + \mathbb{T}_p^{RE} \hat{p} + \mathbf{t}_d^{RE} x_d + \mathbf{t}_c^{RE} x_c, \quad (4)$$

where $x_c = x_n + x_e$ and $x_d = x_n - x_e$ stand for the two mechanical modes of the Sagnac interferometer, namely the *common* and the *differential* arm elongation modes or cARM mode and dARM mode. The transfer matrices

\mathbb{T}_i , \mathbb{T}_i^{RE} and \mathbb{R}_i define the coupling of DP input field \hat{i} to the corresponding output port. The other three matrices are of more interest to us, i.e. \mathbb{T}_p , \mathbb{T}_p^{RE} and \mathbb{R}_p , as they describe how laser fluctuations \hat{p} couple to the corresponding output ports of the interferometer. It is straightforward to show (see [21] for details) that these transfer matrices, in case of imbalanced beam splitter with $R_{\text{BS}} \neq T_{\text{BS}}$, follow the well known structure of the tuned optomechanical interferometer transfer matrix (see, e.g., [27, 28]):

$$\mathbb{T}_i = 2\sqrt{R_{\text{BS}}T_{\text{BS}}}e^{2i\beta_{\text{sag}}}\begin{bmatrix} 1 & 0 \\ -\mathcal{K}_{\text{sym}} & 1 \end{bmatrix}, \quad (5)$$

$$\mathbb{R}_i = (R_{\text{BS}} - T_{\text{BS}})e^{2i\beta_{\text{sag}}}\begin{bmatrix} 1 & 0 \\ 0 & 1 \end{bmatrix}, \quad (6)$$

$$\mathbb{T}_p = (R_{\text{BS}} - T_{\text{BS}})e^{2i\beta_{\text{sag}}}\begin{bmatrix} 1 & 0 \\ -4\mathcal{K}_{\text{arm}} & 1 \end{bmatrix}, \quad (7)$$

$$\mathbb{R}_p = -2\sqrt{R_{\text{BS}}T_{\text{BS}}}e^{2i\beta_{\text{sag}}}\begin{bmatrix} 1 & 0 \\ -\mathcal{K}_{\text{asym}} & 1 \end{bmatrix}, \quad (8)$$

$$\mathbb{T}_i^{\text{RE}} = \sqrt{T_{\text{BS}}}e^{2i\beta_{\text{sag}}}\begin{bmatrix} 1 & 0 \\ -2R_{\text{BS}}\mathcal{K}_{\text{sym}} & 1 \end{bmatrix}, \quad (9)$$

$$\mathbb{T}_p^{\text{RE}} = \sqrt{R_{\text{BS}}}e^{2i\beta_{\text{sag}}}\begin{bmatrix} 1 & 0 \\ 4\mathcal{K}_{\text{arm}} - 2T_{\text{BS}}\mathcal{K}_{\text{sym}} & 1 \end{bmatrix}, \quad (10)$$

with diagonal elements describing the purely optical response (with fixed mirrors position), whereas the lower off-diagonal term, featuring the so called optomechanical coupling factor \mathcal{K} first introduced by Kimble *et al* [27], embraces the details of interaction of mechanical degrees of freedom of the interferometer with the corresponding light field (via radiation pressure). Response of the interferometer to both, differential and common mechanical motion of the mirrors can be written as:

$$\mathbf{t}_d = -e^{i\beta_{\text{sag}}}\frac{\sqrt{2\mathcal{K}_{\text{sym}}}}{x_{\text{SQL}}}\begin{bmatrix} 0 \\ 1 \end{bmatrix}, \quad (11)$$

$$\mathbf{t}_c = ie^{i\beta_{\text{sag}}}\frac{(R_{\text{BS}} - T_{\text{BS}})\sqrt{2\mathcal{K}_{\text{asym}}}}{x_{\text{SQL}}}\begin{bmatrix} 0 \\ 1 \end{bmatrix}, \quad (12)$$

$$\mathbf{t}_d^{\text{RE}} = e^{i\beta_{\text{sag}}}\frac{\sqrt{2R_{\text{BS}}\mathcal{K}_{\text{sym}}}}{x_{\text{SQL}}}\begin{bmatrix} 0 \\ 1 \end{bmatrix}, \quad (13)$$

$$\mathbf{t}_c^{\text{RE}} = -ie^{i\beta_{\text{sag}}}\frac{\sqrt{2R_{\text{BS}}\mathcal{K}_{\text{asym}}}}{x_{\text{SQL}}}\begin{bmatrix} 0 \\ 1 \end{bmatrix}, \quad (14)$$

$$\mathbf{q}_d = \begin{bmatrix} 0 \\ 0 \end{bmatrix}, \quad (15)$$

$$\mathbf{q}_c = -e^{i\beta_{\text{sag}}}\frac{2\sqrt{2R_{\text{BS}}T_{\text{BS}}\mathcal{K}_{\text{asym}}}}{x_{\text{SQL}}}\begin{bmatrix} 0 \\ 1 \end{bmatrix}, \quad (16)$$

where $\beta_{\text{sag}} = 2\beta_{\text{arm}} + \frac{\pi}{2}$ is the Sagnac-specific additional phase shift that signal sidebands at frequency Ω

acquire in the course of propagation through the interferometer. $x_{\text{SQL}} = \sqrt{\frac{2\hbar}{M\Omega^2}}$ stands for the free mass displacement standard quantum limit (SQL). Symmetric and asymmetric optomechanical coupling factors of imperfect Sagnac interferometer are defined the same way as in [21]:

$$\mathcal{K}_{\text{sym}} = 4\mathcal{K}_{\text{arm}}\sin^2\beta_{\text{arm}} \simeq \frac{8\Theta_{\text{arm}}\gamma_{\text{arm}}}{(\Omega^2 + \gamma_{\text{arm}}^2)^2}, \quad (17)$$

$$\mathcal{K}_{\text{asym}} = 4\mathcal{K}_{\text{arm}}\cos^2\beta_{\text{arm}} \simeq \frac{8\Theta_{\text{arm}}\gamma_{\text{arm}}^3}{\Omega^2(\Omega^2 + \gamma_{\text{arm}}^2)^2}. \quad (18)$$

with $\beta_{\text{arm}} = \arctan\frac{\Omega}{\gamma_{\text{arm}}}$ the phase shift acquired by a sideband field in one arm cavity. $\gamma_{\text{arm}} = \frac{cT_{\text{ITM}}}{4L}$ is the half-bandwidth of the arm cavities with length L and input mirror power transmissivity T_{ITM} .

$\mathcal{K}_{\text{arm}} = \frac{2\Theta\gamma_{\text{arm}}}{\Omega^2(\gamma_{\text{arm}}^2 + \Omega^2)}$ is the optomechanical coupling factor of this arm with $\Theta = \frac{4\omega_p P_{\text{arm}}}{McL}$ the normalised

power, where P_{arm} is the circulating in each arm of an equivalent Michelson, M is the reduced mass of the dARM mode and L is the length of the arm. Note that $\mathcal{K}_{\text{sym}} + \mathcal{K}_{\text{asym}} = 4\mathcal{K}_{\text{arm}}$, which will be used later.

2.3. Balanced homodyne readout

One sees that asymmetry of the BS couples a fraction of pump laser light to the DP of the interferometer. This creates a non-zero DC component of the signal light (i.e. a component at the carrier frequency) that can be easily obtained from the I/O-relations above if one sets $\Omega \rightarrow 0$ and $\mathcal{K}_{\text{arm}} \rightarrow 0$,

$$\mathbf{O} = (R_{\text{BS}} - T_{\text{BS}})\mathbf{P}, \quad (19)$$

where the corresponding DC fields are expressed in terms of pump field at the main BS, \mathbf{P} . Analogously, one can derive the DC component of the LO beam for all three choices of the LO.

- (i) $\mathbf{L}_{\text{dir}} \propto \mathbf{P}$ for the direct LO option;
- (ii) $\mathbf{L}_{\text{AR}} \propto \mathbf{B}^{\text{RE}} \propto \sqrt{R_{\text{BS}}}\mathbf{P}$ for the BS AR coating reflection LO option;
- (iii) $\mathbf{L}_{\text{co}} \propto \mathbf{Q} \propto -2\sqrt{R_{\text{BS}}T_{\text{BS}}}\mathbf{P}$ for the *co-moving* LO option;

As shown in [29, 30], the fluctuation part of the readout photocurrent of the balanced homodyne detector is proportional to a sum of following terms:

$$I_{\text{HD}} \propto \hat{\mathbf{o}}^\dagger \mathbb{H} \hat{\mathbf{L}} + \mathbf{O}^T \mathbb{H} \hat{\mathbf{L}}, \quad (20)$$

where

$$\mathbb{H} = \begin{bmatrix} \cos \phi & -\sin \phi \\ \sin \phi & \cos \phi \end{bmatrix}, \quad (21)$$

with ϕ defining the homodyne angle. $\hat{\mathbf{L}}$ stands for the noise fields of the LO. For $\phi = \pi/2$ (phase quadrature readout), the photocurrent can be further simplified as

$$I_{\text{HD}} \propto |\mathbf{L}| \hat{o}_s - |\mathbf{O}| \hat{l}_s, \quad (22)$$

The potential of noise cancellation can be readily seen from this expression, for the phase noise in the two optical paths comes from the same source, i.e. from the pump laser. Following we continue to demonstrate how the quantum noise cancellation is tailored by properly choosing the LO delivery port. The $\hat{\mathbf{L}}$ field for three choices of the LO we consider here can be written along the same lines as corresponding classical amplitudes of the LO \mathbf{L} :

- (i) $\hat{\mathbf{l}}_{\text{dir}} \propto \hat{\mathbf{p}}$ for the direct LO option;
- (ii) $\hat{\mathbf{l}}_{\text{AR}} \propto \hat{\mathbf{b}}^{\text{RE}}$ for the BS AR coating reflection LO option;
- (iii) $\hat{\mathbf{l}}_{\text{co}} \propto \hat{\mathbf{q}}$ for the *co-moving* LO option.

At low frequencies, the main contribution to the quantum noise comes from the off-diagonal radiation pressure term in the transfer matrices, as \mathcal{K}_{arm} and $\mathcal{K}_{\text{asym}}$ both rise steeply as $\Omega \rightarrow 0$. Indeed, we substitute equations (2), (3) into equation (20), leaving only the leading terms, one can get the low-frequency contribution to the readout photocurrent from BP for the *co-moving* LO option the following expression:

$$I_{\text{co}}^{\text{BP}} \propto \mathcal{I}_{\text{co}}[(4\mathcal{K}_{\text{arm}} - \mathcal{K}_{\text{asym}})\sin \phi - 2\cos \phi] \hat{p}_c = \mathcal{I}_{\text{co}}[\mathcal{K}_{\text{sym}}\sin \phi - 2\cos \phi] \hat{p}_c. \quad (23)$$

Similarly, for BSAR LO option one can get:

$$I_{\text{BSAR}}^{\text{BP}} \propto \mathcal{I}_{\text{BSAR}}[\mathcal{K}_{\text{sym}}\sin \phi - 2\cos \phi] \hat{p}_c, \quad (24)$$

where

$$\mathcal{I}_{\text{co}} = 2\sqrt{R_{\text{BS}}T_{\text{BS}}}(R_{\text{BS}} - T_{\text{BS}})e^{2i\beta_{\text{sag}}|\mathbf{P}|}, \quad (25)$$

$$\mathcal{I}_{\text{BSAR}} = 2\sqrt{R_{\text{BS}}T_{\text{BS}}}(T_{\text{BS}} - R_{\text{BS}})e^{2i\beta_{\text{sag}}|\mathbf{P}|}. \quad (26)$$

With homodyne angle $\phi = \pi/2$, we simply have

$$I^{\text{BP}} \propto \mathcal{K}_{\text{sym}} \hat{p}_c, \quad (27)$$

for both the *co-moving* LO and the LO derived from the BSAR coating reflection. This expression shows partial cancellation of steep low-frequency dependence and only the *speed-metre-like* term remains, which manifests in flat low-frequency dependence. This remaining term, as we discuss later, stems from the differential back-action force driven by the BP amplitude fluctuations represented by a cosine quadrature operator \hat{p}_c . Even though, since this remaining term is proportional to $|R_{\text{BS}} - T_{\text{BS}}|$ which refers to the beam splitter asymmetry, as shown in equations (25), (26), its contribution is always much smaller than the quantum noise contribution from DP in terms of any realistic beam splitter imbalance. However, for LO derived directly from main laser, the expression has no radiation pressure related contribution in the second term in equation (20), hence

$$I_{\text{dir}}^{\text{BP}} \propto \mathcal{K}_{\text{arm}} \hat{p}_c, \quad (28)$$

and the contribution from the BP-driven common motion of the interferometer mirrors remains uncompensated.

The physics behind this cancellation stems from the very principle of the balanced homodyne readout, where any fluctuations and variations of light that drive both, the LO and the signal light in the same way, are cancelled by design. Hence the partial cancellation of quantum noise that we demonstrated above comes from this insensitivity to the common phase signal produced by the common part of the radiation pressure force, created by the BP fluctuations $\hat{\mathbf{p}}$, i.e. $\hat{F}_c^{\text{r.p.}} = (\hat{F}_n^{\text{r.p.}} + \hat{F}_e^{\text{r.p.}})/2$ where $\hat{F}_{e,n}^{\text{r.p.}}$ stand for radiation pressure forces in each of the arms. The remaining uncompensated part stems from the non-zero differential radiation pressure force, $\hat{F}_d^{\text{r.p.}} = (\hat{F}_n^{\text{r.p.}} - \hat{F}_e^{\text{r.p.}})/2$, ensuing from the imbalance of the amplitudes of the reflected and transmitted light at the asymmetric main beam-splitter.

2.4. Quantum noise limited sensitivity of Sagnac interferometer with BP noise cancellation

It is straightforward now to calculate the QNLS power spectral density expressions for all three choices of LO, using the derived earlier I/O-relations for both, the BP and the DP of the interferometer. It requires knowing the transfer matrices of the BHD photocurrent in all three considered schemes on the input fluctuation fields, $\hat{\mathbf{i}}$ and $\hat{\mathbf{p}}$. In order to simplify the equation, the rotation matrix \mathbb{H} is absorbed into \mathbf{L} and \mathbf{O} . After expressing the LO fluctuations field, $\hat{\mathbf{I}}$, in terms of $\hat{\mathbf{i}}$ and $\hat{\mathbf{p}}$ one gets from (20):

$$\hat{\mathbf{I}}_{\text{dir}} \propto \mathbf{L}_{\text{dir}}^{\text{T}} \mathbb{T}_i \hat{\mathbf{i}} + (\mathbf{L}_{\text{dir}}^{\text{T}} \mathbb{T}_p + \mathbf{O}^{\text{T}}) \hat{\mathbf{p}} + t_d^{\text{dir}} x_d + t_c^{\text{dir}} x_c, \quad (29)$$

$$\hat{\mathbf{I}}_{\text{co}} \propto (\mathbf{L}_{\text{co}}^{\text{T}} \mathbb{T}_i + \mathbf{O}^{\text{T}} \mathbb{R}_i) \hat{\mathbf{i}} + (\mathbf{L}_{\text{co}}^{\text{T}} \mathbb{T}_p + \mathbf{O}^{\text{T}} \mathbb{R}_p) \hat{\mathbf{p}} + t_d^{\text{co}} x_d + t_c^{\text{co}} x_c, \quad (30)$$

$$\hat{\mathbf{I}}_{\text{BS,AR}} \propto (\mathbf{L}_{\text{AR}}^{\text{T}} \mathbb{T}_i + \mathbf{O}^{\text{T}} \mathbb{T}_i^{\text{RE}}) \hat{\mathbf{i}} + (\mathbf{L}_{\text{AR}}^{\text{T}} \mathbb{T}_p + \mathbf{O}^{\text{T}} \mathbb{T}_p^{\text{RE}}) \hat{\mathbf{p}} + t_d^{\text{AR}} x_d + t_c^{\text{AR}} x_c, \quad (31)$$

where the last two terms stand for the signal part of the BHD photocurrent caused by the differential and common signal motion of the mirrors, respectively. For the general case of arbitrary homodyne angle, ϕ_{LO} , the corresponding expressions for the dARM and cARM responses in all three cases read:

$$t_d^{\text{dir}} = \text{ie}^{i\beta_{\text{sag}}} \frac{\sqrt{2\mathcal{K}_{\text{sym}}}}{x_{\text{SQL}}} \sin \phi_{\text{LO}}, \quad t_c^{\text{dir}} = \text{e}^{i\beta_{\text{sag}}} (R_{\text{BS}} - T_{\text{BS}}) \frac{\sqrt{2\mathcal{K}_{\text{asym}}}}{x_{\text{SQL}}} \sin \phi_{\text{LO}}, \quad (32)$$

$$t_d^{\text{co}} = \text{ie}^{i\beta_{\text{sag}}} \frac{\sqrt{8R_{\text{BS}} T_{\text{BS}} \mathcal{K}_{\text{sym}}}}{x_{\text{SQL}}} \sin \phi_{\text{LO}}, \quad t_c^{\text{co}} = 0, \quad (33)$$

$$t_d^{\text{AR}} = \text{ie}^{i\beta_{\text{sag}}} \frac{\sqrt{8R_{\text{BS}} (T_{\text{BS}})^2 \mathcal{K}_{\text{sym}}}}{x_{\text{SQL}}} \sin \phi_{\text{LO}}, \quad t_c^{\text{AR}} = 0. \quad (34)$$

Note that for the *co-moving* LO and for the BS AR-coating reflected LO there is an additional advantage of zero sensitivity to the common motion of the arms (cARM degree of freedom). It cuts off the potential coupling of noise from the much loosely controlled cARM degree of freedom into the readout channel of the Sagnac interferometer. Finally, one can calculate the QNLS power spectral density of a Sagnac interferometer, in the units of differential displacement of the arms using the following well-known general formula:

$$S_{\text{LO option}}^x = \frac{\langle \text{in} | \hat{I}_{\text{LO option}}(\Omega) \circ \hat{I}_{\text{LO option}}(\Omega') | \text{in} \rangle}{|t_{\text{LO option}}|^2}. \quad (35)$$

The general formula reads:

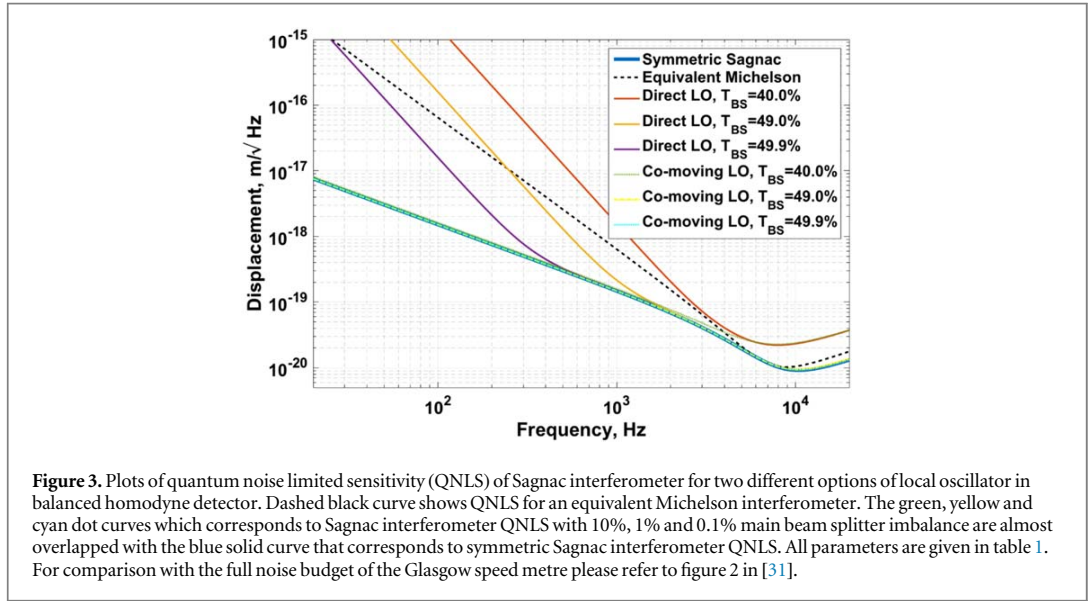
$$\begin{aligned} S_{\text{co}}^x(\Omega) &= S_{\text{DP,co}}^x + S_{\text{BP,co}}^x + S_{\text{PO,co}}^x \\ &= \frac{(\mathbf{L}^{\text{T}} \mathbb{T}_i + \mathbf{O}^{\text{T}} \mathbb{R}_i) \mathbb{S}^i (\mathbb{T}_i^{\dagger} \mathbf{L} + \mathbb{R}_i^{\dagger} \mathbf{O})}{|\mathbf{L}^{\text{T}} \mathbf{t}_d|^2} + \frac{(\mathbf{L}^{\text{T}} \mathbb{T}_p + \mathbf{O}^{\text{T}} \mathbb{R}_p) \mathbb{S}^p (\mathbb{T}_p^{\dagger} \mathbf{L} + \mathbb{R}_p^{\dagger} \mathbf{O})}{|\mathbf{L}^{\text{T}} \mathbf{t}_d|^2} + \frac{T_p \mathbf{O}^{\text{T}} \mathbf{O}}{|\mathbf{L}^{\text{T}} \mathbf{t}_d|^2}, \end{aligned} \quad (36)$$

where we assumed that the power reflectivity/transmissivity of the pick-off beam splitter is equal to R_p/T_p and there is an additional noise term, S_{PO}^x due to vacuum fields, entering the open port of this beam splitter. Here \mathbb{S}^a is the spectral density matrix for the input light $\hat{\mathbf{a}}(\Omega)$, defined as

$$2\pi S_{ij}^a(\Omega) \delta(\Omega - \Omega') = \langle \text{vac} | \hat{a}_i(\Omega) \circ \hat{a}_j^{\dagger}(\Omega') | \text{vac} \rangle, \quad (37)$$

where averaging goes over the vacuum quantum state of light $|\text{vac}\rangle$ and $\{i, j\} = \{c, s\}$. Substitution of (5) and (11) gives for the components of the QNLS the following formulae:

$$S_{\text{DP,co}}^x = \frac{x_{\text{SQL}}^2}{2} \frac{1 + [\mathcal{K}_{\text{sym}}^* - (8R_{\text{BS}} T_{\text{BS}} - 1) \cot \phi_{\text{LO}}]^2}{\mathcal{K}_{\text{sym}}^*}, \quad (38)$$



$$S_{BP,co}^x = \frac{x_{SQL}^2 (R_{BS} - T_{BS})^2 [\mathcal{K}_{sym} - 2 \cot \phi_{LO}]^2}{2 \mathcal{K}_{sym}}, \quad (39)$$

$$S_{PO,co}^x = \frac{x_{SQL}^2 T_p (R_{BS} - T_{BS})^2}{2 R_p \mathcal{K}_{sym}^* \sin^2 \phi_{LO}}, \quad (40)$$

where $\mathcal{K}_{sym}^* = 4R_{BS} T_{BS} \mathcal{K}_{sym}$ is the new effective optomechanical coupling factor with account for BS asymmetry. The suppression of noise due to the double measurement scheme of the SSM and BHD, the *speedmeter frequency dependence* of the quantum noise at low frequencies, is seen in figure 3.

3. Relative laser intensity noise requirement

The direct implication of suppression of laser noise contribution to the QNLS, discussed earlier and shown in figure 3, is the much relaxed relative laser intensity noise (RIN) requirements, ensuing from the significantly weakened transfer function from BP amplitude quadrature to the BHD readout following from the equations (27) and (28).

In this section, we consider as an example the SSM proof-of-principle experiment being built in the University of Glasgow [31]. Due to the complexity of the instrument, we have eschewed analytical calculation in favour of the numerical, using FINESSE [24] to simulate the RIN requirement. This is done by simulating the quantum noise at the BHD detection port, finding the transfer function of input laser power noise at the BP to detection port, and dividing quantum noise by the transfer function then by the input laser power.

The transfer functions from the input laser amplitude fluctuations to the BHD readout port with homodyne angle $\pi/2$ and $\pi/4$ are shown in figure 4. And the main beam-splitter asymmetry is characterised by setting $R_{BS} = 0.501$. As we can see, the transfer functions for *co-moving* and BSAR LO options are significantly weakened compared to the main laser LO option in low frequency for both homodyne angles. Another feature that we notice is the difference between the two readout quadratures in high frequency for three LO options. That can be understood from the equation (27), since for phase quadrature readout, the transfer function of the amplitude quadrature noise is just proportional to \mathcal{K}_{sym} , which decrease in high frequency according to equation (17). However, on an alternative homodyne angle as shown in equation (23) and (24), the amplitude noise gets coupled to the readout constantly and dominates in high frequency. From the two equations, we can also understand the dip at a specific frequency that indicates a cancellation between the frequency dependent back action noise and the constantly coupled amplitude noise for the case $\phi = \frac{\pi}{4}$. We note that the gap between *co-moving* LO option and BSAR LO option comes from the relatively weak LO power from BSAR as shown in table 1. In this experimental set up, the power of the laser we use is 1.7 W and the AR reflection is 100 ppm. So that the presentation for BSAR option here is only on the state of principle illustration but not for realistic implementation for this experiment.

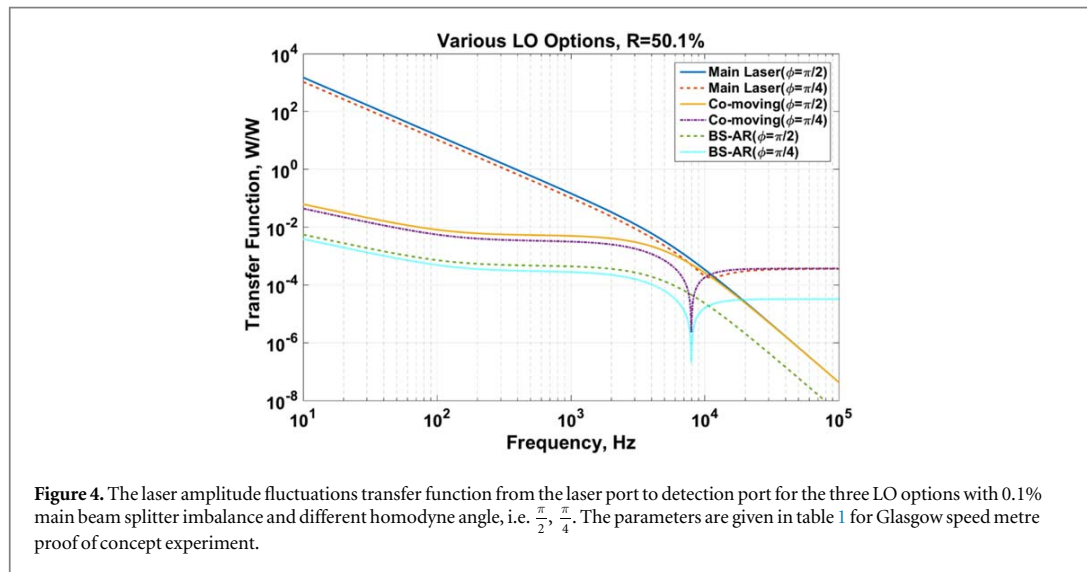
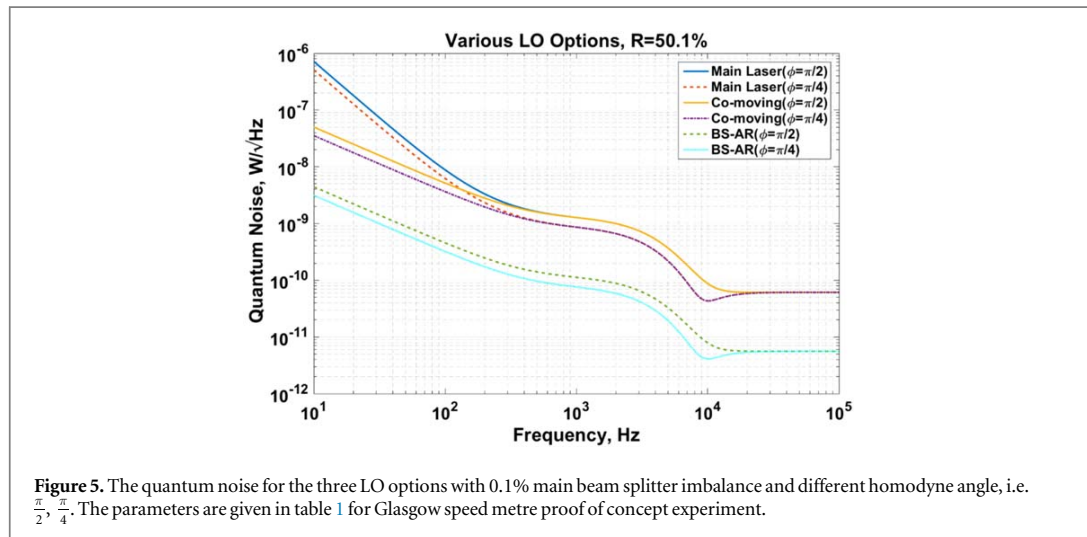
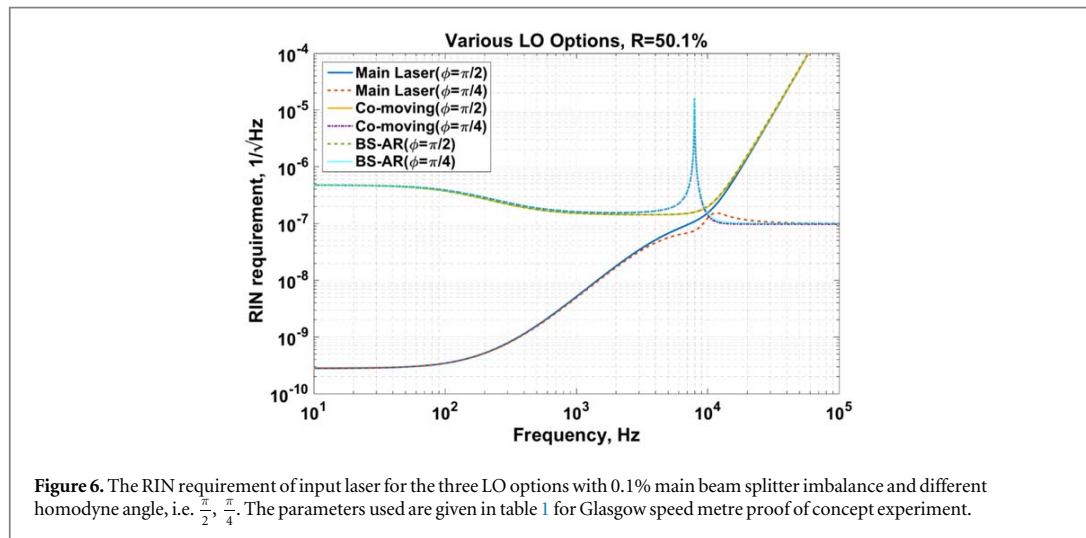


Table 1. Parameters of the Glasgow SSM experiment.

Parameter	Value
Arm cavity length L	1.3 m
Optical power P	1.7 W at beam splitter, ~ 1 kW in the arms
Arm cavity round trip loss	≤ 25 ppm
Optic mass m	Arm cavity input test mass (ITM) 860 mg, arm cavity end test mass (ETM) 100 g
Transmissivities T and reflectivities R	Central beamsplitter, $R_{BS} = T_{BS} = 0.5$, ITM, $T_{ITM} = 700$ ppm
Main Laser LO and <i>co-moving</i> LO power	10 mW
BSAR LO power	0.078 mW
Main readout	Balanced homodyne detector with suspended optical local oscillator path



The figure 5 shows the quantum noise for the three LO options with different readout quadratures. Figure 6 shows the RIN requirement. As expected, the RIN requirement get relaxed by three orders of magnitude below 100 Hz by selecting co-moving or BSAR LO options.



4. Summary

Speed-metre configurations of GW interferometers are known to provide a significant improvement of quantum noise limited sensitivity at low frequencies because by suppression of quantum back-action noise using QND measurement of speed [28, 32]. This advantage increases the signal-to-noise ratio (SNR) of speed-metre-based GW detectors for compact binary coalescences by at least two orders of magnitude if compared to the equivalent Michelson interferometer in the quantum-noise-limited case [33]. Zero-area Sagnac interferometer is one of the possible ways to realise the GWD based on speed-metre principle. However it was shown [21] that, in a non-ideal realistic case of asymmetric beam splitter, the fluctuations of the laser pump couple into the readout port of the interferometer, thereby creating an excess radiation pressure noise that significantly worsens the QNLS of speed metre interferometer and hence its SNR. In this work, we demonstrate that using a balanced homodyne readout scheme with a particular choice of the LO option this detrimental effect can be almost completely attenuated.

Picking the LO beam from the reflected light at the pumping port of the interferometer (the *co-moving* LO option), or from the direct reflection off the main beam splitter's AR coating (the BSAR LO option), one can significantly reduce the magnitude of the transfer function of the laser fluctuations from the pumping port to the readout one and qualitatively change its frequency dependence at low frequencies. We show analytically that this partial cancellation of laser fluctuations stems from the very nature of the BHD scheme that is inherently insensitive to any common variations of light phase in LO and signal beam of the BHD driven by input laser fluctuations. We further confirm our analytical findings by numerical simulation of the Glasgow proof-of-principle speed-metre interferometer set-up and estimating the relative laser intensity noise requirements for it. Our simulation shows that at frequency of 100 Hz the RIN decreases by 3 orders of magnitude, from $4 \times 10^{-10}/\sqrt{\text{Hz}}$ to $4 \times 10^{-7}/\sqrt{\text{Hz}}$ if the *co-moving* or BSAR LO option is chosen versus the conventional *direct* pick-off of the LO beam from the main laser. It is worth noting here that these 3 orders of magnitude mean reducing the RIN requirement from a very challenging value which is beyond the best achieved so far [34–36] to a value which is easily achievable.

This feature of Sagnac interferometer can, in principle, be expanded to any scheme of speed-metre interferometer that uses the Sagnac-type way of performing the velocity measurement, where signal sidebands co-propagate with the carrier light throughout the main interferometer, including the polarisation-based speed metres [15, 16, 33]. Hence, we report here the method that solves the challenges originating from beam splitter asymmetry of a real speed-metre interferometer setup by using a balanced homodyne readout scheme with a particular choice of a LO beam.

Acknowledgments

The authors are very grateful to our colleagues from the LIGO-Virgo Scientific Collaboration (LVC) for illuminating discussions and invaluable feedback on the research presented in this paper. TZ, SS, PD, JSH, EAH, SSL, SH and SLD were supported by the European Research Council (ERC- 2012-StG: 307245). SLD was supported by the Lower Saxonian Ministry of Science and Culture within the frame of Research Line

(Forschungslinie) QUANOMET Quantum- and Nano-Metrology. The work of EK and FYK was supported by the Russian Foundation for Basic Research Grants 14-02-00399 and 16-52-10069. FYK was also supported by the LIGO NSF Grant PHY-1305863. SS was supported by the European Commission Horizon 2020 Marie-Skodowska-Curie IF Actions, grant agreement 658366. PD, JB were supported by STFC consolidated grant, ST/N005422/1.

ORCID iDs

E Knyazev  <https://orcid.org/0000-0002-9621-5967>

A S Bell  <https://orcid.org/0000-0003-1523-0821>

S L Danilishin  <https://orcid.org/0000-0001-7758-7493>

References

- [1] Abbott B P *et al* 2016 Observation of gravitational waves from a binary black hole merger *Phys. Rev. Lett.* **116** 061102
- [2] Abbott B P *et al* 2016 Gw151226: observation of gravitational waves from a 22-solar-mass binary black hole coalescence *Phys. Rev. Lett.* **116** 241103
- [3] Abbott B P *et al* 2017 Gw170104: observation of a 50-solar-mass binary black hole coalescence at redshift 0.2 *Phys. Rev. Lett.* **118** 221101
- [4] Abbott B P *et al* 2017 GW170814: a three-detector observation of gravitational waves from a binary black hole coalescence *Phys. Rev. Lett.* **119** 141101
- [5] Abbott B P *et al* 2017 GW170608: observation of a 19 solar-mass binary black hole coalescence *Astrophys. J. Lett.* **851** L35
- [6] Abbott B P *et al* 2017 GW170817: observation of gravitational waves from a binary neutron star inspiral *Phys. Rev. Lett.* **119** 161101
- [7] Abbott B P *et al* 2017 Multi-messenger observations of a binary neutron star merger *Astrophys. J. Lett.* **848** L12
- [8] Harry G M and (The LIGO Scientific Collaboration) 2010 Advanced LIGO: the next generation of gravitational wave detectors *Class. Quantum Grav.* **27** 084006
- [9] Abbott B P *et al* 2018 Prospects for observing and localizing gravitational-wave transients with advanced LIGO, advanced Virgo and KAGRA *Living Rev. Relativ.* **21** 3
- [10] Braginsky V B and Khalili F J 1990 Gravitational wave antenna with QND speed meter *Phys. Lett. A* **147** 251–6
- [11] Braginsky V B, Gorodetsky M L, Khalili F Y and Thorne K S 2000 Dual-resonator speed meter for a free test mass *Phys. Rev. D* **61** 044002
- [12] Braginsky V B and Khalili F Y 1996 Quantum nondemolition measurements: the route from toys to tools *Rev. Mod. Phys.* **68** 1–11
- [13] Purdue P and Chen Y 2002 Practical speed meter designs for quantum nondemolition gravitational-wave interferometers *Phys. Rev. D* **66** 122004
- [14] Chen Y 2003 Sagnac interferometer as a speed-meter-type, quantum-nondemolition gravitational-wave detector *Phys. Rev. D* **67** 122004
- [15] Danilishin S L 2004 Sensitivity limitations in optical speed meter topology of gravitational-wave antennas *Phys. Rev. D* **69** 102003
- [16] Wang M, Bond C, Brown D, Brückner F, Carbone L, Palmer R and Freise A 2013 Realistic polarizing sagnac topology with dc readout for the Einstein telescope *Phys. Rev. D* **87** 096008
- [17] Huttner S H *et al* 2017 Candidates for a possible third-generation gravitational wave detector: comparison of ring-Sagnac and sloshing-Sagnac speedmeter interferometers *Class. Quantum Grav.* **34** 024001
- [18] Knyazev E, Danilishin S, Hild S and Khalili F Y 2017 Speedmeter scheme for gravitational-wave detectors based on EPR quantum entanglement *Phys. Lett. A* **382** 2219–25
- [19] Sun K-X, Fejer M M, Gustafson E and Byer R L 1996 Sagnac interferometer for gravitational-wave detection *Phys. Rev. Lett.* **76** 3053–6
- [20] Beyersdorf P T, Fejer M M and Byer R L 1999 Polarization sagnac interferometer with a common-path local oscillator for heterodyne detection *J. Opt. Soc. Am. B* **16** 1354–8
- [21] Danilishin S L, Gräf C, Leavey S S, Hennig J, Houston E A, Pascucci D, Steinlechner S, Wright J and Hild S 2015 Quantum noise of non-ideal Sagnac speed meter interferometer with asymmetries *New J. Phys.* **17** 043031
- [22] Sun K-X, Gustafson E K, Fejer M M and Byer R L 1997 Polarization-based balanced heterodyne detection method in a Sagnac interferometer for precision phase measurement *Opt. Lett.* **22** 1359–61
- [23] Sun K-X, Fejer M M, Gustafson E K and Byer R L 1997 Balanced heterodyne signal extraction in a postmodulated Sagnac interferometer at low frequency *Opt. Lett.* **22** 1485–7
- [24] Freise A, Heinzl G, Lück H, Schilling R, Willke B and Danzmann K 2004 Frequency-domain interferometer simulation with higher-order spatial modes *Class. Quantum Grav.* **21** S1067
- [25] Caves C M and Schumaker B L 1985 New formalism for two-photon quantum optics: I. Quadrature phases and squeezed states *Phys. Rev. A* **31** 3068–92
- [26] Caves C M and Schumaker B L 1985 New formalism for two-photon quantum optics: II. Mathematical foundation and compact notation *Phys. Rev. A* **31** 3093–111
- [27] Kimble H J, Levin Y, Matsko A B, Thorne K S and Vyatchanin S P 2002 Conversion of conventional gravitational-wave interferometers into QND interferometers by modifying their input and/or output optics *Phys. Rev. D* **65** 022002
- [28] Danilishin S L and Khalili F Y 2012 Quantum measurement theory in gravitational-wave detectors *Living Rev. Relativ.* **15** 5
- [29] Steinlechner S *et al* 2015 Local-oscillator noise coupling in balanced homodyne readout for advanced gravitational wave detectors *Phys. Rev. D* **92** 072009
- [30] Zhang T *et al* 2017 Effects of static and dynamic higher-order optical modes in balanced homodyne readout for future gravitational waves detectors *Phys. Rev. D* **95** 062001
- [31] Gräf C *et al* 2014 Design of a speed meter interferometer proof-of-principle experiment *Class. Quantum Grav.* **31** 215009
- [32] Chen Y, Danilishin S L, Khalili F Y and Müller-Ebhardt H 2011 QND measurements for future gravitational-wave detectors *Gen. Relativ. Gravit.* **43** 671–94
- [33] Danilishin S L, Knyazev E, Voronchev N V, Khalili F Y, Gräf C, Steinlechner S, Hennig J-S and Hild S 2018 A new quantum speed-meter interferometer: measuring speed to search for intermediate mass black holes *Light: Sci. Appl.* **7** 11

- [34] Seifert F, Kwee P, Heurs M, Willke B and Danzmann K 2006 Laser power stabilization for second-generation gravitational wave detectors *Opt. Lett.* **31** 2000–2
- [35] Kwee P, Willke B and Danzmann K 2011 New concepts and results in laser power stabilization *Appl. Phys. B* **102** 515–22
- [36] Junker J, Oppermann P and Willke B 2017 Shot-noise-limited laser power stabilization for the AEI 10 m prototype interferometer prototype interferometer *Opt. Lett.* **42** 755–8

Chapter 6

On the misalignment and alignment of Sagnac speed meter interferometer

Speed meter configurations are much more complicated compared with conventional Michelson interferometer. Practically, they face the challenges of more possible imperfections due to the complexities of the configurations. Danalishin made the analyses on the main beam splitter asymmetric and intra cavity loss in plane wave mode profile [69]. With further analysis, the negative effect of beamsplitter asymmetric can be mostly compensated by choosing a special LO beam in balanced homodyne readout [49], which is introduced in Chapter. 5.

Up to now, there are few investigations on the effects of the speed meter internal misalignment with higher optical modes (HOMs) taken into account. To achieve optimal sensitivity of the interferometer detector, usually several independent length degrees of freedom need to be controlled within small ranges to maintain the operating point. It is also essential to keep the angular degrees of freedom of the cavity mirrors on their operating points to maintain the maximum power, reduce the optical loss and reduce the loss, reduce jitter noise and other technical noise couplings [70]. Due to the very low loss requirements of the ERC proof of concept speed meter experiment (stemming from realising a speed meter using only a meter scale baseline), very good alignment control is vital for this experiment.

This chapter is around the misalignment and alignment of Sagnac speed meter. In Sec.6.1, I review the Sagnac speed meter input output (I/O) relations in plane wave mode profile; In sec. 6.2, I describe the general I/O relation of misaligned optics; In Sec. 6.3, I calculate the impacts of misalignments from several typical optical components in the Sagnac interferometer on the quantum noise limited sensitivity; In Sec. 6.4, I use the Glasgow SSM experiment optical layout as an example to propose possible auto-alignment sensing and control strategies based on simulation software, *Finesse* [67].

6.1 Sagnac interferometer in plane wave mode profile

Before stepping into the Hermite-Gauss profile, I remind the reader of the of the standard tools for calculations of quantum noise, i.e. I/O relations and the two-photon formalism. Defining the input field a and output field b , the I/O relations for an interferometer can be written in the form of

$$b = \mathbb{T}a + \mathbf{R} \frac{x}{x_{\text{SQL}}}, \quad (6.1)$$

where \mathbb{T} is the interferometer transfer matrix, \mathbf{R} is the interferometer response vector for the test mass displacement, $x_{\text{SQL}} = \sqrt{\frac{2\hbar}{M\Omega^2}}$ is the the standard quantum limit for the square root of the single-side spectral density of test mass displacement $x(\Omega)$ with corresponding effective mode mass M . Using a balanced homodyne readout (see Chapter. 3,4,??) it is possible to realise reading out any arbitrary readout quadrature. [56, 67]. I introduce the local oscillator classical field as L . The quantum noise spectral density can then be calculated as

$$S_x = x_{\text{SQL}}^2 \frac{L^T \mathbb{H}^\dagger \mathbb{T} S_a \mathbb{T}^\dagger \mathbb{H} L}{|\mathbf{L}^T \mathbb{H} \mathbf{R}|^2}. \quad (6.2)$$

where the homodyne angle is quantified by one rotation matrix \mathbb{H} ,

$$\mathbb{H} = \begin{bmatrix} \cos \Phi & -\sin \Phi \\ \sin \Phi & \cos \Phi \end{bmatrix}. \quad (6.3)$$

And S_a is the spectral density matrix of the input field.

In a Sagnac speed meter interferometer, there are two fields that travel through each of the arm cavities in opposing directions (see Fig. 1.7 or Fig. 1 in Chapter. 5). In either cavity, both circulating modes contribute to the radiation pressure force. The I/O relation of an cavity in Sagnac interferometer, e.g. for the clockwise output of cavity N can be calculated as

$$b_{RN} = \underbrace{e^{2i\beta(\Omega)} \begin{bmatrix} 1 & 0 \\ -2R_{BS}\mathcal{K} & 1 \end{bmatrix}}_{\mathbb{T}_{RN}^{\text{arm}}} a_{RN} + \underbrace{e^{2i\beta(\Omega)} \begin{bmatrix} 0 & 0 \\ -2\sqrt{R_{BS}T_{BS}}\mathcal{K} & 0 \end{bmatrix}}_{\mathbb{T}_{LN}^{b,a}} a_{LN} + \underbrace{e^{i\beta(\Omega)} \begin{bmatrix} 0 \\ \sqrt{4R_{BS}\mathcal{K}} \end{bmatrix}}_{\mathbf{R}_{RN}^{\text{arm}}} \frac{\sqrt{2}x}{x_{\text{SQL}}}, \quad (6.4)$$

where the index ‘R’ represent the clockwise propagating light fields and the index ‘L’ represents the anti-clockwise direction. \mathcal{K} is the optomechanical Kimble factor, which is defined

as

$$\mathcal{K} = \frac{2\Theta\gamma}{\Omega^2(\gamma^2 + \Omega^2)}, \quad (6.5)$$

where $\gamma = \frac{cT}{4L}$ is the half-bandwidth of the cavities with cavity length L and the input test mass power transmittivity T , $\Theta \equiv \frac{4\omega P}{McL}$ is the normalised circulating power in the arm, P is the circulating power in the cavity in one direction, M is the effective mass of the interferometer differential arm elongation modes (dARM) mode. $\beta = \arctan\left(\frac{\Omega}{\gamma}\right)$ is the phase shift that the sidebands with frequency Ω acquire when propagating through and then reflecting off the cavity.

The beam splitter relations can be introduced as

$$\begin{aligned} a_{LE} &= -\sqrt{R_{BS}}i + \sqrt{T_{BS}}p, \\ a_{RN} &= \sqrt{T_{BS}}i + \sqrt{R_{BS}}p, \end{aligned} \quad (6.6)$$

where the dark port and bright port inputs are represented by i and p , respectively. The cavities connection relations are defined as:

$$\begin{aligned} a_{RE} &= b_{RN}, \\ a_{LN} &= b_{LE}. \end{aligned} \quad (6.7)$$

In the detuning-less case (*i.e.* the carrier fields are resonant in the arm cavities), the two output fields from two cavities that recombine at the beam splitter can be solved out as [69]

$$\begin{aligned} b_{LN} &= \mathbb{T}_{LN}^{\text{arm}} \left[\mathbb{T}_{RE}^{b,a} \mathcal{F}_{RN} + \mathcal{F}_{LE} \right] + \mathcal{F}_{LN}, \\ b_{RE} &= \mathbb{T}_{RE}^{\text{arm}} \left[\mathcal{F}_{RN} + \mathbb{T}_{LN}^{b,a} \mathcal{F}_{LE} \right] + \mathcal{F}_{RE}, \end{aligned} \quad (6.8)$$

where

$$\begin{aligned} \mathcal{F}_{LN} &= \mathbb{T}_{RN}^{b,a} a_{RN} + \mathbf{R}_{LN}^{\text{arm}} \frac{x_N}{x_{\text{SQL}}}, \quad \mathcal{F}_{RN} = \mathbb{T}_{RN}^{\text{arm}} a_{RN} + \mathbf{R}_{RN}^{\text{arm}} \frac{x_N}{x_{\text{SQL}}}, \\ \mathcal{F}_{LE} &= \mathbb{T}_{LE}^{\text{arm}} a_{LE} + \mathbf{R}_{LE}^{\text{arm}} \frac{x_E}{x_{\text{SQL}}}, \quad \mathcal{F}_{RE} = \mathbb{T}_{RE}^{b,a} a_{RE} + \mathbf{R}_{RE}^{\text{arm}} \frac{x_E}{x_{\text{SQL}}}. \end{aligned} \quad (6.9)$$

The dark port and bright port output fields can be written as

$$\begin{aligned} o &= -\sqrt{R_{BS}}b_{RE} + \sqrt{T_{BS}}b_{LN}, \\ q &= \sqrt{T_{BS}}b_{RE} + \sqrt{R_{BS}}b_{LN}, \end{aligned} \quad (6.10)$$

where I define the dark port and bright port output fields as o and q , respectively. Finally,

the dark and bright port output fields can be solved out in the form of

$$\begin{aligned} o &= \mathbb{T}_i i + \mathbb{T}_p p + \mathbf{t}_- x_- + \mathbf{t}_+ x_+ . \\ q &= \mathbb{R}_i i + \mathbb{R}_p p + \mathbf{q}_- x_- + \mathbf{q}_+ x_+ . \end{aligned} \quad (6.11)$$

The response vector for the common motion and differential motion of the two arm cavities are defined as \mathbf{t}_+ and \mathbf{t}_- at dark port and \mathbf{q}_+ and \mathbf{q}_- at bright port. The common and differential motions are defined as

$$\begin{aligned} x_+ &= x_N + x_E , \\ x_- &= x_N - x_E . \end{aligned} \quad (6.12)$$

In the case of perfectly symmetric Sagnac,

$$\mathbb{T}_i = e^{2i\beta_{\text{sag}}} \begin{bmatrix} 1 & 0 \\ -\mathcal{K}_{\text{sag}} & 1 \end{bmatrix} , \quad (6.13)$$

$$\mathbf{t}_- = -e^{i\beta_{\text{sag}}} \frac{\sqrt{2\mathcal{K}_{\text{sag}}}}{x_{\text{SQL}}} \begin{bmatrix} 0 \\ 1 \end{bmatrix} , \quad (6.14)$$

where $\beta_{\text{sag}} = 2\beta + \frac{\pi}{2}$ and $\mathcal{K}_{\text{sag}} = 4\mathcal{K} \sin^2 \beta$. Since in the perfectly symmetric case, there is no coupling between bright port input and dark port output and no coupling of common mode displacement at the dark port, \mathbb{T}_p and \mathbf{t}_+ are empty. Then the quantum noise spectral density can be derived straightforwardly according to Eq. 6.2.

6.2 I/O relations for misaligned optics

In this section, I provide the mathematical description for considering the misalignments that occur in the interferometer by describing the I/O relations of misaligned optics. Misalignments create the coupling between the fundamental mode and HOMs, which can be described by complex coupling coefficients [71][63]. In order to compatible with the I/O relations in two-photo formalism, I represent these coefficients in matrix format. A traveling beam a contains multimode components, a^i , where the fundamental mode is named as a^0 . After misalignment, the field a' in new spatial modes can be expressed as

$$\begin{bmatrix} a'^0 \\ a'^1 \\ \vdots \end{bmatrix} = \underbrace{\begin{bmatrix} \mathbb{M}^{00} & \mathbb{M}^{01} & \dots \\ \mathbb{M}^{10} & \mathbb{M}^{11} & \dots \\ \vdots & \vdots & \ddots \end{bmatrix}}_{\mathbb{M}} \begin{bmatrix} a^0 \\ a^1 \\ \vdots \end{bmatrix} \quad (6.15)$$

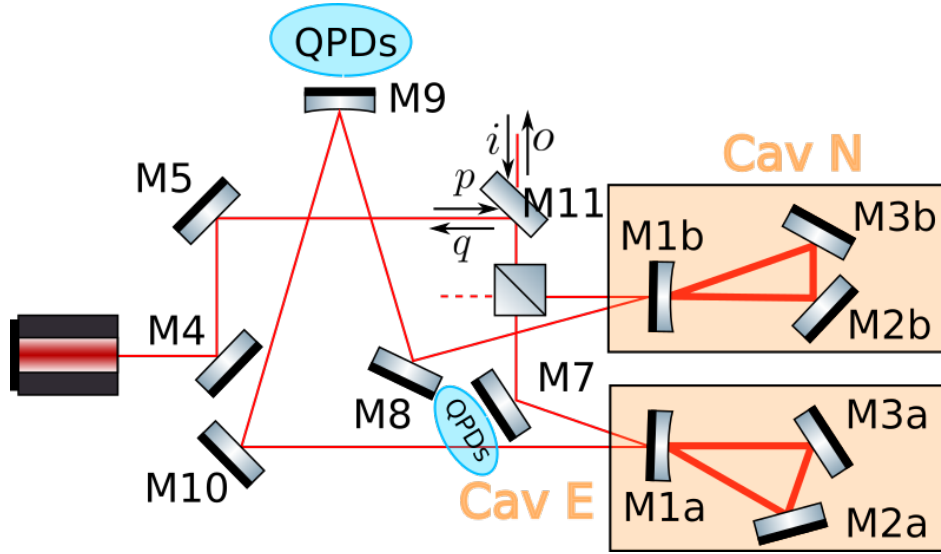


Figure 6.1: Simplified diagram of optical layout of the Glasgow Sagnac speed meter proof of concept experiment. The detailed optical layout is shown in Fig. 2.2 (chapter 2). In addition, the positions of the sets of quadrant photodiodes (QODs) for the purpose of alignment sensing are indicated by blue ellipse. ‘Cav’ represents cavity, ‘M’ represents mirror, i and p are the input fields of dark and bright port; o and q are the output fields of dark and bright ports.

where the matrix \mathbb{M}^{kj} describes how the j -th mode of the a field contributes to the k -th mode of the a' field. Each \mathbb{M}^{kj} is a 2×2 matrix. And the whole matrix \mathbb{M} needs to satisfy the unitarity relation $\mathbb{M}^\dagger \mathbb{M} = \mathbb{I}$, as a consequence of the law of energy conservation, where \mathbb{I} is the identity matrix. Each \mathbb{M}^{kj} can be written as

$$\mathbb{M}^{kj} = \mathcal{M}^{kj} \begin{bmatrix} \cos \phi_{kj} & -\sin \phi_{kj} \\ \sin \phi_{kj} & \cos \phi_{kj} \end{bmatrix}. \quad (6.16)$$

It contains the absolute value \mathcal{M}^{kj} and the phase information due to a different travel distance (including the Gouy phase effect). The detailed calculations of mode coupling matrixes are introduced in [63]. The I/O relation for a plane wave mode profile (see Eq. 9.6) can be transformed to describe Hermite-Gauss mode profiles as:

$$\begin{bmatrix} \mathbf{b}^0 \\ \mathbf{b}^1 \\ \vdots \end{bmatrix} = \underbrace{\mathbb{M} \begin{bmatrix} \mathbb{T} & 0 & \cdots \\ 0 & \mathbb{I} & \cdots \\ \vdots & \vdots & \ddots \end{bmatrix}}_{\mathbb{T}} \underbrace{\mathbb{M} \begin{bmatrix} \mathbf{a}^0 \\ \mathbf{a}^1 \\ \vdots \end{bmatrix}}_{\mathbb{R}} + \underbrace{\mathbb{M} \begin{bmatrix} \mathbf{R} & 0 & \cdots \\ 0 & \mathbf{I} & \cdots \\ \vdots & \vdots & \ddots \end{bmatrix}}_{\mathbb{R}} \begin{bmatrix} x \\ x^1 \\ \vdots \end{bmatrix} \frac{1}{x_{\text{SQL}}}. \quad (6.17)$$

I note that two mode coupling matrixes are applied onto the input field and the transfer matrix \mathbb{T} , respectively. The first matrix is in charge of fitting the original beam into the cavity eigen mode frame, the second one is in charge of converting the output field from the frame of the cavity to the original input beam frame. They are always identical. I also note

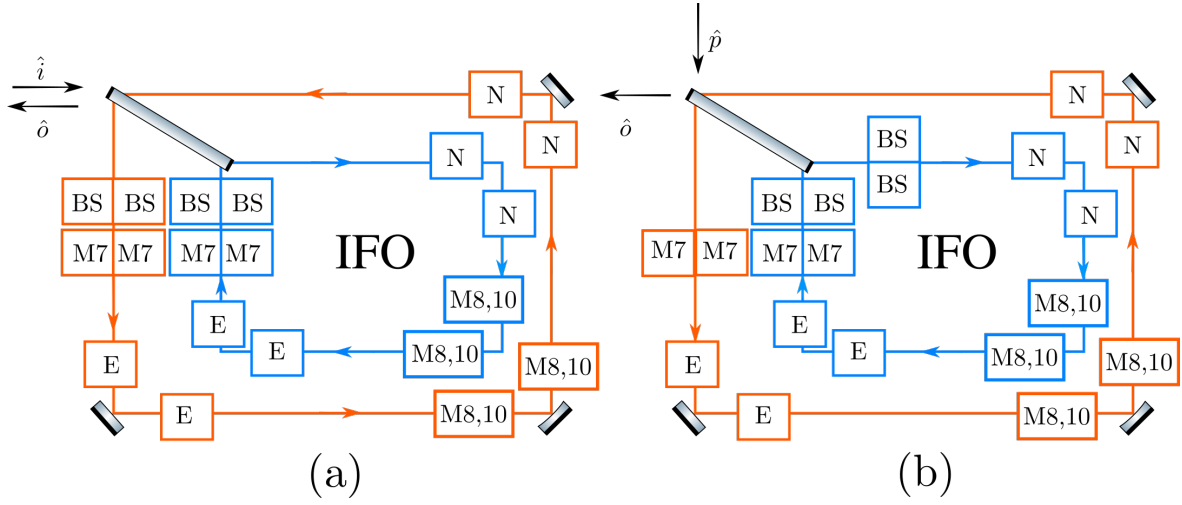


Figure 6.2: Simplified flow chart of the I/O relation of the interferometer according to Fig. 6.1. Each block represents a mode coupling matrix. There are two blocks in terms of an misalignment of one component. One is in charge of fitting the input beam into the eigen mode frame defined by the optical component, another one is in charge of converting the output field from the frame defined by the optical component to the original input beam frame. Blue traces represent the ‘R’ direction traveling fields, orange traces represent the ‘L’ direction traveling fields. (a) is the flow chart for dark port input (b) is the flow chart for laser bright port input.

that, the cavity transfer matrix \mathbb{T} and response vector \mathbf{R} are different from the ideal case due to the different circulating power caused by misalignment. Thus I require to modify the corresponding Kimble factor. The Kimble factor is proportional to both the back action force and the output response to the test mass motion. One example of this modification is shown in the asymmetric Sagnac case in plane wave mode profile, *i.e.*, in Eq. 6.4.

For the misalignment of a single plane mirror, one just need to replace the transfer matrix \mathbb{T} for cavity by an identity matrix \mathbb{I} , *ie.*

$$\begin{bmatrix} \mathbf{b}^0 \\ \mathbf{b}^1 \\ \vdots \end{bmatrix} = \mathbb{M} \begin{bmatrix} \mathbb{I} & 0 & \cdots \\ 0 & \mathbb{I} & \cdots \\ \vdots & \vdots & \ddots \end{bmatrix} \mathbb{M} \begin{bmatrix} \mathbf{a}^0 \\ \mathbf{a}^1 \\ \vdots \end{bmatrix}. \quad (6.18)$$

In the case of a curved mirror, it is more complicated, since the mirror modifies the complex-valued parameter q of the fundamental mode by a similar effect to that of a thin lens following the ABCD-matrix method [72, 73]. In the SSM experiment, there is one concave mirror connecting the arm cavities, *i.e.* M9 in Fig. 6.1. The radius of curvature of this mirror is designed to match the wave front of the incoming beam, which means the values of complex-valued parameter q of the beam are symmetrically identical on the incoming path and outgoing path. So we can ignore the effect of the distance of the beam propagation between the two cavities when considering the alignment and mode matching of the two arm cavities in Sagnac interferometer. This makes the modelling of I/O relation of the full

interferometer in Hermite-Gauss mode profile more simple.

6.3 Static misalignments in Sagnac Interferometer and quantum noise

In this section I analyse the possible misalignments that can happen in the Sagnac interferometer. In a Sagnac interferometer, there are three parts that determine its overall performance of quantum noise limited sensitivity, *i.e.* the main beam splitter, the mirror connecting the arm cavities and the two arm cavities themselves. I split the alignment of the full interferometer up into three parts: 1) the alignment between the beam transmitted through the main beamsplitter and cavity E; 2) the alignment of the reflection beam from main beamsplitter to cavity N; 3) the alignment between the two arm cavities.

For my analyses I will use the optical layout of Glasgow SSM experiment as a realistic example. This simplified version is shown in Fig. 6.1. Two aspects need to be considered in order to establish the I/O relation for the full interferometer in the Hermite-Gauss modes profile: (1) The mode coupling process due to misalignments, which is the content in Sec. 6.2; (2) Changes of the circulating fields in the cavity which change both, the response function of the cavity output field to the cavity mirrors' displacement and the total radiation pressure force. The two aspects for the full interferometer can be better traced by treating the dark port and bright port inputs separately as shown in Fig. 6.2. The part (a) in Fig. 6.2 shows how the I/O relation from dark port input to dark port output in the Hermite-Gauss modes profile should be defined based on the I/O relation in the plane wave mode profile in Sec. 6.1. The (b) part helps to figure out how the powers of circulating fields in the cavities and in both directions are scaled regarding different misalignments. It has to be noted that for a misalignment, there are two misalignment directions which can be quantified by two conjugate mode coupling matrixes.

Starting from these decoupled three degrees of freedom, I analyse several special sets of misalignment conditions:

- A. The cavities connection mirrors (CM) M8 and M10 are misaligned.
- B. Cavities N and E are misaligned in the opposite direction by the same magnitude, which I refer to as pure **out-of-phase cavity misalignment**.
- C. Cavities N and E are misaligned in the same direction with same magnitude, which I refer to as pure **in-phase cavity misalignment**.
- D. Either cavity N or E is misaligned, which I refer to as **individual cavity misalignment**.

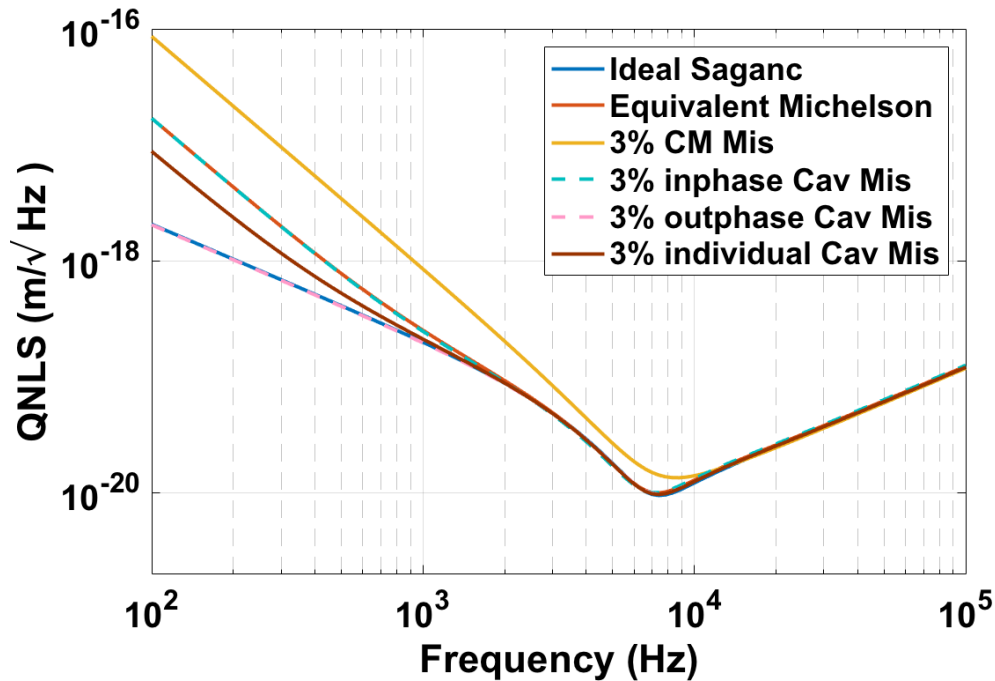


Figure 6.3: The quantum noise limited sensitivity of Glasgow speed meter experiment in cases of different misalignment conditions.

The resulting quantum noise limited sensitivity is shown in Fig. 6.3. The results can be understood with the help of Fig. 6.2.

- A. In terms of the effects of misalignment of the CM, it is actually straightforward to refer to the effects of optical loss between the two cavities.
- B. The effects of arm cavities out-of-phase misalignment is more complex and can be understood as following.

Firstly, we analyse the scaling of the power of the circulating fields in the two cavities. Mathematically, the pure out-of-phase cavity misalignment means that the coupling matrixes for the N and E cavity are conjugate. The coupling of modes from the output of one cavity to the input of the other is just a reciprocating process because the two 'N', 'E' matrixes are conjugate, as can be seen from part (b) in Fig. 6.2. The powers of circulating beams in both cavities and in both directions are actually balanced but with a reduced value. So it is equivalent to a power loss of the laser at the bright input port of the interferometer.

Secondly, we analyse the modes distributions of quantum fields according to part (a) in Fig. 6.2. In the part (a) of Fig. 6.2, the misalignments of optics at the dark port inputs can be disregarded, because the dark port input is just vacuum. Then before the quantum fields in the two paths of the two traveling directions recombine on the main beamsplitter, the spatial modes of them are defined by cavity E and cavity

N, respectively. The spatial mode matrices of the two cavities are conjugate and we only care about the fundamental mode field which is the overlapped part, so partial quantum fields which circulated in the arm cavities are lost towards HOMs. This is equivalent to the *output loss*.

In summary, the impacts of cavity out-of-phase misalignment can be summarised as following:

- Loss of input power.
- Output loss, which is equivalent to imperfect photo diode quantum efficiency.

The first effect is also why one can notice that in the back action noise dominated low frequency region, the quantum noise limited sensitivity is even slightly lower than with ideal alignment.

C. The similar understanding process of the two cases above can be applied to the pure in-phase cavity misalignment.

Firstly, there is a similar effect to that of CM misalignment, which refers to the optical loss between the two cavities. In this case, the two 'N', 'E' matrices are identical, so mathematically, the modes coupling from the output of one cavity to the input of the other is a one way coupling according to Fig. 6.2. The mathematical mechanism of this part is actually the same as the CM misalignment.

Secondly, a fraction of the two laser beams transmitted through the main beamsplitter do not enter into the two arm cavities due to the misalignment. So it is again equivalent to a power loss of the laser at the bright input port of the interferometer.

In summary, the impacts of the cavity in phase misalignment can be summarised as following:

- Loss of input power.
- Optical loss between the two arm cavities.

D. The individual cavity misalignment is actually straightforward to refer to the effects of optical loss of one cavity.

I note that, the conditions I compute above are somehow artificial, because in reality it is not always possible to decouple the three degrees freedom. However, the current results have already shown the necessity of aligning the interferometer accurately. In next section, I simulate the possible auto-alignment strategies using the example of the Glasgow Sagnac speed meter experiment.

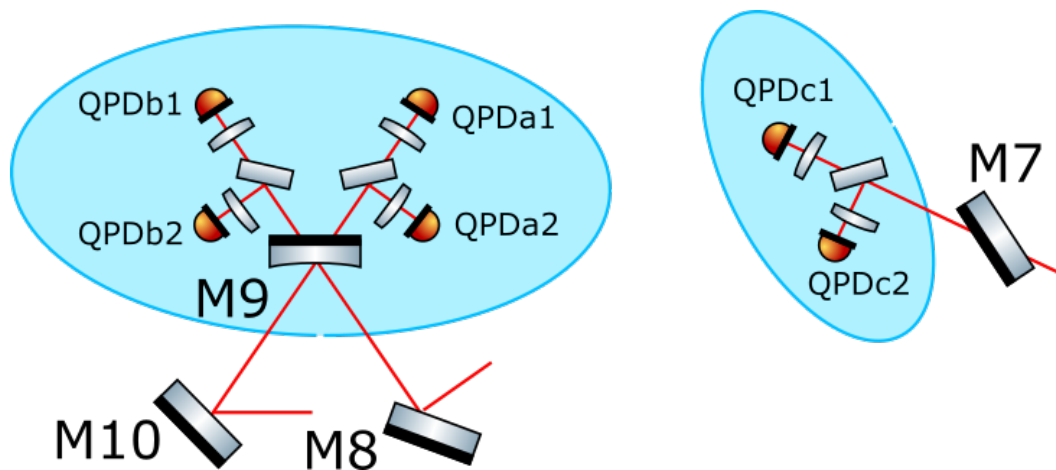


Figure 6.4: Diagram of showing the locations of differential wave front sensing schemes.

6.4 Autoalignment strategies for dynamic misalignment

In this section, I investigate the sensing and control of the dynamic misalignment in the Glasgow SSM experiment. In order to being able to simulate the alignment error signals corresponding to the degrees of freedom discussed above, I had to develop a suitable input file for the Finesse software, that works with HOMs. Indeed, the original Finesse file that I used initially caused some confusion, because the plane wave mode case and the Hermite-Gauss mode case did not give identical results. The problem originated from the fact that in Finesse all optics are defined as thin optics, while in reality the thickness of the curved mirror, *e.g.* ITMs, would modify the gaussian beam parameters of the transmitted beams similar to the effect of a lens. After defining the two surfaces of each ITM separately and adding a fused silica space between, the resulting sensitivity in Hermite-Gauss mode coincides with that in plane wave profile. With this issue resolved, I can start simulation.

The differential wave front sensing sensors for the alignment between the input laser and the two cavities are placed behind M9 with two pairs of QPDs, QPDa (QPDa1, QPDa2) and QPDb, (QPDb1, QPDb2), as shown in Fig. 6.4. In terms of control of the alignment between the two cavities. I put a set of differential wave front sensing scheme behind M7 with one pair of QPDs, QPDc (QPDc1, QPDc2), as shown in Fig. 6.4. This method is called the *Ward method* [74].

In order to validate how well the sensing signals can map multiple independent degrees of freedom and evaluate the controllability of a system, one can define the vector space of the mirrors to be controlled, \mathbf{B} , with each vector, $\vec{\beta}_i$, and the space of normalised signal vectors, \mathbf{S} , with each vector, \vec{s}_i [75]. The mirrors angular positions can be mapped by the photodiode signals via the relation:

$$\mathbf{S} = \mathbf{O}\mathbf{B}. \quad (6.19)$$

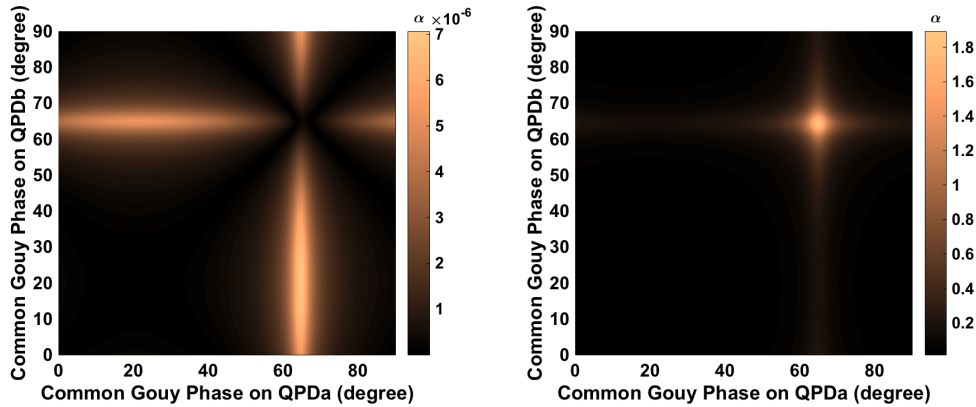


Figure 6.5: Results of the computation of quality parameter of \mathbb{O}_A in pitch for two sets of mirrors: (1) M5, M7, M4, M11; (2) M5, M7, M4, M6. The colour bar indicates quality parameter. The x-axis and y-axis indicates the common Gouy phase of QPDa and QPDb. The left plot corresponds to (1), the right plot corresponds to (2).

where \mathbb{O} is defined as *optical matrix*. The reconstructed volume in the space of the mirrors can be computed by using the *wedge product* as:

$$V = |\det(\mathbb{O})|. \quad (6.20)$$

$V = 0$ tells the system is completely degenerate while $V = 1$ tells the system is perfectly decoupled. In the case of $0 \leq V \leq 1$, an equivalent spatial separation between the degrees of freedom of the alignment system can be computed by constructing another matrix which spawns the same volume. It is constructed by making all vectors to be orthogonal except one and the one to be misaligned with respect to the first vector by an angle α , named as *quality parameter*:

$$\alpha = \arcsin(|\det(\mathbb{O})|). \quad (6.21)$$

α is then an indication of the controllability of system given a matrix \mathbb{O} .

Since the arm cavities are more stable systems compared with the input beams, we can treat them as the reference. We treat the mirrors' pitch and yaw separately, since they are independent in the ideal case. Obviously, there are only two mirrors, M8 and M10, responsible to the alignment between two cavities. However, there are five mirrors on the input path to the two cavities, *i.e.* M4, M5, M11, M6, M7. If we want to sense and control all the seven mirrors, it will not be possible to distinguish them with six signals¹ as the system is underdetermined. In order to stabilise the system, it is not necessary to get all mirrors under control. Usually, one pair of mirrors can provide the shift and tilt degrees of freedom of a beam and allow us to perfectly align the input beam to the eigenmode of a cavity. I select four mirrors among M4, M5, M11, M6, M7 for the purpose of input beams alignment

¹As we know, in the Ward sensing system, the demodulation phases of QPDs do not give differential impacts on the error signals of beam shift and tilt [76], so there only six independent signals of the six QPDs.

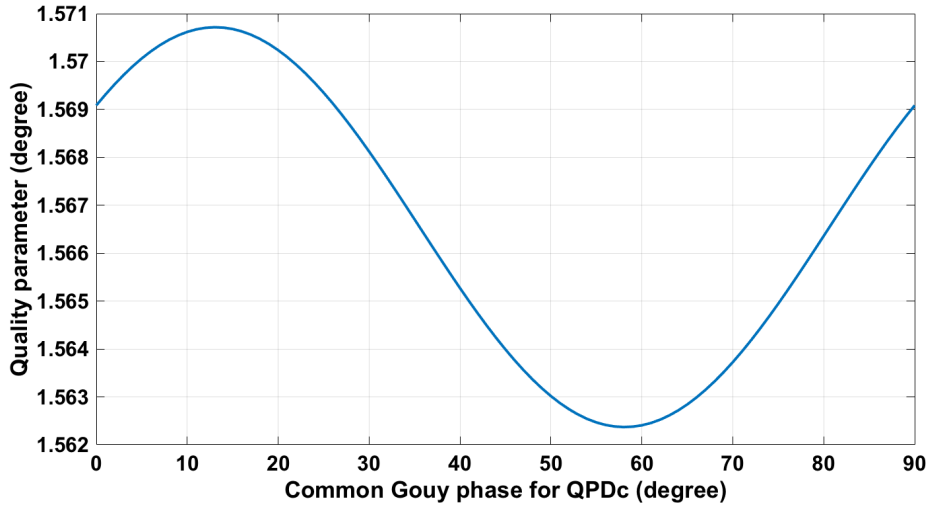


Figure 6.6: Results of the computation of quality parameter of \mathbb{O}_D in pitch indicating the relation of mirrors: M8, M10 and two signals of QPDc. The y-axis indicates quality parameter. The x-axis indicates the Gouy phase of QPDc1.

to the two cavities. In our system, M7 is placed after the beam splitter and only effects the input beam alignment to cavity E; M6 is a beamsplitter and mainly effects the alignment of the reflected beam to cavity N. In the following I will investigate two options: (1) M5, M7, M4, M11, M8, M10 are used for the purpose of control; (2) M5, M7, M4, M6, M8, M10 are used for the purpose of control. Firstly, I tried to test whether the six signals can map the angular displacements space of the six mirrors. The whole sensing scheme can be described as

$$\underbrace{\begin{bmatrix} \vec{s}_{QPDa1} \\ \vec{s}_{QPDa2} \\ \vec{s}_{QPDb1} \\ \vec{s}_{QPDb2} \\ \vec{s}_{QPDc1} \\ \vec{s}_{QPDc2} \end{bmatrix}}_{\mathbf{S}} = \mathbb{O} \underbrace{\begin{bmatrix} \vec{\beta}_{M5} \\ \vec{\beta}_{M7} \\ \vec{\beta}_{M4} \\ \vec{\beta}_{M11} \\ \vec{\beta}_{M8} \\ \vec{\beta}_{M10} \end{bmatrix}}_{\mathbf{B}}, \quad (6.22)$$

or

$$\underbrace{\begin{bmatrix} \vec{s}_{QPDa1} \\ \vec{s}_{QPDa2} \\ \vec{s}_{QPDb1} \\ \vec{s}_{QPDb2} \\ \vec{s}_{QPDc1} \\ \vec{s}_{QPDc2} \end{bmatrix}}_{\mathbf{S}} = \mathbb{O} \underbrace{\begin{bmatrix} \vec{\beta}_{M5} \\ \vec{\beta}_{M7} \\ \vec{\beta}_{M4} \\ \vec{\beta}_{M6} \\ \vec{\beta}_{M8} \\ \vec{\beta}_{M10} \end{bmatrix}}_{\mathbf{B}}. \quad (6.23)$$

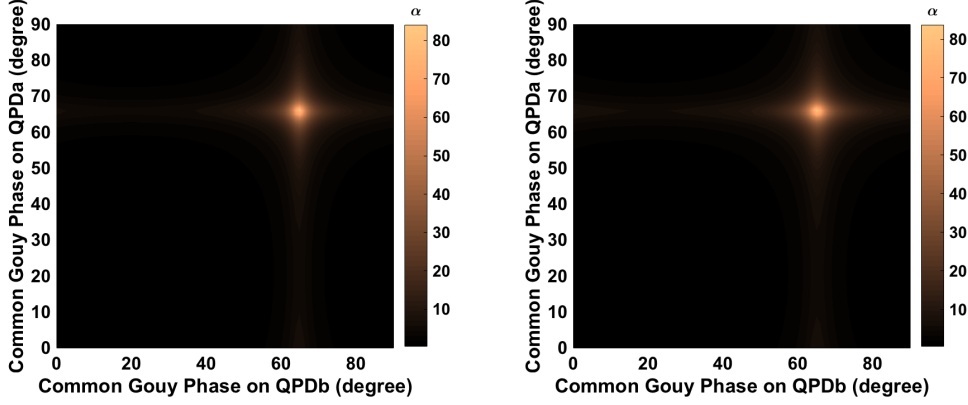


Figure 6.7: Results of the computation of quality parameter of $\mathbb{M}_{\text{con}}^{ab}$ in pitch indicating the relation of the four signals of QPDa and QPDb and two sets of mirrors: (1) M5, M7, M4, M11; (1) M5, M7, M4, M6. The colour bar indicates quality parameter. The x-axis and y-axis indicates the common Gouy phase of QPDa and QPDb. The left plot corresponds to (1), the right plot corresponds to (2).

Since only RF signals are detected, obviously misalignments of M8 and M10 are not sensible to QPDa and QPDb, thus the optical matrix \mathbb{O} will be in the form of

$$\mathbb{O} = \begin{bmatrix} \mathbb{O}_A & 0 \\ \mathbb{O}_C & \mathbb{O}_D \end{bmatrix}. \quad (6.24)$$

Mathematically, there is

$$|\det(\mathbb{O})| = |\det(\mathbb{O}_A)| |\det(\mathbb{M}_D)|. \quad (6.25)$$

So we can evaluate the controllability of the entire system by computing the quality parameter of \mathbb{O}_A and \mathbb{O}_D separately.

Firstly, I tried to find the optimal quality parameter of \mathbb{O}_A . In Finesse, I put one common Gouy phase on QPDa1 and QPDa2, another common Gouy phase on QPDb1 and QPDb2. And I added 90 degrees phase difference between them in each pair. The total signal of each QPD are normalised to be 1. In pitch direction, the quality parameter of \mathbb{O}_A as a function of two common Gouy phases is shown in Fig. 6.5. As we can observe, the optimal quality parameters of \mathbb{O}_A of the two scheme are around 7×10^{-6} degree and 1.8 degree, respectively. Both values are quite low.

Secondly, I tried to compute the quality parameter of \mathbb{O}_D . In Finesse, I put a common Gouy phases on QPDC1 and QPDC2 and added 90 degrees phase difference between them. In pitch direction, the quality parameters of \mathbb{O}_D as a function of common Gouy phase are shown in Fig. 6.6. As we can observe, the optimal quality parameters of \mathbb{O}_D is around 1.57 degree.

Overall, we have to conclude that the six signals cannot well map the angular displacements space of any the two sets of the six mirrors. The signals of QPDa and QPDb are strongly overlapped because the impacts of the misalignments of M4, M5, M11 on QPDa are identical to these on QPDb. The signals of QPDC not only contain information of M8, M10, but also

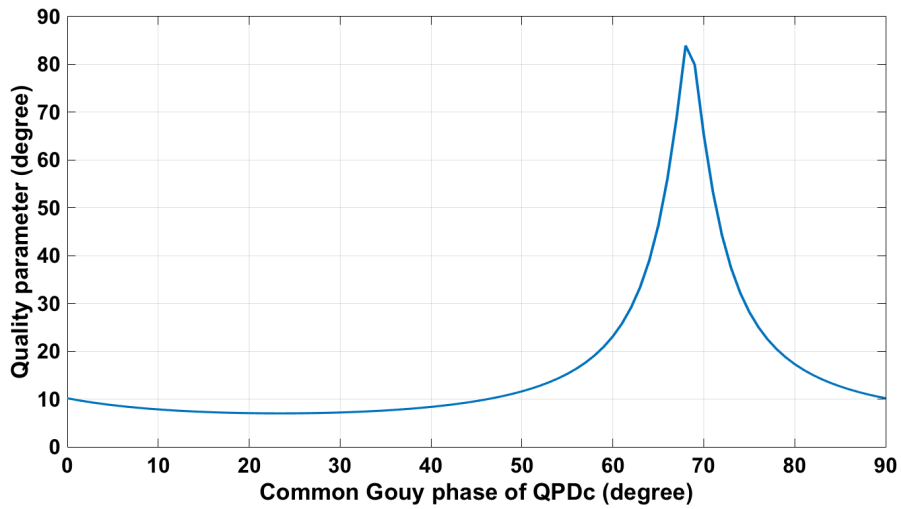


Figure 6.8: Results of the computation of quality parameter of $\mathbb{O}_{\text{con}}^c$ in pitch indicating the relation of two signals of QPDC and mirrors, M8, M10. The y-axis indicates quality parameter. The x-axis indicates the Gouy phase of QPDC1.

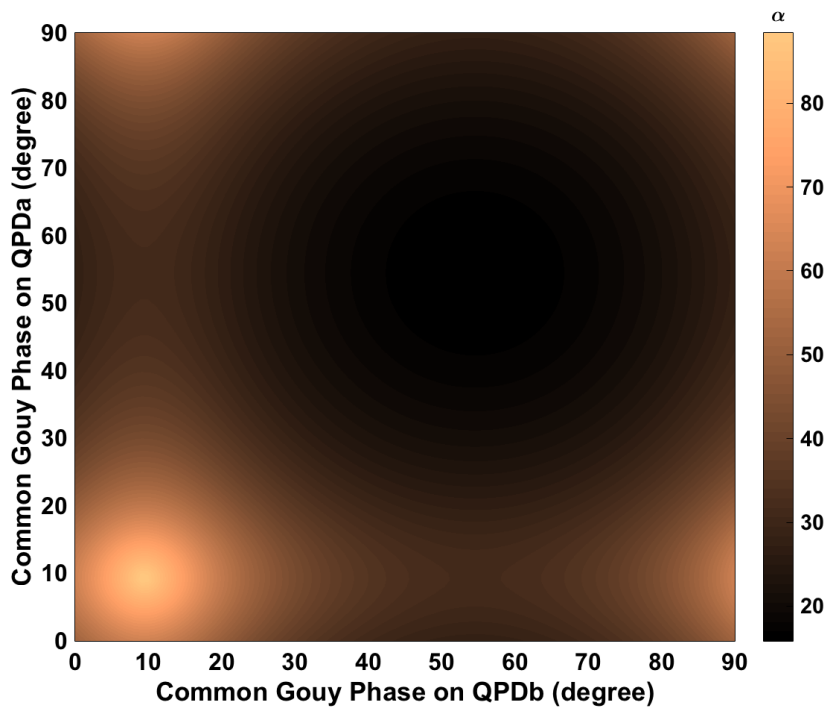


Figure 6.9: Results of the computation of quality parameter of \mathbb{O}_A in pitch for two sets of mirrors: M1a, M2a, M1b, M2b. The colour bar indicates quality parameter. The x-axis and y-axis indicates the common Gouy phase of QPDA and QPDb.

M1a, M2a, M1b, M2b. While, this does not mean the whole system is not controllable, in practice, we can select one pair of mirrors for controlling the beam input alignment to cavity E and another pair of mirrors for controlling the beam input alignment to cavity N by applying servos with different design such as large gain difference. And M8, M10 are for controlling the alignment of the beam between two cavities with cavity E as the reference. The control relations are then given by

$$\begin{bmatrix} \vec{\beta}_{M5} \\ \vec{\beta}_{M7} \\ \vec{\beta}_{M4} \\ \vec{\beta}_{M11} \end{bmatrix} = \mathbb{M}_{\text{con}}^{ab} \begin{bmatrix} \vec{s}_{QPD1a} \\ \vec{s}_{QPD2a} \\ \vec{s}_{QPD1b} \\ \vec{s}_{QPD2b} \end{bmatrix}, \quad (6.26)$$

or

$$\begin{bmatrix} \vec{\beta}_{M5} \\ \vec{\beta}_{M7} \\ \vec{\beta}_{M4} \\ \vec{\beta}_{M6} \end{bmatrix} = \mathbb{M}_{\text{con}}^{ab} \begin{bmatrix} \vec{s}_{QPD1a} \\ \vec{s}_{QPD2a} \\ \vec{s}_{QPD1b} \\ \vec{s}_{QPD2b} \end{bmatrix}, \quad (6.27)$$

and

$$\begin{bmatrix} \vec{\beta}_{M8} \\ \vec{\beta}_{M10} \end{bmatrix} = \mathbb{M}_{\text{con}}^c \begin{bmatrix} \vec{s}_{QPD1c} \\ \vec{s}_{QPD2c} \end{bmatrix}, \quad (6.28)$$

where $\mathbb{O}_{\text{con}}^{ab}$ are in the form of $\begin{bmatrix} \times & 0 \\ 0 & \times \end{bmatrix}$. The quality parameters of $\mathbb{O}_{\text{con}}^{ab}$ and $\mathbb{O}_{\text{con}}^c$ for pitch as a function of common Gouy phase are shown in Fig. 6.7 and Fig. 6.8. As we can observe, with common Gouy phase on QPDa and QPDb of 65 degree, the optimal quality parameter of $\mathbb{O}_{\text{con}}^{ab}$ raises up to about 80 degree. Also we find the two schemes to give almost identical results because M11 and M6 are very close in terms of spatial location. With a common Gouy phase on QPDC of 68 degree, the optimal quality parameter of $\mathbb{O}_{\text{con}}^c$ is over 80 degree. This tells us that each pair of mirrors can cover two orthogonal degrees of freedom of the beam misalignment (beam shift and tilt) using the corresponding cavities as the reference. As an example, the optimal control matrix indicating the control relation of the signals from QPDa and QPDb and M5, M7, M4, M11 can be computed as

$$\begin{bmatrix} \vec{\beta}_{M5} \\ \vec{\beta}_{M7} \\ \vec{\beta}_{M4} \\ \vec{\beta}_{M11} \end{bmatrix} = \begin{bmatrix} -0.39 & -0.76 & 0 & 0 \\ 0.92 & 0.65 & 0 & 0 \\ 0 & 0 & -0.73 & -0.74 \\ 0 & 0 & 0.68 & -0.68 \end{bmatrix} \begin{bmatrix} \vec{s}_{QPD1a} \\ \vec{s}_{QPD2a} \\ \vec{s}_{QPD1b} \\ \vec{s}_{QPD2b} \end{bmatrix}. \quad (6.29)$$

The optimal control matrix indicating the control relation of the signals from QPDC and

M8, M10 can be computed as

$$\begin{bmatrix} \vec{\beta}_{M8} \\ \vec{\beta}_{M10} \end{bmatrix} = \begin{bmatrix} 0.63 & 0.71 \\ -0.78 & 0.71 \end{bmatrix} \begin{bmatrix} \vec{s}_{QPD1c} \\ \vec{s}_{QPD2c} \end{bmatrix}. \quad (6.30)$$

Another way is to take the input beam as the reference and control the cavity mirrors following the jittering of the input beam. For this analysis I select M1a, M2a, M1b, M2b for the control purpose. Again I computed the quality parameter of $\mathbb{O}_{\text{con}}^{ab}$. The results are shown in Fig. 6.9. As we can observe, at common Gouy phases for both QPDa and QPDb around 10 degree, there is optimal quality parameter of 80 degree. With this set up, the optimal control matrix of the whole system can be computed as

$$\begin{bmatrix} \vec{\beta}_{M1a} \\ \vec{\beta}_{M2a} \\ \vec{\beta}_{M1b} \\ \vec{\beta}_{M2b} \end{bmatrix} = \begin{bmatrix} 0.44 & -0.88 & 0 & 0 \\ 0.9 & 0.48 & 0 & 0 \\ 0 & 0 & 0.45 & -0.88 \\ 0 & 0 & 0.89 & 0.48 \end{bmatrix} \begin{bmatrix} \vec{s}_{QPD1a} \\ \vec{s}_{QPD2a} \\ \vec{s}_{QPD1b} \\ \vec{s}_{QPD2b} \end{bmatrix}. \quad (6.31)$$

In the same manner, the optimal control relation for yaw direction can be computed as

$$\begin{bmatrix} \vec{\beta}_{M5} \\ \vec{\beta}_{M7} \\ \vec{\beta}_{M4} \\ \vec{\beta}_{M11} \end{bmatrix} = \begin{bmatrix} -0.73 & 0.74 & 0 & 0 \\ 0.68 & 0.68 & 0 & 0 \\ 0 & 0 & -0.69 & 0.73 \\ 0 & 0 & 0.72 & 0.68 \end{bmatrix} \begin{bmatrix} \vec{s}_{QPD1a} \\ \vec{s}_{QPD2a} \\ \vec{s}_{QPD1b} \\ \vec{s}_{QPD2b} \end{bmatrix}, \quad (6.32)$$

or

$$\begin{bmatrix} \vec{\beta}_{M1a} \\ \vec{\beta}_{M2a} \\ \vec{\beta}_{M3a} \\ \vec{\beta}_{M4a} \end{bmatrix} = \begin{bmatrix} -0.54 & -0.84 & 0 & 0 \\ 0.84 & -0.54 & 0 & 0 \\ 0 & 0 & 0.55 & 0.84 \\ 0 & 0 & -0.83 & 0.54 \end{bmatrix} \begin{bmatrix} \vec{s}_{QPD1a} \\ \vec{s}_{QPD2a} \\ \vec{s}_{QPD1b} \\ \vec{s}_{QPD2b} \end{bmatrix}, \quad (6.33)$$

and

$$\begin{bmatrix} \vec{\beta}_{M8} \\ \vec{\beta}_{M10} \end{bmatrix} = \begin{bmatrix} 0.72 & -0.71 \\ -0.69 & -0.71 \end{bmatrix} \begin{bmatrix} \vec{s}_{QPD1c} \\ \vec{s}_{QPD2c} \end{bmatrix}. \quad (6.34)$$

6.5 Summary

In this chapter, I developed an analysis of the effects of misalignments in a Sagnac speed meter and provided the foundation to calculate quantum noise in the conditions of several misaligned optics. The alignment of the Sagnac interferometer can be decoupled into three parts: 1) the alignment between the beam transmitted through the main beamsplit-

ter and cavity E; 2) the alignment of the reflection beam from main beamsplitter to cavity N; 3) the alignment between the two arm cavities. I analysed several special misalignment conditions defining as: (1) connection mirrors misalignment; (2) out-of-phase cavity misalignment; (3) in-phase cavity misalignment; (4) individual cavity misalignment. The impact of connection mirrors misalignment can be summarised as optical loss between the two cavities. The impacts of cavity out-of-phase misalignment can be summarised as loss of input power and interferometer output loss, which is equivalent to imperfect photo diode quantum efficiency. Impacts of cavity in phase misalignment can be summarised as loss of input power and optical loss between the two arm cavities. Individual cavity misalignment can be summarised as optical loss of an individual cavity. With the example of Glasgow SSM experiment layout, I discussed possible sensing and control strategies for the interferometer alignment. The dynamic alignment of the three parts can be well covered with the sensing schemes shown in Fig. 6.1, the control matrices were modelled.

Chapter 7

Backscattering effects on quantum noise of ring cavities

In this chapter, I analyse another optical imperfection in a ring resonator of a Sagnac speed meter and its impact on quantum noise, *i.e.*, optical backscattering. I refer to the back scattering phenomenon due to the interaction of the laser beam and an imperfect mirror surface. In the case of coherent scattering, the scattering surface will not affect the intrinsic properties rather only the propagation direction of the propagating beam [1]. The scattering angle usually depends on the spatial frequency of the mirror surface roughness and flatness. At low spatial frequency, the distribution of the scattered light fields will cover a small angle range. For one specific spatial frequency, one scattering field coincides exactly with the counter propagating cavity mode, and is hence called backscattering.

In a ring cavity, the backscattering inside the cavity creates coupling between two directions circulation modes and induce more complex interactions between the laser beams and the test mass. In Sec. 7.1, I introduce the optical I/O relations of a beamsplitter with the micro-roughness surface considering the backscattering; in Sec. 7.2, the I/O relations of a ring cavity with movable input test mass are derived; in Sec. 7.3, the quantum noise limited sensitivity in displacement of the ring cavity is calculated and the resulting features are analysed; in Sec. 7.3.1, I calibrate the displacement sensitivity into strain sensitivity; in Sec. 7.3.2, the quantum constraint theory of a multipoles system is applied to validate the calculations. The same topic is investigated in [1]. As an extension, in this chapter, I investigate not only the weak backscattering but also stronger ones. Employing a detailed analytical calculation, I present the mechanism and impacts of the backscattering distinguished into three different characteristic cases based on the level of the backscattering amplitude.

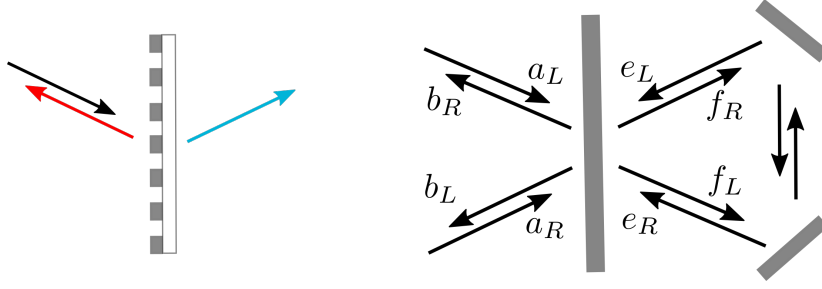


Figure 7.1: Left: The diagram that shows the input beam, transmission backscattering beam (blue) and reflection back scattering beam (red) around a beamsplitter; Right: the diagram that shows the relations among input fields, output fields and intra cavity fields in a ring cavity. a and b present the input and output field, e and f are the intra cavity fields. The subscript R represents clockwise propagation direction, L represents the anti-clockwise propagation direction.

7.1 Optical I/O relations of a beamsplitter

In the case of the ring cavity with a low transmission input mirror, which is the usual case for arm cavities in gravitational wave detectors, considering the smallness of the power of other scattering modes and that they only leak into free space (equivalent to optical loss), I only consider the backscattered modes that travel along with the normal modes routes. I consider both the reflection scattering and transmission scattering as shown in the left of Fig. 7.1. I assume the power of scattering field is scaled by one back scattering coefficient ϵ and the corresponding power reflectivity and transmissivity of the mirror [1]. The I/O relations of input and output fields on the input coupler of the ring cavity is shown in the right of Fig. 7.1. Mathematically, the I/O relations on the input mirror of a single cavity can be defined in the following formate,

$$\begin{bmatrix} b_R \\ b_L \\ f_R \\ f_L \end{bmatrix} = \begin{bmatrix} -\sqrt{R} & \sqrt{\epsilon R} e^{i\phi_{r1}} & \sqrt{T} & \sqrt{\epsilon T} e^{i\phi_{t1}} \\ \sqrt{\epsilon R} e^{i\phi_{r2}} & -\sqrt{R} & \sqrt{\epsilon T} e^{i\phi_{t2}} & \sqrt{T} \\ \sqrt{T} & \sqrt{\epsilon T} e^{i\phi_{r3}} & \sqrt{R} & \sqrt{\epsilon R} e^{i\phi_{r3}} \\ \sqrt{\epsilon T} e^{i\phi_{t4}} & \sqrt{T} & \sqrt{\epsilon R} e^{i\phi_{r4}} & \sqrt{R} \end{bmatrix} \begin{bmatrix} a_R \\ a_L \\ e_R \\ e_L \end{bmatrix}, \quad (7.1)$$

where ϕ_{ij} , ϕ_{rj} represent the phase gained by the scattered fields in transmission and reflection. Constrained by the energy conservation law, the bounding conditions can be derived as following,

$$\begin{aligned} \phi_{r1} &= -\phi_{r2} + \pi = \phi_{r3} = -\phi_{r4} + \pi, \\ \phi_{t1} &= -\phi_{t2} + \pi = \phi_{t3} + \pi = -\phi_{t4}, \\ \phi_{t4} &= \phi_{r2} - \pi. \end{aligned} \quad (7.2)$$

or

$$\begin{aligned}
\phi_{r1} &= -\phi_{r2} - \pi = \phi_{r3} = -\phi_{r4} - \pi, \\
\phi_{i1} &= -\phi_{i2} - \pi = \phi_{i3} - \pi = -\phi_{i4}, \\
\phi_{i4} &= \phi_{r2} + \pi.
\end{aligned} \tag{7.3}$$

In principle, due to the random distribution of roughness on the mirror surface, any phases satisfy the above relation are possible. In this chapter, I assume one special case, *i.e* the left and right modes phase are symmetric. In this case, the backscattering coefficients should be purely imaginary. In the case of the first phase relations set, $\phi_{r1} = \frac{\pi}{2}$, the I/O matrix is

$$\begin{bmatrix} b_R \\ b_L \\ f_R \\ f_L \end{bmatrix} = \begin{bmatrix} -\sqrt{R} & i\sqrt{\epsilon R} & \sqrt{T} & i\sqrt{\epsilon T} \\ i\sqrt{\epsilon R} & -\sqrt{R} & i\sqrt{\epsilon T} & \sqrt{T} \\ \sqrt{T} & -i\sqrt{\epsilon T} & \sqrt{R} & i\sqrt{\epsilon R} \\ -i\sqrt{\epsilon T} & \sqrt{T} & i\sqrt{\epsilon R} & \sqrt{R} \end{bmatrix} \begin{bmatrix} a_R \\ a_L \\ e_R \\ e_L \end{bmatrix} \tag{7.4}$$

In the case of the second phase relations set, $\phi_{r1} = -\frac{\pi}{2}$, the I/O matrix is

$$\begin{bmatrix} b_R \\ b_L \\ f_R \\ f_L \end{bmatrix} = \begin{bmatrix} -\sqrt{R} & -i\sqrt{\epsilon R} & \sqrt{T} & -i\sqrt{\epsilon T} \\ -i\sqrt{\epsilon R} & -\sqrt{R} & -i\sqrt{\epsilon T} & \sqrt{T} \\ \sqrt{T} & i\sqrt{\epsilon T} & \sqrt{R} & -i\sqrt{\epsilon R} \\ i\sqrt{\epsilon T} & \sqrt{T} & -i\sqrt{\epsilon R} & \sqrt{R} \end{bmatrix} \begin{bmatrix} a_R \\ a_L \\ e_R \\ e_L \end{bmatrix} \tag{7.5}$$

In following calculation process, I take the first set of sign conventions as the example.

7.2 Opto-mechanical I/O relations of a ring cavity

After confirming the phase and amplitude of the backscattered fields, in this section, I will derive the complete I/O relation of the cavity with moveable input mirror following the conventional procedures in [27].

According to Eq. 7.4, there is

$$\begin{aligned}
f_R &= \sqrt{T}a_R - i\sqrt{\epsilon T}a_L + \sqrt{R}e_R + i\sqrt{\epsilon R}e_L + 2ik \left(\sqrt{R}E_R + i\sqrt{\epsilon R}E_L \right) x, \\
f_L &= \sqrt{T}a_L - i\sqrt{\epsilon T}a_R + \sqrt{R}e_L + i\sqrt{\epsilon R}e_R + 2ik \left(\sqrt{R}E_L + i\sqrt{\epsilon R}E_R \right) x,
\end{aligned} \tag{7.6}$$

where x represents the displacement of the movable input test mass, $E_{L,R}$ represents DC intra cavity field. It can be excited by both external force and laser radiation pressure force. The round trip travel time of the light is defined as $\tau = \frac{2L}{c}$. The intra cavity sidebands

gain phase shift ' $\Omega\tau$ ' after traveling the round trip. So the relation between the intra cavity fields e and f are,

$$e_R = f_R e^{i\Omega\tau}, \quad e_L = f_L e^{i\Omega\tau}. \quad (7.7)$$

By substituting Eq. 7.6 into Eq. 7.7, there is

$$\begin{aligned} e_R &= \left[\sqrt{T}a_R - i\sqrt{\epsilon T}a_L + \sqrt{R}e_R + i\sqrt{\epsilon R}e_L + 2ik \left(\sqrt{R}E_R + i\sqrt{\epsilon R}E_L \right) x \right] e^{i\Omega\tau}, \\ e_L &= \left[\sqrt{T}a_L - i\sqrt{\epsilon T}a_R + \sqrt{R}e_L + i\sqrt{\epsilon R}e_R + 2ik \left(\sqrt{R}E_L + i\sqrt{\epsilon R}E_R \right) x \right] e^{i\Omega\tau}. \end{aligned} \quad (7.8)$$

With the single mode approximation [27], Eq. 7.8 can be derived as,

$$\begin{aligned} e_R &= \frac{\left[\sqrt{T}a_R - i\sqrt{\epsilon T}a_L + i\sqrt{\epsilon R}e_L + 2ik(\sqrt{R}E_R + i\sqrt{\epsilon R}E_L)x \right] e^{i\Omega\tau}}{1 - \sqrt{R}e^{i\Omega\tau}} \\ &= \frac{\left[\sqrt{T}a_R - i\sqrt{\epsilon T}a_L + i\sqrt{\epsilon R}e_L + 2ik(\sqrt{R}E_R + i\sqrt{\epsilon R}E_L)x \right]}{e^{-i\Omega\tau} - \sqrt{R}} \\ &= \frac{\left[\sqrt{T}a_R - i\sqrt{\epsilon T}a_L + i\sqrt{\epsilon R}e_L + 2ik(\sqrt{R}E_R + i\sqrt{\epsilon R}E_L)x \right]}{1 - i\tau\Omega - (1 - \frac{T+\epsilon}{2})} \\ &= \frac{\left[\sqrt{T}a_R - i\sqrt{\epsilon T}a_L + i\sqrt{\epsilon R}e_L + 2ik(\sqrt{R}E_R + i\sqrt{\epsilon R}E_L)x \right]}{(\gamma - i\Omega)\tau}, \\ e_L &= \frac{\left[\sqrt{T}a_L - i\sqrt{\epsilon T}a_R + i\sqrt{\epsilon R}e_R + 2ik(\sqrt{R}E_L + i\sqrt{\epsilon R}E_R)x \right]}{(\gamma - i\Omega)\tau}. \end{aligned} \quad (7.9)$$

Since the backscattering coefficients ϵ is much smaller than the cavity transmissivity T , I ignore in the equations above the effect of ϵ to the effective half bandwidth γ . By defining $\gamma = \frac{T}{2\tau}$, e_R can be written as

$$\begin{aligned} e_R &= \frac{\sqrt{T}a_R - i\sqrt{\epsilon T}a_L}{(\gamma - i\Omega)\tau} + \frac{i\sqrt{\epsilon R}}{(\gamma - i\Omega)\tau} \frac{(\sqrt{T}a_L - i\sqrt{\epsilon T}a_R + i\sqrt{\epsilon R}e_R)}{(\gamma - i\Omega)\tau} \\ &\quad + \frac{2ik(\sqrt{R}E_R + i\sqrt{\epsilon R}E_L)x}{(\gamma - i\Omega)\tau} + \frac{i\sqrt{\epsilon R}}{(\gamma - i\Omega)\tau} \frac{2ik(\sqrt{R}E_L + i\sqrt{\epsilon R}E_R)x}{(\gamma - i\Omega)\tau}. \end{aligned} \quad (7.10)$$

For simplicity here, I define two effective factors ,

$$\delta = \frac{\sqrt{\epsilon}}{\gamma\tau}, \quad y = \frac{\Omega}{\gamma}. \quad (7.11)$$

So that I can simplify Eq. 7.9 as

$$\begin{aligned} e_R &= \sqrt{\frac{2}{\gamma\tau}} \left[\left(\frac{1}{1-iy} + \frac{\gamma\tau\delta^2}{(1-iy)^2} \right) a_R + \left(\frac{i\delta}{(1-iy)^2} - \frac{i\delta\gamma\tau}{1-iy} \right) a_L \right] \frac{1}{B(\Omega)} + U_R^x, \\ e_L &= \sqrt{\frac{2}{\gamma\tau}} \left[\left(\frac{1}{1-iy} + \frac{\gamma\tau\delta^2}{(1-iy)^2} \right) a_L + \left(\frac{i\delta}{(1-iy)^2} - \frac{i\delta\gamma\tau}{1-iy} \right) a_R \right] \frac{1}{B(\Omega)} + U_L^x, \end{aligned} \quad (7.12)$$

where

$$B(\Omega) = 1 + \frac{\delta^2 R}{(1-iy)^2}, \quad (7.13)$$

and

$$\begin{aligned} U_R &= \frac{2ik \left(\sqrt{R}E_R + i\sqrt{\epsilon R}E_L \right)}{(\gamma - i\Omega)\tau} + \frac{i\sqrt{\epsilon R}}{(\gamma - i\Omega)\tau} \frac{2ik \left(\sqrt{R}E_L + i\sqrt{\epsilon R}E_R \right)}{(\gamma - i\Omega)\tau} \frac{1}{B(\Omega)}, \\ U_L &= \frac{2ik \left(\sqrt{R}E_L + i\sqrt{\epsilon R}E_R \right)}{(\gamma - i\Omega)\tau} + \frac{i\sqrt{\epsilon R}}{(\gamma - i\Omega)\tau} \frac{2ik \left(\sqrt{R}E_R + i\sqrt{\epsilon R}E_L \right)}{(\gamma - i\Omega)\tau} \frac{1}{B(\Omega)}. \end{aligned} \quad (7.14)$$

For convenience, I write the field relations in the two-photo formalism. According to Eq. 7.12, when $\Omega = 0$, the DC intra cavity fields amplitudes can be written out as

$$\begin{aligned} E_R &= \sqrt{\frac{2}{\gamma\tau}} \left\{ (1 + \gamma\tau\delta^2) \begin{bmatrix} A_R \\ 0 \end{bmatrix} + (\delta - \delta\gamma\tau) \begin{bmatrix} 0 \\ A_L \end{bmatrix} \right\} \frac{1}{B(0)}, \\ E_L &= \sqrt{\frac{2}{\gamma\tau}} \left\{ (1 + \gamma\tau\delta^2) \begin{bmatrix} A_L \\ 0 \end{bmatrix} + (\delta - \delta\gamma\tau) \begin{bmatrix} 0 \\ A_R \end{bmatrix} \right\} \frac{1}{B(0)}. \end{aligned} \quad (7.15)$$

With the single mode approximation, the radiation pressure force can be calculated as

$$F_{rp} = F_0 + F_x = 2\hbar k \left(\mathbf{E}_R^T e_R + \mathbf{E}_L^T e_L \right). \quad (7.16)$$

In the following I assume that the backscattering coefficient ϵ is no larger than 1ppm, *i.e.* $\delta \leq 10$ and then neglect the smallness term. The displacement independent radiation pressure force can be derived as

$$\begin{aligned} F_0 &= \frac{4\hbar k}{\gamma\tau} \left\{ \left[\frac{1}{1-iy} - \frac{\delta^2}{(1-iy)^2} \right] \left(\begin{bmatrix} A_R & 0 \end{bmatrix} a_R + \begin{bmatrix} A_L & 0 \end{bmatrix} a_L \right) \right. \\ &\quad \left. + \left[\frac{\delta}{1-iy} + \frac{\delta}{(1-iy)^2} \right] \left(\begin{bmatrix} 0 & A_R \end{bmatrix} a_L + \begin{bmatrix} 0 & A_L \end{bmatrix} a_R \right) \right\} \frac{1}{B(\Omega)B(0)}, \end{aligned} \quad (7.17)$$

and the dynamic radiation pressure force can be derived as

$$F_x = -\frac{16\hbar k^2 x}{\gamma^2 \tau^2} \frac{\delta(1+\delta^2)}{(1-iy)^2} |A_R A_L| \frac{1}{\mathcal{B}(\Omega)\mathcal{B}(0)^2}. \quad (7.18)$$

The equation of motion of the moveable mirror in frequency domain can be written as

$$(\chi^{-1} + K_{rig}) x = F_0 + F_x + F_{GW}, \quad (7.19)$$

where $\chi = -\frac{1}{\mu\Omega^2}$ is the free mass mechanical susceptibility with effective mass μ and $K_{rig}x = F_x$. According to the dynamic radiation pressure force derived above, it is straightforward to write out the optical rigidity,

$$K_{rig} = -\frac{16\hbar k^2}{\gamma^2 \tau^2} \frac{\delta(1+\delta^2)}{(1-iy)^2} |A_R A_L| \frac{1}{\mathcal{B}(\Omega)\mathcal{B}(0)^2}. \quad (7.20)$$

A new effective mechanical susceptibility can be defined as

$$\chi_{new} = \frac{1}{\chi^{-1} + K_{rig}}. \quad (7.21)$$

The output b_R can be written in terms of a_R, a_L and e_R as

$$b_R = -\sqrt{R}a_R + i\sqrt{\epsilon R}a_L + \sqrt{T}e_R. \quad (7.22)$$

In general the I/O relations usually take the form of

$$b_R = \left(\mathbb{T}_{sh}^R + \mathbb{T}_{rp}^R \right) a_R + \left(\mathbb{T}_{sh}^L + \mathbb{T}_{rp}^L \right) a_L + \underbrace{\left(\mathbf{R}_R + \mathbf{R}_L \right)}_{\mathbf{R}_x} x, \quad (7.23)$$

where \mathbb{T}_{sh} represents shot noise only transfer matrix, \mathbb{T}_{rp} represents back action only transfer matrix and \mathbf{R} is the response function of the output field to the mirror displacement. Summarising the derived equations of field relation and mirror dynamics, it is then straightforward to get the response vectors and transfer matrices. The response vectors can be derived as

$$\mathbf{R}_R = \frac{4kx}{\gamma\tau} \left\{ \left[\frac{1}{1-iy} - \frac{\delta^2}{(1-iy)^2} \right] \begin{bmatrix} 0 \\ A_R \end{bmatrix} - \left[\frac{\delta}{1-iy} + \frac{\delta}{(1-iy)^2} \right] \begin{bmatrix} A_L \\ 0 \end{bmatrix} \right\} \frac{1}{\mathcal{B}(\Omega)\mathcal{B}(0)}, \quad (7.24)$$

$$\mathbf{R}_L = 4k\delta \left\{ \left[\frac{\delta^2}{(1-iy)^2} - \frac{1}{1-iy} \right] \begin{bmatrix} A_L \\ 0 \end{bmatrix} - \left[\frac{\delta}{1-iy} + \frac{\delta}{(1-iy)^2} \right] \begin{bmatrix} 0 \\ A_R \end{bmatrix} \right\} \frac{1}{\mathcal{B}(\Omega)\mathcal{B}(0)}. \quad (7.25)$$

I note than the contribution of \mathbf{R}_L is also a smallness term which can be neglected. The shot noise transfer matrixes can be derived as

$$\mathbb{T}_{sh}^R = \frac{1+iy}{1-iy} \begin{bmatrix} 1-\delta^2 & 0 \\ 0 & 1-\delta^2 \end{bmatrix} \frac{1}{\mathcal{B}(\Omega)}, \quad (7.26)$$

$$\mathbb{T}_{sh}^L = \frac{1}{(1-iy)^2} \begin{bmatrix} 0 & -2\delta \\ 2\delta & 0 \end{bmatrix} \frac{1}{\mathcal{B}(\Omega)}. \quad (7.27)$$

The back action only matrixes can be derived as

$$\begin{aligned} \mathbb{T}_{rp}^R = \frac{16\hbar k^2}{\gamma^2 \tau^2} \chi_{new} & \left\{ \left[\frac{1}{(1-iy)^2} - \frac{2\delta^2}{(1-iy)^3} + \frac{\delta^4}{(1-iy)^4} \right] \begin{bmatrix} 0 & 0 \\ A_R^2 & 0 \end{bmatrix} \right. \\ & + \left[\frac{\delta}{(1-iy)^2} + \frac{\delta}{(1-iy)^3} - \frac{\delta^3}{(1-iy)^3} - \frac{\delta^3}{(1-iy)^4} \right] \begin{bmatrix} 0 & 0 \\ 0 & A_R A_L \end{bmatrix} \\ & - \left[\frac{\delta}{(1-iy)^2} - \frac{\delta^3}{(1-iy)^3} + \frac{\delta}{(1-iy)^3} - \frac{\delta^3}{(1-iy)^4} \right] \begin{bmatrix} A_R A_L & 0 \\ 0 & 0 \end{bmatrix} \\ & \left. - \left[\frac{\delta^2}{(1-iy)^2} + \frac{2\delta^2}{(1-iy)^3} + \frac{\delta^2}{(1-iy)^4} \right] \begin{bmatrix} 0 & A_L^2 \\ 0 & 0 \end{bmatrix} \right\} \frac{1}{\mathcal{B}(0)^2 \mathcal{B}(\Omega)^2}, \end{aligned} \quad (7.28)$$

$$\begin{aligned} \mathbb{T}_{rp}^L = \frac{16\hbar k^2}{\gamma^2 \tau^2} \chi_{new} & \left\{ \left[\frac{1}{(1-iy)^2} - \frac{2\delta^2}{(1-iy)^3} + \frac{\delta^4}{(1-iy)^4} \right] \begin{bmatrix} 0 & 0 \\ A_R A_L & 0 \end{bmatrix} \right. \\ & + \left[\frac{\delta}{(1-iy)^2} + \frac{\delta}{(1-iy)^3} - \frac{\delta^3}{(1-iy)^3} - \frac{\delta^3}{(1-iy)^4} \right] \begin{bmatrix} 0 & 0 \\ 0 & A_R^2 \end{bmatrix} \\ & - \left[\frac{\delta}{(1-iy)^2} - \frac{\delta^3}{(1-iy)^3} + \frac{\delta}{(1-iy)^3} - \frac{\delta^3}{(1-iy)^4} \right] \begin{bmatrix} A_L^2 & 0 \\ 0 & 0 \end{bmatrix} \\ & \left. - \left[\frac{\delta^2}{(1-iy)^2} + \frac{2\delta^2}{(1-iy)^3} + \frac{\delta^2}{(1-iy)^4} \right] \begin{bmatrix} 0 & A_R A_L \\ 0 & 0 \end{bmatrix} \right\} \frac{1}{\mathcal{B}(0)^2 \mathcal{B}(\Omega)^2}. \end{aligned} \quad (7.29)$$

7.3 Amplitude quantum noise spectral density in displacement

In this section, I quantify the quantum noise spectral density of a single ring cavity and analyse the impacts of backscattering. Using the level of the backscattering amplitude we can distinguish 3 scenarios: weak backscattering, *i.e.* $\delta \ll 1$, critical backscattering, *i.e.* $\delta = 1$ and strong back scattering, *i.e.* $1 < \delta \leq 10$.

Weak backscattering

Weak backscattering means the backscattering coefficient is much smaller than 1 ppm, *i.e.* $|\delta|$ is much smaller than 1. In this case, I can get further approximated form of transfer matrices simplified from Eq. 7.26 to Eq. 7.29,

$$\mathbb{T}_{sh}^R = \frac{1+iy}{1-iy} \begin{bmatrix} 1 & 0 \\ 0 & 1 \end{bmatrix}, \quad \mathbb{T}_{sh}^L = \frac{1}{(1-iy)^2} \begin{bmatrix} 0 & -2\delta \\ 2\delta & 0 \end{bmatrix}. \quad (7.30)$$

$$\mathbb{T}_{rp}^R = \frac{16\hbar k^2 \chi_{new}}{\gamma^2 \tau^2 (1-iy)^2} \begin{bmatrix} 0 & 0 \\ A_R^2 & 0 \end{bmatrix}, \quad \mathbb{T}_{rp}^L = \frac{16\hbar k^2 \chi_{new}}{\gamma^2 \tau^2 (1-iy)^2} \begin{bmatrix} 0 & 0 \\ A_R A_L & 0 \end{bmatrix}. \quad (7.31)$$

One can already observe that the only significant difference comes from the new mechanical susceptibility modified by the optical rigidity when both input light fields are considered. Let us have a closer look the the DC intra cavity fields circulating in the 'R' direction. According to the backscattering phases derived in Sec. 7.1 and Eq. 7.15, only the component coupling from the 'L' input field due to backscattering is on the phase quadrature (the orthogonal quadrature with respect to the field circulating in 'R' direction which originates from 'R' input). When the two inputs are identical, the modified mechanical susceptibility can be written as

$$\chi_{new} = \frac{1}{-\mu\Omega^2 \left[1 + \delta \frac{16\hbar k^2}{m\Omega^2 \gamma^2 \tau^2 (1-iy)^2} \right]}, \quad (7.32)$$

Compared with the free mass mechanical susceptibility, the new one is more rigid in low frequency. The quantum noise amplitude spectral densities of the ring cavity are shown in Fig. 7.2. Both positive and negative δ that refer to the two sets of backscattering phases derived in Sec. 7.1 are considered. I take the ring cavity in the SSM experiment as described in Chapter. 2 as an example. The pump power is 1.7 W at each input port, the cavity ITM mass is 1 g and two ETMs are 100 g, respectively. The cavity ITM transmission is 632 ppm. We see that displacements are significantly suppressed at low frequencies. A peak representing the mechanical resonance shows up in the case of positive optical rigidity.

Critical backscattering

The critical backscattering occurs for $\epsilon = \frac{T^2}{4}$, *i.e.* $|\delta|=1$. According to Eq. 7.26, in this case, one input mode contribution will be totally cancelled at its corresponding output port. This destructive interference happens between the intra cavity field transmission and the direct reflection of the input field. One interesting feature in this case is that the output response to mirror displacements shows a speed meter like trend (see lower right subplot of Fig. 7.3.) This can be seen from Eq. 7.24. It results from the destructive interference between the sidebands of circulating mode in the intrinsic direction and the sidebands coupling from backscattering of the intra cavity mode circulating in the opposite direction. These two

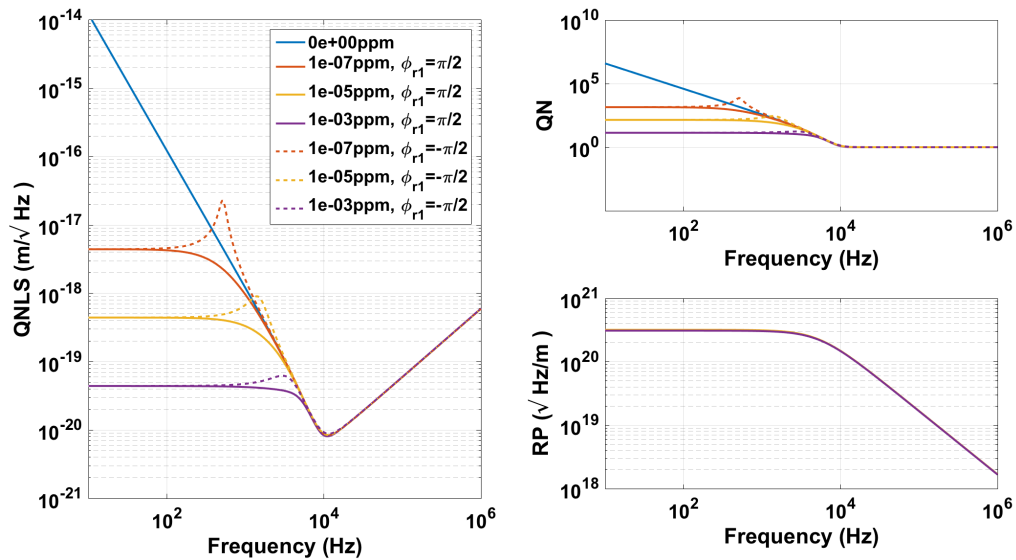


Figure 7.2: The quantum noise limited sensitivity (QNLS), quantum noise (QN) and response of a single ring cavity which is pump by two identical beams. The backscattering magnitudes are weak backscattering. The cavity and laser parameters used in the calculation represent the SSM experiment and are stated Chapter. 2. The two inputs powers are 1.7 W for each. The cavity effective mass is 1 g. The cavity ITM transmission is 632 ppm.

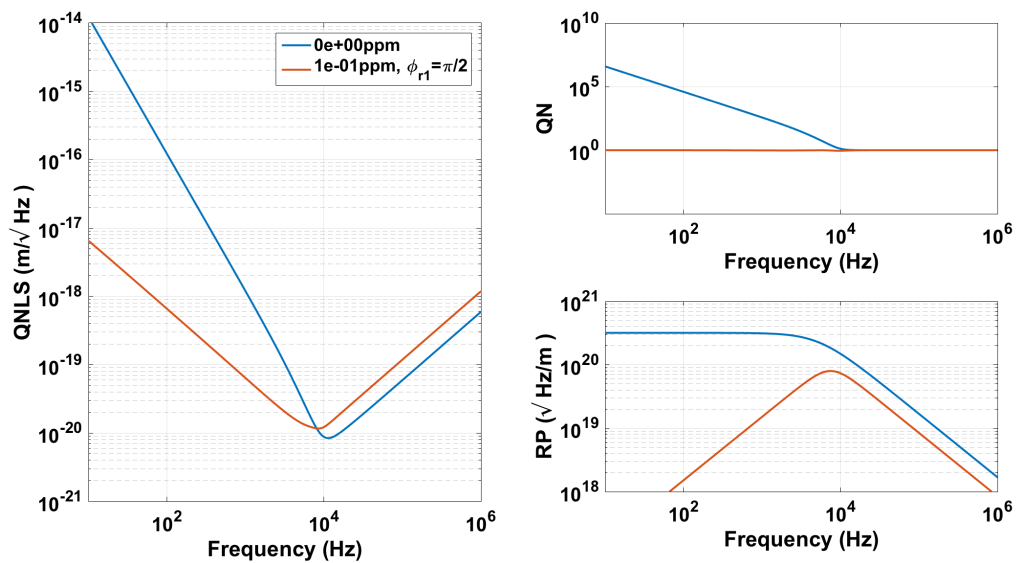


Figure 7.3: The QNLS, QN and response of a single ring cavity which is pumped by two identical beams. The backscattering strength is critical backscattering. The cavity and laser parameters in the calculation represent the SSM experiment and are stated in Chapter. 2. The two inputs powers are 1.7 W for each. The cavity effective mass is 1 g. The cavity ITM transmission is 632 ppm.

interfering components originate from the same input field. The backscattering fields are of even numbers of backscattering process. Meanwhile, the backscattered sidebands gain time delays.

However, it is not a speed meter configuration, although in the displacement sensitivity, the *speed-meter-like* trend can be observed at low frequency. It is again because that the optical rigidity suppresses the displacement originating from displacement independent radiation pressure force. Regarding to the displacement independent radiation pressure force, according to Eq. 7.17, part of the radiation pressure force is *speed-meter-like* cancelled, however, the part originating from backscattering fields of odd numbers of backscattering process is not cancelled.

Strong backscattering

Strong back scattering refers to cases when the backscattering coefficient is larger than 0.1 ppm and smaller than 1 ppm, *i.e.* $1 < \delta \leq 10$. In this case, at the output port, the fields from backscattering are stronger than the intrinsic modes, resulting in a drastically increased optical rigidity. The new effective mechanical susceptibility can be derived as,

$$\chi_{new} = \frac{1}{-\mu\Omega^2(1 + \delta(1 + \delta^2)\frac{16\hbar k^2}{\mu\Omega^2\gamma^2\tau^2(1-iy)^2})}, \quad (7.33)$$

Comparing Eq. 7.33 with Eq. 7.32, we can find that the terms proportional δ^2 which was neglected in Eq. 7.32 plays the dominant role in the strong backscattering case. Let us consider again the example of the mode circulating in the 'R' direction. The two dominated DC components on the amplitude quadrature are neither the intrinsic circulating mode in 'R' direction nor the reflection backscattering of odd numbers of backscattering process from intrinsic circulating mode in 'L' direction. Rather the two dominated components are the reflection backscattering from the intrinsic circulating mode in 'L' direction and the reflection backscattering from the part of circulating mode in 'L' direction which comes from the reflection backscattering of the odd order from the intrinsic circulating mode in 'R' direction. The quantum noise limited sensitivities, quantum noise spectral densities and responses are shown in Fig. 7.4.

7.3.1 Strain sensitivity calibration

We have seen in the previous section that in ring cavities with backscattering the displacement sensitivities at low frequencies are better than in the ideal case without backscattering. This is because of the effects of optical rigidity, which is common for both radiation pressure force and external forces. However, only the effects of optical rigidity on radiation pressure force appear in the displacement sensitivity. So in this section, I calibrate the

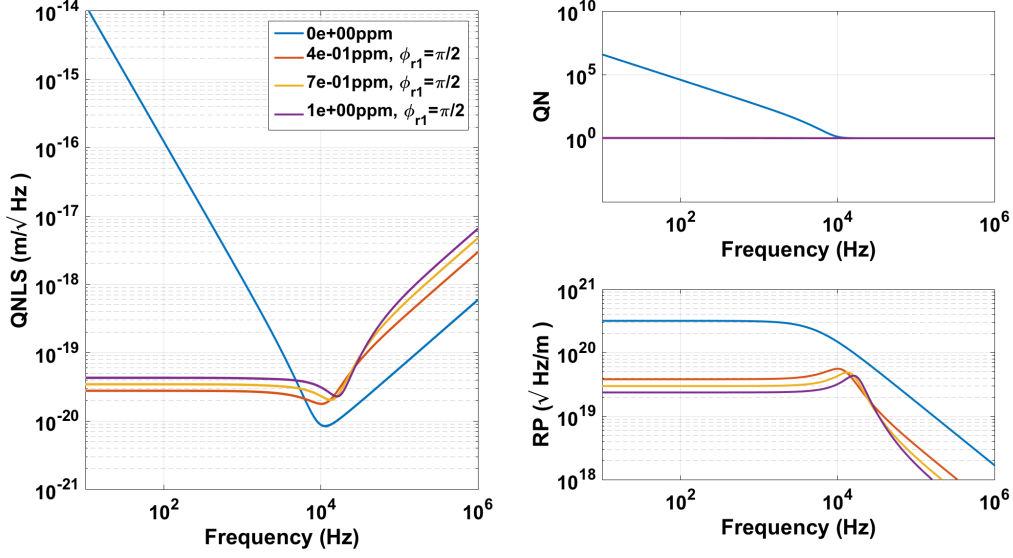


Figure 7.4: The QNLS, QN and response of a single ring cavity which is pumped by two identical beam in the case of strong backscattering. The cavity and laser parameters in the calculation represent the SSM experiment and are stated in Chapter. 2. The two inputs powers are 1.7 W for each. The cavity effective mass is around 1 g. The cavity ITM transmission is around 632 ppm.

displacement sensitivity to strain sensitivity.

The equation of motion of the mirror driven by gravitational wave strain can be described as

$$F(t) = (\chi^{-1} + K_{rig})x(t) = \mu \ddot{h}(t) \frac{L}{2}. \quad (7.34)$$

In the frequency domain, this translates to

$$(\chi^{-1} + K_{rig})x(\Omega) = -\mu \Omega^2 h(\Omega) \frac{L}{2}. \quad (7.35)$$

When the optical rigidity is zero, the displacement is just proportional to strain, since $\chi = -\frac{1}{\mu \Omega}$. While with backscattering, the cavity mirror's dynamic at low frequencies is dominated by the optical rigidity effect. To calibrate the displacement sensitivity to strain sensitivity, I only need to derive the strain response of the ring cavity, which relates to the displacement response as

$$\mathbf{R}_h = -\chi_{new} \mu \Omega^2 \mathbf{R}_x \frac{L}{2}. \quad (7.36)$$

In the case of weak backscattering, the strain sensitivity of the ring cavity is shown in Fig. 7.5. Observed from Fig. 7.5, the strain sensitivities in all cases are almost identical. That again proves that the dynamics of the cavity mirror driven by both the radiation pressure force and gravitational wave tidal force are modified in the same way due to backscattering. The effects get compensated in the quantum noise limited sensitivity in strain.

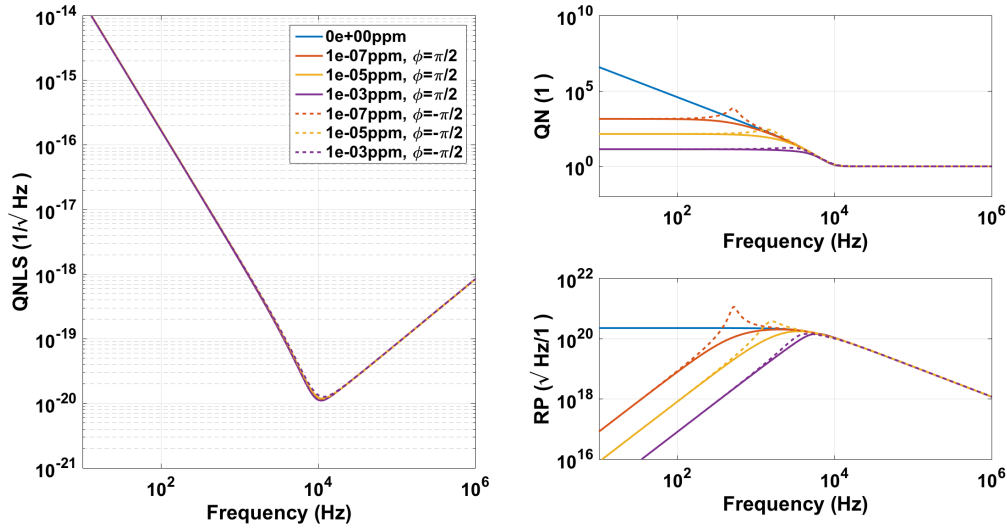


Figure 7.5: The QNLS in strain, QN and strain response of a single ring cavity which is pumped by two identical beams for weak backscattering. The cavity and laser parameters used in the calculation represent the SSM experiment and are stated in Chapter. 2. The two inputs powers are 1.7 W for each. The cavity effective mass is 1 g. The cavity ITM transmission is 632 ppm.

7.3.2 Quantum constraints of 2×4 pole system

The purpose of this section is originally to validate the correctness of the calculations done above, since these results appeared very counter-intuitive at the earlier stages of the investigations. From another point of view, the ring cavity with two inputs and two outputs is a typical multipole optomechanical system. Since interesting quantum backscattering phenomena are involved, it is also worthwhile to test the general quantum constraints of a multipole system using this case as an example. The theory of linear quantum $2 \times N$ pole systems is introduced by Braginsky and Khalili in [38]. Miao further investigated two new equalities in the constraints in the case of an ideal quantum limited 2×2 poles system in [77]. In this section, I take the mathematical description of continuous linear measurement in the existing literature and I apply it to the special example of the quantum backscattering in ring cavities.

In a multiple poles system, the general solutions of the Heisenberg equation of motion are,

$$Z_j(t) = Z_j^0(t) + \int_{-\infty}^{\infty} dt' \sum_{i=1}^N \chi_{Z_j F_i}(t-t') q(t') \quad (7.37)$$

$$F_j(t) = F_j^0(t) + \int_{-\infty}^{\infty} dt' \sum_{i=1}^N \chi_{F_j F_i}(t-t') q(t'),$$

where Z is the output of the detector, F is the input which refers to the radiation pres-

sure force, χ_{ZF} quantifies the detector's response to the system variable q , which is the displacement in my case and χ_{FF} quantifies the dynamical back action.

Going into frequency domain, in the case of the 2×4 poles system there are two inputs and two outputs:

$$\begin{aligned} Z_1(\omega) &= Z_1^0(\omega) + \chi_{Z_1 F_1}(\omega)q(\omega) + \chi_{Z_1 F_2}(\omega)q(\omega), \\ Z_2(\omega) &= Z_2^0(\omega) + \chi_{Z_2 F_1}(\omega)q(\omega) + \chi_{Z_2 F_2}(\omega)q(\omega), \\ F_1(\omega) &= F_1^0(\omega) + \chi_{F_1 F_1}(\omega)q(\omega) + \chi_{F_1 F_2}(\omega)q(\omega), \\ F_2(\omega) &= F_2^0(\omega) + \chi_{F_2 F_1}(\omega)q(\omega) + \chi_{F_2 F_2}(\omega)q(\omega). \end{aligned} \quad (7.38)$$

The susceptibility and the unsymmetrised spectral density are related as [77]

$$\chi_{AB}(\omega) - \chi_{BA}^* = (i/\hbar)[S_{AB}(\omega) - S_{BA}(-\omega)]. \quad (7.39)$$

The symmetrised spectral density \bar{S}_{AB} , is related with S_{AB} as [77]

$$\bar{S}_{AB}(\omega) = [S_{AB}(\omega) + S_{BA}(-\omega)]/2. \quad (7.40)$$

Following the standard approach in [38, 77], I define a auxiliary operator,

$$Q = \int d\omega [\alpha_1^* Z_1^0(\omega) + \beta_1^*(\omega) F_1^0(\omega) + \alpha_2^* Z_2^0(\omega) + \beta_2^*(\omega) F_2^0(\omega)], \quad (7.41)$$

where α, β are arbitrary functions. Since the value of the product of this operator is positive definite [38, 77], it means in terms of unsymmetrized spectral density, there is

$$\int_{-\infty}^{\infty} d\omega \begin{bmatrix} \alpha_1^* & \lambda Z \alpha_2^* & \beta_1^* & \beta_2^* \end{bmatrix} \underbrace{\begin{bmatrix} S_{Z_1 Z_1} & S_{Z_1 Z_2} & S_{Z_1 F_1} & S_{Z_1 F_2} \\ S_{Z_1 Z_2}^* & S_{Z_2 Z_2} & S_{Z_2 F_1} & S_{Z_2 F_2} \\ S_{Z_1 F_1}^* & S_{Z_2 F_1}^* & S_{F_1 F_1} & S_{F_1 F_2} \\ S_{Z_1 F_2}^* & S_{Z_2 F_2}^* & S_{F_1 F_2}^* & S_{F_2 F_2} \end{bmatrix}}_{\mathbb{S}} \begin{bmatrix} \alpha_1 \\ \alpha_2 \\ \beta_1 \\ \beta_2 \end{bmatrix} \geq 0. \quad (7.42)$$

So that there is the constrain,

$$\det(\mathbb{S}) \geq 0. \quad (7.43)$$

And the relations in Eq. 7.39 and Eq. 7.40 results in

$$S_{AB} = \bar{S}_{AB} \pm \frac{\hbar}{2i}(\chi_{AB} - \chi_{BA}^*). \quad (7.44)$$

In a simpler case, e.g. a 2×2 poles system, \mathbb{S} is a 2 by 2 matrix and the quantum constrain

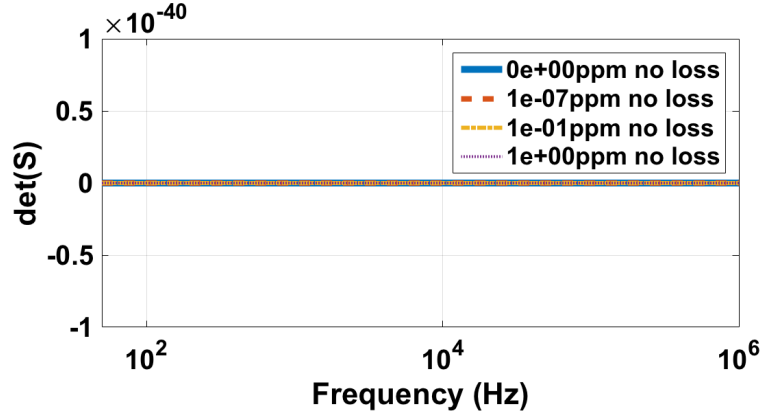


Figure 7.6: The determinate of spectral density \mathbb{S} in terms of different values of backscattering coefficients.

can be derived as

$$\bar{S}_{ZZ}(\omega)\bar{S}_{FF}(\omega) - |\bar{S}_{ZF}|^2 \geq \frac{\hbar}{4} |\chi_{ZF}|^2 \pm \hbar \text{Im}[\bar{S}_{ZF}^* \chi_{ZF}(\omega) - \chi_{FF}(\omega) \bar{S}_{ZZ}]. \quad (7.45)$$

However, in the case we are interested here it would be too lengthy to derive a similar form as above for a 2 X 4 poles system. Since each unsymmetrized spectral density term can be represented by the symmetrized spectral density and susceptibility according to Eq. 7.44, it is enough to check the validity already based on Eq. 7.43. In this special example of , the port ‘1’ and port ‘2’ refers to port ‘R’ and port ‘L’, respectively. The symmetrised double sided spectral density, e.g. $\bar{S}_{Z_1 Z_1}$, $\bar{S}_{Z_1 Z_2}$ can be written as

$$\bar{S}_{Z_1 Z_1} = \frac{1}{2} \left\{ \begin{bmatrix} \cos \theta_1 & \sin \theta_1 \end{bmatrix} \left(\mathbb{T}_{sh}^R (\mathbb{T}_{sh}^R)^\dagger + \mathbb{T}_{sh}^L (\mathbb{T}_{sh}^L)^\dagger \right) \begin{bmatrix} \cos \theta_1 \\ \sin \theta_1 \end{bmatrix} \right\}, \quad (7.46)$$

$$\begin{aligned} \bar{S}_{Z_1 Z_2} = \frac{1}{4} \left\{ \begin{bmatrix} \cos \theta_1 & \sin \theta_1 \end{bmatrix} (\mathbb{T}_{11} \mathbb{T}_{21}^\dagger + \mathbb{T}_{12} \mathbb{T}_{22}^\dagger) \begin{bmatrix} \cos \theta_2 \\ \sin \theta_2 \end{bmatrix} \right. \\ \left. + \begin{bmatrix} \cos \theta_2 & \sin \theta_2 \end{bmatrix} (\mathbb{T}_{21}^* \mathbb{T}_{11}^\dagger + \mathbb{T}_{22}^* \mathbb{T}_{12}^\dagger) \begin{bmatrix} \cos \theta_1 \\ \sin \theta_1 \end{bmatrix} \right\}, \end{aligned} \quad (7.47)$$

where θ_1, θ_2 are the arbitrary readout angles of the two port. In a similar way we can derive the calculations of the other auto and cross spectral densities according to their definitions . I note that, in terms of the spectral density of force, there are no readout quadratures existing by definition. Finally, when $\theta_1 = \theta_2 = \pi/2$, the determinate of matrix \mathbb{S} is shown in Fig. 7.6, which conforms to equality in the general quantum constraint.

7.3.3 Summary

In summary, the current findings of backscattering effects on quantum noise can be explained by two clues: the optical rigidity effects due to the backscattering coupling between circulating modes in two directions onto orthogonal quadratures; the destructive interference between two dominating fields originating from the same input field. The former one only exists when there are two identical input beams. The latter one shows significant effects in the critical backscattering case. In this chapter, with the basis of the work done in [1], the research was carried out in a more analytical way and the mechanisms of impacts of backscattering on quantum noise of a triangular cavity were presented in terms of three characteristic levels of backscattering amplitude.

Chapter 8

Analysis of imperfections of EPR type speed meters and squeezing

In this chapter, some of the follow up investigations for a new type of speed meter based on Einstein-Podolsky-Rosen (EPR) entanglement [78] are described. In Sec. 8.1, I review the features of EPR speed meter. In Sec. 8.2, I develop a framework which allows to take optical loss and several imperfections into account. I show their impacts on the quantum noise limited sensitivity. In Sec. 8.3, I analyse how squeezing can help to improve the overall sensitivity further in the optimal way and mitigate the impact of signal loss on the sensitivity of the EPR speed meter scheme in intermediate frequency band.

8.1 EPR speed meter conception

As introduced in Chapter. 1, the speed measurement can be realised by doing even numbers of sequential position measurements and designing a π phase shift between two in each pair. In Sagnac type speed meter, the arm cavity decay time provides the time delay among the sequential measurements.

The EPR speed meter scheme can be treated as two Michelson interferometers featuring correlated radiation pressure but have different bandwidths. The two different effective bandwidths features a time delay between two position measurement. In signal recycled Fabry-Pérot-Michelson interferometer, the two correlated effective Michelson modes can be achieved by pumping two orthogonal polarisation light into one configuration. The different effective bandwidth of the two modes can be constructed by inserting a quarter wave plat in the signal recycling cavity. Thus one polarisation 'sees' an interferometer featuring RSE, i.e. having a broad bandwidth, while the other polarisation mode gains an additional $\frac{\pi}{2}$ phase shift and hence 'sees' an interferometer with signal recycling, i.e. a comparably

narrow bandwidth. The outputs of two modes are combined on a polarisation beamsplitter with a 45 degree rotation. One readout schemes at the '+' port of the beamsplitter measures the speed of test masses, another independent readout scheme at the '-' port of the beam-splitter measures the position of test masses. The common radiation pressure force can be known and further cancelled in a EPR way by measuring the amplitude quadrature of the '+' port output field and the phase quadrature of the '-' port output field.

8.2 Impacts of imperfections

In this section I build the full framework which allows to calculate the quantum noise limited sensitivity in the cases of various imperfections.

The derivation of the full speed meter interferometer can be started from the derivation of the I/O relation of a Fabry-Pérot cavity. The well know optical I/O relation of a resonate FP cavity is recognised as

$$b = \mathcal{T}a + \mathcal{N}n + \mathcal{G} \begin{bmatrix} 0 \\ 1 \end{bmatrix} x, \quad (8.1)$$

where I define the output field as 'b', the input field from cavity ITM as 'a', input field from cavity ETM 'n' and mirrors' differential displacement 'x'. The corresponding optical transfer functions \mathcal{T} , \mathcal{N} and output response to displacement are recognised as

$$\mathcal{T} = \frac{\gamma_{ITM} - \gamma_{ETM} + i\Omega}{\gamma - i\Omega}, \quad (8.2)$$

$$\mathcal{N} = \frac{2\sqrt{\gamma_{ITM}\gamma_{ETM}}}{\gamma - i\Omega}, \quad (8.3)$$

$$\mathcal{G} = \frac{2\omega_0 E}{\gamma - i\Omega} \sqrt{\frac{\gamma_{ITM}}{cL}}, \quad (8.4)$$

and

$$\begin{aligned} \gamma_{ITM} &= \frac{cT_{ITM}}{4L}, \\ \gamma_{ETM} &= \frac{cT_{ETM}}{4L}. \end{aligned} \quad (8.5)$$

L is the length of the cavity, Ω is the angular frequency of sidebands caused by mirrors motion. The cavity half band width is $\gamma = \gamma_{ITM} + \gamma_{ETM}$. Note that in the case of a lossless cavity, the transmission of ETM can be treated as 0. The normalised circulating amplitude

inside the cavity E is defined as

$$E = \sqrt{\frac{2I}{\hbar\omega_0}}, \quad (8.6)$$

where I is the circulating power. ω_0 is the angular frequency of the laser. The radiation pressure force driven by both input fields from ITM and loss port is,

$$F_{rad} = \hbar G a_c + \frac{2\omega_0 E}{\gamma - i\Omega} \sqrt{\frac{\gamma_{ETM}}{cL}} n_c. \quad (8.7)$$

The cavity mirror displacements are driven by both radiation pressure noise and external force, *e.g.* gravitational wave tidal force. The mirror displacement is recognised as

$$x = \chi [F_{rad} + F_{GW}], \quad (8.8)$$

where χ is the mechanical susceptibility of the test masses. By summarising the equations above, the optomechanical I/O relation of a single cavity, taking mirror dynamics and radiation pressure into account, can be derived into the form of

$$b = \mathbb{T}a + \mathbb{N}n + \mathbf{R}x_{GW}, \quad (8.9)$$

where \mathbb{T} and \mathbb{N} are the transfer matrixes for corresponding input field from ITM and ETM. \mathbf{R} is the response vector to the gravitational wave induced mirrors displacements. In terms of the I/O relation of a Fabry-Pérot Michelson interferometer, the main beam splitter relations are introduced as

$$a^N = \frac{p+i}{\sqrt{2}}, a^E = \frac{p-i}{\sqrt{2}}, o = \frac{b^N - b^E}{\sqrt{2}}, \quad (8.10)$$

where the bright port and dark port input fields are symbolised as p and i , the input and output fields of North and East cavities are marked with subscript N and E . Hence, the Fabry-Perot cavity Michelson interferometer's optomechanical I-O relation can be derived as

$$o = \mathbb{T}_{MI}i + \mathbb{N}_{MI}n + \mathbf{R}_{MI}x_{GW}^d, \quad (8.11)$$

where

$$\mathbb{T}_{MI} = \mathbb{T}, \mathbb{N}_{MI} = \mathbb{N}, \mathbf{R}_{MI} = \mathbf{R}/\sqrt{2}. \quad (8.12)$$

Here $n = (n^N - n^E)/\sqrt{2}$ represents the effective vacuum coupling due to optical loss of both cavities. x_{GW}^d is defined as

$$x_{GW}^d = x_{GW}^N - x_{GW}^E. \quad (8.13)$$

In a EPR type speed meter, there are two Michelson position meter modes with different

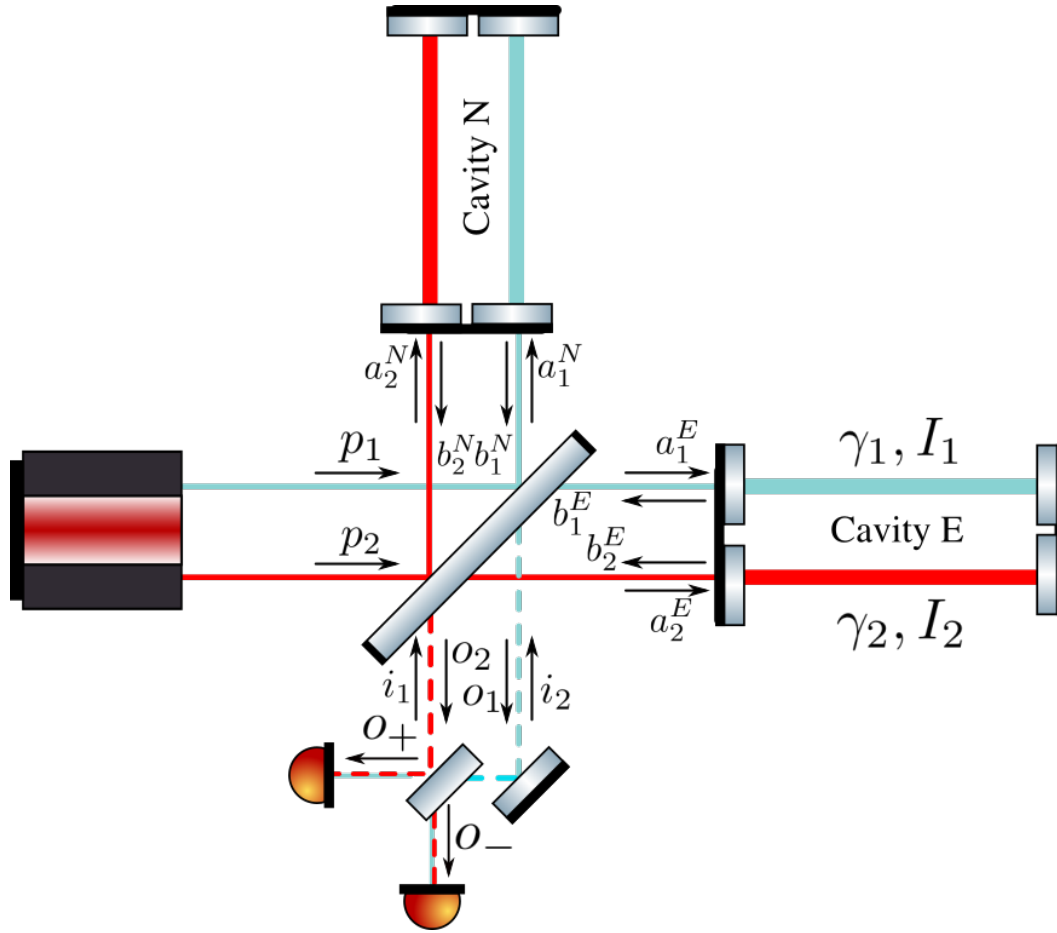


Figure 8.1: Conceptual demonstration of the EPR speed meter. For clarity the blue and red light beams are drawn separately in this diagram, while in the real implementation these beams would be exactly on top of each other. The red and light blue traces represent two orthogonal modes in polarisation. The process of measurement is described in the main text.

effective bandwidth. The broad band mode is named as mode ‘1’ and the narrow band mode is named as mode ‘2’. The circulating power distributions in the cavity of the two modes should obey

$$\Theta_1 = \frac{\gamma_1 \Theta (1 + \varepsilon)}{\gamma_1 + \gamma_2}, \quad \Theta_2 = \frac{\gamma_2 \Theta (1 + \varepsilon)}{\gamma_1 + \gamma_2}, \quad (8.14)$$

where Θ represents the total effective circulating power. The circulating power and half bandwidth of the two modes are labeled by subscription 1 and 2. I take into account a possible error in power distribution as ε . Note that, when calculating the I/O relation of each mode, the back action force created by the other mode is necessary to be taken into account, which is the key to create correlations between the two mode. Finally, in order to create two entangled states, the two outputs fields are overlapped on a polarisation beamsplitter which is rotated by 45 degree. The two output ports after the beamsplitter are named as + and -, respectively.

Table 8.1: Parameters used in the sensitivity modelling

$M=200$ kg	Reduced mass of the interferometer
$L =4000$ m	Arm Length
$\omega_0=2\pi c/1550$ nm	Optical pump frequency
$I=3$ MW	Cavity circulating power
$\gamma_1=2\pi \times 500$ Hz	Half bandwidth of EPR speed meter broadband mode
$\gamma_2=2\pi \times 30$ Hz	Half bandwidth of EPR speed meter narrow band mode
$\gamma_{MI}=2\pi \times 500$ Hz	Half bandwidth of Fabry-Perot cavity Michelson position meter
$\gamma_2=2\pi \times 125$ Hz	Half bandwidth of Sagnac speed meter

In terms of the output fields at the interferometer dark port, there are the relations

$$\hat{\sigma}_+ = \frac{\sqrt{T}\hat{\sigma}_1 + \sqrt{R}\hat{\sigma}_2}{\sqrt{2}}, \quad \hat{\sigma}_- = \frac{\sqrt{T}\hat{\sigma}_1 - \sqrt{R}\hat{\sigma}_2}{\sqrt{2}}, \quad (8.15)$$

In terms of the input field from the dark port, there are the relations

$$\hat{i}_1 = \frac{\sqrt{T}\hat{i}_+ + \sqrt{R}\hat{i}_-}{\sqrt{2}}, \quad \hat{i}_2 = \frac{\sqrt{T}\hat{i}_+ - \sqrt{R}\hat{i}_-}{\sqrt{2}}, \quad (8.16)$$

where

$$T = \frac{1}{2} - \xi, \quad T = \frac{1}{2} + \xi. \quad (8.17)$$

The possible imbalance of the polarisation beamsplitter is introduced as ξ . Gathering the relations above, the transfer matrix from the input fields to the output fields at '+' and '-' port can be calculated. So that the final optical I/O relation for the full interferometer can

be calculated in the form of

$$\begin{aligned} o_+ &= \mathcal{T}_+ i_- + \mathcal{R}_+ i_+ + \mathcal{N}_+ n + \mathcal{G}_+ \begin{bmatrix} 0 \\ 1 \end{bmatrix} x^d, \\ o_- &= \mathcal{T}_- i_- + \mathcal{R}_- i_+ + \mathcal{N}_- n + \mathcal{G}_- \begin{bmatrix} 0 \\ 1 \end{bmatrix} x^d, \end{aligned} \quad (8.18)$$

where $\mathcal{T}_{+,-}, \mathcal{R}_{+,-}, \mathcal{N}_{+,-}$ are the optical transfer functions from the corresponding input fields to the output fields of '+' and '-' port, $\mathcal{G}_+ \begin{bmatrix} 0 \\ 1 \end{bmatrix}$ and $\mathcal{G}_- \begin{bmatrix} 0 \\ 1 \end{bmatrix}$ are the response function of the output fields of '+' and '-' port to the dark mode mirrors displacements. The optomechanical I/O relation can be written as

$$\begin{aligned} o_+ &= \mathbb{T}_+ i_- + \mathbb{R}_+ i_+ + \mathbb{N}_+ n + \mathbf{R}_+ x_{\text{GW}}^d, \\ o_- &= \mathbb{T}_- i_- + \mathbb{R}_- i_+ + \mathbb{N}_- n + \mathbf{R}_- x_{\text{GW}}^d, \end{aligned} \quad (8.19)$$

where $\mathbb{T}_{+,-}, \mathbb{R}_{+,-}, \mathbb{N}_{+,-}$ are the optomechanical transfer matrices from the corresponding input fields to the output field of the '+' and '-' ports, \mathbf{R}_+ and \mathbf{R}_- are the response functions of the output fields of '+' and '-' port to the dark mode mirrors displacements caused by a gravitational wave tidal force. The differential speed information of the mirrors motion is contained in phase quadrature of the output field at '-' port. Meanwhile, the '-' port output field contains also the contribution from radiation pressure force driven by the '+' port input. So that although the amplitude quadrature of the '+' port output does not contain any mechanical motion information, it is entangled with the mechanical motion information in phase quadrature of the '-' port output. So that this entanglement can be removed in the EPR way by measuring the two orthogonal quadratures at the two ports, *i.e.*, phase quadrature of '-' port and amplitude quadrature of '+' port, and combining the photocurrents in the optimal way of obtaining the best quantum noise limited sensitivity.

The resulting optimal power spectral density is derived as

$$S_{opt} = \frac{S_{++}S_{--} - S_{+-}S_{-+}}{S_{++} + S_{--} - S_{+-} - S_{-+}}, \quad (8.20)$$

in which each term represents the auto spectral density or cross spectral density for the corresponding channels that are indicated by the subscripts. The way of calculating cross spectral densities for a 2x4 poles system was introduced in Sec. 7.3.2.

As shown in Fig. 8.2, the EPR speed meter is most sensitive to the output loss, *e.g.* the imperfect quantum efficiency of the photodiodes. The effects of arm loss, polarisation beam-splitter imbalance and power distribution on two polarisation mode are relative weak. The parameters are listed in Table. 8.1, which are identical to the parameters in [78].

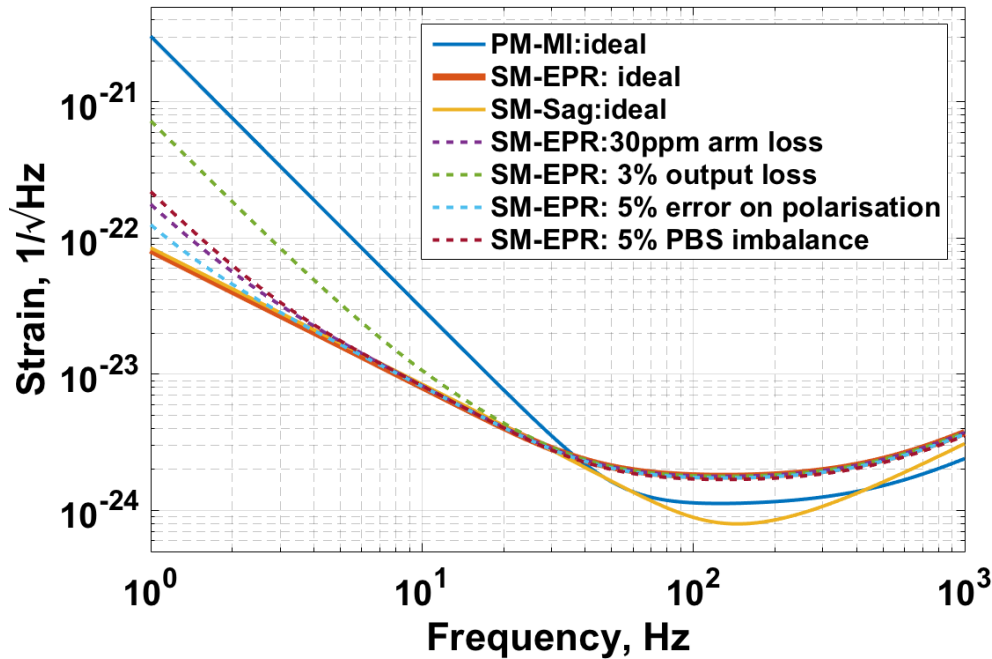


Figure 8.2: Quantum noise limited sensitivity of Michelson position meter, Sagnac speed meter and EPR speed meters which also include various types of imperfections. The Michelson position meter parameters are identical to the broad band mode of the ERP speed meter. The bandwidth of Sagnac speed meter is chosen to realise that the radiation pressure noise magnitude in low frequency is same as the shot noise magnitude.

One feature discussed in [78] is that the EPR speed meter can be shot noise limited above γ_2 . Since the speed meter behaviour occurs anyway only up to γ_2 , a moderate optical power could be chosen to get a shot noise limited position meter behaviour above this frequency. However, it is worse by around a factor of $\sqrt{2}$ compared with Michelson interferometer whose bandwidth is the same as the bandwidth of EPR speed meter broad band mode. This can be observed in Fig. 8.2. It is obvious from comparing Eq. 30 and Eq. 27 in [78]. This can also be understood intuitively, since only half of the mechanical motion information is detected at the ‘-’ port. In terms of a concrete design for gravitational wave detection, the parameters need to be optimised in detail. One way to improve the quantum noise limited sensitivity is utilising squeezing. In next section, I introduce how to improve the overall sensitivity by injecting two-modes squeezing.

8.3 Squeezing enhancement

Different from the 2×2 pole system, in which only one input and one output are involved, there are two inputs and two outputs correlated in the EPR speed meter configuration. The technique of squeezing modifies the input fields allowing that on the desired quadrature, signal and squeezed fluctuations are measured without degrading the SNR with anti-

squeezing fluctuations. So the ways of tailoring the input squeezing are decided by the anticipant result of measurement. Following this logic, in order to find the optimal way of implementing squeezing in this complex multi poles system, I start by deriving the photocurrents of the EPR speed meter.

Assuming there are no imperfections, the relation between optical transfer functions from input fields to the output fields at '+' and '-' ports in Eq. 8.19 and the optical transfer functions from input to the output fields in each Michelson position meter mode can be derived based on the derivations in Sec. 8.2 as

$$\begin{aligned}\mathcal{T}_+ = \mathcal{R}_- &= \frac{\mathcal{T}_1 - \mathcal{T}_2}{2}, \quad \mathcal{G}_+ = \frac{\mathcal{G}_1 + \mathcal{G}_2}{\sqrt{2}}, \\ \mathcal{T}_- = \mathcal{R}_+ &= \frac{\mathcal{T}_1 + \mathcal{T}_2}{2}, \quad \mathcal{G}_- = \frac{\mathcal{G}_1 - \mathcal{G}_2}{\sqrt{2}}.\end{aligned}\quad (8.21)$$

Summarising the derived equations in Sec. 8.2, the photocurrent on general readout quadrature can be derived as

$$\begin{aligned}C_+ &\propto \cos \phi_+ (\mathcal{R}_+ a_+^c + \mathcal{T}_+ a_-^c) + \sin \phi_+ (\mathcal{R}_+ a_+^s + \mathcal{T}_+ a_-^s) + \sin \phi_+ \hbar \chi \mathcal{G}_+ (\mathcal{G}_+ a_+^c + \mathcal{G}_- a_-^c) \\ &\quad + \sin \phi_+ \mathcal{G}_+ x_{\text{GW}}^d, \\ C_- &\propto \cos \phi_- (\mathcal{R}_- a_+^c - \mathcal{T}_- a_-^c) + \sin \phi_- (\mathcal{T}_- a_-^s - \mathcal{R}_- a_+^s) + \sin \phi_- \hbar \chi \mathcal{G}_- (\mathcal{G}_+ a_+^c + \mathcal{G}_- a_-^c) \\ &\quad + \sin \phi_- \mathcal{G}_- x_{\text{GW}}^d,\end{aligned}\quad (8.22)$$

where ϕ_+ and ϕ_- are the homodyne angles of the readouts at '+' and '-' ports. In order to obtain a pure speed meter, the corresponding homodyne angles ϕ_+ and ϕ_- can be chosen as 0 and $= \frac{\pi}{2}$. Thus we obtain

$$\begin{aligned}C_+ &\propto \mathcal{R}_+ a_+^c + \mathcal{T}_+ a_-^c, \\ C_- &\propto \mathcal{T}_- a_-^s + \mathcal{R}_- a_+^s + \hbar \chi \mathcal{G}_- \mathcal{G}_+ a_+^c + \hbar \chi \mathcal{G}_-^2 a_-^c + \mathcal{G}_- x_{\text{GW}}\end{aligned}\quad (8.23)$$

In the '-' port, the noise term induced by a_+^c can be subtracted by the known information from the '+' port by implementing filters in post analysis. Thus the optimal result can be obtained by combining the two parts in the way that $\mathcal{R}_+ C_- - \hbar \chi \mathcal{G}_- \mathcal{G}_+ C_+$. The noise photocurrents normalised to gravitational wave signals in displacement can be calculated as

$$C_{opt} \propto \frac{\mathcal{T}_-}{\mathcal{G}_-} a_-^s + \frac{\mathcal{R}_-}{\mathcal{G}_-} a_+^s + \hbar \chi \left(\mathcal{G}_- - \mathcal{G}_+ \frac{\mathcal{T}_+}{\mathcal{R}_+} \right) a_-^c. \quad (8.24)$$

It can be transformed into matrix format as

$$C_{opt} = \begin{bmatrix} 0 & 1 \end{bmatrix} \frac{\mathcal{R}_-}{\mathcal{G}_-} \begin{bmatrix} 1 & 0 \\ 0 & 1 \end{bmatrix} a_+ + \begin{bmatrix} 0 & 1 \end{bmatrix} \frac{\mathcal{T}_-}{\mathcal{G}_-} \begin{bmatrix} 1 & 0 \\ \mathcal{K}_{\text{EPR}} & 1 \end{bmatrix} a_-, \quad (8.25)$$

where $\mathcal{K}_{\text{EPR}} = \hbar\chi\frac{\mathcal{G}_-}{\mathcal{T}_-}(\mathcal{G}_- - \mathcal{G}_+\frac{\mathcal{T}_+}{\mathcal{R}_+})$. When the input fields a_+ and a_- are in squeezed state, the power spectral density of the optimal photocurrents can be written as [27]

$$\begin{aligned} S_{opt} = & \begin{bmatrix} 0 & 1 \\ 0 & 1 \end{bmatrix} \\ & \left\{ \frac{\mathcal{R}_-}{\mathcal{G}_-} \begin{bmatrix} 1 & 0 \\ 0 & 1 \end{bmatrix} \begin{bmatrix} \cos\theta_+ & -\sin\theta_+ \\ \sin\theta_+ & \cos\theta_+ \end{bmatrix} \begin{bmatrix} e^{2r_+} & 0 \\ 0 & e^{-2r_+} \end{bmatrix} \begin{bmatrix} \cos\theta_+ & \sin\theta_+ \\ -\sin\theta_+ & \cos\theta_+ \end{bmatrix} \left(\frac{\mathcal{R}_-}{\mathcal{G}_-} \begin{bmatrix} 1 & 0 \\ 0 & 1 \end{bmatrix} \right)^\dagger \right. \\ & + \frac{\mathcal{R}_+}{\mathcal{G}_-} \begin{bmatrix} 1 & 0 \\ \mathcal{K}_{\text{EPR}} & 1 \end{bmatrix} \begin{bmatrix} \cos\theta_- & -\sin\theta_- \\ \sin\theta_- & \cos\theta_- \end{bmatrix} \begin{bmatrix} e^{2r_-} & 0 \\ 0 & e^{-2r_-} \end{bmatrix} \begin{bmatrix} \cos\theta_- & \sin\theta_- \\ -\sin\theta_- & \cos\theta_- \end{bmatrix} \\ & \left. \left(\frac{\mathcal{R}_+}{\mathcal{G}_-} \begin{bmatrix} 1 & 0 \\ \mathcal{K}_{\text{EPR}} & 1 \end{bmatrix} \right)^\dagger \right\} \begin{bmatrix} 0 \\ 1 \end{bmatrix}, \quad (8.26) \end{aligned}$$

where r_+ and r_- are the squeezing factors defining the strength of squeezing, θ_+ and θ_- define the squeezing quadratures. Simplifying the equation above, I define

$$\mathbf{V}_+ = \begin{bmatrix} 0 & 1 \end{bmatrix} \frac{\mathcal{R}_-}{\mathcal{G}_-}, \quad \mathbf{V}_- = \begin{bmatrix} 0 & 1 \end{bmatrix} \frac{\mathcal{T}_-}{\mathcal{G}_-} \begin{bmatrix} 1 & 0 \\ \mathcal{K}_{\text{EPR}} & 1 \end{bmatrix}. \quad (8.27)$$

Then there is

$$\begin{aligned} S_{opt} = & e^{2r_+}(\mathbf{V}_+^c \cos\theta_+ + \mathbf{V}_+^s \sin\theta_+)^2 + e^{-2r_+}(-\mathbf{V}_+^c \sin\theta_+ + \mathbf{V}_+^s \cos\theta_+)^2 \\ & + e^{2r_-}(\mathbf{V}_-^c \cos\theta_- + \mathbf{V}_-^s \sin\theta_-)^2 + e^{-2r_-}(-\mathbf{V}_-^c \sin\theta_- + \mathbf{V}_-^s \cos\theta_-)^2. \end{aligned} \quad (8.28)$$

It is the straightforward to obtain that, in order to get the minimal quantum noise spectral density with squeezing injection from the + and - port, the rotation angle should follow

$$\theta_+ = \text{atan} \left(-\frac{\mathbf{V}_+^c}{\mathbf{V}_+^s} \right) = 0, \quad \theta_- = \left(-\frac{\mathbf{V}_-^c}{\mathbf{V}_-^s} \right) = \text{atan}(-\mathcal{K}_{\text{EPR}}). \quad (8.29)$$

The sensitivity curves that demonstrate the squeezing enhancement are shown in Fig. 8.3. As a conclusion, in order to get the best overall enhancement of the sensitivity via squeezing, two squeezed vacuum injections are required. The ‘-’ port squeezing requires frequency dependent rotation, while the ‘+’ port squeezing is frequency independent. When into both ports squeezing with the same squeezing factor are input, there is an overall sensitivity improvement across the whole frequency band by the squeezing factor. By enhancing the ‘+’ port squeezing, the intermediate frequency sensitivity, *i.e.* $\gamma_2 < \Omega < \gamma_1$, can be further improved. This can be understood with the help with Eq. 8.25. The shot noise stream consists of two components contributed from two uncorrelated inputs. It is evident that low frequencies, *i.e.* $\Omega \ll \gamma_2$, and high frequency, *i.e.* $\Omega \gg \gamma_1$, $|\mathcal{R}_-| \approx 0$. However, in

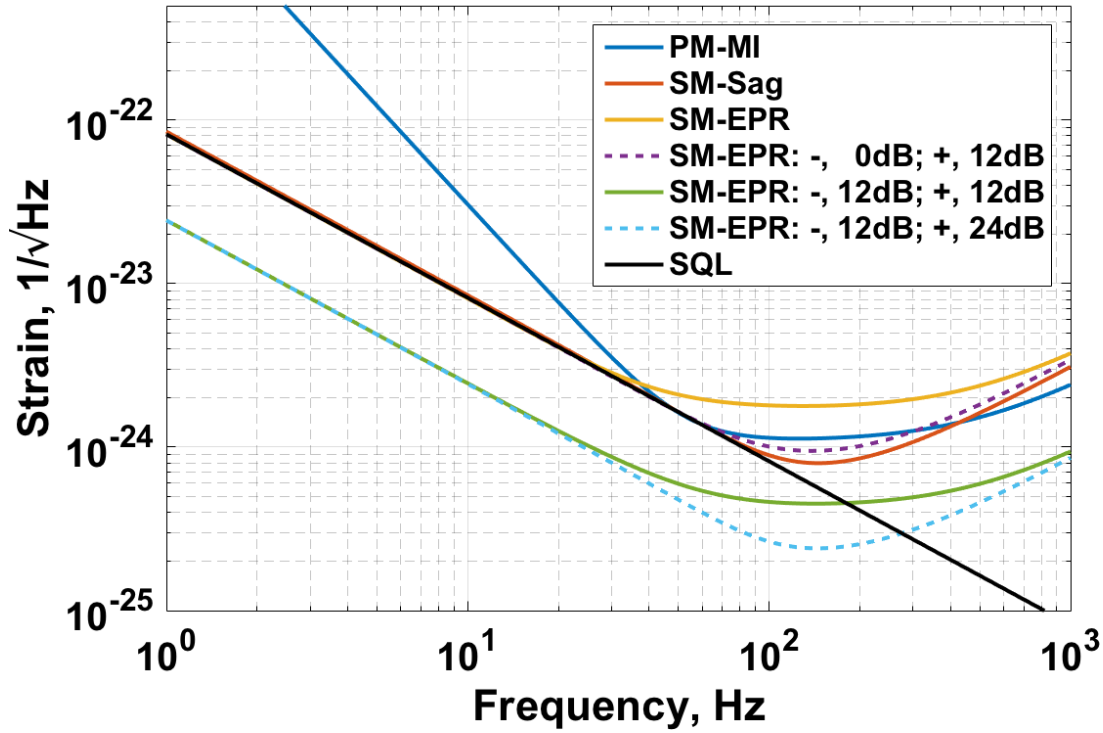


Figure 8.3: Quantum noise limited sensitivity in strain of Michelson position meter, Sagnac speed meter and EPR speed meters with optimised different levels of squeezing injection from ‘+’ and ‘-’ port.

the intermediate frequency range, the absolute values of \mathcal{R}_- and \mathcal{T}_- are compatible. More specifically, there is

$$\left| \frac{\mathcal{R}_-}{\mathcal{T}_-} \right| = \frac{(\gamma_1 + \gamma_2)\Omega}{\gamma_1\gamma_2 + \Omega^2}. \quad (8.30)$$

In the frequency range from γ_2 to γ_1 , we find that $\left| \frac{\mathcal{R}_-}{\mathcal{T}_-} \right| > 1$. So that the squeezing injection in + port helps the intermediate frequency sensitivity with a great effort.

8.4 Summary

The EPR speed meter was proposed in [78] with several advantages, for example, it is simple to be realised by taking minor extensions on the traditional Michelson configuration and it can be switched between speed meter mode and position meter mode without any replacement of hardwares, rather simply by switching the readout quadrature of the ‘+’ output from amplitude quadrature to phase quadrature.

In this chapter, I extended the work in [78]. Here we prove the compatibility of the scheme with the injection of squeezed light. In Sec. 8.3, I showed how squeezing should be implemented in EPR speed meter, *i.e.* inject two-mode squeezing into both ‘-’ and ‘+’ ports in a

frequency dependent and independent way, respectively. It is worthwhile to mention that the '+' port input vacuum contaminates the shot noise limited sensitivity mainly at intermediate frequency. This impact can be mitigated by injecting phase quadrature squeezed vacuum.

In Sec. 8.2, I developed a complete framework which allows me to quantify the effect of loss and several potential imperfections on the quantum noise limited sensitivity of the EPR speed meter. As it turned out, the output loss shows the most drastic impact on low frequency sensitivity with a moderate loss factor.

In terms of implementing EPR speed meter into future generation gravitational wave detectors, parameter studies and the comparison between different types of speed meters are still ongoing.

Chapter 9

An acceleration meter

In the field of gravitational wave detection, the current detectors are all position meters. In the quantum regime, the position measurement induces the back action noise due to the force actuating on the test mass. There is a Heisenberg-like uncertainty relation that constrains the measurement noise and back action noise as introduced in Section. 1.4 and uncovered in [77]. Speed meters are recognised as back action evasion schemes, since the momentum is a conserved variable in quantum measurements. However, in speed measurements, the quantum noise is still limited by back action noise at low frequencies, since the momentum is not anymore proportional to the velocity under driving of radiation pressure. Further analysis reveals momentum, $P = mv - gSM(t)a_c$, where $gSM(t)$ is the strength of coupling between the light and the mirrors' mechanical motion, and $a_c = (a + a^\dagger)/2$ is the amplitude quadrature of light, which is proportional to the radiation pressure force [48]. While the input observable to gravitational wave detector is actually the gravitational wave tidal force. One may consider to treat the force actuating on the mirror as the observable and measuring the acceleration of the mirror motion. Thus a weaker coupling between light to the acceleration of the mirror in low frequency should be expected. In this Chapter, I develop the concept of an acceleration meter and the corresponding configuration for its realisation. The acceleration meter conception could also be potentially interesting to general opto-mechanical system.

In the same manner as used in Sec. 1.4.4 , I introduce the expression of an acceleration measurement,

$$\ddot{x}(\Omega) = \Omega^2 \cdot \chi(\Omega)[\Omega^2 \cdot F_{BA}(\Omega) + F_{ext}\Omega] + Z(\Omega) \quad (9.1)$$

The noise spectral density in displacement can be calculated as

$$S = \frac{S_Z}{\Omega^4} + \Omega^4 |\chi(\Omega)|^2 S_F \quad (9.2)$$

Compared with the position measurement, at low frequencies, the acceleration measure-

ment is dominated by shot noise instead of back action noise. With a stronger back action evasion, the shot noise raises up due to the the signal reduction. The interferometer is a phase meter in nature. The phase is directly modulated by test mass position motion so the shot noise is white noise in terms of position measurement in the cavity half bandwidth. In the same manner, radiation pressure noise is white noise in terms of force measurement in the cavity half bandwidth. So the weights of the sensing noise and back action noise can be traded off by choosing different measurement observables.

9.1 Acceleration measurement

In Sec. 1.4.4, I introduced two types of speed meters, the circulation polarisation speed meter based on the Michelson interferometer and the Sagnac speed meter interferometer. Based on the understandings introduced in Sec. 1.4.4, it is possible to get an acceleration meter by combining the two typologies, *i.e.* by implementing the circulation polarisation scheme on a Sagnac interferometer as shown in Fig. 9.1. Firstly, the left circulation polarisation light goes over the Sagnac and senses the differential speed information $\dot{x}_{\text{darm}}(t_1)$. Then the dARM mode sidebands will be transformed into p polarisation by the QWP. They enter into the interferometer again from the dark port after reflecting from the PCM and traveling through the QWP as the right circulation fields. So they interact with the right circulation polarisation bright carrier light in the interferometer. The carrier needs to acquire $N\pi$ phase shift, where N is a even number, as it propagates from the QWP towards PCMs and reflects off. The clockwise and anti-clockwise traveling signal sidebands in the Sagnac on right circulation polarisation can be written as

$$\begin{aligned}\delta\phi_{\text{CW}} &\propto \sqrt{T}\dot{x}_{\text{darm}}(t_1) + x_{\text{N}}(t_2) + x_{\text{E}}(t_2 + \Delta t), \\ \delta\phi_{\text{CCW}} &\propto -\sqrt{R}\dot{x}_{\text{darm}}(t_1) + x_{\text{E}}(t_2) + x_{\text{N}}(t_2 + \Delta t),\end{aligned}\tag{9.3}$$

where Δt is the time delay between the light's interactions with cavity mirrors in the N and E cavities. The fields in the two directions will interfere at the main beam splitter again resulting as

$$\ddot{x}_{\text{darm}}(t_1) \propto -\sqrt{R}\delta\phi_{\text{CW}} + \sqrt{T}\delta\phi_{\text{CCW}} = \dot{x}_{\text{darm}}(t_2) - \dot{x}_{\text{darm}}(t_1)\tag{9.4}$$

where $R = T = \frac{1}{2}$, $t_2 - t_1 = 2\Delta t$. Considering the time delay $2\Delta t$ is still small compared with low frequency gravitational wave signal period, acceleration measurements should be able to be realised based on this configuration.

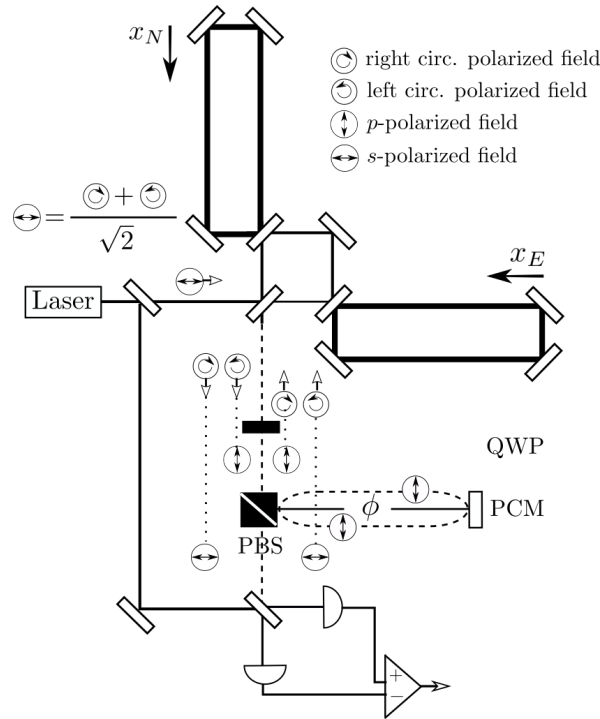


Figure 9.1: Schematic of Sagnac based circulation polarisation acceleration meter. The measurement process is described in the main text.

9.2 Quantum noise

Again, I start from the I/O relation of the single arm cavity for calculating the quantum noise spectral density of this configuration. Then I compare its quantum behaviour with speed meter and position meter. Since in one arm cavity there are two light travel directions (clockwise and anticlock wise) and two orthogonal polarisation for each of these directions, there are four back action effects terms. I split the back action terms out from the I/O relation of one single cavity, e.g I/O relation for the right circulation polarisation and clockwise direction of cavity E can be written as

$$b_{rRE} = \mathbb{T}_{rRE}^{\text{arm}} a_{rRE} + \mathbb{T}_{rLE}^{b,a} a_{rLE} + \mathbb{T}_{lRE}^{b,a} a_{lRE} + \mathbb{T}_{lLE}^{b,a} a_{lLE} + \mathbf{R}_{rRE} x_E, \quad (9.5)$$

and where symbol $a = (a_c, a_s)^T$ and $b = (b_c, b_s)^T$ represent the input and output fields of cavities, respectively. $\mathbb{T}_{rRE}^{\text{arm}}$, $\mathbb{T}_{rLE}^{b,a}$, $\mathbb{T}_{lRE}^{b,a}$ and $\mathbb{T}_{lLE}^{b,a}$ are the optical transfer matrices and back action only transfer matrices for input fields of the corresponding directions and polarisations, which are indicated by subscripts. R means clock-wise direction, L means anti-clockwise direction. r means right circulation polarisation, l means left circulation polarisation. Considering two cavities, two traveling directions and two circulation polarisation modes, there should be eight equations for describing the full interferometer I/O relations.

The optical transfer matrix and back action only transfer matrix can be written as

$$\begin{aligned}\mathbb{T}^{\text{arm}} &= e^{2i\beta} \begin{bmatrix} 1 & 0 \\ -\mathcal{K} & 1 \end{bmatrix}, \\ \mathbb{T}^{\text{b.a.}} &= e^{2i\beta} \begin{bmatrix} 0 & 0 \\ -\mathcal{K} & 0 \end{bmatrix},\end{aligned}\tag{9.6}$$

where \mathcal{K} is the Kimble optomechanical factor [25] for a single cavity defined as

$$\mathcal{K} = \frac{2\Theta\gamma}{\Omega^2(\gamma^2 + \Omega^2)},\tag{9.7}$$

and where all the symbols were already defined in Chapter. 6. $\beta = \arctan\left(\frac{\Omega}{\gamma}\right)$ is the phase shift that the light sidebands with frequency Ω acquire after propagating through and then reflecting off the cavity.

The main beam splitter I-O relations can be easily written out, *e.g.*

$$\begin{aligned}a_{rRN} &= \sqrt{T_{BS}}i_r + \sqrt{R_{BS}}p_r, \\ a_{rLE} &= -\sqrt{R_{BS}}i_r + \sqrt{T_{BS}}p_r, \\ a_{lRN} &= \sqrt{T_{BS}}i_l + \sqrt{R_{BS}}p_l, \\ a_{lLE} &= -\sqrt{R_{BS}}i_l + \sqrt{T_{BS}}p_l, \\ o_l &= \sqrt{T_{BS}}b_{lLN} - \sqrt{R_{BS}}b_{lRE},\end{aligned}\tag{9.8}$$

where symbols i, p represent the dark port and bright port input fields, symbol o, q represent the dark port and bright port output fields. The dark and bright input fields in p-polarisation can be written as a linear combination of left and right circulating fields as

$$\begin{aligned}i_p &= (i_r + i_l)/\sqrt{2}, \\ p_p &= (p_r + p_l)/\sqrt{2}.\end{aligned}\tag{9.9}$$

The Sagnac inner field relations are given by:

$$\begin{aligned}a_{lRE} &= b_{lRN}, a_{rRE} = b_{rRN}, \\ a_{lLE} &= b_{lLE}, a_{rLN} = b_{rLE}.\end{aligned}\tag{9.10}$$

The acquired Φ phase shift in the polarisation circulating cavity can be represented by a matrix \mathbb{P} ,

$$\mathbf{i}_r = \mathbb{P}\mathbf{o}_l,\tag{9.11}$$

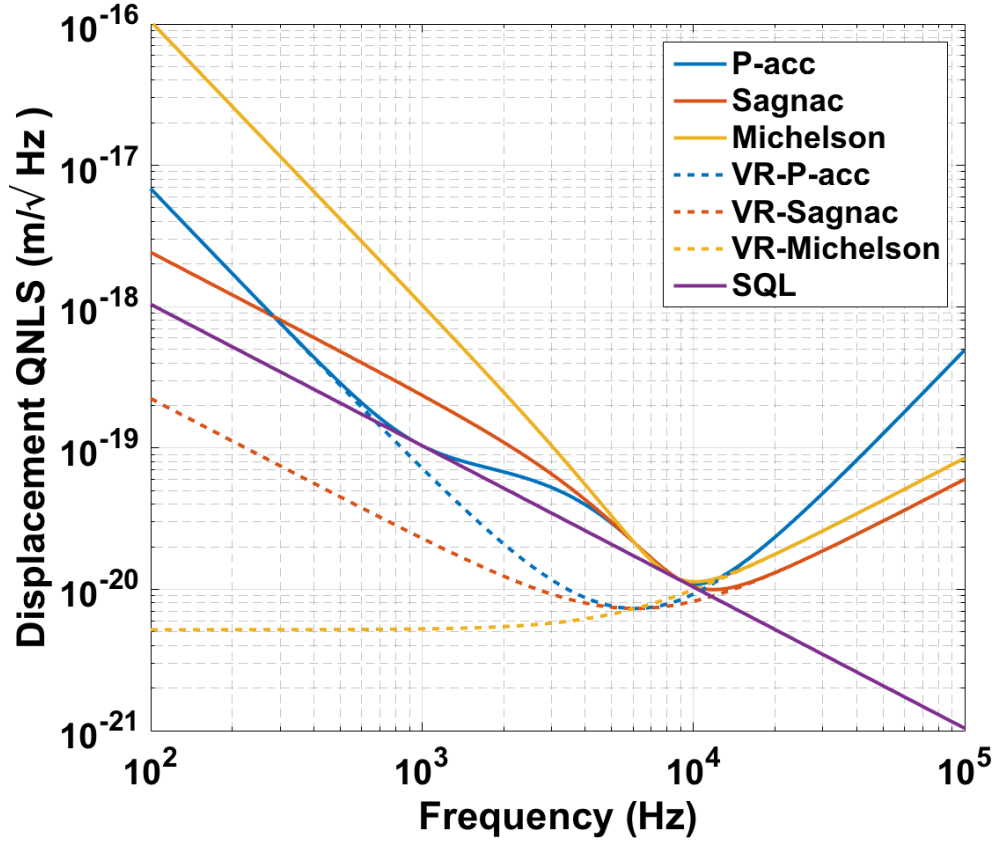


Figure 9.2: Quantum noise limited sensitivity of three different types of interferometer: polarisation circulation acceleration meter, Sagnac speed meter and Michelson position meter. The input laser power of the Michelson position meter is chosen as twice of the polarisation circulation acceleration meter and Sagnac speed meter, in order to guarantee they have identical circulating power. The other parameters of the three meters are chosen the same as for the Glasgow SSM experiment. The solid traces represent the conventional case, the dash traces represent the case of ideal variational readout.

where \mathbb{P} is the rotation matrix:

$$\mathbb{P} = \begin{bmatrix} \cos(\Phi) & -\sin(\Phi) \\ \sin(\Phi) & \cos(\Phi) \end{bmatrix}. \quad (9.12)$$

Finally the full configuration I-O relation can be derived in the form of

$$\mathbf{o}_p = \mathbf{o}_r = e^{2i\beta_{acc}} \begin{bmatrix} 1 & 0 \\ -\mathcal{K}_{acc} & 1 \end{bmatrix} \mathbf{i}_p + e^{i\beta_{acc}} \begin{bmatrix} 0 \\ \sqrt{2\mathcal{K}_{acc}} \end{bmatrix} \frac{x_{darm}}{x_{SQL}} \quad (9.13)$$

And the quantum noise limited sensitivity with the homodyne detection angle ζ can be calculated as

$$S = \frac{x_{SQL}^2 e^{-2r} + [\cot \zeta - \mathcal{K}_{acc}]^2 e^{2r}}{2 \mathcal{K}_{acc}}, \quad (9.14)$$

where r represents the frequency independent squeezing strength. This expression can also be used for speed meter and position meter by replacing \mathcal{K}_{acc} by the corresponding Kimble optomechanical factors of speed meter and position meter.

For Michelson position meter, Sagnac speed meter, polarisation circulation speed meter and polarisation circulation acceleration meter with identical input laser power, cavity length and dARM mode effective test mass, there are the relations

$$\begin{aligned}\mathcal{K}_{\text{Sag}} &= 4\mathcal{K}_{\text{MI}} \sin^2 \beta, \\ \mathcal{K}_{\text{P-spe}} &= 2\mathcal{K}_{\text{MI}} \sin^2 \beta, \\ \mathcal{K}_{\text{P-acc}} &= 2\mathcal{K}_{\text{P-spe}} \sin^2 2\beta,\end{aligned}\tag{9.15}$$

where \mathcal{K}_{MI} is the Kimble optomechanical factor of a Fabry-Pérot Michelson interferometer. If $\cot \zeta = \mathcal{K}$, the back action term can be cancelled completely. This technique is called variational readout [25, 79].

In order to make a fair comparison of the different types of meters, I decided to set them all to identical circulating power. Again I use as example the parameters of the proof of concept SSM experiment in the University of Glasgow [57, 69] for the Sagnac speed meter model. the same input power is for the polarisation circulation acceleration meter, while doubled input power is for Michelson position meter.

Fig. 9.2 shows the results of my analysis: the solid traces show the quantum noise limited sensitivity of three types of meters, while the dash line show the quantum noise limited sensitivity of the corresponding meters employing variational readout. At low frequencies (below 1000 Hz) the acceleration meter sensitivity follows the same trend as the position meter, however, it does not benefit from variational readout. That tells, acceleration meter can achieve very strong back action noise cancellation in low frequency, however shot noise raise up because of signal reduction in low frequency.

In Fig. 9.3, the dash-dots line show the quantum noise limited sensitivity of the three types of interferometers with squeezing injection. By injecting 10dB frequency independent squeezing, the acceleration meter gets improved sensitivity in both low frequency and high frequency, only the intermediate frequency sensitivity which is dominated by radiation pressure noise gets worse. The similar behaviour can be observed for increasing the laser power.

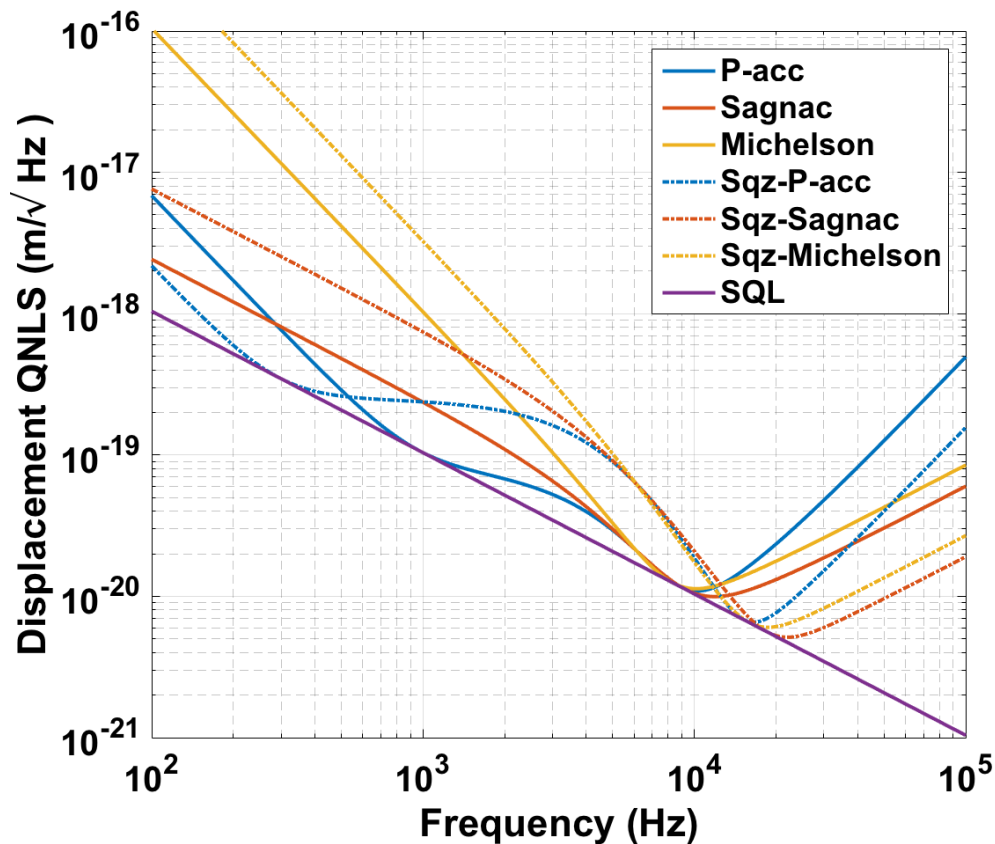


Figure 9.3: Quantum noise limited sensitivity of three different types of interferometer: polarisation circulation acceleration meter, Sagnac speed meter and Michelson position meter. The input laser power of Michelson position meter is chosen as twice of the polarisation circulation acceleration meter and Sagnac speed meter guaranteeing they have the identical intra cavity circulating power. The other parameters of the three meters are chosen as the same as the Glasgow SSM experiment. The solid traces represent the conventional case, the dash traces represent the case of injecting 10 dB frequency independent squeezing.

9.3 Summary

In terms of this particular acceleration meter configuration, we can observe that there are two frequencies at which the sensitivity touches the standard quantum limit. This results in better sensitivity of this acceleration meter compared with a Michelson interferometer below 10000 Hz. Of course, the parameters used in this example give high radiation pressure noise in the Michelson position meter model, whether this acceleration meter configuration with parameters of real gravitational wave detectors can show this superiority significantly is still worthwhile investigation.

Alternative configurations need to be investigated if this particular configuration is too complex to be taken as an realistic engineering program. If the superiority of acceleration meter stated above also holds for a more realistic model, more detailed considerations for the acceleration meter concept could be developed for the future.

Chapter 10

Conclusions

The design sensitivities of the current gravitational wave detectors are limited by quantum noise nearly over the whole detection band. Speed meter is considered to be an option for the future generation gravitational wave detectors. The Sagnac speed meter proof of concept experiment is currently carried out in Glasgow. We aimed to demonstrate a factor of 3-5 superiority of the quantum radiation pressure noise limited sensitivity from the 100 Hz to 1000 Hz, compared to an equivalent Michelson interferometer. Since in the Sagnac interferometers, the light fields traveling in two directions share the same path and always interfere destructively at the signal port, conventional DC readout is unsuitable. Therefore, balanced homodyne detection was planned to be implemented in the SSM experiment.

In terms of implementing suspended BHD, Chapter. 3 investigated one practical problem, *i.e.* misalignment and mismatch between the separated local oscillator and signal beam. My analysis provided a framework allowing to solve arbitrary misalignments or mismatches and it can be applied to any interferometer configuration. The results were applied to the Glasgow proof of concept experiment. One of the main discoveries was that the misalignments between LO and signal on the output path only degrades the amplitude spectral density of the shot noise limited part of the quantum noise noise sensitivity, while the sensitivity in the back-action noise limited range is not affected by misalignments. In addition, we investigated the mechanism of noise coupling in dynamic misalignments due to beam jitter, which creates time varying HOMs. Based on the suspension models used in SSM experiment, we found that the seismically introduced beam jitter noise is well below the quantum noise level in the experiment in the targeted frequency range of 100-1000 Hz.

In Chapter. 4, I discussed several practical issues in terms of implementing balanced homodyne readout in A+, including derivations of local oscillator stability requirement, several options of output mode cleaner arrangement, local oscillator backscattering effects and sensing and control for different degrees of freedom in the balanced homodyne readout. Conservatively, in order to suppress the seismic noise via pure passive isolation systems and

to guarantee the required LO stability, several triple stage suspensions would be required for delivering the LO beam towards the BHD beam splitter. We compared the advantages and disadvantages of various options of the BHD optical layout and we found, considering the noise requirements imposed by thermal noise of the OMC itself, that placing two OMCs after the BHD beamsplitter to be the most practical option. We found that the POP option is in all cases less susceptible compared with BSAR option to LO backscattering noise, leading a better choice for the delivery of the LO.

It was shown theoretically that an asymmetry of the main beamsplitter can lead to a reduction of the quantum noise limited sensitivity of the Sagnac speed meter at low frequencies. This is because the radiation pressure noises created by the input field fluctuations from the laser port couple into the readout port of the interferometer as excess noises. In Chapter. 5, we proposed an approach to solve this problem by utilising balanced homodyne readout and choosing a proper local oscillator delivery port. Picking the local oscillator beam from the reflection beam at interferometer laser port (the *co-moving* LO option), or from the direct reflection off the main beam splitter's AR coating (the BSAR LO option), the magnitude of the transfer function of the laser fluctuations from the pumping port to the readout one can be significantly reduced. We showed analytically that this cancellation of laser fluctuations stems from the very nature of the BHD scheme that is inherently insensitive to any common variations of light phase in the LO and signal beam of the BHD driven by input laser fluctuations. Taking the SSM experiment as an example, at a frequency of 100Hz the RIN requirement decreases by 3 orders of magnitude, from $4 \times 10^{-10} / \sqrt{\text{Hz}}$ to $4 \times 10^{-7} / \sqrt{\text{Hz}}$ if the *co-moving* or BSAR LO option was chosen vs. the conventional *direct* pick-off of the LO beam from the main laser. That means it reduced the RIN requirement from a very challenging value to one that is easily achievable.

Misalignment is not only a problem in the balanced homodyne readout, but also in the Sagnac interferometer itself. In Chapter. 6, the effect of misalignment onto the quantum noise limited sensitivity of the Glasgow SSM experiment is calculated. I analysed several special misalignment conditions separated into the following cases: (1) connection mirrors misalignment; (2) out-of-phase cavity misalignment; (3) in-phase cavity misalignment; (4) individual cavity misalignment. We found that the impact of connection mirrors misalignment can be summarised as optical loss between the two cavities. Impacts of cavity out-of-phase misalignment can be summarised as loss of input power and interferometer output loss which is equivalent to imperfect photo diode quantum efficiency. Impacts of cavity in phase misalignment can be summarised as loss of input power and optical loss between the two arm cavities. Individual cavity misalignment can be summarised as optical loss of one cavity. Strategies for the implementation of an auto-alignment scheme in the SSM experiment were also discussed.

Similar to the Fabry-Perot resonators in the arms of gravitational wave detectors based

on the Michelson configuration, in a Sagnac speed meter interferometer, ring cavities are required. Different from linear cavities, the circulating beams in the ring cavities and the normal of the input mirror are not on the same line. The backscattering inside the ring cavity can create coupling between two modes circulating in opposite directions. In Chapter. 7, we analysed the effect of backscattering on quantum noise of a ring cavity when conducting measurement at one output port. Starting from previous work in [1], I developed a more detailed analysis. The mechanisms of impacts of backscattering were presented in terms of three levels of backscattering amplitude: weak backscattering ($\delta \ll 1$), critical backscattering ($\delta = 1$), strong backscattering ($1 < \delta \leq 10$). The current findings of backscattering effects on quantum noise can be explained by two clues: the optical rigidity effects due to the backscattering coupling between circulating modes in two directions onto orthogonal quadratures; the destructive interference between two dominating fields originating from the same input field. The former one only exists when there are two identical input beams. The latter one shows significant effects in the critical backscattering case. Again the results were carried out using the Glasgow SSM as an example.

In addition to the Sagnac interferometer, other more advanced types of speed meter have been proposed by the community, including one based on the principle of Einstein Podolsky Rosen entanglement. In Chapter. 8, I analysed the effect of several imperfections on quantum noise in the EPR speed meter and proved its compatibility with frequency dependent squeezing. As it turned out, the output loss showed the most drastic impact on the sensitivity at low frequencies. In terms of implementing an EPR speed meter into future generation gravitational wave detectors, further parameter studies and the comparison between different types of speed meters are required and such efforts are currently ongoing.

In Chapter. 9, I proposed an acceleration meter configuration based on the combination of the Sagnac speed meter and polarisation circulation speed meter. As it turned out, the acceleration meter is shot noise limited in both low frequencies and high frequencies. I observed that there are two frequencies at which the sensitivity touches the standard quantum limit. This leads to better sensitivity of this acceleration meter at low frequencies, compared to Michelson interferometer. In the future, less complex acceleration meter configurations could be investigated.

Appendix A

Comparison of lossy variational readout versus speed meter

Variational readout can in principle evade the back action noise by building correlations between shot noise and radiation pressure noise in the readout process [25, 79]. Speed meter can also partially cancel the radiation pressure noise by partially cancelling the radiation pressure force.

Both of them are low frequency back action evasion scheme. With no doubt that the ideal variational readout scheme is better than speed meter, however, it is more susceptible to optical loss compared with speed meter in an realistic environment. In this appendix, I compare the Michelson interferometer employing a variational readout scheme, considering output loss, with a speed meter, . As we showed in Eq. 9.6, the simple form of the quantum noise power spectral density of an interferometer can be written as

$$S = \frac{h_{\text{SQL}}}{2} \frac{1 + (\cot \phi - \mathcal{K})^2}{\mathcal{K}}. \quad (\text{A.1})$$

With out affecting the interferometer infrastructure, we can clearly see that, by tuning the readout angel as following

$$\text{acot} \phi = \mathcal{K}, \quad (\text{A.2})$$

the minimal value of the spectral density can be achieved. In this process, the back action noise is completely evaded. Allowing for optical loss modifies the I/O relation as

$$o = \sqrt{1 - \eta} \left[e^{2i\beta(\Omega)} \begin{bmatrix} 1 & 0 \\ -\mathcal{K} & 1 \end{bmatrix} i + e^{i\beta(\Omega)} \begin{bmatrix} 0 \\ \sqrt{2\mathcal{K}} \end{bmatrix} \frac{h}{h_{\text{SQL}}} \right] + \eta n, \quad (\text{A.3})$$

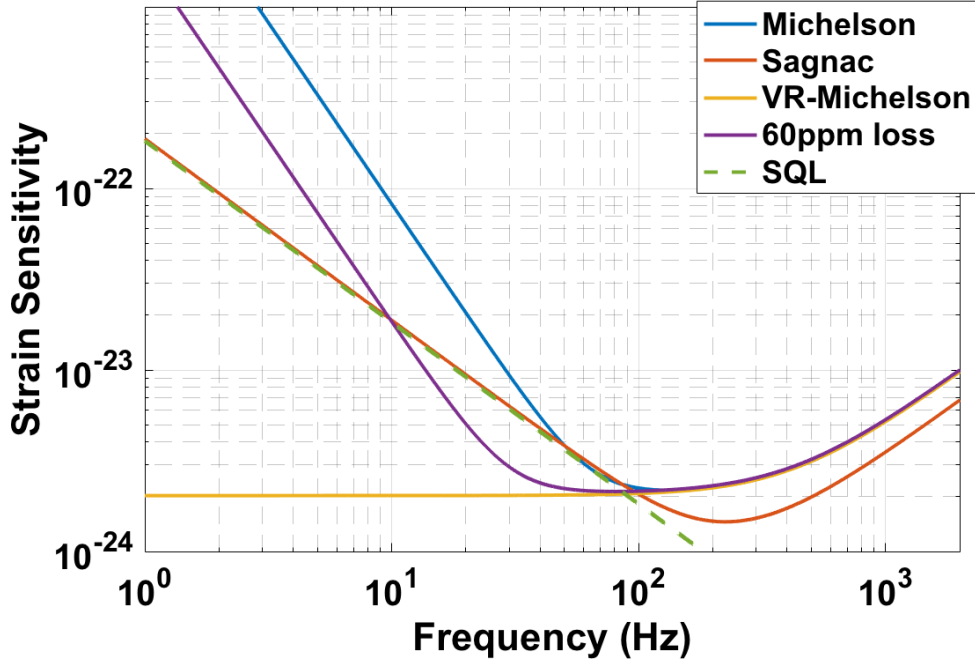


Figure A.1: Quantum noise limited strain sensitivities of a Michelson position meter, Michelson position meter with loss-free variational readout, Michelson position meter with variational readout featuring 60ppm roundtrip loss and a speed meter. The parameters used for this analysis resemble the Advanced LIGO design configuration. A readout angle of $\pi/2$ is chosen for the conventional advanced LIGO and Sagnac speed meter model.

where η is the coefficient of loss in power. Thus the resulting power spectral density is [79]

$$S = \frac{h_{\text{SQL}}}{2} \frac{1 + \frac{\eta}{1-\eta} \frac{1}{\sin^2 \phi} + (\cot \phi - \mathcal{K}_{\text{PM/SM}})^2}{\mathcal{K}_{\text{PM/SM}}}. \quad (\text{A.4})$$

Because of the appearance of loss term, η , the optimal angle needs to satisfy $\cot \phi = (1 - \eta)\mathcal{K}_{\text{PM/SM}}$. Thus the position meter quantum noise spectral density with a lossy variational readout scheme can be derived as [79]

$$S_{\text{LV,PM}} = \frac{h_{\text{SQL}}}{2} \left(\frac{1}{1-\eta} \frac{1}{\mathcal{K}_{\text{PM}}} + \eta \mathcal{K}_{\text{PM}} \right). \quad (\text{A.5})$$

Measuring on phase quadrature, the ideal speed meter sensitivity can be calculated as

$$S_{\text{ID,SM}} = \frac{h_{\text{SQL}}}{2} \left(\frac{1}{\mathcal{K}_{\text{SM}}} + \mathcal{K}_{\text{SM}} \right). \quad (\text{A.6})$$

When $\cot \phi = \mathcal{K}_{\text{SM}}(0)$, the speed meter is optimised for low frequency sensitivity.

To calculate the sensitivity of the position meter with variational readout and optical losses, I use the instrument parameters of advanced LIGO and the transmission of the filter cavity

ITM, $T_f = 0.0012$, which is the design value for the implementation of frequency dependent squeezing in A+. The radiation pressure noise in the advanced LIGO design is fairly low, so the speed meter with same parameters does not show its superiority. Thus for considering a Sagnac type speed meter, I choose its effective bandwidth as half of the effective bandwidth of the position meter model, which can be achieved by adopting a signal recycling mirror with an alternative transmissivity.

With comparative instrument parameters, the lossless variational readout position meter is always much better than a speed meter at low frequencies. However, the sensitivity of lossy variational readout position meter at low frequencies raise as $1/f^2$ towards DC, thus there will be a crossing point on a certain frequency for which the lossy variational readout position meter and the speed meter give exactly the same performance. The relation of frequency and loss factor at the crossing point is shown in Fig. A.2 and Fig. A.3. The left y-axis represents the loss factor, the right y-axis presents the equivalent loss coefficients of filter cavity. The calibration relation between the loss factor and the equivalent loss coefficients of filter cavity is [80]

$$1 - \eta \approx \frac{\epsilon}{T_f}. \quad (\text{A.7})$$

According to Fig. A.1 and Fig. A.2, with only taking the filter cavity loss into account, *i.e.* 60 ppm round trip loss, the superiority of lossy variational readout scheme compared with the speed meter can be observed from 8 Hz to 100 Hz. However, in advanced LIGO, the current total loss from the sources on the readout chain including output Faraday isolator, OMC, photodiode and mode matching, *etc.* is up to 20% [81]. According to Fig. A.1 and Fig. A.2, with this total loss factor, the lossy variational readout scheme can only present its superiority compared with the speed meter from 20 Hz to 100 Hz. Even though we can expect upgrades of the detector performance in terms of output loss, assuming 10% total loss can be achieved, the lossy variational readout is still only better above 14 Hz. We find the speed meter is more attractive than variational readout with realistic losses.

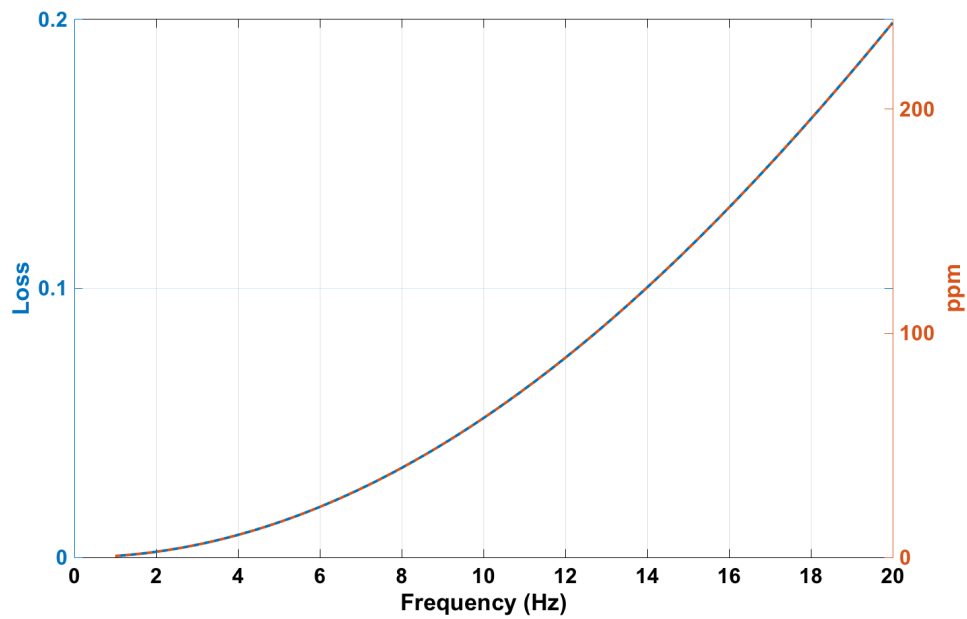


Figure A.2: The relation of frequency and loss factor at the crossing point of the sensitivity between the lossy variational readout position meter and the sensitivity of the speed meter. The left y-axis presents the loss factor, the right y-axis represents the equivalent loss coefficients of the filter cavity.

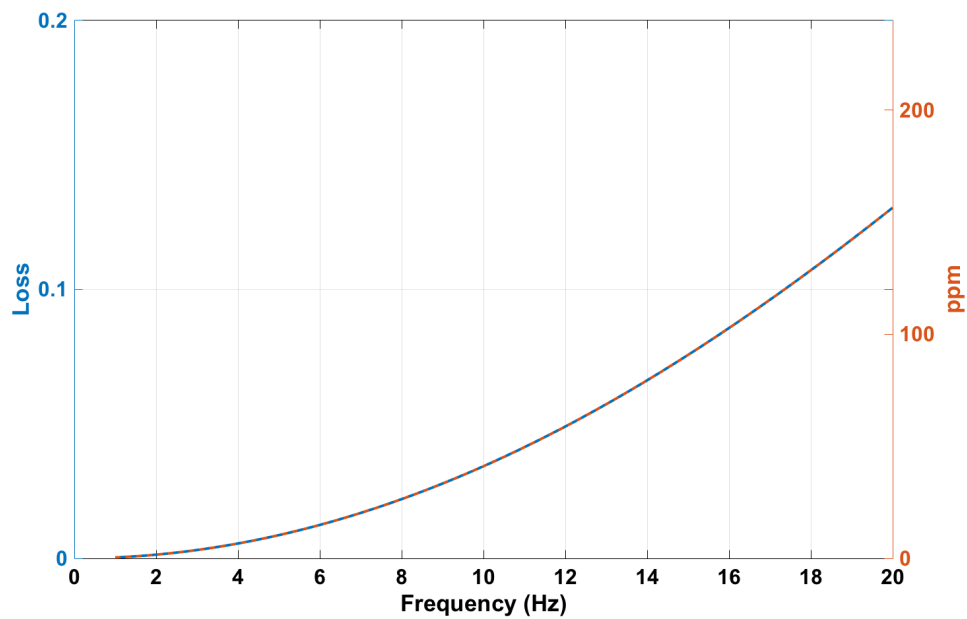


Figure A.3: The relation of frequency and loss factor at the crossing point of the sensitivity between lossy variational readout position meter and the sensitivity of low frequency optimised speed meter. The left y-axis is for loss in power, the right y-axis is for equivalent loss of filter cavity.

Appendix B

Finesse input file of A+ for balanced homodyne readout

```
%%% FTblock header
#-----
# An A+ design file originlly made for the BHD workshop
#in October 2018.
# This file is based on the full design aLIGO model and then
# adapted for the new design choices
#-----
# CHANGES
#-----
%%% FTend header

%%% FTblock laser
#####
# Laser and input optics
l L0 125 0.0 0.0 ni
bs jitter 1 0 0 0 ni n0 dump dump

s lmod1 1 n0 n1

# modulators for core interferometer sensing -
#Advanced LIGO, CQG, 2015
# http://iopscience.iop.org/article/10.1088/0264-9381/32/7/074001/
meta#cqg507871s4-8
```

```
# 9MHz (CARM, PRC, SRC loops)
```

```
const f1 9099471
```

```
const f2 45497355
```

```
mod mod1 $f1 0.18 1 pm n1 n2
```

```
s lmod2 1 n2 n3
```

```
# 45MHz (MICH, SRC loops)
```

```
mod mod2 $f2 0.18 1 pm n3 nLaserOut
```

```
#####
```

```
%%% FTend laser
```

```
%%% FTblock IMC
```

```
#####
```

```
s sIMCin 0 nLaserOut nMC1in
```

```
bs1 MC1 6000u 0 0 44.59 nMC1in nMC1refl nMC1trans nMC1fromMC3
```

```
s sMC1_MC2 16.24057 nMC1trans nMC2in
```

```
bs1 MC2 0 0u 0 0.82 nMC2in nMC2refl nMC2trans dump
```

```
s sMC2_MC3 16.24057 nMC2refl nMC3in
```

```
attr MC2 Rc 27.24
```

```
bs1 MC3 6000u 0 0 44.59 nMC3in nMC3refl nMC3trans nMCreturn_refl
```

```
s sMC3substrate 0.0845 $nsilica nMC3trans nMC3ARin
```

```
bs2 MC3AR 0 0 0 28.9661 nMC3ARin dump nIMCout dump
```

```
s sMC3_MC1 0.465 nMC3refl nMC1fromMC3
```

```
#####
```

```
%%% FTend IMC
```

```
%%% FTblock HAM2
```

```
#####
```

```
s sHAM2in 0.4282 nIMCout nIM11
```

```
# IM1 a.k.a. SM1
```

```
bs1 IM1 0 0 0 53 nIM11 nIM12 dump dump
```

```

s sIM1_IM2 1.2938 nIM12 nIM21

# IM2 a.k.a. PMMT1
bs1 IM2 0 0 0 7 nIM21 nIM22 dump dump
attr IM2 Rc 12.8

s sIM2_FI 0.260 nIM22 nFI1

# Input faraday isolator
dbs FI nFI1 nFI2 nFI3 nREFL

s sFI_IM3 0.910 nFI3 nIM31

# IM3 a.k.a PMMT2
bs1 IM3 0 0 0 7.1 nIM31 nIM32 dump dump
attr IM3 Rc -6.24

s sIM3_IM4 1.210 nIM32 nIM41

# a.k.a SM2
bs1 IM4 0 0 0 45 nIM41 nHAM2out dump dump
#####
%%% FTend HAM2

%%% FTblock PRC
#####
s sPRCin 0.4135 nHAM2out nPRM1

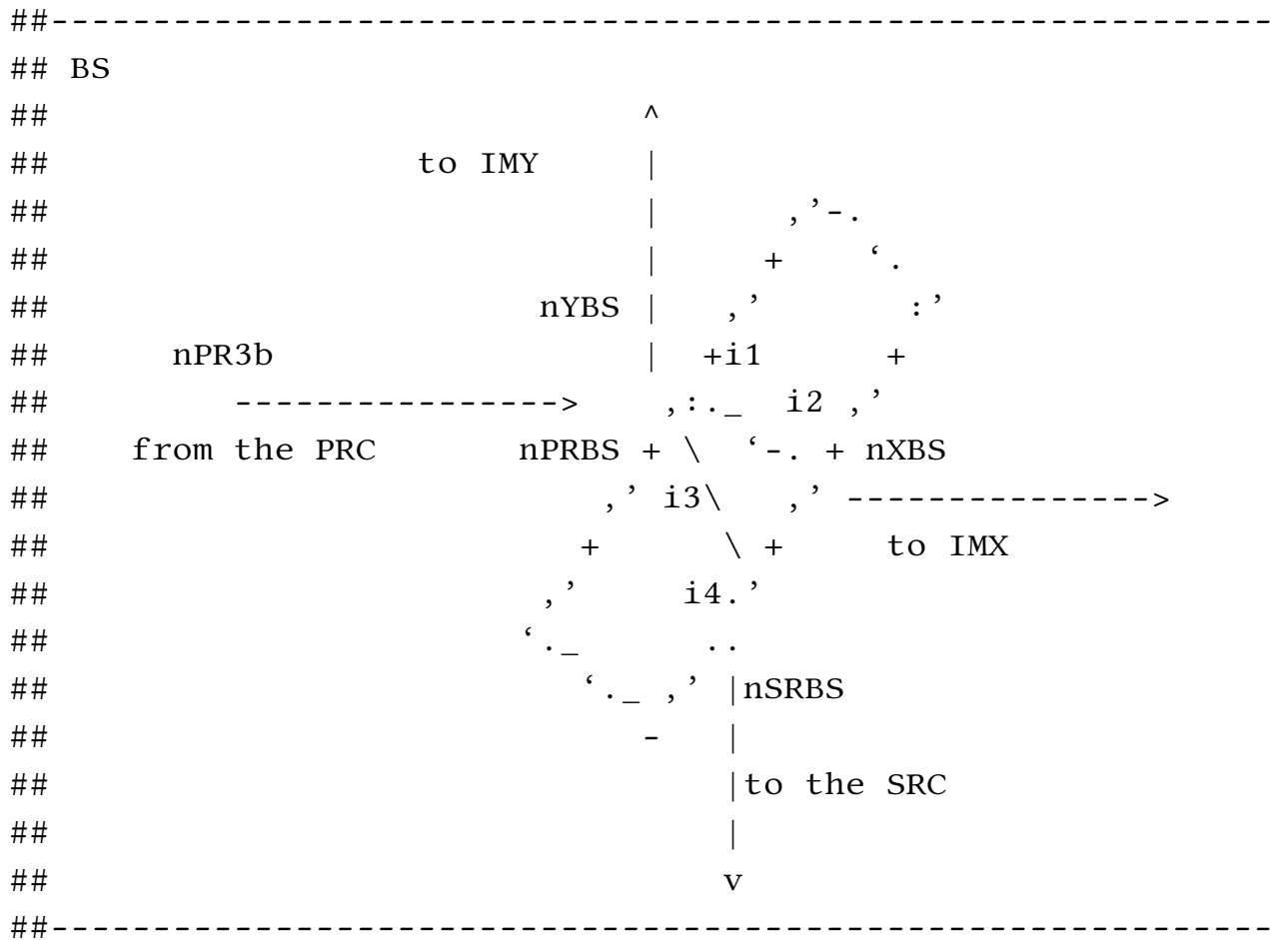
# PRM
# AR surface
m2 PRMAR 0 40u 0 nPRM1 nPRMs1
# Substrate
s sPRMsub1 0.0737 $nsilica nPRMs1 nPRMs2
# HR surface
m1 PRM 0.03 8.5u $phi_PRM nPRMs2 nPRM2
attr PRM Rc 11.009
# Distance between PRM and PR2
s lp1 16.6107 nPRM2 nPR2a

```

```
# PR2
bs1 PR2 250u $Mloss 0 -0.79 nPR2a nPR2b nPOP nAPOP
attr PR2 Rc -4.545
# Distance from PR2 to PR3
s lp2 16.1647 nPR2b nPR3a
# PR3
bs1 PR3 0 $Mloss 0 0.615 nPR3a nPR3b dump dump
attr PR3 Rc 36.027
# Distance from PR3
s lp3 19.5381 nPR3b nPRBS
```

```
#####
%%% FTend PRC
```

```
%%% FTblock BS
#####
# BS beamsplitter
```



```
bs1 BS 0.5 $Mloss $phi_BS 45 nPRBS nYBS nBSi1 nBSi3
```

```

s BSsub1 0.0687 $nsilica nBSi1 nBSi2
s BSsub2 0.0687 $nsilica nBSi3 nBSi4
bs2 BSAR1 50u 0 0 -29.195 nBSi2 dump14 nXBS nPOX
bs2 BSAR2 50u 0 0 29.195 nBSi4 dump15 nSRBS dump16

```

```

#####
%%% FTend BS

```

```

%%% FTblock Yarm

```

```

#####
# Distance from beam splitter to Y arm input mirror
s ly1 5.0126 nYBS nITMY1a

```

```

lens ITMY_lens $LY_f nITMY1a nITMY1b
s sITMY_th2 0 nITMY1b nITMY1

```

```

# Y arm input mirror

```

```

m2 ITMYAR 0 20u 0 nITMY1 nITMYs1
s ITMYsub 0.2 $nsilica nITMYs1 nITMYs2
m1 ITMY 0.014 $Mloss $phi_ITMY nITMYs2 nITMY2
attr ITMY Rc -1934

```

```

# Y arm length

```

```

s LY $Larm nITMY2 nETMY1

```

```

# Y arm end mirror

```

```

m1 ETMY 5u $Mloss $phi_ETMY nETMY1 nETMYs1
s ETMYsub 0.2 $nsilica nETMYs1 nETMYs2
m2 ETMYAR 0 500u 0 nETMYs2 nPTY
attr ETMY Rc 2245
attr ETMY mass 40
attr ITMY mass 40

```

```

#####
%%% FTend Yarm

```

```

%%% FTblock Xarm

```

```

#####

```

```
# Distance from beam splitter to X arm input mirror
s lx1 4.993 nXBS nITMX1a
```

```
lens ITMX_lens $LX_f nITMX1a nITMX1b
s sITMX_th2 0 nITMX1b nITMX1
```

```
# X arm input mirror
m2 ITMXAR 0 20u 0 nITMX1 nITMXs1
s ITMXsub 0.2 $nsilica nITMXs1 nITMXs2
m1 ITMX 0.014 $Mloss $phi_ITMX nITMXs2 nITMX2
attr ITMX Rc -1934
```

```
# X arm length
s LX $Larm nITMX2 nETMX1
```

```
# X arm end mirror
m1 ETMX 5u $Mloss $phi_ETMX nETMX1 nETMXs1
s ETMXsub 0.2 $nsilica nETMXs1 nETMXs2
m2 ETMXAR 0 500u 0 nETMXs2 nPTX
attr ETMX Rc 2245
attr ETMX mass 40
attr ITMX mass 40
```

```
#####
%%% FTend Xarm
```

```
%%% FTblock SRC
```

```
#####
```

```
# Distance to SR3
s ls3 19.3661 nSRBS nSR3b
# SR3
bs1 SR3 0 $Mloss 0 0.785 nSR3b nSR3a dump dump
attr SR3 Rc 35.972841
# Distance from SR3 to SR2
s ls2 15.4435 nSR3a nSR2b
# SR2
bs1 SR2 0 $Mloss 0 -0.87 nSR2b nSR2a dump dump
```

```

attr SR2 Rc -6.406
# Distance from SR2 to SRM
s ls1 15.7586 nSR2a nSRM1
# Signal recycling mirror SRM-08
m1 SRM 0.32 8.7u $phi_SRM nSRM1 nSRMs1
s SRMsub 0.0749 $nsilica nSRMs1 nSRMs2
m2 SRMAR 0 50n 0 nSRMs2 nSRM2
attr SRM Rc -5.6938

s sSRM_FI 0.7278 nSRM2 nFI2a

#####
%%% FTend SRC

%%% FTblock OUTPATH
#####
# Directional beam splitter (ideal Faraday Isolator with 4 ports)
# -----
# Description of node connections, inputNode --> outputNode
# --
# nFI2a (SRM)      --> nFI2c (OMC)
# nFI2b (SQZ)     --> nFI2a (SRM)
# nFI2c (OMC)     --> nFI2d (Unused)
# nFI2d (Unused) --> nFI2b (SQZ)

dbs FI2 nFI2a nFI2b nFI2c nFI2d

# Distance FI2 --> OM0, length guess
s sFI_OMo 2 nFI2c nOM0a

# Initial steering mirror on HAM6 for AS
bs1 OM0 0.01 0 0 45 nOM0a nOM0b nAS nOM0d

#s sSI2BS 0.8 nOM0b nSIBS1 #####new
#bs SIWaist 1 0 0 0 nSIBS1 nSIBS2 nSIBS3 nSIBS4 #####new

s sOM0_BHDBS 1 nOM0b nBHDBSc # OM0 to BHD BS, length guess

```

```

# BHD BS
bs1 BHDBS 0.5 0 0 0 nBHDBSa nBHDBSb nBHDBSc nBHDBSd

# Path from BHD BS to OMCA
s sBSHD_OMA1 0.01 nBHDBSa nOMA1a
bs1 OMA1 0 0 0 0 nOMA1a nOMA1b dump dump
s sOMA1_OMA2 1.5 nOMA1b nOMA2a
bs1 OMA2 0 0 0 0 nOMA2a nOMA2b dump dump
s sOMA2_OMA3 1 nOMA2b nOMA3a
bs1 OMA3 0 0 0 45 nOMA3a nOMA3b dump dump
s sOMA3_OMC 0.5 nOMA3b nOMCA_ICa

attr OMA1 Rc 1.03729872
attr OMA2 Rc 1.23953474

# Path from BHD BS to OMCB
s sBSHD_OMB1 0.01 nBHDBSd nOMB1a
bs1 OMB1 0 0 0 0 nOMB1a nOMB1b dump dump
s sOMB1_OMB2 1.5 nOMB1b nOMB2a
bs1 OMB2 0 0 0 0 nOMB2a nOMB2b dump dump
s sOMB2_OMB3 1 nOMB2b nOMB3a
bs1 OMB3 0 0 0 45 nOMB3a nOMB3b dump dump
s sOMB3_OMC 0.5 nOMB3b nOMCB_ICa

attr OMB1 Rc 1.03729872
attr OMB2 Rc 1.23953474
#####
%%% FTend OUTPATH

%%% FTblock LO
#####
# ref G1800283
s sPR2_LOM 5 nPOP nLOMa
bs LOM 1 0 0 45 nLOMa nLOMb dump dump
s LOM_LOLens 5 nLOMb nLOLensa
lens LOLens -12.8 nLOLensa nLOLensb
s sL2BS 0.8 nLOLensb nBS1

```

```

bs BHDANG 1 0 0 0 nBS1 nBS2 nBS3 nBS4
s sLOLens_BHDBS 0.2 nBS2 nBHDBSb
#####
%%% FTend LO

```

```

%%% FTblock OMCA
#####
# OMCA (as built parameters original OMC: D1300507-v1)
bs1 OMCA_IC 0.0076 10u 0 2.7609 nOMCA_ICa nOMCA_ICb nOMCA_ICc
nOMCA_ICd
# Input Coupler IC (flat mirror)
s sICA_OCA 0.2815 1 nOMCA_ICc nOMCA_OCa
# Distance from IC to OC
bs1 OMCA_OC 0.0075 10u 0 4.004 nOMCA_OCa nOMCA_OCb nBHD1
nOMCA_OCd
# Output Coupler OC (flat mirror)
s sOCA_CMA1 0.2842 1 nOMCA_OCb nOMCA_CM1a
# Output Coupler OC (flat mirror)
bs1 OMCA_CM1 36u 10u 0 4.004 nOMCA_CM1a nOMCA_CM1b nOMCA_CM1c
nOMCA_CM1d
# Curved Mirror CM1
attr OMCA_CM1 Rc 2.57321
s sCMA1_CMA2 0.2815 1 nOMCA_CM1b nOMCA_CM2a
# Curved Mirror CM1
bs1 OMCA_CM2 35.9u 10u 0 4.004 nOMCA_CM2a nOMCA_CM2b nOMCA_CM2c
nOMCA_CM2d
# Curved Mirror CM2
attr OMCA_CM2 Rc 2.57369
s sCMA1_ICA 0.2842 1 nOMCA_CM2b nOMCA_ICd
# Distance from CM2 to IC
#####
%%% FTend OMCA

```

```

%%% FTblock OMCB
#####
# OMCB (as built parameters original OMC: D1300507-v1)

```

```

bs1 OMCB_IC 0.0076 10u 0 2.7609 nOMCB_ICa nOMCB_ICb nOMCB_ICc
nOMCB_ICd
# Input Coupler IC (flat mirror)
s sICB_OCB 0.2815 1 nOMCB_ICc nOMCB_OCa
# Distance from IC to OC
bs1 OMCB_OC 0.0075 10u 0 4.004 nOMCB_OCa nOMCB_OCb nBHD2
nOMCB_OCd
# Output Coupler OC (flat mirror)
s sOCB_CMB1 0.2842 1 nOMCB_OCb nOMCB_CM1a
# Output Coupler OC (flat mirror)
bs1 OMCB_CM1 36u 10u 0 4.004 nOMCB_CM1a nOMCB_CM1b nOMCB_CM1c
nOMCB_CM1d
# Curved Mirror CM1
attr OMCB_CM1 Rc 2.57321
s sCMB1_CMB2 0.2815 1 nOMCB_CM1b nOMCB_CM2a
# Curved Mirror CM1
bs1 OMCB_CM2 35.9u 10u 0 4.004 nOMCB_CM2a nOMCB_CM2b nOMCB_CM2c
nOMCB_CM2d
# Curved Mirror CM2
attr OMCB_CM2 Rc 2.57369
s sCMB1_ICB 0.2842 1 nOMCB_CM2b nOMCB_ICd
# Distance from CM2 to IC
#####
%%% FTend OMCB

%%% FTblock cavities
#####
cav cavIMC MC2 nMC2in MC2 nMC2refl
cav cavXARM ITMX nITMX2 ETMX nETMX1
cav cavYARM ITMY nITMY2 ETMY nETMY1
cav cavSRX SRM nSRM1 ITMX nITMXs2
cav cavSRY SRM nSRM1 ITMY nITMYs2
cav cavPRX PRM nPRM2 ITMX nITMXs2
cav cavPRY PRM nPRM2 ITMY nITMYs2
cav cavOMCA OMCA_IC nOMCA_ICc OMCA_IC nOMCA_ICd
cav cavOMCB OMCB_IC nOMCB_ICc OMCB_IC nOMCB_ICd

#####

```

```
%%% FTend cavities
```

```
%%% FTblock constants
```

```
#####
const nsilica 1.44963098985906
const nTGG 1.954
const nCalcite 1.65846
const Mloss 37.5u
const Larm 3994.4692
const fM 36.397884M
const fP 54.596826M
const LY_f 34.5k          # lens ITMY
const LX_f 34.5k          # lens ITMX
#####
%%% FTend constants
```

```
%%% FTblock tunings
```

```
#####
const phi_SRM 90.0
const phi_PRM 0.0
const phi_ITMX 0.0
const phi_ITMY 0.0
const phi_ETMX 0.0
const phi_ETMY 0.0
const phi_BS 0
#####
%%% FTend tunings
```

```
%%% FTblock commands
```

```
#####
maxtem 0
#printnoises
#noxaxis

#pd P nETMX1
#qnoised n 1 $fs nETMX1
#fsig noise 1
```

```
fsig sigX ETMX phase 1 0 1  
fsig sigY ETMY phase 1 180 1
```

```
#hd QNLS 180 nBHD1 nBHD2
```

```
xaxis sigX f log 10 5000 999  
yaxis abs
```

```
#####  
%% FTend commands
```

Appendix C

Finesse input file of Glasgow SSM experiment

```
%%% FTblock ssm_reference_constants
const Pin 3.4
# twice the nominal power, see header for detailed explanation
const nFS 1.44963 # refractive idx of fused silica

## RF modulation stage
const EOM1.fRF 15M
const EOM1.midx 0.3
const EOM2.fRF 100M
const EOM2.midx 0

## lengths of OptoCad ray segments
const lrs2 250.E-3 # input -> M4
const lrs3 145.981E-3 # M4 -> M5
const lrs4 253.9E-3 # M5 -> M11
const lrs5 75.1016E-3 # M11 -> M6
const lrs7 99.8598E-3 # M6 -> M7
const lrs8 303.5388E-3 # M7 -> M1a
const lrs10 1.3279 # M1a -> M2a
const lrs11 0.2040966 # M2a -> M3a
const lrs12 1.328 # M3a -> M1a
const lrs17 400.0202E-3 # M1b -> M6
const lrs19 1.3281 # M1b -> M2b
const lrs20 0.2037275 # M2b -> M3b
```

```
const lrs21 1.3281          # M3b -> M1b
const lrs23 505.5960E-3 # M1a -> M10
const lrs24 326.5940E-3 # M10 -> M9
const lrs25 261.2865E-3 # M9 -> M8
const lrs26 556.0402E-3 # M8 -> M1b

## mirror parameters
const M1a{p}.refl 0.999368
const M1a{p}.trns 0.000632
const M1a{p}.loss 0
const M1a{p}.phi 0
const M1a{p}.aoi 0
const M1a{p}.roc -8
const M1a{p}.mass 0.85m
const M1a{p}.thickness 0.005

const M2a{p}.refl 0.9999966
#const M2a{p}.trns 3.4u
# this is 50percent of the total round-trip loss
const M2a{p}.loss 0
const M2a{p}.phi 0
const M2a{p}.aoi 0
#const M2a{p}.roc 0
const M2a{p}.mass 100m

const M3a{p}.refl 0.9999966
#const M3a{p}.trns 3.4u
# this is 50percent of the total round-trip loss
const M3a{p}.loss 0
const M3a{p}.phi 0
const M3a{p}.aoi 0
#const M3a{p}.roc 0
const M3a{p}.mass 100m

const M1b{p}.refl 0.999368
const M1b{p}.trns 0.000632
const M1b{p}.loss 0
const M1b{p}.phi 0
```

```
const M1b{p}.aoi 0
const M1b{p}.roc -8
const M1b{p}.mass 0.85m
const M1b{p}.thickness 0.005

const M2b{p}.refl 0.9999966
#const M2b{p}.trns 3.4u
# this is 50percent of the total round-trip loss
const M2b{p}.loss 0
const M2b{p}.phi 0
const M2b{p}.aoi 0
#const M2b{p}.roc 0
const M2b{p}.mass 100m

const M3b{p}.refl 0.9999966
#const M3b{p}.trns 3.4u
# this is 50percent of the total round-trip loss
const M3b{p}.loss 0
const M3b{p}.phi 0
const M3b{p}.aoi 0
#const M3b{p}.roc 0
const M3b{p}.mass 100m

const M4.refl 1
const M4.loss 0
const M4.phi 0
const M4.aoi 45
#const M4.roc
#const M4.mass

const M5.refl 1
const M5.loss 0
const M5.phi 0
const M5.aoi 45
#const M5.roc
#const M5.mass

const M6{p}.refl 0.5
```

```
const M6{p}.loss 0
const M6{p}.phi 0
const M6{p}.aoi 29.19505498
#const M6{p}.roc
#const M6{p}.mass
```

```
const M7.refl 1
const M7.loss 0
const M7.phi 0
const M7.aoi 49.39870535
#const M7.roc
#const M7.mass
```

```
const M8{p}.refl 1
const M8{p}.loss 0
const M8{p}.phi 0
const M8{p}.aoi 43.33405689
#const M8{p}.roc
#const M8{p}.mass
```

```
const M9{p}.refl 1
const M9{p}.loss 0
const M9{p}.phi 0
const M9{p}.aoi 5.477377081
const M9{p}.roc 5.13
#const M9{p}.mass
```

```
const M10{p}.refl 1
const M10{p}.loss 0
const M10{p}.phi 0
const M10{p}.aoi 42.25439783E0
#const M10{p}.roc
#const M10{p}.mass
```

```
const M11.refl 0.5
const M11.loss 0
const M11.phi 0
const M11.aoi 45
```

```

#const M11.roc
#const M11.mass

#####
%%% FTend

%%% FTblock ssm_reference_ifoskeleton

## Beam path from laser source up to main BS
l i1 $Pin 0 n0a
s rs0 0 n0a n0b
mod EOM1 $EOM1.fRF $EOM1.midx 1 pm n0b n0c
s rs00 0 n0c n0d
mod EOM2 $EOM2.fRF $EOM2.midx 1 pm n0d n0
s rs2 $lrs2 n0 nM4w
bs2 M4 $M4.refl $M4.loss $M4.phi $M4.aoi nM4w nM4n
nDump1 nDump2
s rs3 $lrs3 nM4n nM5n
bs2 M5 $M5.refl $M5.loss $M5.phi $M5.aoi nM5w nM5n
nDump3 nDump4
s rs4 $lrs4 nM5w nM11w
bs2 M11 $M11.refl $M11.loss $M11.phi $M11.aoi nM11w nM11n
nM11e nM11s
s rs5 $lrs5 nM11n nM6{p}w

#####
## Central BS
bs2 M6{p} $M6{p}.refl $M6{p}.loss $M6{p}.phi $M6{p}.aoi
nM6{p}w nM6{p}n
nM6{p}e nM6{p}s

#####
## Cavity a
s rs7 $lrs7 nM6{p}e nM7w
bs2 M7 $M7.refl $M7.loss $M7.phi $M7.aoi nM7w nM7n
nDump5 nDump6

s rs8 $lrs8 nM7n nm1a_1w

```

```

m1 m1a_1 1 0 0 nm1a_1w nm1a_1s
s r1a_med_1 $M1a{p}.thickness $nFS nm1a_1s nM1a{p}n

bs1 M1a{p} $M1a{p}.trns $M1a{p}.loss $M1a{p}.phi $M1a{p}.aoi
nM1a{p}w nM1a{p}n nM1a{p}e nM1a{p}s
attr M1a{p} Rc $M1a{p}.roc
attr M1a{p} mass $M1a{p}.mass

s rs12 $lrs12 nM3a{p}n nM1a{p}e
bs2 M3a{p} $M3a{p}.refl $M3a{p}.loss $M3a{p}.phi $M3a{p}.aoi
nM3a{p}w nM3a{p}n nM3a{p}e nM3a{p}s
attr M3a{p} mass $M3a{p}.mass

s rs11 $lrs11 nM2a{p}n nM3a{p}w

bs2 M2a{p} $M2a{p}.refl $M2a{p}.loss $M2a{p}.phi $M2a{p}.aoi
nM2a{p}w nM2a{p}n nDump9 nDump10
#bs2 M2a{p} $M2a{p}.refl $M2a{p}.loss $M2a{p}.phi $M2a{p}.aoi
nM2a{p}w nM2a{p}n nM2a{p}e nM2a{p}s
attr M2a{p} mass $M2a{p}.mass

s rs10 $lrs10 nM1a{p}s nM2a{p}w

cav AC_a M1a{p} nM1a{p}s M1a{p} nM1a{p}e

#####
# Path between cavities a and b
s r1a_med_2 $M1a{p}.thickness $nFS nM1a{p}w nm1a_2s
m1 m1a_2 1 0 0 nm1a_2w nm1a_2s
s rs23 $lrs23 nm1a_2w nM10{p}n

bs2 M10{p} $M10{p}.refl $M10{p}.loss $M10{p}.phi $M10{p}.aoi
nM10{p}w nM10{p}n nDump11 nDump12

s rs24 $lrs24 nM10{p}w nM9{p}n

#bs M9{p} 1 0 0 5.477377081 nM9{p}w nM9{p}n nDump13 nDump14
bs2 M9{p} $M9{p}.refl $M9{p}.loss $M9{p}.phi $M9{p}.aoi

```

```

nM9{p}w nM9{p}n nM9{p}e nM9{p}s
# w/o 'dumps', i.e. vacuum may creep in
attr M9{p} Rc $M9{p}.roc

s rs25 $lrs25 nM9{p}w nM8{p}w

bs2 M8{p} $M8{p}.refl $M8{p}.loss $M8{p}.phi $M8{p}.aoi
nM8{p}w nM8{p}n nDump15 nDump16

s rs26 $lrs26 nM8{p}n nm1b_1w

#####
## Cavity b

m1 m1b_1 1 0 0 nm1b_1w nm1b_1s
s r1b_med_1 $M1b{p}.thickness $nFS nm1b_1s nM1b{p}w

#bs2 M1b{p} $M1b{p}.refl $M1b{p}.loss $M1b{p}.phi $M1b{p}.aoi
nM1b{p}w nM1b{p}n nM1b{p}e nM1b{p}s
bs1 M1b{p} $M1b{p}.trns $M1b{p}.loss $M1b{p}.phi $M1b{p}.aoi
nM1b{p}w nM1b{p}n nM1b{p}e nM1b{p}s
attr M1b{p} Rc $M1b{p}.roc
attr M1b{p} mass $M1b{p}.mass

s rs19 $lrs19 nM1b{p}s nM2b{p}w

bs2 M2b{p} $M2b{p}.refl $M2b{p}.loss $M2b{p}.phi $M2b{p}.aoi
nM2b{p}w nM2b{p}n nDump17 nDump18
#bs2 M2b{p} $M2b{p}.refl $M2b{p}.loss $M2b{p}.phi $M2b{p}.aoi
nM2b{p}w nM2b{p}n nM2b{p}e nM2b{p}s
attr M2b{p} mass $M2b{p}.mass

s rs20 $lrs20 nM2b{p}n nM3b{p}w

bs2 M3b{p} $M3b{p}.refl $M3b{p}.loss $M3b{p}.phi $M3b{p}.aoi
nM3b{p}w nM3b{p}n nDump19 nDump20
attr M3b{p} mass $M3b{p}.mass

```

```

s rs21 $lrs21 nM3b{p}n nM1b{p}e

cav AC_b M1b{p} nM1b{p}s M1b{p} nM1b{p}e

s rs17 $lrs17 nM6{p}n nm1b_2w
m1 m1b_2 1 0 0 nm1b_2w nm1b_2s
s r1b_med_2 $M1b{p}.thickness $nFS nm1b_2s nM1b{p}n

#####
%% FTend

# reflected light from central BS: nM11s
# main output of Sagnac: nM6{p}s

# checking cavity parameters
maxtem 3
retrace force
#trace 2

# sagnac output
s out1 1 nM6{p}s nHD1

# sagnac reflection through M11
s out3 1n nM11s nHD2

fsig sig1 M2a{p} 1 0 0.5
fsig sig2 M2b{p} 1 180 0.5

## homodyne with Sagnac reflected port as LO
bs dHD .5 .5 0 0 nHD1 nout1 nout2 nHD2

qhds _bhd 180 nout1 nout2
scale meter _bhd
beam b1 nHD1
beam b2 nHD2

xaxis sig1 f log 100 100k 999
yaxis log abs

```


Bibliography

- [1] D. Pascucci. “On optics surface imperfections and their effects on the sensitivity of speed meters”. PhD thesis. University of Glasgow, 2019.
- [2] B. Abbott et al. “Observation of Gravitational Waves from a Binary Black Hole Merger”. In: *Phys. Rev. Lett.* 116 (6 2016), p. 061102. DOI: 10.1103/PhysRevLett.116.061102.
- [3] S. S. Leavey. “Enhancing the sensitivity of future laser-interferometric gravitational wave detectors”. PhD thesis. University of Glasgow, 2017.
- [4] J. B. Camp and N. J. Cornish. “Gravitational wave astronomy”. In: *Annu. Rev. Nucl. Part. Sci.* 54 (2004), pp. 525–577.
- [5] Y. Chen et al. “Interferometers for Displacement-Noise-Free Gravitational-Wave Detection”. In: *Phys. Rev. Lett.* 97 (15 2006), p. 151103. DOI: 10.1103/PhysRevLett.97.151103.
- [6] Y. Chen and S. Kawamura. “Displacement- and Timing-Noise-Free Gravitational-Wave Detection”. In: *Phys. Rev. Lett.* 96 (23 2006), p. 231102. DOI: 10.1103/PhysRevLett.96.231102.
- [7] J.-S. Hennig. “Mirror suspensions for the Glasgow Sagnac speed meter”. PhD thesis. University of Glasgow, 2018.
- [8] M. Cerdonio, L. Conti, A. Heidmann, and M. Pinard. “Thermoelastic effects at low temperatures and quantum limits in displacement measurements”. In: *Phys. Rev. D* 63 (8 2001), p. 082003. DOI: 10.1103/PhysRevD.63.082003.
- [9] B. J. J. Slagmolen et al. “Direct Measurement of the Spectral Distribution of Thermal Noise”. In: (2004).
- [10] G. D. Domenico, S. Schilt, and P. Thomann. “Simple approach to the relation between laser frequency noise and laser line shape”. In: *Appl. Opt.* 49.25 (2010), pp. 4801–4807. DOI: 10.1364/AO.49.004801.
- [11] M. Bassan. *Advanced Interferometers and the Search for Gravitational Waves*. Vol. 404. Nov. 2013. DOI: 10.1007/978-3-319-03792-9.

- [12] M. Bassan. “Advanced interferometers and the search for gravitational waves”. In: *Astrophysics and Space Science Library* 404 (2014), pp. 275–290.
- [13] R. W. P. Drever et al. “Laser phase and frequency stabilization using an optical resonator”. In: *Applied Physics B* 31.2 (1983), pp. 97–105. ISSN: 1432-0649. DOI: 10 . 1007/BF00702605.
- [14] E. D. Black. “An introduction to Pound–Drever–Hall laser frequency stabilization”. In: *American journal of physics* 69.1 (2001), pp. 79–87.
- [15] H. B. Callen and T. A. Welton. “Irreversibility and Generalized Noise”. In: *Phys. Rev.* 83 (), pp. 34–40.
- [16] R. F. Greene and H. B. Callen. “On the Formalism of Thermodynamic Fluctuation Theory”. In: *Phys. Rev.* 83 (6 1951), pp. 1231–1235. DOI: 10 . 1103/PhysRev . 83 . 1231.
- [17] H. B. Callen and R. F. Greene. “On a Theorem of Irreversible Thermodynamics”. In: *Phys. Rev.* 86 (5 1952), pp. 702–710. DOI: 10 . 1103/PhysRev . 86 . 702.
- [18] S. Reid and I. W. Martin. “Development of mirror coatings for gravitational wave detectors”. In: *Coatings* 6.4 (2016), p. 61.
- [19] G. Hammond, S. Hild, and M. Pitkin. “Advanced technologies for future ground-based, laser-interferometric gravitational wave detectors”. In: *Journal of Modern Optics* 61.sup1 (Dec. 2014), S10–S45. DOI: 10 . 1080/09500340 . 2014 . 920934.
- [20] N. A. Robertson et al. “Quadruple suspension design for Advanced LIGO”. In: *Classical and Quantum Gravity* 19.15 (2002), pp. 4043–4058. DOI: 10 . 1088 / 0264 - 9381/19/15/311.
- [21] D. Coyne. “The A+ Upgrade: Expanding the Advanced LIGO Horizon”. In: *LIGO Document* (2018).
- [22] N. Nakagawa, B. A. Auld, E. Gustafson, and M. M. Fejer. “Estimation of thermal noise in the mirrors of laser interferometric gravitational wave detectors: Two point correlation function”. In: *Review of Scientific Instruments* 68.9 (1997), pp. 3553–3556. DOI: 10 . 1063 / 1 . 1148321. eprint: <https://doi.org/10.1063/1.1148321>.
- [23] C. FABRY. “Theorie et applications d’ une nouvelle methods de spectroscopie interferentielle”. In: *Ann. Chim. Ser.* 7 16 (1899), pp. 115–144.
- [24] V. B. Braginsky, Y. I. Vorontsov, and K. S. Thorne. “Quantum Nondemolition Measurements”. In: *Science* 209.4456 (1980), pp. 547–557. ISSN: 0036-8075. DOI: 10 . 1126 / science . 209 . 4456 . 547.

- [25] H. J. Kimble, Y. Levin, A. B. Matsko, K. S. Thorne, and S. P. Vyatchanin. “Conversion of conventional gravitational-wave interferometers into quantum nondemolition interferometers by modifying their input and/or output optics”. In: *Phys. Rev. D* 65 (2001), p. 022002. DOI: 10.1103/PhysRevD.65.022002.
- [26] Y. Chen, S. L. Danilishin, F. Y. Khalili, and H. Müller-Ebhardt. “QND measurements for future gravitational-wave detectors”. In: *General Relativity and Gravitation* 43.2 (2011), pp. 671–694. ISSN: 1572-9532. DOI: 10.1007/s10714-010-1060-y.
- [27] S. L. Danilishin and F. Y. Khalili. “Quantum Measurement Theory in Gravitational-Wave Detectors”. In: *Living Reviews in Relativity* 15.5 (2012). DOI: 10.1007/lrr-2012-5.
- [28] K. Arai. “Loss map measurement at Caltech 40 m lab”. In: *LIGO Document* (2015).
- [29] C. M. Caves and B. L. Schumaker. “New formalism for two-photon quantum optics. I. Quadrature phases and squeezed states”. In: *Phys. Rev. A* 31 (5 1985), pp. 3068–3092. DOI: 10.1103/PhysRevA.31.3068.
- [30] B. L. Schumaker and C. M. Caves. “New formalism for two-photon quantum optics. II. Mathematical foundation and compact notation”. In: *Phys. Rev. A* 31 (5 1985), pp. 3093–3111. DOI: 10.1103/PhysRevA.31.3093.
- [31] A. Buonanno and Y. Chen. “Quantum noise in second generation, signal-recycled laser interferometric gravitational-wave detectors”. In: *Phys. Rev. D* 64 (4 2001), p. 042006. DOI: 10.1103/PhysRevD.64.042006.
- [32] A. Buonanno and Y. Chen. “Scaling law in signal recycled laser-interferometer gravitational-wave detectors”. In: *Phys. Rev. D* 67 (6 2003), p. 062002. DOI: 10.1103/PhysRevD.67.062002.
- [33] J. Mizuno. “Comparison of optical configurations for laser-interferometric gravitational-wave detectors [microform] /”. In: (Feb. 2019).
- [34] A. Buonanno and Y. Chen. “Signal recycled laser-interferometer gravitational-wave detectors as optical springs”. In: *Phys. Rev. D* 65 (4 2002), p. 042001. DOI: 10.1103/PhysRevD.65.042001.
- [35] S Hild et al. “DC-readout of a signal-recycled gravitational wave detector”. In: *Classical and Quantum Gravity* 26.5 (2009), p. 055012. DOI: 10.1088/0264-9381/26/5/055012.
- [36] T. T. Fricke et al. “DC readout experiment in Enhanced LIGO”. In: *Classical and Quantum Gravity* 29.6 (2012), p. 065005. DOI: 10.1088/0264-9381/29/6/065005.

- [37] P. Fritschel, M. Evans, and V. Frolov. “Balanced homodyne readout for quantum limited gravitational wave detectors”. In: *Opt. Express* 22.4 (2014), pp. 4224–4234. DOI: 10.1364/OE.22.004224.
- [38] V. B. Braginsky and F. Y. Khalili. *Quantum measurement*. Cambridge University Press, 1995.
- [39] F. Khalili et al. “Negative optical inertia for enhancing the sensitivity of future gravitational-wave detectors”. In: *Phys. Rev. D* 83 (6 2011), p. 062003. DOI: 10.1103/PhysRevD.83.062003.
- [40] T. L. S. Collaboration. “A gravitational wave observatory operating beyond the quantum shot-noise limit”. In: *Nature Physics* 7 (Sept. 2011), 962 EP –.
- [41] B Willke et al. “The GEO-HF project”. In: *Classical and Quantum Gravity* 23.8 (2006), S207–S214. DOI: 10.1088/0264-9381/23/8/s26.
- [42] C Affeldt et al. “Advanced techniques in GEO 600”. In: *Classical and Quantum Gravity* 31.22 (2014), p. 224002. DOI: 10.1088/0264-9381/31/22/224002.
- [43] J. Aasi et al. “Enhanced sensitivity of the LIGO gravitational wave detector by using squeezed states of light”. In: *Nat Photon* 7.8 (Aug. 2013), pp. 613–619.
- [44] S. L. Danilishin, F. Y. Khalili, and H. Miao. “Advanced quantum techniques for future gravitational-wave detectors”. In: *arXiv preprint arXiv:1903.05223* (2019).
- [45] V. Braginsky and F. Khalili. “Gravitational wave antenna with QND speed meter”. In: *Physics Letters A* 147.5 (1990), pp. 251–256. ISSN: 0375-9601. DOI: [http://dx.doi.org/10.1016/0375-9601\(90\)90442-Q](http://dx.doi.org/10.1016/0375-9601(90)90442-Q).
- [46] P. Purdue and Y. Chen. “Practical speed meter designs for quantum nondemolition gravitational-wave interferometers”. In: *Phys. Rev. D* 66 (12 2002), p. 122004. DOI: 10.1103/PhysRevD.66.122004.
- [47] Y. Chen. “Sagnac interferometer as a speed-meter-type, quantum-nondemolition gravitational-wave detector”. In: *Phys. Rev. D* 67 (12 2003), p. 122004. DOI: 10.1103/PhysRevD.67.122004.
- [48] S. L. Danilishin et al. “A new quantum speed-meter interferometer: measuring speed to search for intermediate mass black holes”. In: *Light: Science & Applications* 7.1 (2018), p. 11. DOI: 10.1038/s41377-018-0004-2.
- [49] T Zhang et al. “Quantum noise cancellation in asymmetric speed metres with balanced homodyne readout”. In: *New Journal of Physics* 20.10 (2018), p. 103040. DOI: 10.1088/1367-2630/aae86e.

- [50] M Hewitson et al. “Charge measurement and mitigation for the main test masses of the GEO 600 gravitational wave observatory”. In: *Classical and Quantum Gravity* 24.24 (2007), pp. 6379–6391. doi: 10 . 1088/0264-9381/24/24/013.
- [51] S. M. Aston et al. “Update on quadruple suspension design for Advanced LIGO”. In: *Classical and Quantum Gravity* 29.23 (2012), p. 235004. doi: 10 . 1088 / 0264 - 9381/29/23/235004.
- [52] R. Weiss and D Kelley. “Collection of reports on Barkhausen noise”. In: *LIGO Document* 900061 (2008), p. 2009.
- [53] J.-S. Hennig et al. “Demonstration of a switchable damping system to allow low-noise operation of high- Q low-mass suspension systems”. In: *Phys. Rev. D* 96 (12 2017), p. 122005. doi: 10 . 1103/PhysRevD . 96 . 122005.
- [54] F.J.RAAB and S.E.WHITCOMB. “Estimation of special optical properties of a triangular ring cavity”. In: *LIGO Document* (1992).
- [55] S. S. Leavey et al. *Control of a velocity-sensitive audio-band quantum non-demolition interferometer*. 2016. arXiv: 1603 . 07756 [gr-qc].
- [56] S. Steinlechner et al. “Local-oscillator noise coupling in balanced homodyne readout for advanced gravitational wave detectors”. In: *Phys. Rev. D* 92 (7 2015), p. 072009. doi: 10 . 1103/PhysRevD . 92 . 072009.
- [57] C Gräf et al. “Design of a speed meter interferometer proof-of-principle experiment”. In: *Classical and Quantum Gravity* 31.21 (2014), p. 215009.
- [58] K. Izumi and D. Sigg. “Advanced LIGO: length sensing and control in a dual recycled interferometric gravitational wave antenna”. In: *Classical and Quantum Gravity* 34.1 (2016), p. 015001. doi: 10 . 1088/0264-9381/34/1/015001.
- [59] H. Yu et al. “Prospects for Detecting Gravitational Waves at 5 Hz with Ground-Based Detectors”. In: *Phys. Rev. Lett.* 120 (14 2018), p. 141102. doi: 10 . 1103 / PhysRevLett . 120 . 141102.
- [60] L Barsotti, M Evans, and P Fritschel. “Alignment sensing and control in advanced LIGO”. In: *Classical and Quantum Gravity* 27.8 (2010), p. 084026. doi: 10 . 1088 / 0264-9381/27/8/084026.
- [61] T. Zhang et al. “Plans for the A+ Balanced Homodyne readout”. In: *LIGO Document* (2018).
- [62] A. Freise and K. A. Strain. “Interferometer Techniques for Gravitational-Wave Detection”. In: *Living Reviews in Relativity* 13.1 (2010). doi: 10 . 1007/1rr-2010-1.

- [63] T. Zhang et al. “Effects of static and dynamic higher-order optical modes in balanced homodyne readout for future gravitational waves detectors”. In: *Phys. Rev. D* 95 (6 2017), p. 062001. DOI: 10 . 1103/PhysRevD . 95 . 062001.
- [64] K Arai et al. “Some thoughts on polarization BHD”. In: *LIGO Document* ().
- [65] and J Aasi et al. “Advanced LIGO”. In: *Classical and Quantum Gravity* 32.7 (2015), p. 074001. DOI: 10 . 1088/0264-9381/32/7/074001.
- [66] Y Hang. “Some studies on the BHD sensing and control for A+”. In: *LIGO Document* (2018).
- [67] A Freise et al. “Frequency-domain interferometer simulation with higher-order spatial modes”. In: *Classical and Quantum Gravity* 21.5 (2004), S1067–S1074. DOI: 10 . 1088/0264-9381/21/5/102.
- [68] B. P. Abbott et al. “Binary Black Hole Population Properties Inferred from the First and Second Observing Runs of Advanced LIGO and Advanced Virgo”. In: *The Astrophysical Journal* 882.2 (2019), p. L24. DOI: 10 . 3847/2041-8213/ab3800.
- [69] S. L. Danilishin et al. “Quantum noise of non-ideal Sagnac speed meter interferometer with asymmetries”. In: *New Journal of Physics* 17.4 (2015), p. 043031.
- [70] P. Fritschel et al. “Alignment of an interferometric gravitational wave detector”. In: *Appl. Opt.* 37.28 (1998), pp. 6734–6747. DOI: 10 . 1364/AO . 37 . 006734.
- [71] F. Bayer-Helms. “Coupling coefficients of an incident wave and the modes of a spherical optical resonator in the case of mismatching and misalignment”. In: *Appl. Opt.* 23.9 (1984), pp. 1369–1380. DOI: 10 . 1364/AO . 23 . 001369.
- [72] H. Kogelnik. “On the Propagation of Gaussian Beams of Light Through Lenslike Media Including those with a Loss or Gain Variation”. In: *Appl. Opt.* 4.12 (1965), pp. 1562–1569. DOI: 10 . 1364/AO . 4 . 001562.
- [73] H. Kogelnik and T. Li. “Laser Beams and Resonators”. In: *Appl. Opt.* 5.10 (1966), pp. 1550–1567. DOI: 10 . 1364/AO . 5 . 001550.
- [74] D Babusci et al. “Alignment procedure for the VIRGO interferometer: Experimental results from the Frascati prototype”. In: *Physics Letters A* 226 (Feb. 1997), pp. 31–40. DOI: 10 . 1016/S0375-9601(96)00907-3.
- [75] M Mantovani and A Freise. “Evaluating mirror alignment systems using the optical sensing matrix”. In: *Journal of Physics: Conference Series* 122 (2008), p. 012026. DOI: 10 . 1088/1742-6596/122/1/012026.

- [76] D Babusci et al. “Alignment procedure for the VIRGO interferometer: experimental results from the Frascati prototype”. In: *Physics Letters A* 226.1 (1997), pp. 31 –40. ISSN: 0375-9601. DOI: [https://doi.org/10.1016/S0375-9601\(96\)00907-3](https://doi.org/10.1016/S0375-9601(96)00907-3).
- [77] H. Miao. “General quantum constraints on detector noise in continuous linear measurements”. In: *Phys. Rev. A* 95 (1 2017), p. 012103. DOI: [10.1103/PhysRevA.95.012103](https://doi.org/10.1103/PhysRevA.95.012103).
- [78] E. Knyazev, S. Danilishin, S. Hild, and F. Khalili. “Speedmeter scheme for gravitational-wave detectors based on EPR quantum entanglement”. In: *Physics Letters A* 382.33 (2018). Special Issue in memory of Professor V.B. Braginsky, pp. 2219 –2225. ISSN: 0375-9601. DOI: <https://doi.org/10.1016/j.physleta.2017.10.009>.
- [79] Y. Chen, S. L. Danilishin, F. Y. Khalili, and H. Müller-Ebhardt. “QND measurements for future gravitational-wave detectors”. In: *General Relativity and Gravitation* 43.2 (2011), pp. 671–694.
- [80] H. Miao, H. Yang, R. X. Adhikari, and Y. Chen. “Quantum limits of interferometer topologies for gravitational radiation detection”. In: *Classical and Quantum Gravity* 31.16 (2014), p. 165010. DOI: [10.1088/0264-9381/31/16/165010](https://doi.org/10.1088/0264-9381/31/16/165010).
- [81] W. Christopher et al. “Phase Sensitive Ponderomotive Opto-Mechanical Amplifier”. In: *LIGO Document* (2018).